The Electro - and Photochemical Reduction of CO_2 Mediated by Molecular Catalysts

Gaia Neri

Thesis submitted to the University of Liverpool in partial fulfilment of the degree of Doctor in Philosophy

Abstract

The Electro- and Photocatalytic Reduction of CO_2 Mediated by Molecular Catalysts

Gaia Neri

In this work, molecular complexes of transition metals have been synthesised and studied for their CO_2 reduction ability, either in an electrochemical or photochemical system, with a focus on complexes of nickel with derivatives of the macrocycle cyclam (cyc, cyc = 1,4,8,11-tetraazacyclotetradecane) which are well-known for being extremely active CO_2 reduction electrocatalysts in water.

The cyc framework has been modified with functional groups suitable for binding to semiconductor oxides to obtain the new complexes Ni(cycC) and Ni(cycP) (cycC = 1,4,8,11-tetraazacyclotetradecane-6-carboxylic acid, cycP = {[(1,4,8,11-tetraazacyclotetradecan-1-yl)methyl]phosphonic acid}), and their electrochemical activity towards CO_2 reduction in water has been evaluated. Modification of the ligand framework in the 6 position with a carboxylic acid does not change the CO_2 reduction activity of the complex Ni(cycC) at pH 5, through the use of electrochemical and spectroscopic techniques it was found that there is a large increase in the CO_2 reduction activity at pH 2, proposed to be due to the protonated carboxylic acid acting as an internal proton source. When Ni(cycC) was immobilised on TiO_2 electrodes it was possible to measure the rate of photoinduced electron transfer by using μs-s transient absorption spectroscopy (TAS) under argon in the presence of a hole scavenger, however the carboxylic acid proved unstable under CO_2.

Ni(cycP) was synthesised to provide a stronger binding group to the surface. It was found that functionalisation on the 1 position affected the CO_2 reduction activity in a negative way, however the complex was able to bind strongly to both TiO_2 and ZrO_2. ZrO_2 nanoparticles modified with Ni(cycP) and a ruthenium dye were able to reduce CO_2 to CO in water at pH = 4, with higher rates and turnover numbers compared to the components in solution, when illuminated with visible light. The improvement in activity for the heterogeneous photocatalyst was attributed to a faster electron transfer from the immobilised dye to the immobilised catalyst, calculated through detailed steady-state and transient spectroscopies, which prevented charge recombination. In collaboration with the University of Cambridge, Ni(cycP) has been immobilised on ZnSe quantum dots (QDs) and it has been proven to be an effective photocatalyst for CO_2 reduction to CO in water. We have carried out a detailed ultrafast TAS study on suspensions of the modified QDs, and it has been found that in the presence of a hole scavenger, upon illumination the electrons are excited from the VB to the conduction band (CB), however they rapidly decay to trap states close to the CB to generate a long lived signal. When Ni(cycP) is present, faster decay of the trapped electron signal is observed, which is assigned to fast electronic transfer from the QDs to Ni(cycP).

The knowledge of the mechanisms for CO_2 reduction will allow rational design of better catalysts for CO_2 reduction. In collaboration with the Rutherford Appleton Laboratories, we have designed an *in situ* spectroelectrochemical Sum Frequency Generation (SEC-SFG) technique using the ULTRA laser at the Central Laser facility. We have demonstrated the technique by analysing the redox behaviour of a well-known CO_2 reduction catalyst, $[Mn(bpy)(CO)_3Br]$. We were able to observe the redox species at the electrode surface as a Cyclic Voltammogram was carried out, and to propose the orientation of the species at the surface. Furthermore, the same technique has been applied to the study of the absorption mechanism of Ni(cycC) on the mercury surface, the first step in the catalytic cycle.

List of publications

During my PhD studies, the following papers in peer-reviewed journals have been published:

James J. Walsh, Gaia Neri, Charlotte L. Smith and Alexander J. Cowan, "Electrocatalytic CO_2 reduction with a membrane supported manganese catalyst in aqueous solution", *Chem. Commun.*, 2014,50, 12698-12701

Gaia Neri, James J. Walsh, Calum Wilson, Anna Reynal, Jason Y. C. Lim, Xiaoe Li, Andrew J. P. White, Nicholas J. Long, James R. Durrant and Alexander J. Cowan, "A functionalised nickel cyclam catalyst for CO_2 reduction: electrocatalysis, semiconductor surface immobilisation and light-driven electron transfer", ***Phys. Chem. Chem. Phys.***, 2015,**17**, 1562-1566

James J. Walsh, Charlotte L. Smith, Gaia Neri, George F. S. Whitehead, Craig M. Robertson and Alexander J. Cowan, "Improving the efficiency of electrochemical CO_2 reduction using immobilized manganese complexes", ***Faraday Discuss.***, 2015,**183**, 147-160

Gaia Neri, Iain M. Aldous, James J. Walsh, Laurence J. Hardwick and Alexander J. Cowan, "A highly active nickel electrocatalyst shows excellent selectivity for CO_2 reduction in acidic media", ***Chem. Sci.***, 2016,**7**, 1521-1526

Gaia Neri, Mark Forster, James J. Walsh, C. M. Robertson, T. J. Whittles, Pau Farràs and Alexander J. Cowan, "Photochemical CO_2 reduction in water using a co-immobilised nickel catalyst and a visible light sensitiser", ***Chem. Commun.***, 2016,**52**, 14200-1420.

Acknowledgements

There is a great deal of people which I need to thank, which have contributed, in one way or another, to this thesis. The common denominator between them is their complete belief that I would be able to do this, so much so that they almost convinced me too.

First and foremost, I would like to thank my supervisor Dr Alex Cowan. He has been the best supervisor a PhD student could hope for, and I have the utmost respect for him. He has been a constant source of knowledge and inspiration, and I have learned so much from him. I would also like to thank Alex for creating such good group atmosphere, making it a pleasure to go to work (almost) every day, for teaching me the importance of Friday experiments and for allowing us to build hydrogen powered dolls houses as part of our curriculum.

Secondly, I would like to thank my Post Doc, Dr Jamie Walsh. I have lost count of all the times I went to him for help and advice, and received more than I asked for. He has been a great mentor, great pub buddy, friend and awesome brewer.

I gratefully acknowledge all the colleagues who helped with measurements carried out for the completion of the thesis: our collaborator Dr Anna Reynal, for the help with the Ni(cycC) TAS data; the Reisner group at the University of Cambridge, especially Mr Constantin Sahm and Dr Moritz Kuehnel, for the successful collaboration on the QDs/Ni(cycP) work; our collaborator Dr Paul Donaldson for the setting up and running of the SFG experiments; thank you to Dr Laurence Hardwick and Dr Iain Aldous for the help with the RDE voltammetry, Mr Tom Whittles for the XPS measurements and Mr Jonathan Lee and Mr Mark Forster for all their guidance on the TAS measurements.

Thank you to all the people in the Stephenson Institute, for making it such a lovely place to work. Many of you are dear friends as well as colleagues.

Thank you to the "original Hardwicks", Nick, Iain and Arthur, for welcoming me as an honorary member of their group, and for inviting me to the pub that first Friday of 2013. The wild nights in Krazyhouse on random days have been the best. Thanks to the two musketeers: Arthur for all the smoke/venting-about-chemistry breaks, and to Iain for all the broken "no more than half an hour of work-talk" nights, and for the Poppins. Thanks to Chris for all the Sunday brunch-plus-afternoon pint spent talking about the meaning of life (sort of).

All things considered, my PhD has been a really good period of my life, but for the writing up months, which have been quite stressful. I could not have gone through it while staying relatively sane without the Italian team: Silvia, Stefano and Charlotte (she is learning Italian, she is pretty much one of us now). Their constant support has been incredible, they have kept me happy with bake off parties, red walls and Christmas shenanigans, respectively. To them I would like to say: "Coraggio, pazienza e samba per tutti!"

A special acknowledgement goes to my family, which have not stopped believing in me for a second, and have tolerated my living far away with grace, knowing that I am happy with what I am doing. They are very much like an unmovable mountain, always there when I need them to be, even if I don't know that I do. Grandad, thank you for all the ice-creams.

I would like to thank Mark. Thank you especially for showing me the artistry of Nicolas Cage. Thank you for ham and cheese crumpet sandwiches. Thank you for guiding me across the streets, and for constantly looking after me. Thank you for being you.

Last, but certainly not least, I would like to thank myself: Gaia, well done. I am very proud of you.

Table of abbreviations

The following is a list of commonly abbreviated terms used throughout the thesis. Each term will also be explained the first time that they will be referred to in the main text.

ATR	Attenuated Total Reflectance
bpy	2,2'-Bipyridine
CB	Conduction Band
CV	Cyclic Voltammogram
cyc	1,4,8,12-Tetraazacyclotetradecane
cycC	1,4,8,12-Tetraazacyclotetradecane-6-Carboxylic Acid
cycP	{[(1,4,8,11-Tetraazacyclotetradecan-1-yl)Methyl]Phosphonic Acid}
DFG	Difference Frequency Generation
DFT	Density Functional Theory
DMA	Dimethylamine
DMAET	Dimethylamino Ethanethiol
DMF	Dimethylformamide
DPSC	Double Potential-Step Chronocoulometry
DSSC	Dye-Sensitised Solar Cell
EMIM BF_4	1-Ethyl-3-Methylimidazolium Tetrafluoroborate
Eq.	Equation
EWG	Electron Withdrawing
FE	Faradaic Efficiency
FOWA	Foot-Of-The-Wave Analysis
FTIR	Fourier-Transform Infrared
FTO	Fluorine-Doped Tin Oxide
FWHM	Full width at half maximum
GCE	Glassy Carbon Electrode

HMDE	Hanging Mercury Drop Electrode
IR	Infrared
LSV	Linear Sweep Voltammogram
MeCN	Acetonitrile
MeOH	Methanol
MWCNT	Multi-Walled Carbon Nanotubes
NHE	Normal Hydrogen Electrode
NMR	Nuclear Magnetic Resonance
OTTLE	Optically Transparent Thin Layer Electrochemical Cell
PTFE	Polytetrafluoroethylene
QD	Quantum Dot
RDE	Rotating Disc Voltammetry
RPM	Rotations Per Minute
RuP	$[Ru^{II}$(2,2'-Bipyridine)2(2,2'-Bipyridine-4,4'-Diylbis(Phosphonic Acid)]
SEC	Spectroelectrochemistry
SEIRAS	Surface Enhanced Infrared Absorption Spectroscopy
SFG	Sum Frequency Generation
SHE	Standard Hydrogen Electrode
SHG	Second Harmonic Generation
TAS	Transient Absorption Spectroscopy
$TBAPF_6$	Tetrabutylammonium Hexafluorophsophate
TEA	Triethylamine
TEOA	Triethanolamine
THF	Tetrahydrofuran
TOF	Turnover Frequency
TON	Turnover Number
TRIR	Time Resolved Infrared
VB	Valence Band

Contents

“Per me si va ne la città dolente,
per me si va ne l'etterno dolore,
per me si va tra la perduta gente.
Giustizia mosse il mio alto fattore:
fecemi la divina potestate,
la somma sapienza e 'l primo amore;
dinanzi a me non fuor cose create
se non etterne, e io etterno duro.
Lasciate ogne speranza, o voi ch' intrate.”
-Dante Alighieri

1

Introduction

1.1 CO_2 as a feedstock

The issues related with the depletion of fossil fuels and global warming have stimulated research into alternative, sustainable energy sources in recent decades. The major drawback with renewable sources such as solar and wind power is their intermittency, which makes the exclusive use of such resources impractical. Research into energy storage as a way to solve the intrinsic intermittency of renewable sources, and allow the transport of the energy produced, has therefore seen significant attention in past years.

The reduction of carbon dioxide coupled with the oxidation of water is considered a promising approach to obtain carbon based fuels of various nature, as the products of the CO_2 reduction reaction are highly energy dense, however the one-electron reduction of CO_2 to $CO_2^{\bullet-}$ is highly unfavourable (Eq. (1)).[1] The large overpotential required for this reaction is due to the large reorganisation energy between the linear CO_2 molecule and the bent radical anion. In contrast, proton coupled multi-electron steps can reduce CO_2 to more stable and useful products with much lower energies (Eq. (5)-(6)).

Equation 1-6 - Standard thermodynamic potentials for the reduction of CO_2 at pH = 7 (vs. NHE).

$$CO_2 + e^- \rightarrow CO_2^{\bullet-} \quad E^\circ = -1.90\ V \tag{1}$$

$$CO_2 + 2H^+ + 2e^- \rightarrow CO + H_2O \quad E^\circ = -0.53\ V \tag{2}$$

$$CO_2 + 2H^+ + 2e^- \rightarrow HCO_2H \quad E^\circ = -0.61\ V \tag{3}$$

$$CO_2 + 6H^+ + 6e^- \rightarrow CH_3OH + H_2O \quad E^\circ = -0.38\ V \tag{4}$$

$$CO_2 + 8H^+ + 8e^- \rightarrow CH_4 + 2H_2O \quad E^\circ = -0.24\ V \tag{5}$$

$$2H^+ + 2e^- \rightarrow H_2 \quad E^\circ = -0.41\ V \tag{6}$$

Of particular interest is the two-electron, two-proton reduction of CO_2 to carbon monoxide (Eq. (2)), as it can be accessed at low overpotentials and with the lowest number of electron transferred (CO_2 reduction to methanol occurs at a lower thermodynamic potential, however the requirement of six electrons is kinetically more challenging), and CO can be used as syngas (synthesis gas, mixtures of CO and H_2) to synthesise a wide range of carbon products (Scheme 1).[2]

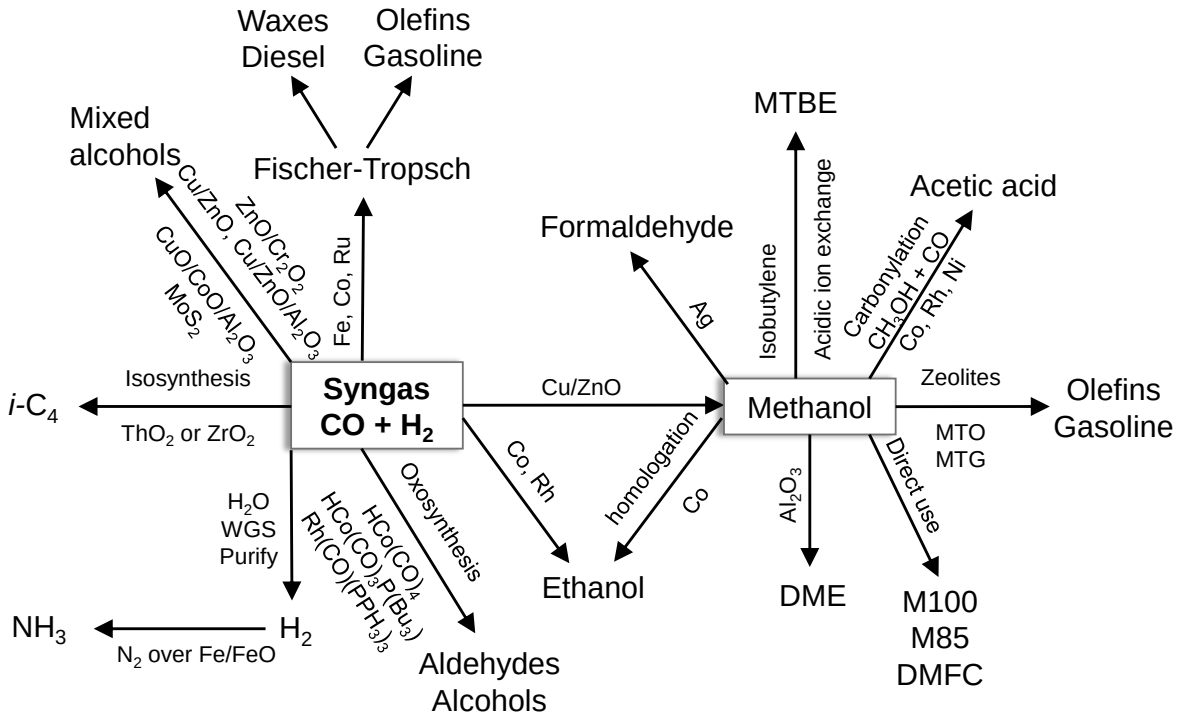

Scheme 1 – Various syngas conversion processes. Reproduced from ref. [3]

Sustainable CO_2 reduction can be achieved thermally (via hydrogenation), electrochemically and photochemically. In the electrochemical case, the use of photovoltaic devices could be envisaged to apply the required potential to drive the electrocatalysis. In photochemical CO_2 reduction, excitation of a light absorber generates charge carriers, which can be transferred to CO_2 either directly (if the light absorber is also the catalyst) or to a CO_2 reduction catalyst.

Despite the progress that has been made both in the electrochemical and photochemical reduction of CO_2, both processes are still far from being able to compete with fossil fuels. This is due to several reasons, including (i) the use of costly materials, organic solvents and, in the case of the photocatalytic CO_2 reduction, of electron donors to prevent charge recombination, (ii) low efficiency, and (iii) high overpotentials.[4,5] For a CO_2 reduction process to be scalable all of these parameters need to be largely improved from the current benchmarks. As the mechanisms that govern CO_2 reduction are for the most part unknown, the investigation of such mechanisms is highly desirable, as it might prove invaluable in the design of better performing CO_2 reduction systems.

1.2 Electrocatalytic CO_2 reduction

1.2.1 Heterogeneous electrocatalysis

The CO_2 reduction in water at Hg and amalgam electrodes has been studied since 1870.[6] Pioneering studies of CO_2 reduction at alternative metal electrodes to Hg or lead were carried out by Hori *et al.* in 1985[7] and in the following years.[8] Since then a wide variety of metal electrodes have been tested for CO_2 reduction, with different metals yielding different CO_2 reduction products: Pb, Hg, In, Sn, Cd, Tl, and Bi make almost exclusively formate and Au, Ag, Zn, Pd, and Ga make predominantly CO.[8] Interestingly, it was found that Cu electrodes reduce CO_2 to a wide distribution of products such as methane, ethylene, and ethanol,[9] however as it has been shown that the intermediate of the reaction is CO, Cu is often considered a CO formation metal.[10] While metal electrodes show high faradaic efficiencies (FE) and current densities, the main drawback remains the large overpotentials required to drive the reaction.

1.2.2 Homogeneous CO_2 reduction

Transition metal complexes are able to coordinate CO_2 with various degrees of strength, and it has been shown that several coordination modes are possible, (Scheme 2).[11–16]

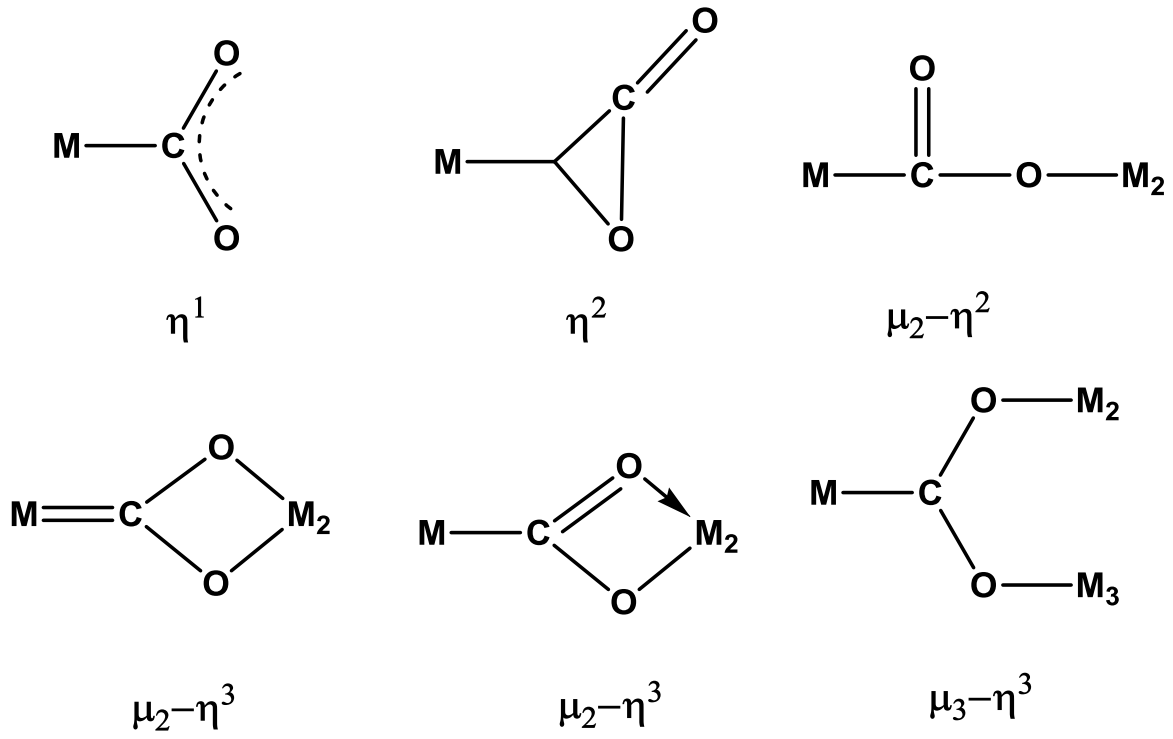

Scheme 2 – Some structural types of metal-CO_2 complexes.

In Scheme 2, the letter η indicates the number of coordination bonds, while the letter μ indicates the number of metal atoms involved in the bonding of one CO_2. All the coordination complexes of CO_2 with transition metals involve a bent structure of the ligand, with complexes showing σ bonding between the metal centre and the carbon atom being the most common, and the linear, O-coordinated mode (M-O=C=O) being very rare.[17] Due to the similarity between the bent structures of CO_2 when coordinated to transition metals and the one electron reduction product $CO_2^{\cdot-}$, transition metal complexes have been studied as homogeneous catalysts for CO_2 and many examples of selective reduction of CO_2, mainly to CO, by molecular catalysts at relatively low overpotentials exist. Several excellent reviews cover the progresses made in the field of homogeneous electrocatalysis,[18–21] here we will attempt to summarise the key discoveries.

The first reports of homogeneous electrocatalysts for CO_2 reduction were in the late 1970s, when metal complexes of phtalocyanins and porphyrins were reported to act as CO_2 reduction electrocatalysts by Toshima *et al.*,[22,23] which showed the production of formate by complexes of cobalt with the porphyrins under study, however they did not report accurate quantification of the reaction products. Since then, several classes of metal complexes have been found to have the ability to catalyse CO_2 reduction.

Following the initial study by Toshima *et al.*[23], porphyrin complexes, with particular regards to iron, have been studied in great detail by Savéant and co-workers.[19] The iron complex of tetraphenylporphyrin (TPP) was found to be efficient for the reduction of CO_2 to CO in DMF (dimethylformamide) ($V_{CO2/CO}$ = -1.45 V_{NHE}), however it was found that the stability of the catalyst was rather poor, due to carboxylation of Fe(TPP) and its subsequent degradation. The addition of Mg^{2+} was found to greatly improve the catalytic activity of Fe(TPP),[24] as well as the addition of weak Brönsted acids such as trifluoroethanol.[25] The increase in catalytic activity was attributed to the stabilisation of the Fe^0(TPP) adduct with CO_2 by the alcohol, and subsequent proton transfer to the adduct.[26]

Alongside iron porphyrins, polypyridyl tricarbonyl complexes of rhenium of the type [Re(L)$(CO)_3$X] have received significant attention since the first report of the activity of [Re(bpy)$(CO)_3$Cl] (bpy = 2,2'-bipyridine) by Lehn and co-workers.[27] The complex is able to reduce CO_2 to CO at a potential of -1.2 V_{NHE} with a 99% FE in DMF solution with 10% added water. The ability to selectively reduce CO_2 in the presence of a large amount of protons in the solution encouraged a number of studies by several research groups,[28] and various modifications of the bpy ligands, solvent mixtures and supporting electrolytes have been tested in order to improve the activity of the CO_2 reduction and to understand the mechanism of the reaction.[29] Similarly to the porphyrin example, the addition of Brönsted acids to solutions of [Re(bpy)$(CO)_3$(py)] (py = pyridine) in acetonitrile (MeCN) appeared to increase the catalytic

activity of the complex, when compared to the dry solutions.[30] Kubiak *at al.*[31] modified the bpy ligand in the 4,4' positions with various substituents and found that the [Re(*t*bu-bpy)$(CO)_3$Cl] complex (where *t*bu-bpy = 4,4'-*tert*-butyl-2,2'-bipyridine) was much more active than the unmodified complex, reaching a second-order rate constant of 1000 M^{-1} s^{-1}, as calculated by rotating disc voltammetry (RDE).

The electrocatalytic reduction of CO_2 by [Mn(bpy)$(CO)_3$Br] was first reported by Deronzier *et al.*[32] in 2011, as a cheaper alternative to the analogue [Re(bpy)$(CO)_3$Cl] catalyst.[29] Unlike its rhenium counterpart, the Mn complex has been shown to be active for CO_2 reduction only in the presence of a high proton concentration (often >5% water).[33] Typical cyclic voltammograms (CVs) of [Mn(bpy)$(CO)_3$Br], under argon and CO_2 in a mixed MeCN/H_2O (5%) solvent are shown in Figure 1(a). Under argon, two main reductions are observed, at -1.26 $V_{Ag/AgCl}$ and -1.48 $V_{Ag/AgCl}$, accompanied by two oxidations, at *ca.* -1.1 $V_{Ag/AgCl}$ and *ca.* -0.1 $V_{Ag/AgCl}$ (the potentials have been converted to the Ag/AgCl reference electrode by converting from the ferrocene *pseudo* reference reported in the figure). The *quasi*-reversible nature of the redox events implies the presence of chemical steps and the nature of the species formed in the experiment has been previously investigated with IR-SEC (Infrared Spectroelectrochemical) techniques (Figure 1(b)).[34] It was found that following the first reduction, loss of the bromide ligand and dimerisation to form [$Mn_2(bpy)_2(CO)_6$] occurs (-1.26 $V_{Ag/AgCl}$). Reduction of the dimer occurs at -1.48 $V_{Ag/AgCl}$, with the dimer breaking apart to form the doubly-reduced penta-coordinated species [Mn(bpy)$(CO)_3]^-$. On the return potential sweep [$Mn_2(bpy)_2(CO)_6$] forms again at the first oxidation wave at -1.1 $V_{Ag/AgCl}$, and is oxidised at -0.1 $V_{Ag/AgCl}$ to form the initial complex. On the second CV cycle, a new reduction feature is often observed at approximately 100 mV (*ca.* 1 $V_{Ag/AgCl}$) positive of the reduction potential of [Mn(bpy)$(CO)_3$Br] which is assigned[35] to the one electron reduction of a solvo complex

$[Mn(bpy)(CO)_3(solv)]^+$, which can also form during the oxidation of $[Mn_2(bpy)_2(CO)_6]$ during the previous potential cycle.

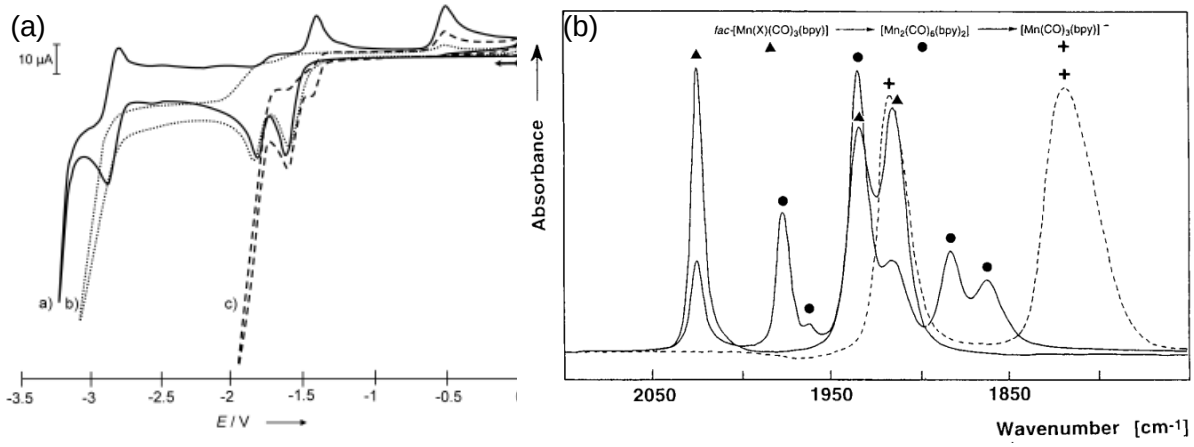

Figure 1 – (a) CVs of $[Mn(bpy)(CO)_3Br]$ at a concentration of 1 mM in MeCN with 0.1 M $TBAPF_6$ (Tetrabutylammonium Hexafluorophsophate) on a glassy carbon electrode (GCE) a) under Ar and under CO_2, b) in dry solvent and c) with 5 % of H_2O; reproduced from ref. [32] (b) IR-SEC of 0.01 M $[Mn(bpy)(CO)_3Br]$ in THF (Tetrahydrofuran) (0.3 M $TBAPF_6$), reproduced from ref. [36]

Upon addition of CO_2 to the dry solution, no significant difference is noted on the CV, Figure 1(a), however doping the solution with a source of protons causes a large increase in current density at the potential corresponding to the second reduction (-1.48 $V_{Ag/AgCl}$), which has been demonstrated to be due to CO_2 reduction to CO, with $[Mn(bpy)(CO)_3]^-$ proposed to be the primary catalytically active species.[32] Based on these SEC measurements and a series of DFT (Density Functional Theory) studies[28,37] a mechanism for CO_2 reduction *via* $[Mn(bpy)(CO)_3]^-$ has been proposed, Scheme 3.[32,33,37]

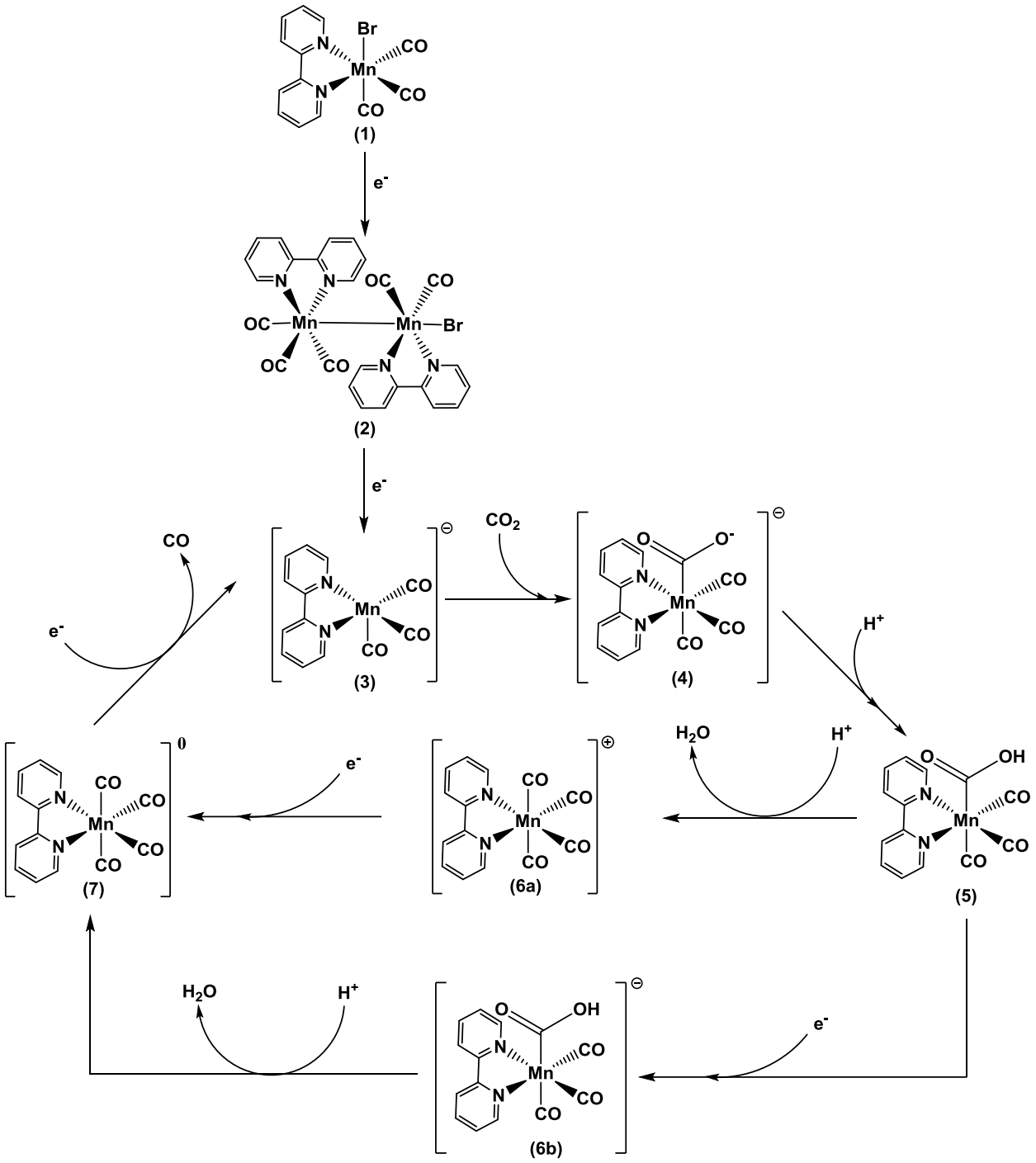

4

Scheme 3 – Proposed mechanism for the electrochemical CO_2 reduction by [Mn(bpy)(CO)$_3$Br].[37]

The active catalytic species has been shown to be the doubly reduced species **3**, which in the first step of the catalytic cycle binds CO_2 with the addition of a proton to form **5**; one electron

reduction leads to the formation of the Mn^0 complex **6b**, which reacts with one more proton to lead to the formation of complex **7**, which finally releases one molecule of carbon monoxide to yield the catalytically active species **3**. The mechanism has been studied through the use of various techniques, such as TRIR (Time Resolved Infrared) spectroscopy,[38] IR-SEC spectroscopy[39,40] and DFT.[37] Of particular note is a pulse-radiolysis and TRIR study that formed a formate bound Mn complex and measured the rate of dimer formation, however many of the key intermediate species in Scheme 3 have yet to be experimentally observed. Furthermore, the presence of a second possible mechanism pathway has also been proposed (Scheme 3), where the second protonation occurs before the second electron transfer, and it is not yet clear which of the two catalytic pathways is the dominant one. In addition, it has been shown that in some derivatives of [Mn(bpy)$(CO)_3$Br] CO_2 reduction can occur *via* interaction of the CO_2 directly with the dimer species.[38]

Since the initial report in 2011 numerous groups have reported modified catalysts based on Mn diimine carbonyls for CO_2 reduction, making this one of the most heavily studied classes of CO_2 reduction catalysts. Kubiak *et al.*[40] have examined the electrocatalytic activity of [Mn(*t*bu-bpy)$(CO)_3$Br] compared to the complex reported by Deronzier[35] and to the rhenium analogue[41] and found that the substituted complex showed similar catalytic activity as the Re counterpart, whilst the activity, and stability, of [Mn(bpy)$(CO)_3$Br] was found to be lower than for the Re complex. In our research group we have modified the bpy in the 4,4'- position[42] with different substituents in order to evaluate the influence of electron donating and electron withdrawing groups (EWG) on catalysis, and found that the addition of EWG such as –COOH shifts the potential of the second reduction, thought to be the one leading to the doubly reduced active species, however under CO_2 only minimal catalytic activity was shown, likely due to the decreased nucleophilicity of the complex upon addition of EWG.

In an effort to reduce the overpotential for CO_2 reduction, a Mn complex with a bulky bpy ligand (mesbpy = =6,6′-dimesityl-2,2′-bipyridine) was synthesised by Kubiak and co-workers.[43] Due to the steric hindrance of the mesbpy ligand, dimerisation was found to be inhibited, and the doubly reduced species $[Mn(mesbpy)(CO)_3]^-$ was found at potentials *ca.* 300 mV more positive than for $[Mn(bpy)(CO)_3Br]$ under argon, however in this initial study the CO_2 reduction catalytic current was found at *ca.* -1.4 V_{NHE}. It was hypothesised that a slow catalytic pathway was occurring in the potential region between the formation of $[Mn(mesbpy)(CO)_3]^-$ and the catalytic current, and in a subsequent study the same authors demonstrated that the addition of a Lewis acid such as Mg^{2+} increases the rate of the slow catalysis by one order of magnitude, at one of the lowest overpotentials ever reported for a molecular electrocatalyst (*ca.* 0.3-0.45 V).

While the above examples show excellent progress has been made in the past decades in the development of efficient and selective CO_2 reduction homogeneous electrocatalysts, all of the studies presented were carried out in organic solvents, often with the addition of small percentages of either water or a weak organic acid to provide a source of protons. Organic solvents are sometimes chosen due to poor solubility of the complexes in aqueous solution, however more commonly the main reason for the choice is that the selectivity for CO_2 reduction is greatly reduced in favour of hydrogen evolution in the proton-rich environment of water, as this latter reaction is favoured by the more positive standard thermodynamic potential ($E^0_{H^+/H_2} = -0.41$ V_{NHE} at pH = 7) compared to the CO_2 reduction reactions (Eq. (1)-(5)). To date, there are only a few examples of catalysts which are selective in water, and some of the most prominent are summarised in Table 1.

Table 1 – Homogeneous electrocatalysts for CO_2 reduction active in aqueous solutions; [(a)] calculated from the potentials where bulk electrolysis experiments were carried out.

	Catalyst	*Electrolyte/Electrode*	*Overpotential[(a)]*	*Major Product*	*FE*	*Ref*
1	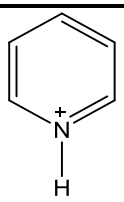	0.1 M KCl + H_2SO_4, pH = 5.4 / Pd	200 mV	CH_3OH	30%	[44]
2	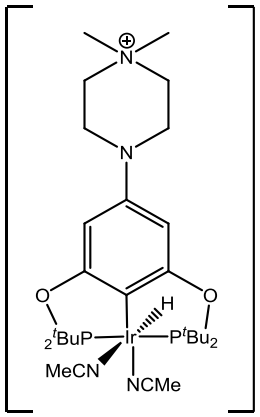	0.1 M $NaHCO_3$ pH = 7, 1% MeCN / GCE	1000 mV	$HCOO^-$	82%	[45]
3	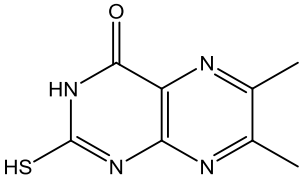	0.1 M KCl, phosphate buffer, pH = 6.3 / GCE	0 mV	CH_3OH	23%	[46]
4	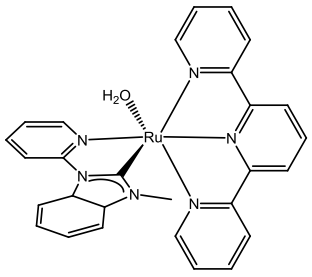	0.1 M $NaHCO_3$, pH = 6.7 / GCE	780 mV	CO	66%	[47]

5	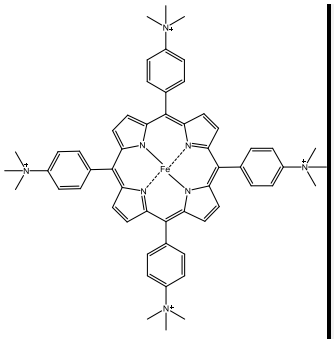	0.1 M KCl, pH = 6.7/GCE	400 mV	CO	98%	[48]
6	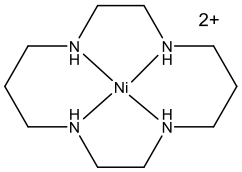	0.1 M KCl/GCE	770 mV	CO	90%	[49]

1.2.3 Ni(cyc) as a CO_2 reduction catalyst in water on Hg

Amongst the most studied classes of molecular catalysts for CO_2 reduction in water are macrocycles of nickel and cobalt; the electrochemical reduction of CO_2 to CO by tetraazamacrocycles complexes was first reported by Fisher and Eisenberg in 1980[50], where they studied derivatives of cyc (1,4,8,11-tetraazacyclotetradecane) complexated with either Co or Ni (Scheme 4).

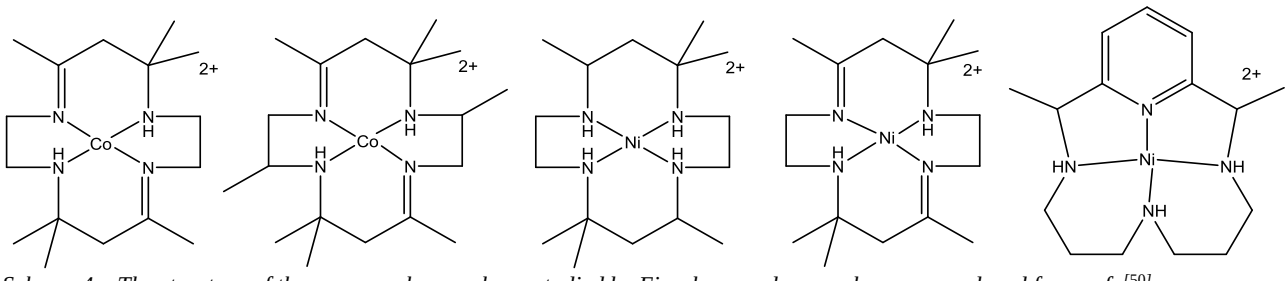

Scheme 4 – The structure of the macrocycle complexes studied by Eisenberg and co-workers – reproduced from ref. [50].

The complexes were shown to be selective for the production of CO over any other carbon products or H_2. No mechanistic insight was proposed at the time, save for the observation that when catalysis was carried out in dry organic solvents (e.g. MeCN) no products were observed

until protons were added to the solution. Subsequently, Sauvage *et al.*[51–53] published a series of detailed electrochemical studies which were focused on the complex Ni(cyc) ([Ni(1,4,8,11-tetraazacyclotetradecane)]$^{2+}$) in water (Scheme 5).

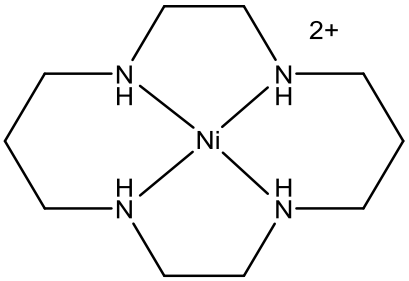

Scheme 5 – Structure of Ni(cyc), drawn in a planar form and omitting hydrogen atoms in the carbon backbone for clarity.

They highlighted that the nickel complex was the most efficient with respect to other metal complexes of the same ligand (such as Co and Fe) and Ni complexes of modified macrocycles. The studies showed that the substrate of the reaction is "free" (solvated) CO_2 in solution, and that the complexes could not react with bicarbonate and carbonate species that form when CO_2 is dissolved in water.[52] This equilibrium is highly dependent on the pH of the solution, and thus the optimal conditions of operation of the complex were established to be between pH values of 4-5. Above pH 5 the catalysis was shown to decrease significantly, due to solvated CO_2 not being present in solution in appreciable concentrations; below pH 4 the complex has been reported[52,54] to lose selectivity, due to the increasing competition of protons to form nickel hydrides. Furthermore, it was shown that the concentration of the complex in solution was not critical in the catalytic current enhancement observed under CO_2,[52,54,55] leading to the assumption that the active species was adsorbed on the electrode surface, with a very small

contribution from the bulk complex in solution. On the basis of their study, the authors[52] proposed a reaction mechanism (Scheme 6):

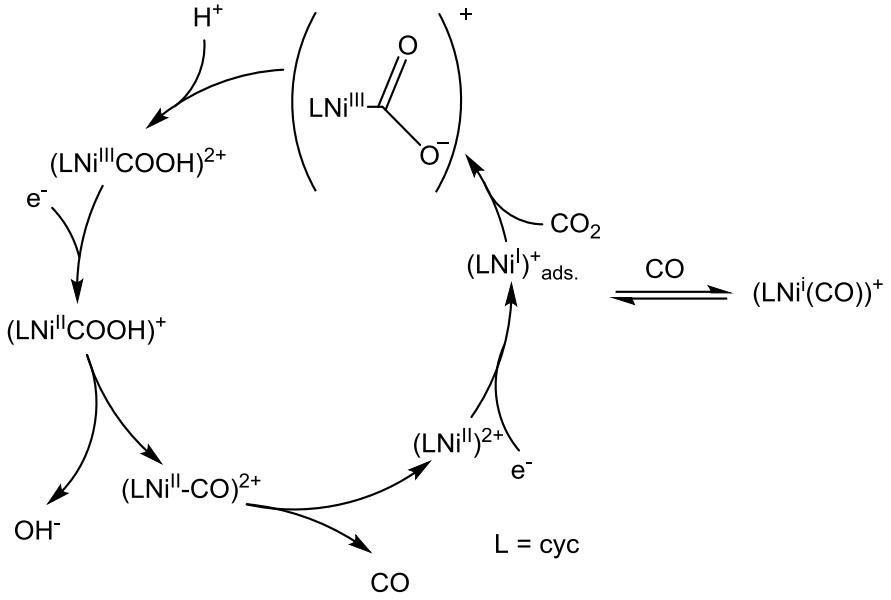

Scheme 6 – Catalytic reaction mechanism for the reduction of CO_2 to CO in water on mercury electrodes by Ni(cyc) as postulated by Sauvage et al.[52]

The efficiency of the complex was attributed to the size of the macrocycle ring, which is known to greatly stabilise $Ni^{II/I}$ complexes,[56,57] and the accessibility of the Ni centre due to the square planar coordination of the ligand. Furthermore, the authors suggested that the formation of the Ni carbonyl complex could be helped by the formation of hydrogen bonds between CO_2 oxygens and the macrocyclic amine protons. This was supported by X-ray crystallography studies that showed an electrostatic repulsion between the amine protons and water molecules, which indicate that the amine hydrogens are slightly acidic, and thus would be able to form hydrogen bonds with the basic oxygen of CO_2. This hypothesis was further reinforced by DFT calculations carried out by Fujita *et al.*[58]

The adsorption of Ni(cyc) to mercury electrodes has been further proved in several studies,[59,60] where amongst other experiments, the preparation of modified electrodes (mercury thin films)

with a preadsorbed Ni^{II} complex was attempted. However the attempts failed, suggesting that the adsorbed species was electrogenerated, i.e. a Ni^{I} species. A detailed investigation on the adsorption mechanism was presented by Anson *et al.*[61] The study showed how the reduced $Ni^{I}(cyc)^{+}$ is indeed the adsorbed species, and it is detectable at the electrode surface at potentials much more positive than the formal redox potential for the $Ni^{II/I}$ couple. They concluded that the one-electron reduction and adsorption on the surface of the electrode are a concerted process, and hypothesised that the stabilisation of the reduced species by the Hg atoms is what causes the adsorption at such positive potentials. A potential dependence on the adsorption was found, with the surface coverage corresponding to roughly half a monolayer for potentials between -0.6 and -1.2 V_{SCE} and reaching a full monolayer at potentials between -1.2 and -1.3 V_{SCE}.

The nature of the adsorbed species has been the subject of numerous investigations, both experimental and theoretical, however to date the structural form on the surface remains unknown. *Ab initio* studies[62,63] have used square planar complexes of nickel with ammonia molecules as a model for Ni(cyc), and found that $Ni^{I}F(NH_3)_4$ can bind CO_2 , but $[Ni^{I}(NH_3)_4]^{+}$ or $[Ni^{II}F(NH_3)_4]^{+}$ cannot. It was suggested that mercury in the adsorbed Ni^{I} species might have the same role as fluorine as the fifth ligand. Other studies[54,61,64] have proposed that the reductive adsorption is accompanied by a structural rearrangement of the complex.

It is well-known that the unmodified complex Ni(cyc) exists in solution as a mixture of the five possible conformers,[65,66] Scheme 7, of which the *trans*-I and *trans*-III are by far the most abundant (~15% and ~85%, respectively). Furthermore, the *trans*-III isomer has been shown[67] to readily interconvert between the diamagnetic, square-planar coordination and the paramagnetic, octahedral geometry. This equilibrium, and therefore the presence of paramagnetic species, is the origin for the very broad ^{1}H-NMR (NMR = nuclear magnetic resonance) spectra that characterise these complexes. DFT calculations have suggested that the

adsorbed form of the reduced complex is in the *trans*-I form.[58] In this conformation, all the amine protons are on the same side of the macrocycle, and are readily available for hydrogen bonding to CO_2.

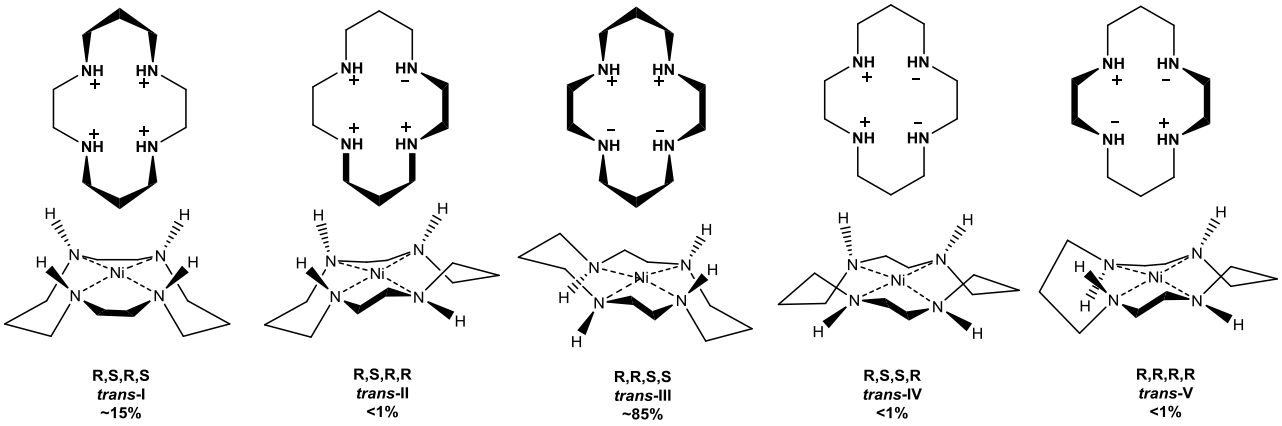

Scheme 7 – The five possible conformational isomers of Ni(cyc) in solution, drawn according the two most common conventions for clarity; + indicates that the hydrogen of the amine group is above the plane of the macrocycle and – indicates that it is below the plane. Both accepted nomenclatures are also reported.

Due to the remarkable properties of Ni(cyc) for the electrocatalytic reduction of CO_2, several studies have been focused on modifying the ligand framework with the aim of improving the catalytic performance. The aza-macrocycle has been modified (Scheme 8) by changing the carbon framework, either adding substituents (L1, L2) or various degrees of unsaturation (L3), or by functionalising the amine groups (L4).

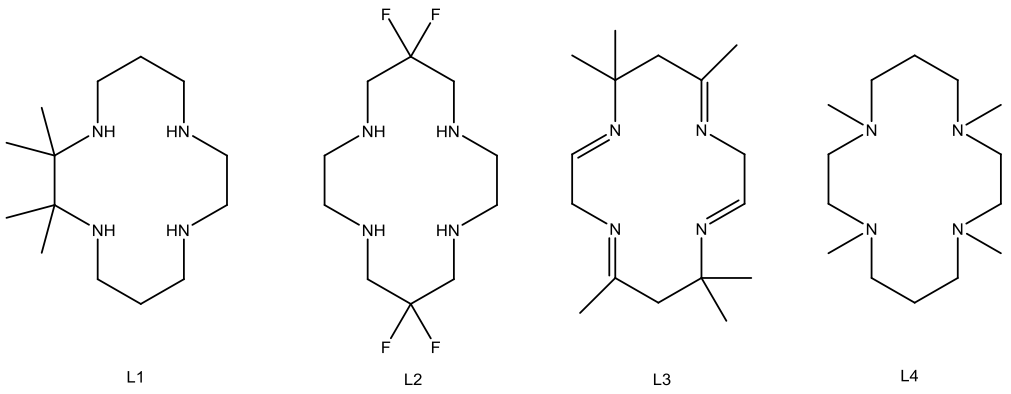

Scheme 8- Examples of functionalisation of the cyc framework with the aim of improving catalysis. Reproduced from [58,68,69].

However, to date almost all the new complexes that have been synthesised and tested have been shown to be less efficient than the parent complex,[70] with complexes which have been N-functionalised showing the highest decrease in activity and selectivity towards CO_2 reduction to CO.[50,53,58,69,71,72] Although sequential methylation of the nitrogens[69] causes a substantial shift in the $Ni^{II/I}$ couple towards positive potentials, the onset for catalysis remains unchanged when compared to the parent Ni(cyc). Furthermore, the catalytic current under CO_2 decreases steadily with the increasing number of methyl groups, becoming negligible with the tetramethylated complex. The reduced catalytic activity upon methylation was attributed to two factors: the reduced ability of the methylated complexes to adsorb on the surface of the Hg electrode due to steric hindrance, and the absence of the amine hydrogens. The N-methylated complexes have been recently studied on a GCE,[49] and the same trend in catalytic activity was shown, indicating that a change in the adsorption on mercury is not the main reason for the decrease in catalytic activity for these complexes. Studies in which the modification was aimed towards obtaining different major conformation geometries in solution were somewhat more successful. Fujita and co-workers[64] initially modified the cyc framework with methyl groups on the carbon backbone (Scheme 9, RSSR-HTIM, RRSS-HTIM and DMC) to obtain complexes which showed different dominant conformers in solution.

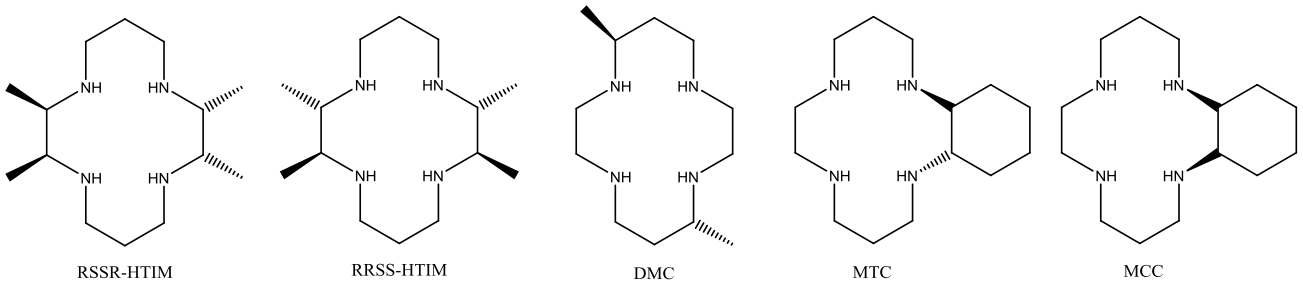

Scheme 9 – Structure of the ligands synthesised by Fujita et al.[54,64]

It was shown that RRSS-$[Ni(HTIM)]^{2+}$ and $[Ni(DMC)]^{2+}$ exhibit larger catalytic currents and more positive onset potentials than the unmodified complex.[64] At the same time, RSSR-

$[Ni(HTIM)]^{2+}$ showed a worse performance than Ni(cyc). The authors proposed that the differences in catalytic activity could be due to (a) structural differences in solution determining different adsorption rates on the mercury electrode, and (b) methyl groups in axial positions hindering the interaction between the metal centre and the mercury electrode. The same authors[54] compared the activity of RRSS-$[Ni(HTIM)]^{2+}$ and $[Ni(DMC)]^{2+}$ with some new complexes which have been modified with a cyclohexane ring to have a fixed conformation (Scheme 9, MTC and MCC). The new catalyst $[Ni(MTC)]^{2+}$ showed onset potentials and catalytic current densities similar to RRSS-$[Ni(HTIM)]^{2+}$, and was more active than $[Ni(MCC)]^{2+}$, confirming the assumptions made in the previous study.

1.2.4 Ni(cyc) on glassy carbon electrodes

Very few studies to date have been devoted to the electrocatalytic reduction of CO_2 by Ni(cyc) on electrodes materials other than mercury. This is due partly to the extended potential window of mercury in aqueous solutions for reductive electrochemistry, which allows the analysis of a potential electrocatalyst without the influence of proton reduction at the electrode complicating the voltammogram.[73] Largely, for a long time in the literature it was assumed that the bulk complex in solution was completely inert to CO_2 reduction, and that the interaction that caused the adsorption of the complex to the electrode surface was peculiar of mercury. While a small number of studies have demonstrated that the ability of Ni(cyc) to adsorb is not restricted to Hg, showing good catalytic currents on tin, lead, and thallium[74], the activity was still lower than on mercury.

Recently Kubiak *et al.*[49] have shown that Ni(cyc) is active on GCEs. This study showed that the complex can be catalytic for CO production over H_2 either in water or in MeCN, however the activity on GCE was found to be much lower than on mercury (the peak of the CV under CO_2 on GCE was 1 mA/cm^2, compared to the value of 11 mA/cm^2 obtained for mercury). Furthermore, a turnover number (TON) of 4 was found at prolonged bulk electrolysis times, in

contrast to the very high numbers found on mercury[52] (over 2000 after two hours at micromolar concentrations). A subsequent study was recently published[75] where the authors investigate in detail the mechanism on GCE in MeCN solutions. Being able to treat the complex as homogeneous allowed for the clarification of several key steps, hypothesised to be common to GCE and Hg electrodes. In addition, IR-SEC measurements confirmed that the decrease in activity often found at longer catalysis times is due to the formation of insoluble adducts of the complex with CO, $[Ni^{I}(cyc)(CO)]^{+}$, as previously shown through electrochemical experiments under CO[76]. DFT calculations of the structure of $[Ni^{I}(cyc)(CO)]^{+3}$ revealed that when CO is bound to nickel it causes a significant distortion of the complex planar structure. The authors speculated that the increased activity of the complex on mercury compared to GCE was due to the interaction of the catalyst on the mercury surface preventing distortion, and reducing the amount of CO adduct forming. They found that adding a CO scavenger (in this example another macrocycle complex of nickel, $[Ni(L4)](Cl)_2$ (Scheme 8), previously found to have a much higher affinity for CO binding than Ni(cyc)[69]) leads to a large increase in the catalytic activity, as the scavenger removes CO more quickly than it can react with the active catalyst.

In the same study, the authors investigated the role of protons in the catalytic activity of Ni(cyc). CVs of the complex were carried out in dry MeCN under argon and CO_2, and water was slowly added at different concentrations. Under CO_2, the $Ni^{II/I}$ couple, which was reversible under argon, became irreversible under CO_2, in addition to being shifted to more positive potentials (*ca.* 30 mV). This was attributed to adventitious water being present either in the solvent or the CO_2 gas cylinder. The binding constants of the complex to CO_2 was reported to be $k_f = 3.2 \times 10^7$ M $^{-1}$ s $^{-1}$ and $k_r = 2.0 \times 10^6$ s $^{-1}$ for the forward and reverse reactions respectively[77] ($K_{eq} = 16$) and thus the process is reversible in the timescales of a fast CV. To confirm the assumption, the addition of small amounts of water caused a more pronounced change with the same trend. When larger amounts of water were added to the solution

(concentrations > 0.2 M) a catalytic peak appeared, which grew in intensity and shifted to more positive potentials with increasing water concentration, until a maximum was reached at a value of 11 M (20% H_2O in MeCN), where the peak reached the potential of the $Ni^{II/I}$ reduction peak under CO_2 in neat water. This behaviour was assigned to a proton dependent electron transfer. Furthermore, when the rate of catalysis was increased by adding a CO scavenger to the solution it was found that the catalytic peak current increased, but the onset potential shifted negatively. This supports the hypothesis of a proton dependent electron transfer, as the increase in rate of catalysis brought about by the addition of the scavenger would cause a faster consumption of protons. These studies validate the assumption that the proton transfer is the rate limiting step in the catalytic mechanism.

The properties of Ni(cyc) at different pH values has been studied in detail on the mercury electrode by Fujita and co-workers[54]. The authors have analysed the behaviour of the current in the CV of CO_2 purged solutions of the complex in water with decreasing pH. It was found that at pH $\leq$ 2 the current was dramatically increased. Interestingly, the CV under argon also showed a large catalytic curve, which masked the $Ni^{II/I}$ couple. Bulk electrolysis experiments revealed that at low pH values the high selectivity for CO was lost, with a ratio of CO:H_2 of 0.8 in the first half hour. Pulse radiolysis experiments were carried out to probe the mechanism at low pH values. A nickel(I) hydride was identified, and the pK_a for this species was estimated to be 1.8. It was suggested that at low pH, formation of $[Ni(cyc)(H)]^{2+}$ is favoured, with subsequent preferential H_2 formation.

1.2.5 Design rules for new CO_2 reduction electrocatalysts

Recently, a number of studies have outlined how the second coordination sphere of a metal complex can be tailored to greatly improve catalysis. Of particular relevance for this thesis is the study published by Savéant *et al.* in 2012[78], which described the catalytic activity for CO_2 reduction to CO by a Fe porphyrin which was modified with phenolic groups, FeTDHPP

(TDHPP = 5,10,15,20- tetrakis(2'6'-dihydrolphenyl) porphyrin), Scheme 10. The activity of the complex has been evaluated by cyclic voltammetry and bulk electrolysis, and it was shown to be much higher than the unmodified porphyrin FeTPP (TPP = tetraphenylporphyrin), which had been reported previously by the same group[26].

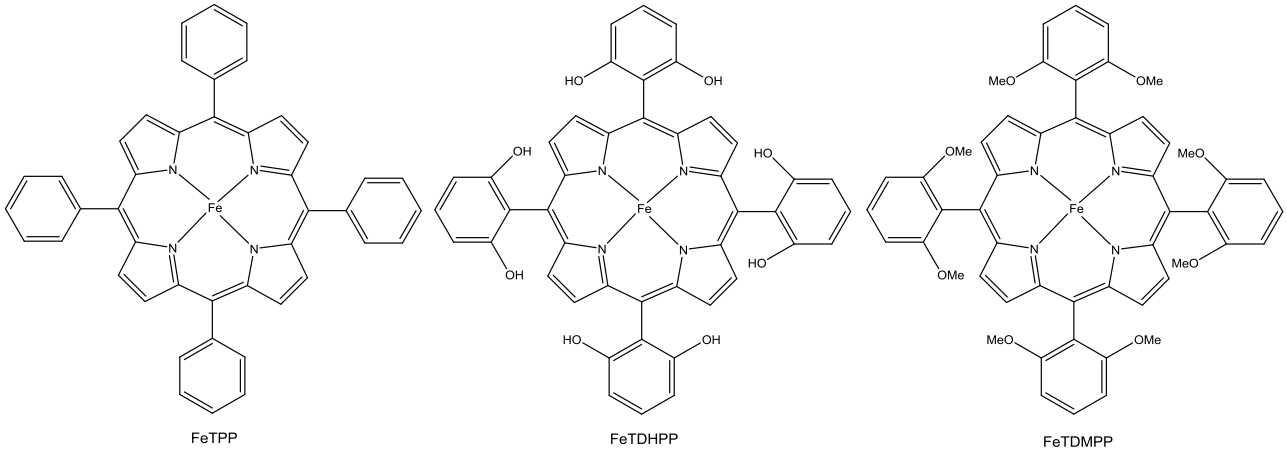

Scheme 10- The iron porphyrin complexes investigated by Savéant et al.[78]

Interestingly, when the hydroxylic groups were replaced with methoxy groups, the catalytic activity decreased significantly. Furthermore, when phenol was added in high concentrations to the FeTPP solution, a large increase in catalytic activity was observed, comparable to the currents obtained with FeTDHPP. In subsequent studies[79,80], the mechanism has been thoroughly explored with experimental and theoretical calculations, and it was proposed that catalysis was accelerated by the presence of the phenolic protons which stabilise CO_2 binding to the Fe^0 through hydrogen bonding. In addition, it was demonstrated that the phenolates reprotonate as soon as one proton is transferred to CO_2, being thus able to participate in the concerted second electron-second proton transfer step.

While examples of catalysts with internal acid/base sources were already available in the literature, for O_2 and proton reduction,[81–83] this was the first example to apply the concept to the reduction of CO_2. Since then, acidic functionalities have been added to several other

catalyst classes. Gobetto *et al.* and Bocarsly *et al.*[84,85] both modified the bpy ligand to obtain new Mn trycarbonyl complexes with hydroxyl functional groups, which showed catalytic activity under CO_2 even in the absence of added Brønsted acids, usually a fundamental requirement of catalysis with Mn bypiridine complexes. Furthermore, the catalytic currents were found to be higher than the ones generated by the parent complex, [Mn(bpy)$(CO)_3$Br], in the presence of acids. Palmore *et al.*[86] showed that the reduction of CO_2 to formate was improved when adding a proton-donor group to the ligand framework of an Ir pincer complex.

During the writing of this thesis another relevant report for this discussion was published by Savéant and co-workers,[87] where the effect of electrostatic interactions of the ligand through space were explored with the synthesis of two new iron porphyrin complexes. Initially, the authors demonstrated that the efficiency found for the WSCAT catalyst (Fe(5,10,15,20-tetrakis(4'-trimethylammoniumphenyl) porphyrin), compound 5 in Table 1) was due to the presence of positive charges ancillary to the Fe centre, by exchanging the *p*-anilinium groups with negatively charged *p*-sulfonated phenyl groups (Fe-*p*-PSULF), and showing how the new complex is a worse catalyst for CO_2 reduction in DMF. The difference in catalytic activity was attributed to the positive charges being able to stabilise CO_2 binding to the Fe by interacting electrostatically with the partial negative charge on the oxygens in CO_2. Subsequently, the theory was further confirmed by carrying out catalysis with a new iron porphyrin, this time functionalised with *o*-anilinium groups as a means of bringing the positive charges closer to the catalytic centre and increasing the electrostatic effect. The result was a much higher current density under CO_2 compared to WSCAT, together with a remarkable 400 mV positive shift in the onset potential.

While all of these examples show how the second coordination sphere of a complex can be modified in a rational manner to tailor to the requirements for catalysis, the studies have all been carried out in organic solvents with added proton sources, as is the case for the majority

of molecular electrocatalysts. Part of the reason sits with the poor solubility in protic solvents of the complexes studied, while part of it resides in the already high concentration of protons in aqueous media, which more often than not promotes the production of H_2, lowering the selectivity. For practical purposes, a catalyst that is efficient and selective in water is highly desirable, as water is the quintessential low-cost, green solvent.

In the second chapter of this work we will focus our efforts on the detailed electrochemical characterisation of a newly synthesised Ni(cyc) derivative, Ni(cycC) (cycC = 1,4,8,11-tetraazacyclotetradecane-6-carboxylic acid), which shows a greatly enhanced catalytic activity for CO_2 reduction at low pH values when compared with the parent complex, likely due to the addition of a labile proton near the reaction centre, in line with the work of Kubiak *et al.*,[88] which proposed that protonation of the CO_2 adduct may be rate limiting. The study of the electrochemical CO_2 reduction by Ni(cycC) demonstrates that the general rules outlined in this section can also be applied to the design of water-active catalysts.

1.2.6 CO_2 reduction using immobilised molecular catalysts

The immobilisation of molecular catalysts on electrode supports has been widely explored as an alternative to homogeneous catalysis or CO_2 reduction at metal electrodes. The strategy has several potential advantages over the two approaches described above: (i) the possibility of using insoluble catalysts in aqueous solutions, therefore avoiding the need of wasteful and expensive organic solvents, (ii) the lowering of the large overpotentials that are typical of metal electrodes, (iii) easier purification of the reaction products, and (iv) high tunability of the molecular structure. Several different approaches have been used to immobilise catalysts on solid electrodes; perhaps one of the most studied methods has been the immobilisation onto an electrode by using a polymer as an inert support. In particular, Nafion membranes have been used to immobilise a variety of CO_2 reduction catalysts, such as $[Re(bpy)(CO)_3Cl]$[89], Ni(cyc)[90] and $[Co(tpy)_2]^{2+}$[91] (tpy = 2,2′:6′,2″-terpyridine). Typically Nafion membranes containing the

molecular catalyst show low current densities under CO_2, together with a preference for proton reduction due to the high local proton environment in the polymer. We have studied the immobilisation of [Mn(bpy)$(CO)_3$Br][92] and some of its derivatives[42] on GCEs using Nafion, with the aim of using the proton-rich environment of the polymer to aid catalysis, as it has been shown that the complex is inactive in the absence of added proton sources. The immobilised complex showed a retention of the selectivity in aqueous phosphate buffer and a positive (*ca.* 100 mV) shift in the catalytic onset potential, demonstrating the validity of the heterogeneous approach, however the current density was low. This was attributed to a small percentage of the catalyst in the membrane being electroactive (0.25%), due to Nafion being a poor conductive material. Addition of multi-walled carbon nanotubes (MWCNT) to the [Mn(bpy)$(CO)_3$Br] membrane, as a high surface area support, significantly increased the number of electroactive sites in the film (11%), causing a dramatic increase in current density under CO_2 (10-fold). Furthermore, FTIR (Fourier-Transform Infrared) experiments of the [Mn(bpy)$(CO)_3$Br]/MWCNT/Nafion membranes indicated a degree of interaction between the nanotubes and the bpy ligand of the manganese complex.

The same approach has been recently used by Robert and co-workers,[93] who have realised a complete electrolyser by fabricating a cathode using their highly water-active porphyrin WSCAT (compound 5 in Table 1) in a Nafion membrane with carbon powder to make the film conductive. In the study, the CO_2 reduction reaction was coupled to water oxidation by using the recently reported[94] CoP_i water oxidation catalyst at the anode. FEs of 90% for CO (10% for H_2) were achieved with the cell over several hours, with an average current density of 0.7 mA cm^{-2}.

Removing the polymer support, which can hinder catalysis due to the poor conductivity, has been achieved by modifying the catalyst with functional groups suitable for electropolymerisation.[95–103] The first use of such a technique for the reduction of CO_2 was

reported by Meyer *et al.*,[98] who modified the bpy ligand of [Re(bpy)$(CO)_3$Cl] with a vinyl group and subsequently electropolymerised the complex on a platinum disc electrode by cycling the potential between *ca.* 0.2 and -1.45 V_{NHE}. Once formed, the film was rinsed and its catalytic activity evaluated on fresh MeCN solutions. The authors found that the TON for the catalysis using the film was 516, compared to the value of 20-40 obtained for the solution electrocatalysis. Since this first report, several other complexes have been modified with vinyl groups for polymerisation. Recently, following a study that showed the high activity of Co protoporphyrins immobilised on pyrolytic graphite electrodes,[104] Bocarsly[105] and co-workers electropolymerised a vinyl cobalt protoporphyrin on GCE and carried out the electrocatalysis in aqueous solutions. They found that the activity of the polymer film on the electrode was comparable to the highly active series of iron porphyrins from Savéant's group, even when the charge transport through the film is expected to be lower than for a solution electrocatalyst.

1.3 Photocatalytic CO_2 reduction

Photocatalytic CO_2 reduction is an attractive research endeavour, due to the possibility of directly using solar energy to drive the reaction, in a mimicry of natural photosynthesis, and therefore it has been widely studied in the past decades.

Photocatalytic reduction of CO_2 in aqueous solutions using various semiconductors (TiO_2, ZnO, CdS, GaP, SiC, WO_3) was reported for the first time in 1979.[106] The reduction process gave methanol and formic acid as the main products, with quantum yields of 1.9×10^{-4} and 5×10^{-4} ($\lambda > 500$ nm), respectively, which, despite being low, demonstrated the potential of the approach. In this approach no additional co-catalyst was added to the system and CO_2 reduction occurred at the semiconductor surface itself. Since the seminal report, several semiconductor materials have been tested for CO_2 reduction, with good results,[107,108] however the issues with the use of oxides remain, including: (i) the fast electron-hole recombination, which prevents

high quantum efficiencies, (ii) the need for wide band gaps, in order to obtain sufficient driving force to achieve CO_2 reduction, which reduces the choice of materials and more importantly prevents the use of visible light, and (iii) the low selectivity, which leads to a distribution of products.

Quantum dots (QDs) have been extensively studied in recent years for a varied range of photocatalytic applications due to their widely tunable optical and electronic properties.[109,110] Quantum dots are semiconductor nanoparticles of sizes varying between 2-20 nm, and can be defined as such when the diameter of the nanocrystal is smaller than the exciton Bohr radius,[111] which varies with the material, and is the spatial extension of electron-hole pairs in semiconductors. This gives rise to a phenomenon called quantum confinement, where energy states become discrete. By using the simple particle-in-the-box model, it is therefore possible to predict the energy level spacing, which will be inversely proportional to R^2: the smaller the particle, the higher the bandgap.[111] The ability to change the bandgap of the material by altering the size of the QD means that light absorption by the semiconductor material can be shifted to the visible region of the spectrum relatively easily, which is one of the main reasons that these materials are so attractive for their use in photocatalytic applications such as water splitting. As a result of the synthetic methods to achieve particle size control, quantum dots are obtained with coordinating ligands (or capping ligands), the nature of which is varied, and usually chosen to impart the synthesised quantum dots desired sizes, composition, morphology and dispersibility in certain solvents. The presence of the capping ligands can be a hindrance for the applications that the QDs were designed for, however removing the ligands from the surface of the QDs generally causes the particles to lose stability and aggregate.

Quantum dots for water splitting have been studied since the '80s[112], and many reports on proton reduction using QDs are available now, with CdX and ZnX chalcogenides (with X = S, Se and Te) being amongst the most studied materials.[109] These materials can be decorated with

precious metals, or coupled with enzymes[113] or molecular complexes of Co and Ni to act as co-catalysts.[114–116] Very few examples of CO_2 reduction carried out using quantum dots have been reported. Typically the nanocrystals are used to sensitise TiO_2[117,118] or in conjunction with CO dehydrogenase[113], of which only the latter was carried out in water, however all of these systems suffered from low quantum yields.

Photocatalytic CO_2 reduction with molecular catalysts is also a widely explored area of research.[5] Homogeneous photocatalysis is usually carried out with a sensitiser molecule and a selective catalyst for CO_2 reduction in a solution of an electron donor. In a few cases the sensitiser is the CO_2 reduction catalyst as well.[119] In other examples, the sensitiser is a semiconductor material in contact with a solution of the CO_2 reduction catalyst. The general mechanism of these systems starts with photoexcitation of the light absorber, which is reductively quenched by the electron donor. The light absorber has to be chosen based on the reductive potential of this reduced species, so that electron transfer to the CO_2 reduction catalyst can occur efficiently to yield the oxidised photosensitiser and a reduced catalyst molecule, which is then able to bind CO_2 and carry out the reduction reaction.

Conjugated metallomacrocycles such as corrins,[120] corroles,[121] porphyrins,[121] and phtalocyanines[122] with a Co or Fe centre have been shown to act as photocatalysts for CO_2 reduction. Such metallomacrocycles strongly absorb visible light and do not require the addition of a photosensitiser. However, these systems suffer from low quantum yields, low catalytic selectivity due to significant production of H_2 and, in case of the Co catalysts, oxygen sensitivity (i.e. they act as O_2 reduction catalysts).

$[Re(bpy)(CO)_3X]$ (X= Cl, Br) has been widely studied as a photocatalyst for CO_2 reduction since its development by Lehn *et al.* in 1983.[123] Initial reports demonstrated that it is capable of selectively producing CO without the use of an added photosensitiser, with a quantum yield

of 0.14 (λ_{max}= 385, 392 nm), which was the highest efficiency for CO_2 photoreduction at the time. Since then, much focus has been given to the tuning of this catalyst to improve its efficiency, primarily by exchanging the X^- ligand.[124–127] Indeed, when X^- was exchanged with a phosphate group, -$P(OEt)_3$, the efficiency for CO production doubled (Φ = 0.38, λ = 365 nm).[125] In a system consisting of a mixed solution of $Re(bpy)(CO)_3(P(OMe)_3)$ and $Re(bpy)(CO)_3MeCN$, even higher quantum yields were achieved (Φ = 0.59, λ = 365 nm).[128] Furthermore, rhenium bipyridine complexes have been used in supramolecular assemblies, with the aim of sensitising the rhenium complex for visible light absorption, where the photocatalytic activity of the dyad has been reported to be improved compared to the separate components.[129–132]

Until recently, manganese carbonyl complexes were thought to be only suitable as CO_2 electrocatalysts due to their extreme light sensitivity. However, it has been reported[133] that when $[Mn(bpy)(CO)_3Br]$ is used in a system with a ruthenium complex as a photosensitiser, formic acid is produced with an 85% selectivity over CO and H_2, with a TON of 149 and a quantum yield of 0.053.[134] The mechanism for the reaction has been investigated by Kubiak *et al.*,[135] by irradiating the similar complex $[Mn(bpy)(CO)_3MeCN]$, and it has been found that the solvent choice significantly influenced the reaction mechanism: the main product was formic acid when the photocatalysis was carried out in DMF, and CO when the reaction was carried out in MeCN. It has been shown that a similar complex of manganese, $[Mn(phen)(CO)_3Br]$ (phen = 1,10-phenanthroline) is an active photocatalyst for the production of formic acid when coupled to an abundant light absorber such as ZnTPP (TPP = tetraphenyl porphyrin).[136] Recently, $[Mn(bpy)(CO)_3Br]$ has been incorporated into a MOF (Metal-Organic Framework)[137] *via* modification of the bpy ligand with Zn bridges, and its photocatalytic activity was studied in DMF/TEOA (TEOA = Triethanolamine) mixtures containing a Ru

polypyridine complex as the sensitiser. It was found that the main product of the reaction was $HCCO^-$, with only traces of CO and H_2, reaching a TON of 110 after 18 hours of irradiation.

Due to its remarkable properties for the electrochemical reduction of CO_2, Ni(cyc) has been employed in photoelectrochemical or photochemical systems, by associating the complex with a light absorber, either a semiconductor or a photosensitiser. Beley *et al.*[138]and Petit *et al.*[139] reported the photoreduction of CO_2 to CO on p-GaAs and p-GaP photocathodes with Ni(cyc) as the molecular catalyst in solution. CO_2 reduction was achieved as low as 200 mV below the thermodynamic potential for CO_2 to CO reduction, at -0.2 V *vs.* NHE. The selectivity of CO over H_2 was found to be 1:2 for p-GaAs and for p-GaP, with FEs between 80% and 100%. Calvin and co-workers[140] reported the photochemical reduction of CO_2 to CO when aqueous solutions of Ni(cyc) containing $[Ru(bpy)_3]^{2+}$ and a sacrificial hole scavenger were illuminated with a visible light source. The ratio of CO to H_2 was found to be highly dependent on the pH of the solution. The best result obtained was at pH 4, yielding 357 μl of CO with no observed H_2 (TON = 4.8). However, this result was obtained by periodic replenishing of the photosensitiser ($[Ru(bpy)_3]^{2+}$ is known to degrade under prolonged irradiation[141,142]) and continuous CO_2 purging. Supramolecular complexes made by assembling a photosensitiser and Ni(cyc) have been synthesised and tested for the photocatalytic reduction of CO_2,[143,144] similarly to other examples of Re/Ru bipyridyl complexes, which have shown high activity for CO_2 reduction to CO in DMF.[145–147] The new compound didn't seem to have a major advantage over the two separate complexes in terms of the yield of products, however it did show higher stability: the UV-vis of the illuminated solution after 24 hours didn't show any particular changes, indicating that photolysis of the photosensitiser was reduced due to the rapid electron transfer from the Ru to the Ni centre. The electron transfer dynamics have been studied by Transient absorption (TA) spectroscopy on a similar system[144]. The new complex did show some CO_2 reduction when illuminated in solution in the presence of a hole scavenger, however

the electron transfer was found to be slow, and on the order of the recombination timescales at the Ru metal centre. This was rationalised by the minimal driving force for the electron transfer, estimated by the CV.

The use of molecular catalysts therefore improves the selectivity for the photochemical reduction of CO_2, however most homogeneous photocatalysts contain expensive and rare metal centres, are being used in organic solvents and have low efficiencies. In recent years, the immobilisation of molecular catalysts to light absorbers *via* covalent interactions have been widely studied as a way to bring together the advantages of both the semiconductor and homogeneous systems. The immobilisation of a molecular catalyst on a semiconductor surface can be seen as introducing a junction, making it possible to separate the photogenerated charges and suppress recombination (Figure 2).

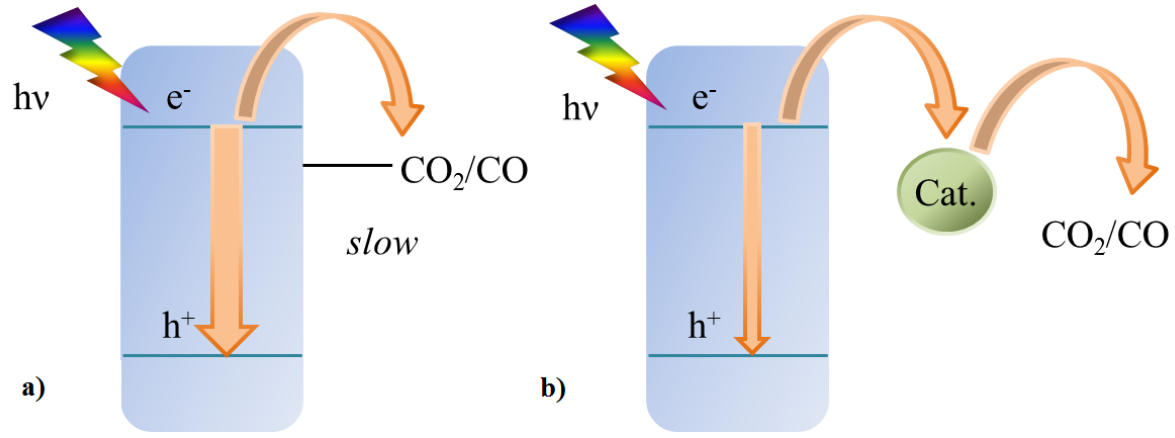

Figure 2 - (a) CO_2 reduction by a semiconductor; (b) CO_2 reduction by a molecular catalyst combined with a photosensitiser.

In addition, the presence of a molecular catalyst ensures selectivity is maintained, potentially even in water. As for the homogeneous photocatalysis case, the two components need to be appropriately chosen so that the energetics are favourable to the CO_2 reduction reaction, e.g., for a semiconductor/catalyst heterogeneous photocatalyst, the conduction band (CB) of the semiconductor has to have a potential more negative than the reduction potential of the

immobilised catalyst, so that electron transfer is favoured; furthermore, the two potential values should be separated enough that the reverse reaction (back electron transfer) is disfavoured.

A seminal report by Sato *et al.* on the immobilisation of a molecular CO_2 reduction catalyst onto a semiconductor surface for engineering hybrid photocatalytic materials was published in 2010.[148–151] Ruthenium catalysts were grafted onto different p-type semiconductors such as N-doped Ta_2O_5 and InP, *via* covalent linkages by functionalising the bpy ligands of the catalysts with carboxylic acid groups. CO_2 reduction was observed in a MeCN/TEA (TEA = triethylamine) mixture under $410 \leq \lambda \leq 750$ nm excitation using TEOA as the sacrificial electron donor. Since then, the immobilisation of molecular catalysts on semiconductor surfaces has been further explored, and it has been shown that higher yields of products can be achieved due to the faster electron transfer from the semiconductor to the anchored catalyst when compared to the catalyst in solution.[152–154] These initial reports spurred a large variety of studies which involved the modification of well-known molecular electrocatalysts with binding groups for anchoring to semiconductor surfaces.[155] $[ReL(bpy)(CO)_3]$ (where L = 3-picoline) was modified with phosphonic groups in the 4 and 4' positions of the bpy ligand for binding to TiO_2, which yielded a much higher CO_2 reduction activity when compared to the catalyst in solution.[119] TAS studies on the immobilised system *vs* the solution system showed that following excitation of the Re complex reductive quenching by the sacrificial electron donor occurred to form a reduced Re catalyst. The key to the enhanced photocatalytic activity was attributed to the much longer lifetime of this reduced complex when immobilised on TiO_2 compared with the solution species.[119]

Recently, Ishitani and co-workers have immobilised a ruthenium complex on graphitic carbon nitride (C_3N_4),[156] and found that in DMA (dimethylacetamide) the heterogeneous system produces HCOOH with a TON of 1000 in 20 hours and a quantum yield of 5.7%. In a following study,[157] activity was found to be greatly enhanced when the catalyst immobilised on Ag-

decorated C_3N_4 was a RuRu' binuclear complex. The photocatalyst showed a 30-fold enhancement in TON compared to the previous system, while maintaining a high selectivity for HCOOH, and it is currently the benchmark for semiconductor/molecular catalyst photocatalysts for CO_2 reduction. Moreover, the activity, albeit slightly reduced, is maintained in water.

In Chapter 2 and 3 we will explore the binding of two differently functionalised Ni(cyc) derivatives on semiconductor oxide films, with the ultimate goal of driving CO_2 reduction photochemically, and we will show that the difference in binding group can significantly alter the properties of the semiconductor/catalyst hybrid system. Furthermore, the second part of Chapter 4 will show the results obtained in collaboration with the Reisner group (University of Cambridge) on the photocatalytic CO_2 reduction to CO by Ni(cycP) (cycP = ((1,4,8,11-tetraazacyclotetradecan-1-yl)methyl)phosphonate) immobilised on ZnSe quantum dots in aqueous solutions and with visible light.

The need to have sufficient driving force between the light absorber and molecular catalyst, in order to have efficient electron transfer, somewhat limits the choice of semiconductors. One alternative way to build a heterogeneous photocatalyst is to sensitise the semiconductor oxide with a dye. This approach has been remarkably successful in the field of photovoltaics, since the discovery of the Gratzel cell,[158] and subsequently in the field of water splitting,[159–162] however similar applications for CO_2 reduction are few to date. In such a system, the photons are absorbed by a dye immobilised on a semiconductor (often TiO_2); following reductive quenching by an electron donor, electron injection from the reduced dye to the TiO_2 occurs, followed by electron transfer from the TiO_2 to the molecular catalyst, which is also anchored on the semiconductor. Kang *et al.*[163] reported in 2014 dye-sensitised photocatalytic CO_2 reduction by using a modified $[Re(bpy)(CO)_3Cl]$, ReC, and an organic dye, immobilised on TiO_2. The material was able to achieve a TON of 435 after four repeated irradiation

experiments. In a follow-up paper, the TON was increased to 570 after 30 hours with the addition of 5% H_2O to the DMF solution, and through Mott-Schottky analysis it was found that the reason for the activity enhancement was a better band alignment due to the flat-band potential of TiO_2 shifting in the presence of water.[164]

In the water splitting field, a further approach has been shown recently, involving the co-immobilisation of dye and catalyst on an inert support as a means of having direct dye-catalyst electron transfer,[165,166] however the same approach has not yet been demonstrated for CO_2 reduction; in the first section of Chapter 4 we will show the photocatalytic activity of a heterogeneous "on-particle" photocatalyst for CO_2 reduction in water composed of a ruthenium dye and a Ni(cyc) catalyst immobilised on a ZrO_2 inert support.

1.4 Study of the mechanisms for CO_2 reduction

Knowing the mechanisms that govern the CO_2 reduction reactions, whether it be electro- or photocatalytic, is highly important, as a deep knowledge of the rules that allow high efficiency and good selectivity may open the path to rational design for improving the CO_2 reduction processes of interest. For the investigation of the electrocatalytic CO_2 reduction reaction, SEC techniques have proven incredibly useful, in particular with regards to the CO_2 reduction by molecular catalysts. In the fifth chapter of this thesis, we have used *in-situ* Sum Frequency Generation (SFG) spectroelectrochemistry to probe the mechanism of CO_2 reduction by [Mn(bpy)$(CO)_3$Br] and Ni(cyc), therefore we present here the basics of the theory behind the technique.

For the photochemical CO_2 reduction processes, the observation of the charge carrier dynamics using transient techniques can give meaningful insights. Throughout this thesis we have used Transient Absorption Spectroscopy (TAS) in order to understand the photochemical systems

we have developed; a brief introduction into this technique is offered later in this section. Initially we discuss the spectroscopic study of electrochemical interfaces.

1.4.1 Spectroelectrochemical techniques

The first report of a SEC experiment was in 1964, where Leedy and co-workers described the change in the p-toluidine UV-Vis spectrum with applied potential.[167] In these experiments a solution was held at a potential to generate the electrochemical species with detection being possible once a significantly high concentration had been generated in the bulk. The initial UV-Vis SEC apparatus described had significant drawbacks, such as the limited choice of electrode materials, which caused unwanted resistance in the electrochemical cell. This was due to the requirement that the electrode had to be transparent to the UV-vis radiation, and therefore metal electrodes, characterised by high conductivities had to be discarded in favour of more resistive, transparent materials such as conducting glass. Despite the experimental challenges the prospects of the technique were such that within a few years several different applications were reported[168]. SEC methods can provide insights into the mechanism of electrochemical processes, by making it possible to generate and characterise electrochemical intermediates that may be short lived or difficult to isolate once generated.

Vibrational spectroscopy offers a route to probe the chemical structure of electrochemical species and IR-SEC experiments were reported in the late 1960s.[169] A modified optically transparent thin-layer electrode (OTTLE) cell[170] (similar to that shown in Scheme 11), which had been previously reported for UV-Vis-SEC experiment, was used to probe the reduction of ninhydrin, with NaCl plates being used in place of the quartz slides previously used for the UV-vis experiments. The use of a thin-layer cell offers several advantages. Firstly the small volume of solution makes the electrochemical generation of a high concentration of a species a relatively fast process. Also if a sufficiently low enough pathlength is employed, thin layer cells allow for the study of electrochemical processes in solvents that may also contain IR

modes across the spectral region of interest. Since the 1960s multiple advances have been made to improve both the design of IR-SEC cells and IR spectrometers, leading to the technique being used in laboratories world-wide.

However some significant limitations do exist with a transmission mode IR-SEC experiment. In particular it can be challenging even with modern FTIR spectrometers to gain very high signal-to-noise ratios for chemically unstable reduced or oxidised species as the rapid breakdown of the species prevents the formation of a high steady state concentration. The strong adsorption of the background electrolytes and solvents can prevent the study of some solvent/electrolyte systems even if an OTTLE cell is employed. Furthermore, the most significant drawback of the IR-SEC method using an OTTLE cell is that it is not specifically probing the electrode surface. Electrochemically generated species can be detected but they are primarily in the bulk solution and the details of electrode/molecules interactions that occur transiently at the electrode surface are lost. Observation of the interaction between the molecular species and interactions at the surface is important as numerous examples exist of systems, such as Ni(cyc) and derivatives, where the nature of the electrode material has a significant effect on the electrochemical reactions occurring.

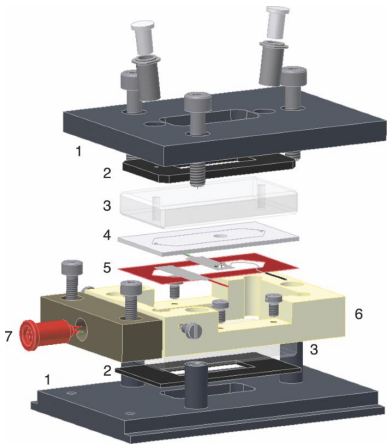

Scheme 11 – Expanded view of the OTTLE cell for transmission IR-SEC measurements. Figure reproduced from [171], 1 = metal cover plates (with filling ports), 2 = rubber gasket, 3 = CaF_2 window, 4 = custom polytetrafluoroethylene (PTFE) spacer, custom polyethylene-electrode spacer, 6 = protective frame, 7 = electrode plug.

1.4.2 SFG spectroscopy

Surface Enhanced Infrared Absorption Spectroscopy (SEIRAS) is a surface specific SEC technique,[172,173] which uses the plasmon resonance of nanostructured thin films (such as Au, Ag) deposited on IR transparent materials to generate a large enhancement in the IR absorptivity of molecules in the very close vicinity of the nanoparticles. SEIRAS substrates are typically prepared by electrochemical roughening of the metal films. Although this is a simple experiment to carry out it has been commonly reported that the roughening processes are difficult to reproduce[174] and the surface can also be modified during the SEC measurement. Furthermore the need to generate a plasmon resonance limits the study of electrode materials, with Au and Ag being the most commonly studied materials.

Sum-Frequency Generation (SFG) spectroscopy is a second order nonlinear experiment originally developed by Shen and co-workers[175] that specifically provides the vibrational spectrum of species at surfaces or interfaces. The high sensitivity of SFG spectroscopy with measurements of sub-monolayer concentrations being readily achieved,[176] has led to it becoming increasingly employed as a technique for the *in situ* study of interfaces[177,178] with applications to heterogeneous catalysis, biophysics and electrode surfaces, amongst others.[179–184]

SFG spectroscopy has been used to study a wide variety of electrochemical interfaces, such as electrodes for battery applications, the structure of the electrolyte at the double layer and the structure of water binding to the surface of the electrode. There are a few examples of SFG spectroscopy used to probe the CO_2 reduction mechanism. Of significance are two studies published by Baldelli[185] and Dlott *et al.*[186] on the interaction between the ionic liquid EMIM-BF_4 (1-Ethyl-3-Methylimidazolium Tetrafluoroborate) and the electrode surface during CO_2

reduction electrocatalysis. Ionic liquids have been known for a few years to be efficient mediators for the electrocatalytic CO_2 reduction using different electrode materials.[187,188] They are able to achieve nearly 100% FEs at low overpotentials, however the mechanism is still unknown. In the field of molecular catalysts for CO_2 reduction, several studies exist that have investigated the structure of complexes immobilised on surfaces; Lian *et al.*[189] have immobilised a [$Re(CO)_3Cl$(dcbpy)] (dcbpy =4,4′-dicarboxy-2,2′-bipyridine) on a single crystal TiO_2 (001) surface. They used SFG spectroscopy to determine the binding mode of the carboxylic acid functional groups and the orientation of the catalyst. In a subsequent study the same authors studied the effect of the length of the anchoring group to the surface on the orientation of the complex, and how this might influence the ability to catalyse the CO_2 reduction. They concluded that the tilt of the complex with respect to the TiO_2 surface increased with higher number of CH_2 groups in the anchoring group, likely due to the highest number of possible conformations of the linker, therefore demonstrating the possibility to rationally assemble a semiconductor/molecular catalyst with a preferred ordering of the complex. In a similar manner, Kubiak *et al.*[190] studied two different rhenium complexes, [Re(4,4′-dicyano-2,2′-bipyridine)$(CO)_3Cl$] and [Re(4-cyano-2,2′-bipyridine)$(CO)_3Cl$], immobilised on gold, finding that the cyano groups are only weakly interacting with the gold surface, forming a monolayer at no applied potential, characterised by a large tilt angle. While these studies demonstrate the usefulness of the SFG technique to study molecular complexes, to date there has been no report focusing on the nature of molecular species at an electrode with the applied potential.

The theory of SFG spectroscopy has been described in detail elsewhere.[191] Here a very brief summary of only the key points is provided, based on these resources. In the fifth chapter, we will utilise IR-Vis SFG, an experiment that involves the use of two pulsed lasers with frequency ω_1 and ω_2. Typically the visible laser is at a fixed wavelength (here *ca.* 800 nm) and the IR is

tunable across the mid-IR. Short (fs-ps) intense pulsed lasers are used as when intense electric fields are generated, the polarisability P of a material will include non-linear terms, expressed by a Taylor expansion in Eq.(1):

$$P(t) = P^0 + \chi^{(1)}E(t) + \chi^{(2)}E^2(t) + \chi^{(3)}E^3(t) \ldots \quad (1)$$

Where P^0 is the static polarisability, E(t) is the electric field, $\chi^{(1)}$ is the susceptibility for linear optical measurements and $\chi^{(2)}$ represents the second order non-linear susceptibility. An electric field with amplitude E at $t = 0$ can be described as a cosine wave with frequency ω (Eq. 2). Therefore for an experiment where only a single frequency of light is incident on the sample we can write the second order polarisability as (Eq 3-5):

$$\mathrm{E}(t) = \mathrm{E}\cos\omega t \quad (2)$$

$$P^2(t) = \chi^{(2)}E^2(t) \quad (3)$$

$$P^2(t) = \chi^{(2)}\,E^2 cos^2\omega t \quad (4)$$

$$P^2(t) = \frac{1}{2}\chi^{(2)}E^2(1 + \ cos2\omega t) \quad (5)$$

With Eq. 5 giving rise to the phenomena of second harmonic generation (SHG), a process which can be thought of as taking two photons of frequency ω to generate a single photon at 2ω. When two photons of different frequency ω_1 and ω_2 are used, as in a SFG experiment, we can write that:

$$E_1(t) = E_1 cos\omega_1 t \text{ and } E_2(t) = E_2 cos\omega_2 t \quad (6)$$

$$P^2(t) = \chi^{(2)}E_1(t)E_1(t) + \ \chi^{(2)}E_2(t)E_2(t) + \ 2\chi^{(2)}E_1(t)E_2(t) \quad (7)$$

$$P^2(t) = \chi^{(2)}\,E_1^2 cos^2\omega_1 t + \ \ \chi^{(2)}\,E_2^2 cos^2\omega_2 t + 2\chi^{(2)}E_1E_2(cos\omega_1 t \ \cdot cos\omega_2 t) \quad (8)$$

As:

$$\cos(x)\cdot\cos(y) = \frac{1}{2}\,[\cos(x-y) + \cos(x+y)] \quad (9)$$

$$P^2(t) = \frac{1}{2}\chi^{(2)}E_1^2(1 + cos2\omega_1 t) + \frac{1}{2}\chi^{(2)}E_2^2(1 + cos2\omega_2 t) + \chi^{(2)}E_1E_2[cos(\omega_1 - \omega_2)t + cos(\omega_1 + \omega_2)t] \quad (10)$$

Giving rise to terms in the polarisation at twice the frequency of the individual photons, a term at the difference of the frequencies (ω_1- ω_2), the difference frequency generation (DFG) and the sum of the frequencies (ω_1+ω_2), SFG.

The intensity of the SFG signal obtained can be shown[191,192] proportional to the square of the 2nd order non-linear susceptibility which contains contribution from a resonance component ($\chi^{(2)}{}_R$) and a non-resonant term ($\chi^{(2)}{}_{NR}$):

$$I_{(\omega_{IR}+\omega_{VIS})} \propto \left|\chi^{(2)}\right|^2 \text{ where } \chi^{(2)} = \chi^{(2)}{}_{NR} + \chi^{(2)}{}_R \quad (11)$$

The non-resonant susceptibility can be considered to be largely wavelength independent and is primarily a function of the surface or interface under study. It can be thought of as an excitation to a virtual vibrational excited state followed by a 2nd transition to a virtual electronic excited state, which then decays with photon emission to the ground state. However it is worth noting that the non-resonant and resonant components of the second order susceptibility are complex, and can interfere with each other, both constructively and destructively, giving rise to positive, negative and derivative looking features in the SFG spectrum which will be dependent upon the frequency of the IR laser. A full description of the role of the non-resonant term in modifying the line-shape of a resonant SFG response is beyond the scope of this thesis however a full description can be found elsewhere.[192]

The resonant susceptibility term becomes non-zero when the frequency of the IR photon matches that of an allowed transition of the surface or species under interrogation. This gives rise to a vibrational excited state which can then be up-converted to a virtual excited state which decays to the ground state with photon emission at $\omega_{SF,}$ essentially the product of a Raman transition and an infrared transition (Figure 3) Hence by measuring the change in SF intensity with IR wavelength it is possible to obtain the vibrational spectrum of species at the surface.

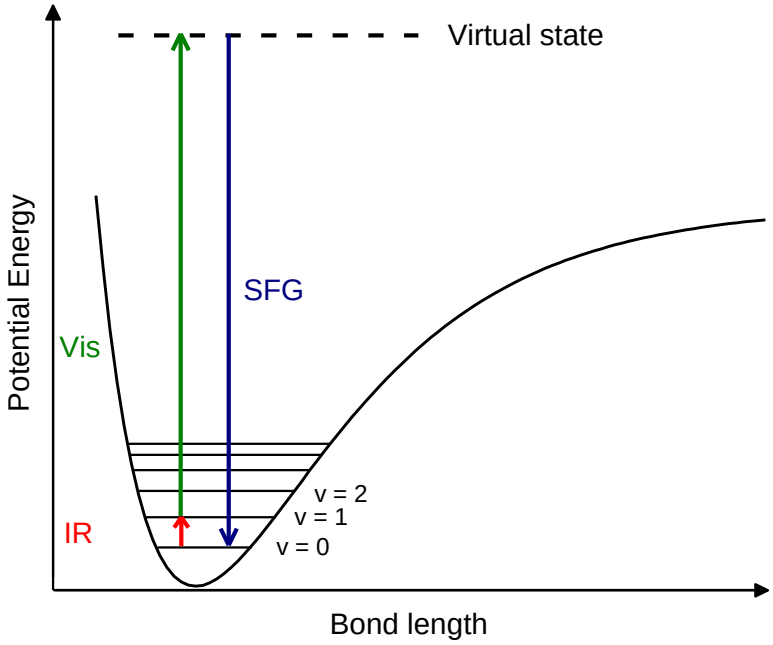

Figure 3 – Schematic representation of the energetic transitions involved during an SFG experiment.

The very high sensitivity of SFG spectroscopy arises from the availability of highly sensitive detectors in the visible region and the intrinsic surface selectivity of the technique. As shown above, the second order polarisability is proportional to the square of the electric field:

$$P^{(2)} = \chi^{(2)} E^2 \text{ i.e. } P^{(2)} \propto E^2 \quad (11)$$

It follows that the 2nd order polarisation induced by an electric field E and –E are the same;

$$P^{(2)}(E) = P^{(2)}(-E) \quad (12)$$

But in a centrosymmetric environment opposite directions are equivalent so the polarisation looks the same in both directions which would give rise to the following equation:

$$P^{(2)}(E) = -P^{(2)}(-E) \quad (13)$$

For equations (*12*) and (13) to hold the induced polarisation would have to be zero, i.e. $\chi^{(2)} = 0$. Therefore we see no 2nd order effects in materials with a centre of inversion (i.e. isotropic media such as the bulk materials in the systems studied). In contrast, the inversion of symmetry is necessarily broken at surfaces, which allows SFG transitions, meaning that SFG spectroscopy can probe species at interfaces.

$\chi^{(2)}$ is a third-rank tensor, and therefore it will have 27 components. For an isotropic surface, only seven components will have a contribution, however as the *x* and *y* directions are equivalent, only four components of the tensor will be non-zero:

$$\chi^{(2)}_{zzz}$$

$$\chi^{(2)}_{zxx} = \chi^{(2)}_{zyy}$$

$$\chi^{(2)}_{xzx} = \chi^{(2)}_{yzy}$$

$$\chi^{(2)}_{xxz} = \chi^{(2)}_{yyz}$$

The polarisation of the incident beams can either be perpendicular to the plane of incidence (P polarisation) or parallel (S polarisation). Considering the contributing components of $\chi^{(2)}$ only four possible combinations of the incident and SF polarisation are possible; furthermore, on metal surfaces, only IR fields with some *z* component will be contributing, due to the high reflectivity of metal surfaces for IR light (in this case the intensities of the *x* and *y* components

are zero when their phase changes upon reflection). In this thesis we have primarily used PPP polarisation.

Table 2 - Contributing polarisation combinations on metal surfaces, reproduced from ref [192]

Polarisation Combination SF:Vis:IR	***$\chi^{(2)}$ Components***	***Seen in metals***
PSP	$\chi^{(2)}_{zyz}$	Yes
SPS	$\chi^{(2)}_{yzy}$	No
PSS	$\chi^{(2)}_{zyy}$	No
PPP	$\chi^{(2)}_{zzz}, \chi^{(2)}_{xxz}$	Yes
	$\chi^{(2)}_{zxx}, \chi^{(2)}_{xzx}$	No

1.4.3 Transient Absorption Spectroscopy

Transient Spectroscopy encompasses a set of pump-probe techniques which are used to characterise short-lived excited states in a material. Here we will concentrate our discussion on Transient Absorption Spectroscopy (TAS) in the UV-Vis. TAS is used to monitor the behaviour of the charge carriers by measuring a change in the optical density in a material following excitation by a laser pulse. Since the first reported use of TAS spectroscopy[193] in 1949 (or flash photolysis) the technique has been greatly improved, and it has been used for a large variety of applications.[129,154,194–196]

In the case of ultrafast TAS (Scheme 12(a)), a high energy laser of specific wavelength is used to excite the material under study. A second low energy white light probe laser is passed through the sample and the change in absorption of this probe after excitation is compared to the ground state absorption. By carrying this measurement out at a range of time delays between the pump and the probe, it is possible to build up a spectrum of ΔA as a function of time and wavelength. For slow applications (μs-s) the electronic response time of equipment are suitable enough to record the ΔA with time continuously following excitation using a CW (continuous

wavelength) light source. In such slow spectrometers (Scheme 12(b)), a monochromator is often employed to isolate a single probe wavelength. A full spectrum of ΔA as a function of time at specific wavelengths λ is then obtained by repeating the measurement at a range of probe λ.

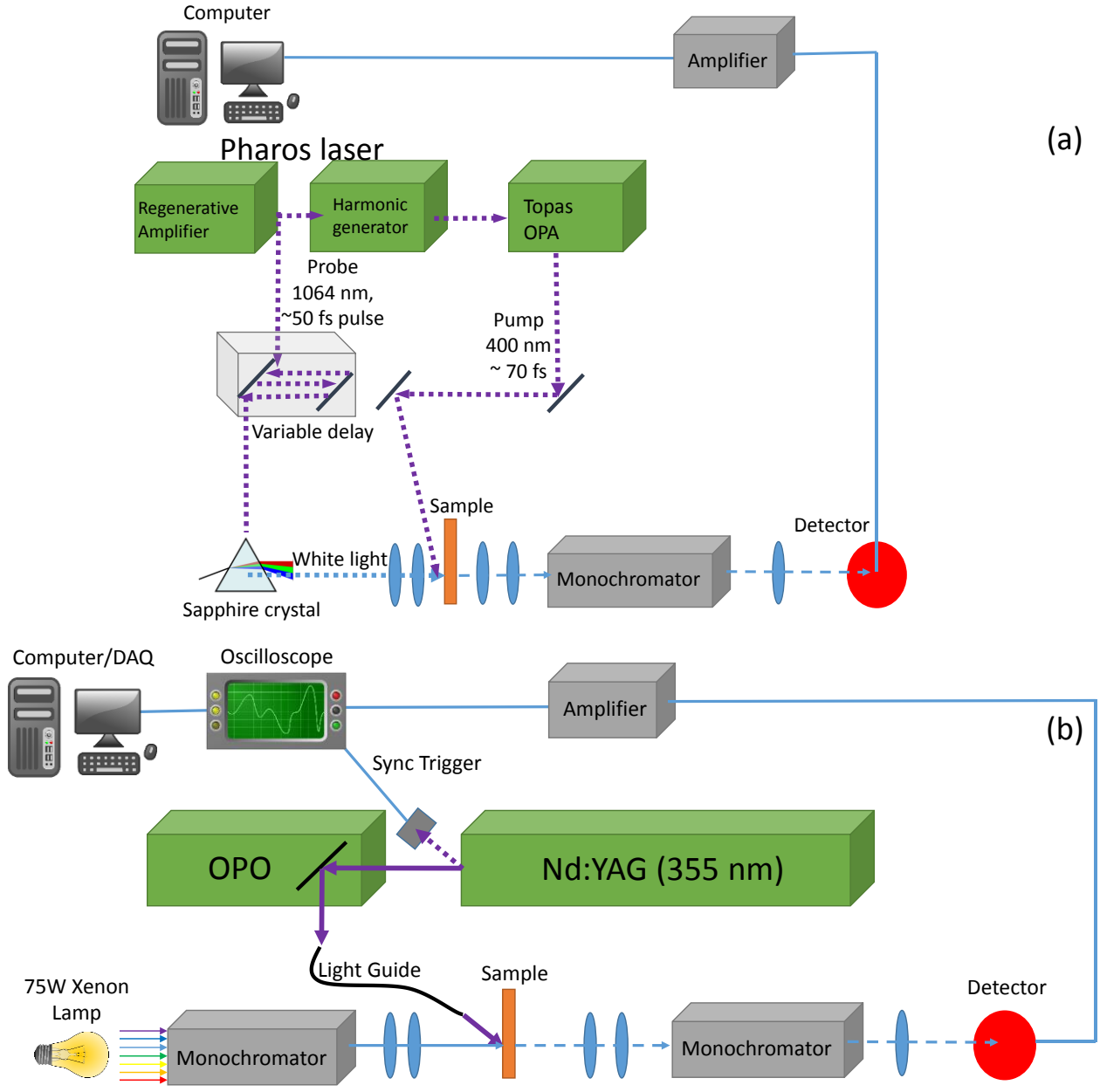

Scheme 12 – Scheme of the (a) ultrafast (ps-ns) and (b) slow (μs-s) TAS spectrometers built in our labs.

Generally, a TA spectrum contains information about any process that alters the optical density following excitation. Such processes include: (i) ground state bleach: this process is due to a fraction of the molecules in the ground state being promoted to an excited state by the laser pulse, causing a decrease in absorbance of the ground state, resulting in a negative signal in the TA spectrum; (ii) excited-state absorption: this arises when the excited state of the molecule under study undergoes optically allowed transitions to higher excited states. This type of processes appears as a positive signal, and the decay of the signal with time represents the lifetime of the excited state. The decay can be a result of electron transfer from the excited state to a different state, such as a trap state or relaxation to the ground state, or transfer to another species; (iii) stimulated emission: following certain transitions, the relaxation of the excited state to the ground state can cause emission of excess energy in the form of photons which can reach the detector, resulting in a perceived decrease in absorption and therefore a negative signal. Furthermore, the stimulated emission will show a Stokes shift with respect to the ground-state bleach; (iv) photo product absorption: reactive intermediates may be formed following excitation, for example an excited electron may transfer from a semiconductor to an adsorbed surface species or to a species in solution. TAS can provide useful insights into the investigation of CO_2 photocatalytic reduction mechanisms, as the technique can potentially follow the charge carrier dynamics during CO_2 reduction catalysis. Even a characterisation of the photogenerated electron kinetics of materials in the absence of the substrate (where no charge transfer occurs) can be useful for understanding efficiency and mechanisms.

The work in this thesis employed the use of a μs-s instrument, which will be described in the Materials and Methods section of Chapter 2, 3 and 4, where the electron transfer dynamics of the Ni(cyc) complexes when immobilised on semiconductors will be studied, and in ref. [197]. Ultrafast fs-ns measurements have also been employed and will be described in Chapter 4

where they have been used to probe the ultrafast charge carrier dynamics in the Ni(cycP)/ZnSe QD photocatalyst for CO_2 reduction in water. The instrument is described in ref. [198]

1.5 References

1. B. Kumar, M. Llorente, J. Froehlich, T. Dang, A. Sathrum, and C. P. Kubiak, *Annu. Rev. Phys. Chem.*, 2012, **63**, 541–569.

2. P. L. Spath and D. C. Dayton, *Preliminary Screening -- Technical and Economic Assessment of Synthesis Gas to Fuels and Chemicals with Emphasis on the Potential for Biomass-Derived Syngas*, Golden, CO, 2003.

3. Jesse Dan Froehlich, 2015.

4. A. J. Morris, G. J. Meyer, and E. Fujita, *Acc. Chem. Res.*, 2009, **42**, 1983–1994.

5. H. Takeda, C. Cometto, O. Ishitani, and M. Robert, *ACS Catal.*, 2016, 70–88.

6. A. Gennaro, A. A. Isse, M.-G. Severin, E. Vianello, I. Bhugun, and J.-M. Savéant, *J. Chem. Soc., Faraday Trans.*, 1996, **92**, 3963–3968.

7. Y. Hori, K. Kikuchi, and S. Suzuki, *Chem. Lett.*, 1985, **14**, 1695–1698.

8. Y. Hori, *Mod. Asp. Electrochem.*, 2008, 89–189.

9. A. A. Peterson, F. Abild-Pedersen, F. Studt, J. Rossmeisl, and J. K. Nørskov, *Energy Environ. Sci.*, 2010, **3**, 1311.

10. Y. Hori, H. Wakebe, T. Tsukamoto, and O. Koga, *Electrochim. Acta*, 1994, **39**, 1833–1839.

11. D. H. Gibson, *Coord. Chem. Rev.*, 1999, **185**, 335–355.

12. A. Behr, *Angew. Chemie Int. Ed. English*, 1988, **27**, 661–678.

13. D. H. Gibson, *Chem. Rev.*, 1996, **96**, 2063–2096.

14. W. Leitner, *Coord. Chem. Rev.*, 1996, **153**, 257–284.

15. X. Yin and J. R. Moss, *Coord. Chem. Rev.*, 1999, **181**, 27–59.

16. D. A. Palmer and R. Van Eldik, *Chem. Rev.*, 1983, **83**, 651–731.

17. I. Castro-Rodriguez, *Science (80-.).*, 2004, **305**, 1757–1759.

18. E. E. Benson, C. P. Kubiak, A. J. Sathrum, and J. M. Smieja, *Chem. Soc. Rev.*, 2009, **38**, 89–99.

19. C. Costentin, M. Robert, and J.-M. Savéant, *Chem. Soc. Rev.*, 2013, **42**, 2423–2436.

20. J. L. Inglis, B. J. MacLean, M. T. Pryce, and J. G. Vos, *Coord. Chem. Rev.*, 2012, **256**, 2571–2600.

21. M. R. Dubois and D. L. Dubois, *Acc. Chem. Res.*, 2009, **42**, 1974–1982.

22. K. Hiratsuka, K. Takahashi, H. Sasaki, and S. Toshima, *Chem. Lett.*, 1977, **6**, 1137–1140.

23. K. Takahashi, K. Hiratsuka, H. Sasaki, and S. Toshima, *Chem. Lett.*, 1979, **8**, 305–308.

24. M. Hammouche, D. Lexa, M. Momenteau, and J. M. Saveant, *J. Am. Chem. Soc.*, 1991, **113**, 8455–8466.

25. I. Bhugun, D. Lexa, and J.-M. Saveant, *J. Am. Chem. Soc.*, 1994, **116**, 5015–5016.

26. I. Bhugun, D. Lexa, and J. Savéant, *J. Am. Chem. Soc.*, 1996, **118**, 1769–1776.

27. J. Hawecker, J.-M. Lehn, and R. Ziessel, *J. Chem. Soc., Chem. Commun.*, 1984, 328–330.

28. K. A. Grice and C. P. Kubiak, *Adv. Inorg. Chem.*, 2014, **66**, 163–188.

29. E. E. Benson, C. P. Kubiak, A. J. Sathrum, and J. M. Smieja, *Chem. Soc. Rev.*, 2009, **38**, 89–99.

30. K.-Y. Wong, W.-H. Chung, and C.-P. Lau, *J. Electroanal. Chem.*, 1998, **453**, 161–170.

31. J. M. Smieja and C. P. Kubiak, *Inorg. Chem.*, 2010, **49**, 9283–9289.

32. M. Bourrez, F. Molton, S. Chardon-Noblat, and A. Deronzier, *Angew. Chemie Int. Ed.*, 2011, **50**, 9903–9906.

33. J. M. Smieja, M. D. Sampson, K. a. Grice, E. E. Benson, J. D. Froehlich, and C. P. Kubiak, *Inorg. Chem.*, 2013, **52**, 2484–2491.

34. F. Hartl, B. D. Rossenaar, G. J. Stor, and D. J. Stufkens, *Recl. des Trav. Chim. des Pays-Bas*, 2010, **114**, 565–570.

35. M. Bourrez, F. Molton, S. Chardon-Noblat, and A. Deronzier, *Angew. Chemie Int. Ed.*, 2011, **50**, 9903–9906.

36. F. Hartl, B. D. Rossenaar, G. J. Stor, and D. J. Stufkens, *Recl. des Trav. Chim. des Pays-Bas*, 1995, **114**, 565–570.

37. C. Riplinger, M. D. Sampson, A. M. Ritzmann, C. P. Kubiak, and E. A. Carter, *J. Am. Chem. Soc.*, 2014, **136**, 16285–16298.

38. D. C. Grills, J. A. Farrington, B. H. Layne, S. V. Lymar, B. A. Mello, J. M. Preses, and J. F. Wishart, *J. Am. Chem. Soc.*, 2014, **136**, 5563–5566.

39. M. V Vollmer, C. W. Machan, M. L. Clark, W. E. Antholine, J. Agarwal, H. F. S. Iii, P. Kubiak, and J. R. Walensky, *Organometallics*, 2015, **34**, 3–12.

40. J. M. Smieja, M. D. Sampson, K. A. Grice, E. E. Benson, J. D. Froehlich, and C. P.

Kubiak, *Inorg. Chem.*, 2013, **52**, 2484–2491.

41. J. M. Smieja and C. P. Kubiak, *Inorg. Chem.*, 2010, **49**, 9283–9289.

42. J. J. Walsh, C. L. Smith, G. Neri, G. F. S. Whitehead, C. M. Robertson, and A. J. Cowan, *Faraday Discuss.*, 2015, **183**, 147–160.

43. M. D. Sampson, A. D. Nguyen, K. a Grice, C. E. Moore, A. L. Rheingold, and C. P. Kubiak, *J. Am. Chem. Soc.*, 2014, **136**, 5460–5471.

44. G. Seshadri, C. Lin, and A. B. Bocarsly, *J. Electroanal. Chem.*, 1994, **372**, 145–150.

45. P. Kang, T. J. Meyer, and M. Brookhart, *Chem. Sci.*, 2013, **4**, 3497–3502.

46. D. Xiang, D. Magana, and R. B. Dyer, *J. Am. Chem. Soc.*, 2014, **136**, 14007–10.

47. P. Kang, Z. Chen, A. Nayak, S. Zhang, and T. J. Meyer, *Energy Environ. Sci.*, 2014, **7**, 4007–4012.

48. C. Costentin, M. Robert, J.-M. Savéant, and A. Tatin, *Proc. Natl. Acad. Sci.*, 2015, **112**, 6882–6886.

49. J. D. Froehlich and C. P. Kubiak, *Inorg. Chem.*, 2012, **51**, 3932–3934.

50. B. Fisher and R. Eisenberg, *J. Am. Chem. Soc.*, 1980, **102**, 7361–7363.

51. M. Beley, J.-P. Collin, R. Ruppert, and J.-P. Sauvage, *J. Chem. Soc. Chem. Commun.*, 1984, 1315.

52. M. Beley, J. P. Collin, R. Ruppert, and J. P. Sauvage, *J. Am. Chem. Soc.*, 1986, **108**, 7461–7467.

53. J. P. Collin, A. Jouaiti, and J. P. Sauvage, *Inorg. Chem.*, 1988, **27**, 1986–1990.

54. J. Schneider, H. Jia, K. Kobiro, D. E. Cabelli, J. T. Muckerman, and E. Fujita, *Energy Environ. Sci.*, 2012, **5**, 9502.

55. M. Fujihira, Y. Hirata, and K. Suga, *J. Electroanal. Chem. Interfacial Electrochem.*, 1990, **292**, 199–215.

56. F. P. Hinz and D. W. Margerum, *Inorg. Chem.*, 1974, **13**.

57. A. Anichini, L. Fabbrizzi, P. Paoletti, and R. M. Clay, *Inorganica Chim. Acta*, 1977, **24**, L21–L23.

58. J. Schneider, H. Jia, J. T. Muckerman, and E. Fujita, *Chem. Soc. Rev.*, 2012, **41**, 2036–2051.

59. M. Fujihira, Y. Hirata, and K. Suga, *J. Electroanal. Chem. Interfacial Electrochem.*, 1990, **292**, 199–215.

60. I. Taniguchi, N. Nakashima, K. Matsushita, and K. Yasukouchi, *J. Electroanal. Chem. Interfacial Electrochem.*, 1987, **224**, 199–209.

61. G. B. Balazs and F. C. Anson, *J. Electroanal. Chem.*, 1992, 322, 325–345.

62. S. Sakaki, *J. Am. Chem. Soc.*, 1990, **112**, 7813–7814.

63. S. Sakaki, *J. Am. Chem. Soc.*, 1992, **114**, 2055–2062.

64. E. Fujita, J. Haff, R. Sanzenbacher, and H. Elias, *Inorg. Chem.*, 1994, **33**, 4627–4628.

65. P. J. C. and E. J. Billo, *Inorg. Chem.*, 1987, **26**, 3224–3226.

66. E. Joseph Billo, P. J. Connolly, D. J. Sardella, J. P. Jasinski, and R. J. Butcher, *Inorganica Chim. Acta*, 1995, **230**, 19–28.

67. J. H. Coates, D. A. Hadi, S. F. Lincoln, H. W. Dodgen, and J. P. Hunt, *Inorg. Chem.*,

1981, **20**, 707.

68. M. Shionoya, E. Kimura, and Y. Iitakas, *J. Am. Chem. Soc.*, 1990, **112**, 9237–9245.

69. K. Bujno, R. Bilewicz, L. Siegfried, and T. A. Kaden, *J. Electroanal. Chem.*, 1998, **445**, 47–53.

70. C. M. Lewandowski, in *Climate Change 2013 - The Physical Science Basis*, ed. Intergovernmental Panel on Climate Change, Cambridge University Press, Cambridge, 2006, pp. 1–30.

71. C. I. Smith, J. A. Crayston, and R. W. Hay, *J. Chem. Soc. Dalt. Trans.*, 1993, 3267–3269.

72. J. Collin and J. P. Sauvage, *Coord. Chem. Rev.*, 1989, **93**, 245–268.

73. H. L. Lord, W. Zhan, and J. Pawliszyn, *Anal. Chim. Acta*, 2010, **677**, 3–18.

74. P. Jacquinot and P. C. Hauser, *Electroanalysis*, 2003, **15**, 1437–1444.

75. J. D. Froehlich and C. P. Kubiak, *J. Am. Chem. Soc.*, 2015, **137**, 3565–3573.

76. G. B. Balazs and F. C. Anson, *J. Electroanal. Chem.*, 1993, **361**, 149–157.

77. C. A. Kelly, B. Q. G. Mulazzani, J. M. Venturi, E. L. Blinn, and M. A. J. R. Ja, *J. Am. Chem. Soc.*, 1995, **117**, 4911–4919.

78. C. Costentin, S. Drouet, M. Robert, and J.-M. Saveant, *Science (80-.).*, 2012, **338**, 90–94.

79. C. Costentin, G. Passard, M. Robert, and J.-M. Savéant, *J. Am. Chem. Soc.*, 2014, **136**, 11821–11829.

80. C. Costentin, G. Passard, M. Robert, and J.-M. Savéant, *Proc. Natl. Acad. Sci.*, 2014,

111, 14990–14994.

81. C. H. Lee, D. K. Dogutan, and D. G. Nocera, *J. Am. Chem. Soc.*, 2011, **133**, 8775–8777.

82. M. Rakowski Dubois and D. L. Dubois, *Acc. Chem. Res.*, 2009, **42**, 1974–1982.

83. C. T. Carver, B. D. Matson, and J. M. Mayer, *J. Am. Chem. Soc.*, 2012, **134**, 5444–5447.

84. F. Franco, C. Cometto, F. Ferrero Vallana, F. Sordello, E. Priola, C. Minero, C. Nervi, and R. Gobetto, *Chem. Commun.*, 2014, **50**, 14670–14673.

85. J. Agarwal, T. W. Shaw, H. F. Schaefer, and A. B. Bocarsly, *Inorg. Chem.*, 2015, **54**, 5285–5294.

86. S. T. Ahn, E. A. Bielinski, E. M. Lane, Y. Chen, W. H. Bernskoetter, N. Hazari, and G. T. R. Palmore, *Chem. Commun.*, 2015, **51**, 5947–5950.

87. I. Azcarate, C. Costentin, M. Robert, and J.-M. Savéant, *J. Am. Chem. Soc.*, 2016, jacs.6b07014.

88. J. D. Froehlich and C. P. Kubiak, *J. Am. Chem. Soc.*, 2015, **137**, 3565–3573.

89. T. Yoshida, K. Tsutsumida, S. Teratani, K. Yasufuku, and M. Kaneko, *J. Chem. Soc. Chem. Commun.*, 1993, **32**, 631–633.

90. A. Jarzębińska, P. Rowiński, I. Zawisza, R. Bilewicz, L. Siegfried, and T. Kaden, *Anal. Chim. Acta*, 1999, **396**, 1–12.

91. T. Yoshida, T. Iida, T. Shirasagi, R. J. Lin, and M. Kaneko, *J. Electroanal. Chem.*, 1993, **344**, 355–362.

92. J. J. Walsh, G. Neri, C. L. Smith, and A. J. Cowan, *Chem. Commun.*, 2014, **50**, 12698–12701.

93. A. Maurin and M. Robert, *J. Am. Chem. Soc.*, 2016, **138**, 2492–2495.

94. D. K. Bediako, A. M. Ullman, and D. G. Nocera, in *Topics in Current Chemistry*, Springer International Publishing, 2015, vol. 371, pp. 173–214.

95. A. R. Guadalupe, D. A. Usifer, K. T. Potts, H. C. Hurrell, A. E. Mogstad, and H. D. Abruna, *J. Am. Chem. Soc.*, 1988, **110**, 3462–3466.

96. C. Arana, M. Keshavarz, K. T. Potts, and H. D. Abruña, *Inorg. Chim. Acta*, 1994, **225**, 285–295.

97. H. C. Hurrell, a. L. Mogstad, D. a. Usifer, K. T. Potts, and H. D. Abruna, *Inorg. Chem.*, 1989, **28**, 1080–1084.

98. T. R. O'Toole, L. D. Margerum, T. D. Westmoreland, W. J. Vining, R. W. Murray, and T. J. Meyer, *J. Chem. Soc. Chem. Commun.*, 1985, 1416.

99. S. Chardon-Noblat, M.-N. Collomb-Dunand-Sauthier, A. Deronzier, R. Ziessel, and D. Zsoldos, *Inorg. Chem.*, 1994, **33**, 4410–4412.

100. E. Portenkirchner, J. Gasiorowski, K. Oppelt, S. Schlager, C. Schwarzinger, H. Neugebauer, G. Knör, and N. S. Sariciftci, *ChemCatChem*, 2013, **5**, 1790–1796.

101. X.-M. Hu, Z. Salmi, M. Lillethorup, E. B. Pedersen, M. Robert, S. U. Pedersen, T. Skrydstrup, and K. Daasbjerg, *Chem. Commun.*, 2016, **52**, 5864–5867.

102. D. Quezada, J. Honores, M. García, F. Armijo, and M. Isaacs, *New J. Chem.*, 2014, **38**, 3606.

103. F. Cecchet, M. Alebbi, C. A. Bignozzi, and F. Paolucci, *Inorg. Chim. Acta*, 2006, **359**, 3871–3874.

104. J. Shen, R. Kortlever, R. Kas, Y. Y. Birdja, O. Diaz-Morales, Y. Kwon, I. Ledezma-Yanez, K. J. P. Schouten, G. Mul, and M. T. M. Koper, *Nat. Commun.*, 2015, **6**, 8177.

105. J. E. Pander, A. Fogg, and A. B. Bocarsly, *ChemCatChem*, 2016, **8**, 3536–3545.

106. T. Inoue, A. Fujishima, S. Konishi, and K. Honda, *Nature*, 1979, 277, 637–638.

107. M. Marszewski, S. W. Cao, J. G. Yu, and M. Jaroniec, *Mater. Horizons*, 2015, **2**, 261–278.

108. J. L. White, M. F. Baruch, J. E. Pander III, Y. Hu, I. C. Fortmeyer, J. E. Park, T. Zhang, K. Liao, J. Gu, Y. Yan, T. W. Shaw, E. Abelev, and A. B. Bocarsly, *Chem. Rev.*, 2015, **115**, 12888–12935.

109. F. E. Osterloh, *Chem. Soc. Rev.*, 2013, **42**, 2294–320.

110. M. B. Wilker, K. J. Schnitzenbaumer, and G. Dukovic, *Isr. J. Chem.*, 2012, **52**, 1002–1015.

111. R. Koole, E. Groeneveld, D. Vanmaekelbergh, A. Meijerink, and C. de Mello Donega, *Nanoparticles Work. Nanosci.*, 2014, 13–51.

112. D. Dung, J. Ramsden, and M. Graetzel, *J. Am. Chem. Soc.*, 1982, **104**, 2977–2985.

113. Y. S. Chaudhary, T. W. Woolerton, C. S. Allen, J. H. Warner, E. Pierce, S. W. Ragsdale, and F. A. Armstrong, *Chem. Commun.*, 2012, **48**, 58.

114. Z. Han, F. Qiu, R. Eisenberg, P. L. Holland, and T. D. Krauss, *Science*, 2012, **338**, 1321–4.

115. J. Huang, K. L. Mulfort, P. Du, and L. X. Chen, *J. Am. Chem. Soc.*, 2012, **134**, 16472–16475.

116. J. Willkomm, N. M. Muresan, and E. Reisner, *Chem. Sci.*, 2015, **6**, 2727–2736.

117. C. Wang, R. L. Thompson, J. Baltrus, and C. Matranga, *J. Phys. Chem. Lett.*, 2010, **1**, 48–53.

118. C. Wang, R. L. Thompson, P. Ohodnicki, J. Baltrus, and C. Matranga, *J. Mater. Chem.*, 2011, **21**, 13452.

119. C. D. Windle, E. Pastor, A. Reynal, A. C. Whitwood, Y. Vaynzof, J. R. Durrant, R. N. Perutz, and E. Reisner, *Chem. - A Eur. J.*, 2015, **21**, 3746–3754.

120. J. Grodkowski and P. Neta, *J. Phys. Chem.*, 2000, **104**, 1848–1853.

121. J. Grodkowski, P. Neta, E. Fujita, A. Mahammed, L. Simkhovich, and Z. Gross, *J. Phys. Chem. A*, 2002, **106**, 4772–4778.

122. J. Grodkowski, T. Dhanasekaran, P. Neta, P. Hambright, B. S. Brunschwig, K. Shinozaki, and E. Fujita, *J. Phys. Chem. A*, 2000, **104**, 11332–11339.

123. J. Hawecker, J.-M. Lehn, and R. Ziessel, *J. Chem. Soc., Chem. Commun.*, 1983, 536–538.

124. H. Hori, F. P. A. Johnson, K. Koike, K. Takeuchi, T. Ibusuki, and O. Ishitani, *J. Chem. Soc. Dalt. Trans.*, 1997, **3**, 1019–1024.

125. H. Hori, F. P. A. Johnson, K. Koike, O. Ishitani, and T. Ibusuki, *J. Photochem. Photobiol. A Chem.*, 1996, **96**, 171–174.

126. H. Hori, J. Ishihara, K. Koike, K. Takeuchi, T. Ibusuki, and O. Ishitani, *J. Photochem. Photobiol. A Chem.*, 1999, **120**, 119–124.

127. H. Hori, K. Koike, M. Ishizuka, K. Takeuchi, T. Ibusuki, and O. Ishitani, *J. Organomet.*

Chem., 1997, **530**, 169–176.

128. H. Takeda, K. Koike, H. Inoue, and O. Ishitani, *J. Am. Chem. Soc.*, 2008, **130**, 2023–31.

129. C. D. Windle, M. W. George, R. N. Perutz, P. A. Summers, X. Z. Sun, and A. C. Whitwood, *Chem. Sci.*, 2015, **6**, 6847–6864.

130. C. D. Windle, M. V. Câmpian, A.-K. Duhme-Klair, E. A. Gibson, R. N. Perutz, and J. Schneider, *Chem. Commun.*, 2012, **48**, 8189.

131. S. Sato, K. Koike, H. Inoue, and O. Ishitani, *Photochem. Photobiol. Sci.*, 2007, **6**, 454–461.

132. K. Kiyosawa, N. Shiraishi, T. Shimada, D. Masui, H. Tachibana, S. Takagi, O. Ishitani, D. A. Tryk, and H. Inoue, *J. Phys. Chem. C*, 2009, **113**, 11667–11673.

133. H. Takeda, H. Koizumi, K. Okamoto, and O. Ishitani, *Chem. Commun.*, 2014, **50**, 1491–1493.

134. H. Takeda, H. Koizumi, K. Okamoto, and O. Ishitani, *Chem. Commun.*, 2014, **50**, 1491–1493.

135. P. L. Cheung, C. W. Machan, A. Y. S. Malkhasian, J. Agarwal, and C. P. Kubiak, *Inorg. Chem.*, 2016, **55**, 3192–3198.

136. J.-X. Zhang, C.-Y. Hu, W. Wang, H. Wang, and Z.-Y. Bian, *Appl. Catal. A Gen.*, 2016, **522**, 145–151.

137. H. Fei, M. D. Sampson, Y. Lee, C. P. Kubiak, and S. M. Cohen, *Inorg. Chem.*, 2015, **54**, 6821–6828.

138. M. Beley, J. P. Collin, J. P. Sauvage, J. P. Petit, and P. Chartier, *J. Electroanal. Chem.*,

1986, **206**, 333–339.

139. P. Chartier and J.-P. Petit, *J. Electroanal. Chem.*, 1989, **269**, 267–281.

140. J. L. Grant, K. Goswami, L. O. Spreer, J. W. Otvos, and M. Calvin, *J. Chem. Soc., Dalt. Trans.*, 1987, 2105–2109.

141. V. Balzani, F. Bouetta, and M. T. Gandolfi, *Org. Chem. Theory*, 1978, 1–64.

142. V. Balzani, L. Moggi, M. F. Manfrin, F. Bolletta, and G. S. Laurence, *Coord. Chem. Rev.*, 1975, **15**, 321–433.

143. E. Kimura, X. Bu, M. Shionoya, S. Wada, and S. Maruyama, *Inorg. Chem.*, 1992, **31**, 4542–4546.

144. C. Herrero, A. Quaranta, S. El Ghachtouli, B. Vauzeilles, W. Leibl, and A. Aukauloo, *Phys. Chem. Chem. Phys.*, 2014, **16**, 12067.

145. B. Gholamkhass, H. Mametsuka, K. Koike, T. Tanabe, M. Furue, and O. Ishitani, *Inorg. Chem.*, 2005, **44**, 2326–2336.

146. S. Sato, K. Koike, H. Inoue, and O. Ishitani, *Photochem. Photobiol. Sci.*, 2007, **6**, 454–461.

147. Y. Tamaki, K. Watanabe, K. Koike, H. Inoue, T. Morimoto, and O. Ishitani, *Faraday Discuss.*, 2012, **155**, 115–127.

148. T. Arai, S. Sato, K. Uemura, T. Morikawa, T. Kajino, and T. Motohiro, *Chem. Commun.*, 2010, **46**, 6944.

149. S. Sato, T. Morikawa, S. Saeki, T. Kajino, and T. Motohiro, *Angew. Chemie Int. Ed.*, 2010, **49**, 5101–5105.

150. S. Sato, T. Arai, T. Morikawa, K. Uemura, T. M. Suzuki, H. Tanaka, and T. Kajino, *J. Am. Chem. Soc.*, 2011, **133**, 15240–15243.

151. T. M. Suzuki, H. Tanaka, T. Morikawa, M. Iwaki, S. Sato, S. Saeki, M. Inoue, T. Kajino, and T. Motohiro, *Chem. Commun.*, 2011, **47**, 8673.

152. J. Willkomm, K. L. Orchard, A. Reynal, E. Pastor, J. R. Durrant, and E. Reisner, *Chem. Soc. Rev. Chem. Soc. Rev*, 2016, **45**, 9–23.

153. A. V. Akimov, R. Jinnouchi, S. Shirai, R. Asahi, and O. V. Prezhdo, *J. Phys. Chem. B*, 2015, **119**, 7186–7197.

154. A. Reynal, J. Willkomm, N. M. Muresan, F. Lakadamyali, M. Planells, E. Reisner, and J. R. Durrant, *Chem. Commun.*, 2014, **50**, 12768–12771.

155. H. Tian, *ChemSusChem*, 2015, **8**, 3746–3759.

156. R. Kuriki, K. Sekizawa, O. Ishitani, and K. Maeda, *Angew. Chemie - Int. Ed.*, 2015, **54**, 2406–2409.

157. R. Kuriki, H. Matsunaga, T. Nakashima, K. Wada, A. Yamakata, O. Ishitani, and K. Maeda, *J. Am. Chem. Soc.*, 2016, **138**, 5159–5170.

158. A. Hagfeldt, G. Boschloo, L. Sun, L. Kloo, and H. Pettersson, *Chem. Rev.*, 2010, **110**, 6595–6663.

159. W. J. Youngblood, S.-H. A. Lee, K. Maeda, and T. E. Mallouk, *Acc. Chem. Res.*, 2009, **42**, 1966–1973.

160. W. J. Youngblood, S.-H. A. Lee, Y. Kobayashi, E. A. Hernandez-Pagan, P. G. Hoertz, T. A. Moore, A. L. Moore, D. Gust, and T. E. Mallouk, *J. Am. Chem. Soc.*, 2009, **131**, 926–927.

161. J. R. Swierk and T. E. Mallouk, *Chem. Soc. Rev.*, 2013, **42**, 2357–2387.

162. J. Willkomm, K. L. Orchard, A. Reynal, E. Pastor, J. R. Durrant, and E. Reisner, *Chem. Soc. Rev.*, 2016, **45**, 9–23.

163. E.-G. Ha, J.-A. Chang, S.-M. Byun, C. Pac, D.-M. Jang, J. Park, and S. O. Kang, *Chem. Commun.*, 2014, **50**, 4462.

164. G. Boschloo and D. Fitzmaurice, *J. Phys. Chem. B*, 1999, **103**, 2228–2231.

165. M. Hansen, F. Li, L. Sun, and B. König, *Chem. Sci.*, 2014, **5**, 2683.

166. M. A. Gross, A. Reynal, J. R. Durrant, and E. Reisner, *J. Am. Chem. Soc.*, 2014, **136**, 356–366.

167. T. Kuwana, R. K. Darlington, and D. W. Leedy, *Anal. Chem.*, 1964, **36**, 2023–2025.

168. M. R. Anderson, C. D. Taylor, M. R. Anderson, and C. D. Taylor, in *Encyclopedia of Analytical Chemistry*, John Wiley & Sons, Ltd, Chichester, UK, 2000.

169. W. R. Heineman, J. N. Burnett, and R. W. Murray, *Anal. Chem.*, 1968, **40**, 1974–1978.

170. R. W. Murray, W. R. Heineman, and G. W. O'Dom, *Anal. Chem.*, 1967, **39**, 1666–1668.

171. S. R. Domingos, H. Luyten, F. Van Anrooij, H. J. Sanders, B. H. Bakker, W. J. Buma, F. Hartl, and S. Woutersen, *Rev. Sci. Instrum.*, 2013, **84**, 33103.

172. D. Roy and J. Fendler, *Adv. Mater.*, 2004, **16**, 479–508.

173. M. Osawa, in *Advances in Electrochemical Science and Engineering*, Wiley- VCH Verlag GmbH, 2006, pp. 269–314.

174. A. Wieckowski, C. Korzeniewski, and B. Braunschweig, *Vibrational Spectroscopy at Electrified Interfaces*, John Wiley & Sons, Inc., Hoboken, NJ, USA, 2013.

175. Y. R. Shen, *Nature*, 1989, 337, 519–525.

176. I. V. Stiopkin, H. D. Jayathilake, A. N. Bordenyuk, and A. V. Benderskii, *J. Am. Chem. Soc.*, 2008, **130**, 2271–2275.

177. J. P. Smith and V. Hinson-Smith, *Anal. Chem.*, 2004, **76**, 287 A-290 A.

178. Z. Dale, University of Illinois at Urbana-Champaign, 2005.

179. C. L. Loch, D. Ahn, and Z. Chen, *J. Phys. Chem. B*, 2006, **110**, 914–918.

180. Z. D. Schultz, S. K. Shaw, and A. A. Gewirth, *J. Am. Chem. Soc.*, 2005, **127**, 15916–15922.

181. G. Q. Lu, A. Lagutchev, D. D. Dlott, and A. Wieckowski, *Surf. Sci.*, 2005, **585**, 3–16.

182. P. Guyot-Sionnest and A. Tadjeddine, *Chem. Phys. Lett.*, 1990, **172**, 341–345.

183. A. Tadjeddine and P. Guyot-Sionnest, *Electrochim. Acta*, 1991, **36**, 1839–1847.

184. J. Wang, M. L. Clarke, X. Chen, M. A. Even, W. C. Johnson, and Z. Chen, *Surf. Sci.*, 2005, **587**, 1–11.

185. S. Baldelli, *J. Phys. Chem. B*, 2005, **109**, 13049–13051.

186. N. García Rey and D. D. Dlott, *J. Phys. Chem. C*, 2015, **119**, 20892–20899.

187. B. A. Rosen, A. Salehi-Khojin, M. R. Thorson, W. Zhu, D. T. Whipple, P. J. A. Kenis, and R. I. Masel, *Science (80-.).*, 2011, **334**, 643–644.

188. B. A. Rosen, W. Zhu, G. Kaul, A. Salehi-Khojin, and R. I. Masel, *J. Electrochem. Soc.*, 2012, **160**, H138–H141.

189. C. L. Anfuso, D. Xiao, A. M. Ricks, C. F. A. Negre, V. S. Batista, and T. Lian, *J. Phys.*

Chem. C, 2012, **116**, 24107–24114.

190. M. L. Clark, B. Rudshteyn, A. Ge, S. A. Chabolla, C. W. Machan, B. T. Psciuk, J. Song, G. Canzi, T. Lian, V. S. Batista, and C. P. Kubiak, *J. Phys. Chem. C*, 2016, **120**, 1657–1665.

191. Y. R. Shen, *J. Phys. Chem. C*, 2012, **116**, 15505–15509.

192. I. M. Lane, University of Cambridge, 2006.

193. R. G. W. Norrish and G. Porter, *Nature*, 1949, 164, 658.

194. R. Berera, R. van Grondelle, and J. T. M. Kennis, *Photosynth. Res.*, 2009, **101**, 105–18.

195. E. Topoglidis, A. E. . Cass, B. O'Regan, and J. R. Durrant, *J. Electroanal. Chem.*, 2001, **517**, 20–27.

196. F. Fabregat-Santiago, J. García-Cañadas, E. Palomares, J. N. Clifford, S. a. Haque, J. R. Durrant, G. Garcia-Belmonte, and J. Bisquert, *J. Appl. Phys.*, 2004, **96**, 6903–6907.

197. A. J. Cowan, J. Tang, W. Leng, J. R. Durrant, and D. R. Klug, *J. Phys. Chem. C*, 2010, **114**, 4208–4214.

198. J. J. Walsh, J. R. Lee, E. R. Draper, S. M. King, F. Jäckel, M. A. Zwijnenburg, D. J. Adams, and A. J. Cowan, *J. Phys. Chem. C*, 2016, **120**, 18479–18486.

"I almost wish I hadn't gone down that rabbit-hole – and yet – and yet – it's rather curious, you know, this sort of life!"

- *Alice in Wonderland*

2

CO_2 reduction by Ni(cycC): electrocatalysis, immobilisation on semiconductor oxides and electron transfer

2.1 Scope of the chapter

As outlined in Chapter 1, the complex Ni(cyc) (cyc = 1,4,8,11-tetraazacyclotetradecane) has been shown to be an excellent CO_2 reduction electrocatalyst in water.[1–3] The complex has been used in both electro-[4] and photocatalytic applications,[5–7] however in the latter cases the results have been somewhat disappointing. The immobilisation of molecular electrocatalysts on semiconductor oxides, to photodrive the CO_2 reduction reaction has been proven a worthwhile approach towards the design of more efficient photocatalysts,[8] however to date no reports of an immobilised Ni(cyc) complex for CO_2 reduction exist to our knowledge. We have envisaged that the modification of the cyc framework with a functional group suitable for immobilisation on semiconductors could lead to new hybrid photocatalysts. Our initial target has therefore been [Ni(1,4,8,11-tetraazacyclotetradecane-6-carboxylic acid)]$^{2+}$ (hereafter named Ni(cycC), Figure 4), as carboxylic acids have been widely used as anchoring ligands in the dye-sensitised solar cells (DSSC) field in order to anchor dyes to TiO_2.

Ni(cycC) has been chosen as a target complex due to the functional group being as far from the amine groups and the metal centre as was possible, Figure 4. This was hypothesised to reduce the negative effects of functional groups on activity and selectivity that have been often reported for this class of catalysts.[2,9] Furthermore, the addition of a carboxylic acid, and therefore a mobile proton source in the ligand framework provided an intriguing scientific question regarding the role of local proton sources in the enhancement of CO_2 reduction electrocatalysis; the beneficial role of mobile protons has been demonstrated across several classes of electrocatalysts, however a similar effect has not yet been reported to occur in water. In the first section of this chapter, the synthesis of Ni(cycC) will be briefly described, followed by a detailed electrochemical study of the properties of the newly synthesised complex towards the electrocatalytic CO_2 reduction in water, both on a Hg and glassy carbon (GCE) electrodes. The adsorption behaviour and pH dependence of the catalyst will be studied and correlated with the differences in activity found at low pH values, and benchmarking of the new electrocatalyst with the existing literature will be provided by carrying out Rotating Disc

Voltammetry (RDE) and Foot-of-the-Wave (FOWA) analysis, in line with the recent trends in the literature.

In the second section of this chapter we will analyse the properties of Ni(cycC) with respect to the immobilisation on nc-TiO_2; the properties of the modified films will be explored using electrochemical and spectroscopic methods. Through the use of Transient Absorption Spectroscopy (TAS) we will demonstrate successful electron tranfer from the TiO_2 to the immobilised Ni(cycC) upon light irradiation under argon, showing the validity of the heterogeneous approach.

2.2 Results and discussion

2.2.1 Synthesis and characterisation

The carboxylic acid derivative of Ni(cyc) was obtained by mixing the functionalised tetraaza macrocycle (1 eq.), which is commercially available, with $NiCl_2$ (1.1 eq) in water in the presence of $NaHCO_3$ (6 eq.) at room temperature. The $NaHCO_3$ is needed to deprotonate the ligand, which is supplied as the HCl salt (cycC·4HCl), where the amine groups are protonated (the pKa values for the parent cyclam ligand have been calculated[10], and they are: pKa_1 = 11.6, pKa_2 = 10.6, pKa_3 = 1.61, pKa_4 = 2.42) allowing easier insertion of nickel in the macrocyclic ring. Initial yields were very poor (< 30%). This was largely due to nickel hydroxide and nickel carbonates forming in the basic environment and precipitating out of solution. When the synthesis was carried out with a smaller amount of $NaHCO_3$ (4 eq.) the reaction had even lower yields (~20%). Higher yields could be achieved by diluting the reaction solution tenfold (from 2 mM to 0.2 mM in $NiCl_2$). Purification of the crude product is carried out by multiple washings with ethanol to remove by filtration the inorganic salts that are a byproduct of the reaction (residual $NaHCO_3$, which is present in large excess, and NaCl, which forms during the reaction). Mass spectrometry (MS) confirmed that the reaction led to the formation of Ni(cycC) by the presence of a single molecular ion of m/z = 301, corresponding to the complex without the chloride counterions. The product was used without further

recrystallisation, as elemental analysis (EA) indicated that the product was pure. Furthermore, EA revealed that in the powder form the complex is in its deprotonated carboxylate form, with a sodium counterion, $[Ni(cycCO_2)]NaCl_2$ (full details, including full crystallographic data, are in section 2.3.1).

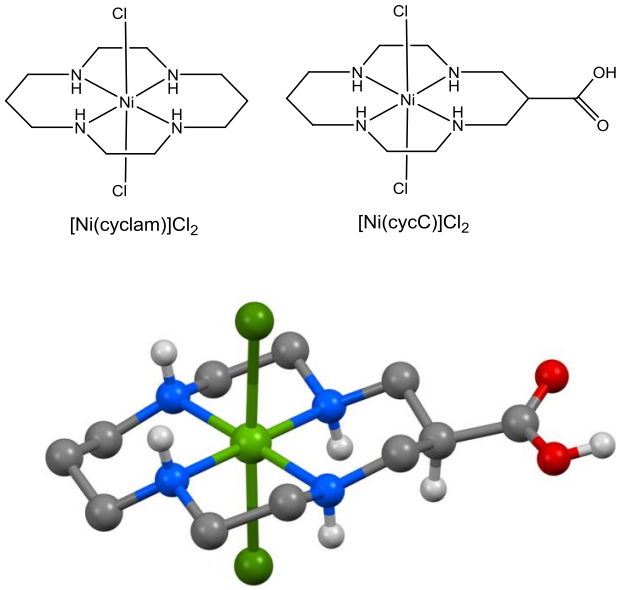

Figure 4 – Structures of $[Ni(cyc)]Cl_2$ and $[Ni(cycC)]Cl_2$ and crystal structure for the new complex. H atoms, except for those bound to N or O are omitted for clarity.

Crystals suitable for single crystal X-ray diffraction are obtained by slow vapour diffusion of hexane in ethanolic solutions of the complex (Figure 4). In the crystal form obtained, the carboxylic acid is protonated, and $[Ni(cycC)]Cl_2$ assumes a distorted octahedral coordination, with the two chlorine ligands occupying the axial sites, and a *R,R,S,S*(*trans-III*) conformation of the ligand[11–13].

It is well known in the literature[14–16] that nickel macrocycle complexes can readily interconvert between the high and low spin states in solution, which is accompanied by a change in geometry (Scheme 13). In strongly coordinating solvents, two solvent molecules occupy the axial sites of a distorted octahedron; in this coordination geometry the nickel is in its high spin state, with two unpaired electrons in the d_{z^2} and the $d_{x^2-y^2}$ orbitals, which are of similar energy, making the complex paramagnetic. In weakly coordinating solvents the d_{z^2} orbital is strongly stabilised with respect to

the $d_{x^2-y^2}$ orbital, which is increased in energy, causing the nickel to assume a square planar geometry where the metal centre is in a low spin state, with the electrons paired. In the case of the most studied $[Ni(cyc)]Cl_2$ complex, the ratio of octahedral and square planar geometries in water at 25°C has been found to be 29% and 71% respectively[17].

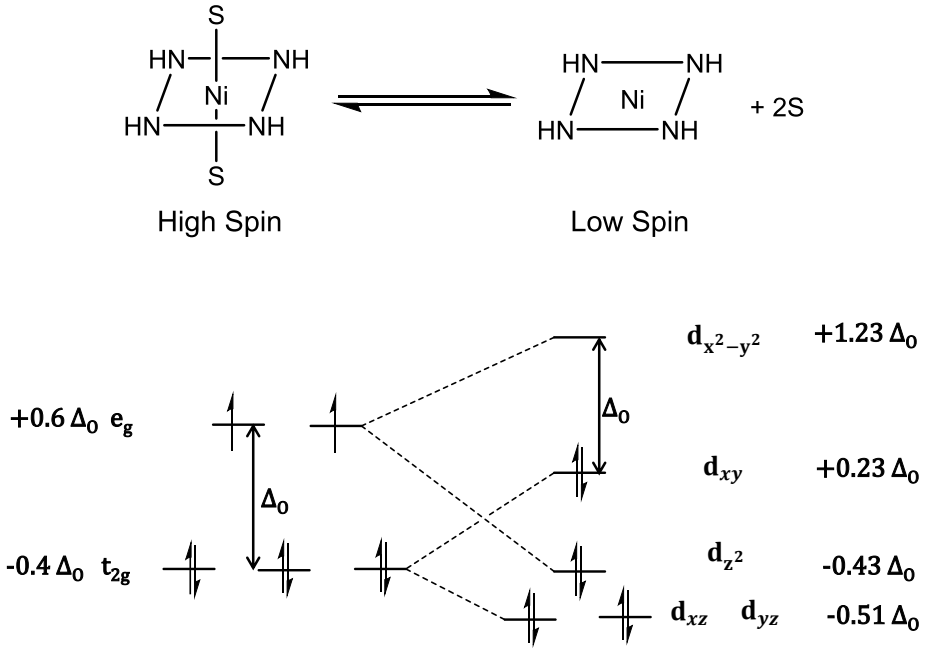

Scheme 13 - Spin interconversion in nickel tetraazamacrocycles complexes (top) and d orbitals splitting for the octahedral and square-planar geometries (bottom).

Aqueous solutions of Ni(cycC) have an orange appearance and a UV-vis spectrum (Figure 5) characterised by one main absorption peak centred at 453 nm, typical of a low-spin square planar geometry, and two weaker absorption bands at 337 and 526 nm, typical of an octahedral geometry. Interestingly, the UV-vis solution of an ethanolic solution (which is pink in colour) shows the disappearance of the peak at 453 nm, indicating that in these conditions the complex is solely present in an octahedral geometry. Assuming that the extinction coefficient remains the same across solvents, the decrease in the peak at 337 nm should give an estimation of the ratios between the octahedral and square planar complexes in water. Surprisingly, from this analysis the octahedral geometry is dominant in aqueous solution (73% at pH 7). This is proposed to be due to the carboxylate functional

group binding to the nickel centre in the axial position (Scheme 14). Such a structure has been reported for the analogue Co complex of cycC[18] and other macrocycle complexes bearing a pendant arm.[19]

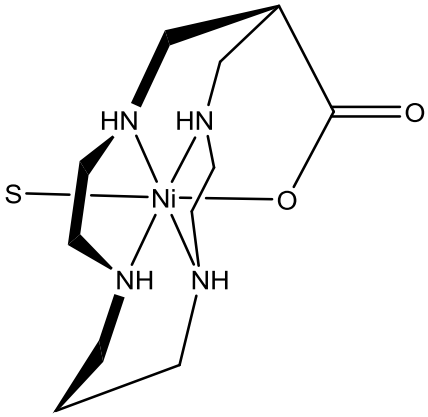

Scheme 14 – Proposed conformation for the binding of the carboxylate to one of the axial positions of the nickel centre, with a solvent molecule coordinating the free axial position.

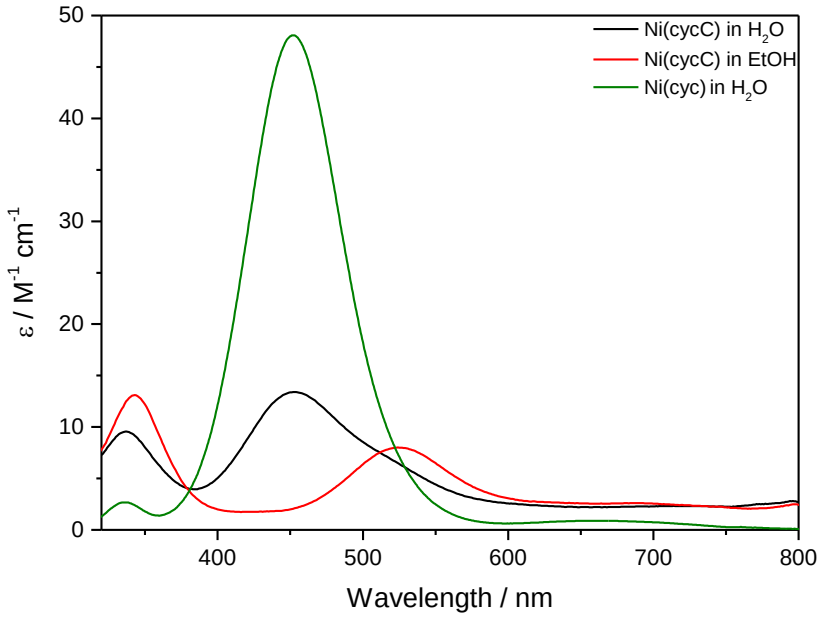

Figure 5 – Solution UV-Vis spectra of Ni(cyc) (10 mM in H_2O) and Ni(cycC) (10 mM in both ethanol and water).

Characterisation of the complex *via* NMR (Nuclear Magnetic Resonance) spectroscopy was prevented by the presence of the octahedral paramagnetic complex in solution, broadening the

spectral lines. The ATR-FTIR (Attenuated Total Reflectance Fourier-Transform Infrared) spectrum of $[Ni(cycCO_2^-Na^+)]Cl_2$ (Figure 6) shows two main bands, at 1580 cm^{-1} and 1345 cm^{-1}. These frequencies are consistent with the ν_{as} and ν_s for a carboxylate anion, rather than a carboxylic acid (ν_s = 1700 cm^{-1}). This confirms that the complex is in the sodium carboxylate form in the solid state, when obtained from the described synthesis, in agreement with elemental analysis.

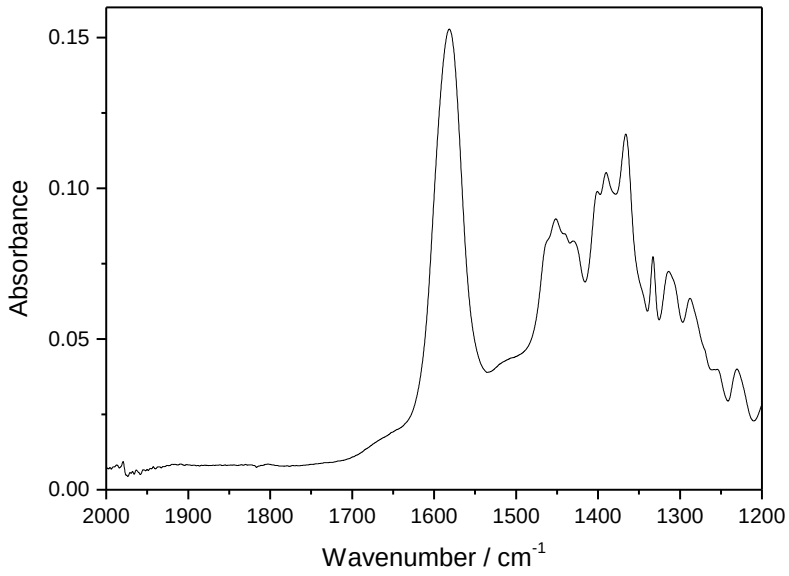

Figure 6 – ATR-FTIR spectrum of powder $[Ni(cycCO_2^-Na^+)]Cl_2$.

2.2.3 CO_2 reduction by Ni(cycC) on mercury electrodes

Mercury electrodes have been the traditional electrode material of choice for reductive electrochemistry in water due to their extended solvent window.[20] In addition to the potential window advantage, Ni(cyc) and derivatives have been shown to be more active on mercury electrodes than any other electrode material[21] due to the catalyst adsorbing on the electrode surface. Therefore we have initially examined the electrochemistry of Ni(cycC) on a HMDE (hanging mercury drop electrode).

The CV (cyclic voltammogram) of Ni(cycC) under argon (Figure 7) shows two main features: a couple at -1.33 V_{NHE} and a "spike" at *ca.* -1.1 $V_{NHE.}$ A similar current spike has been previously reported for Ni(cyc)[22] and proposed to be due to the reductive adsorption of the complex on the Hg surface. Here, the spike is also assigned to the same adsorption mechanism, which will be quantified and rationalised below. The main peak at -1.33 V_{NHE} is assigned to the $Ni^{II/I}$ redox couple in solution. The linear relationship between the peak current density and the square root of the scan rate (inset in Figure 7) indicate that the solution $Ni^{II/I}$ couple can be considered reversible at the scan rates analysed, and under diffusion control.

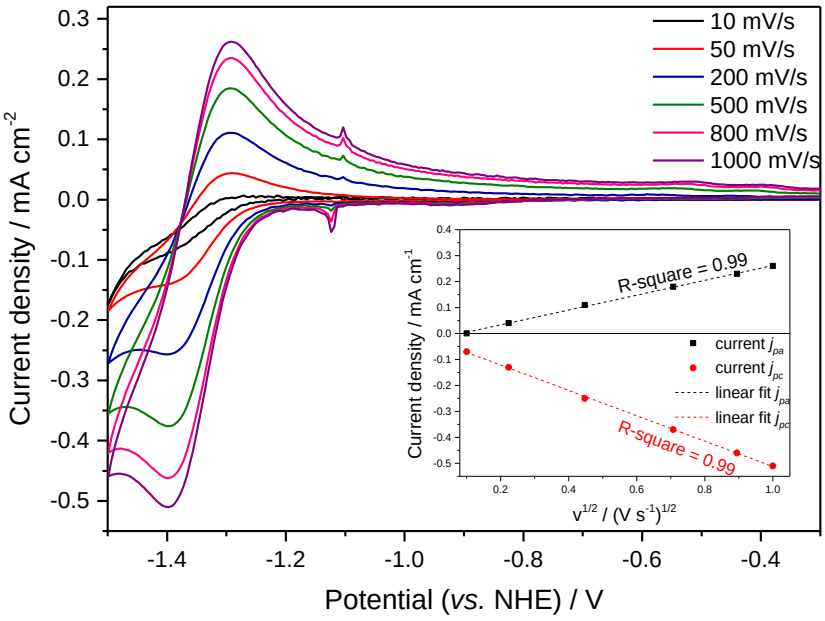

Figure 7 - CVs of 1 mM [Ni(cycC)] in Ar-purged H_2O containing 0.1 M $NaClO_4$ on a HMDE working electrode at increasing scan rates. Inset: dependence of the peak current density for the redox process $Ni^{II/I}$ on the square root of the scan rate.

Figure 8 shows the comparison between the CVs of Ni(cyc) and Ni(cycC) under argon and CO_2. The increase in current density at potentials close to the $Ni^{II/I}$ couple under CO_2 indicates that catalytic reduction of CO_2 is occurring. The results obtained for Ni(cyc) show good agreement with past reports.[23–25] Ni(cycC) shows very similar behaviour to Ni(cyc), however some observations can be made. The increase in current, measured as the i_c/i_p ratio (where i_c is the peak current in the presence

of the reaction substrate (CO_2) and i_p is the peak current for the couple in the absence of CO_2) is slightly higher for Ni(cycC) (i_c/i_p ~ 48) than for Ni(cyc) (i_c/i_p ~ 31); this could be interpreted as a higher catalytic activity for Ni(cycC) than for Ni(cyc), however it is important to note here that the onset in catalytic potential for Ni(cycC) (-1.00 V_{NHE}) is *ca.* 50 mV more negative than for Ni(cyc) (-0.95 V_{NHE}).

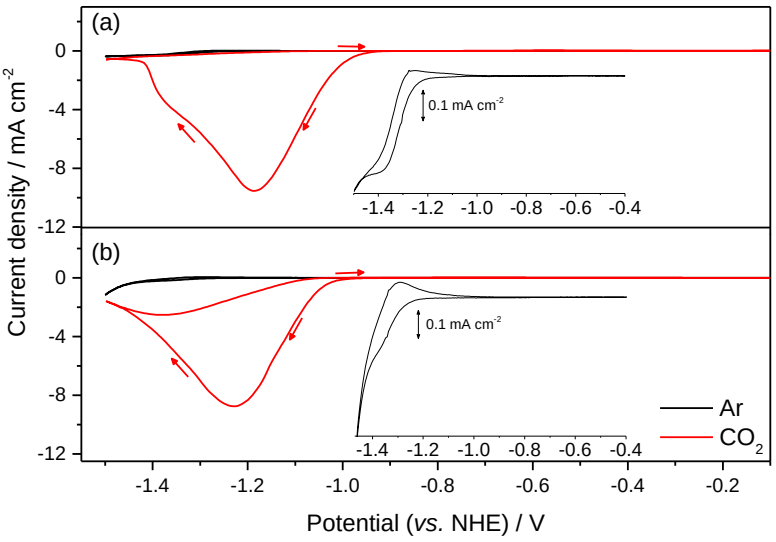

Figure 8 - CV of 1 mM solutions of (a) Ni(cyc) and (b) $[Ni(cycC)]^{2+}$ recorded in 0.1 M $NaClO_4$ at pH 5 purged with either argon (black line) or CO_2 (red line) recorded at 100 mV s^{-1} using a HMDE electrode (0.023 cm^2). The insets show an expansion of the black lines.

The nature of the reduction products has been investigated by carrying out controlled potential electrolysis (CPE) experiments on 0.1 mM solutions of Ni(cycC) at pH = 5 (Figure 9). A Au-Hg amalgam has been used as the working electrode. It has been demonstrated in the past that Ni(cyc) maintains its catalytic properties towards CO_2 reduction on this electrode material.[24] The electrode has been prepared by dipping a gold wire (surface area ≈ 2.5 cm^2) in triple distilled mercury for 1 minute to coat the surface and then drying for at least 2 hours.

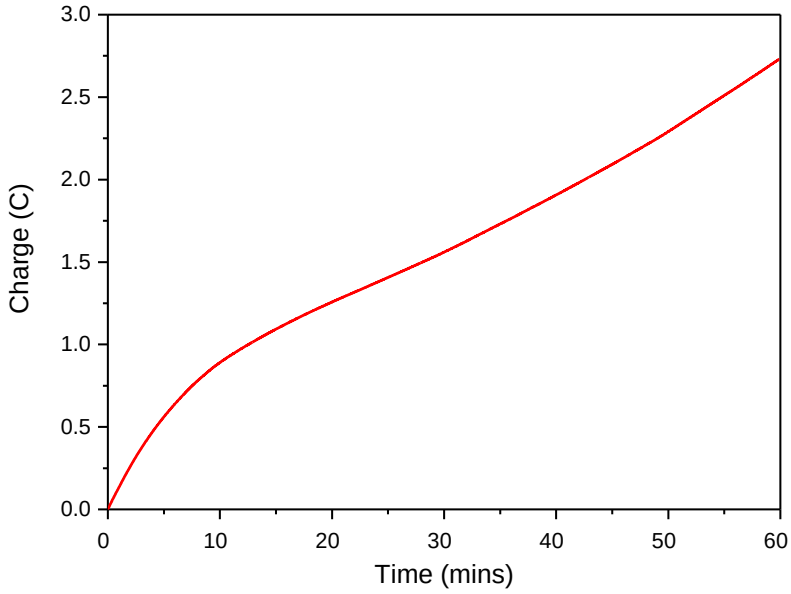

Figure 9 - CPE of a CO_2 purged, 1 x 10^{-4} M solution of Ni(cycC) containing 0.1 M $NaClO_4$, pH 5. The potential was kept at -1.2 V_{NHE} for 1 hour using a Au-Hg amalgam electrode.

The charge *vs.* time plot showed catalysis slowing down after approximately the first ten minutes of CPE. This can be attributed to rapid accumulation of CO at the electrode surface, partially deactivating the complex, as it is known[26,27] that the formation of $Ni^{I}(CO)$ species is a common deactivation pathway for this class of catalysts. Ni(cycC) showed excellent selectivity for CO ($CO:H_2$ ~ 100:1) after 1 hour at a constant potential of -1.2 V_{NHE}, with a charge passed of 2.7 C (Figure 9) and a Faradaic efficiency (FE) of 88%. The Turnover Number (TON), calculated considering the bulk of the catalyst in solution, is 5.3, confirming that the CO_2 reduction is indeed catalytic with respect to Ni(cycC).

The studies outlined above show that the modifications on the carbon backbone of the complex have not significantly affected the catalytic activity of the new complex at pH 5, the operating conditions considered ideal for this class of CO_2 reduction catalysts. The seminal study by Sauvage[28] showed a strong pH dependence for the catalytic activity of Ni(cyc). At pH values higher than *ca.* 6, catalysis is strongly reduced, primarily because of the decrease of free CO_2 present in solution at increasing pH values. On the other hand, although at pH values lower than 4 the CVs under CO_2 show large

catalytic waves, the selectivity for CO production over H_2 rapidly decreases, until at pHs lower than 4, proton reduction becomes the dominant process.[25] The next section will be focused on studying the effect of the pH on catalysis by Ni(cycC).

2.2.4 CO_2 reduction in acidic media – the role of protons

Very recent studies have outlined the importance of the second coordination sphere of molecular complexes for catalytic CO_2 reduction. Of particular relevance to this work are studies[29–32] on the increased rates of catalysis that some complexes have shown when modified with functional groups bearing acidic protons, which have been shown to act as local proton sources. Most of these catalysts have been studied in organic solvents, and a similar effect in aqueous solutions has been shown only in one very recent example in the literature.[33]

The dissolution of CO_2 in water involves the establishment of several equilibrium reactions, which are highly dependent on the pH of the solution:

$$CO_{2(g)} \leftrightharpoons CO_{2(aq)}$$

$$CO_{2(aq)} + H_2O \leftrightharpoons H_2CO_3$$

$$H_2CO_3 + H_2O \leftrightharpoons H_3O^+ + HCO_3^-$$

$$HCO_3^- + H_2O \leftrightharpoons H_3O^+ + CO_3^{2-}$$

Unbuffered solutions saturated with CO_2 have a pH af ca. 4 and a concentration of CO_2(g) of 36 mM. Hydration of dissolved CO_2 is slow; at atmospheric pressure, and pH values lower than 8 the concentration of carbonic acid is low, and the concentration of CO_2 in solution remains constant with changing the pH. As the pH is increased, equations 3 and 4 become faster, and move the equilibrium of equation 2 towards the right, so that at high pH values the concentration of free solvated CO_2 decreases, while the concentrations of bicarbonate and carbonate increase, according to Figure 10:

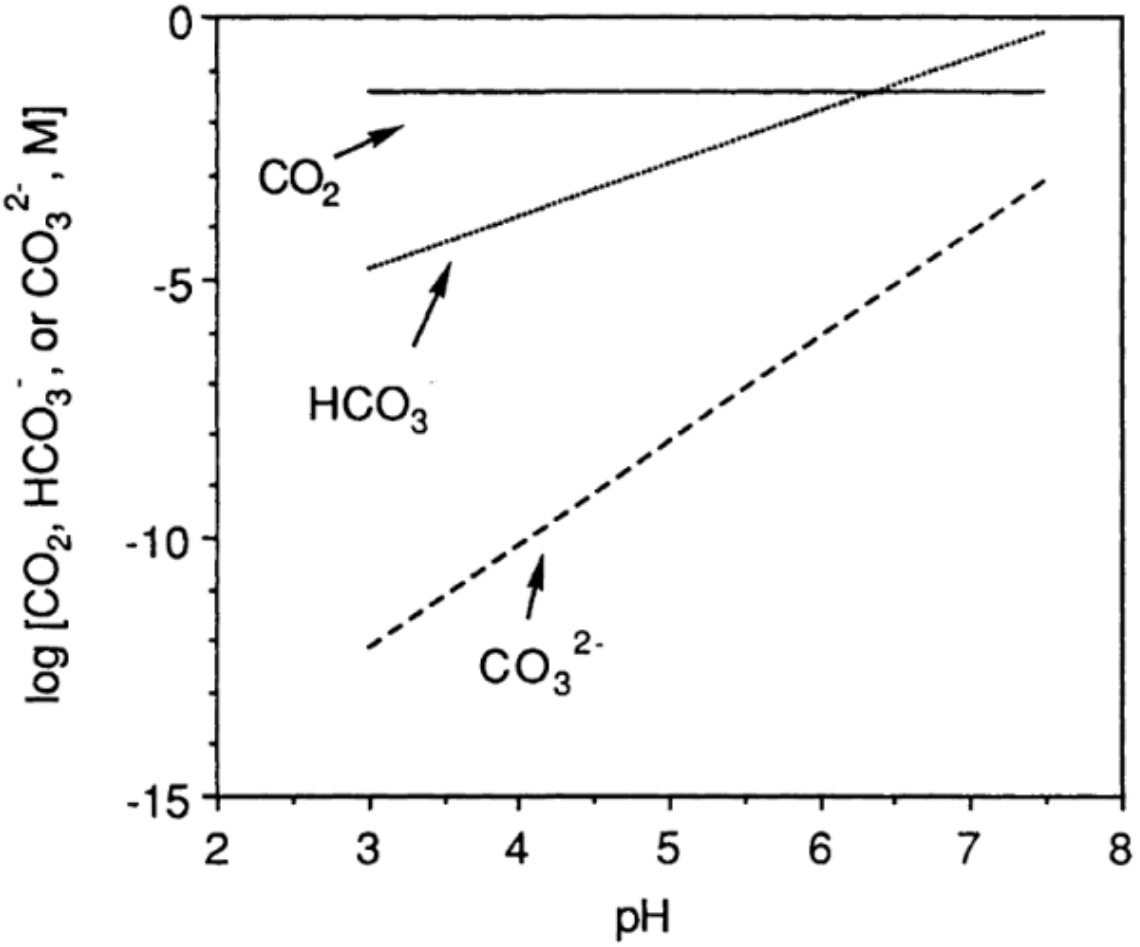

Figure 10 – Species present in aqueous carbon dioxide solutions as a function of pH at a CO2 pressure of 1 atm and a temperature of 25° C. Reproduced from[34]

The presence of a carboxylic acid, and evidence from UV-vis spectra in solution indicating that the cyclam backbone is sufficiently flexible to enable the carboxylate group to directly interact with the nickel centre, prompted us to investigate the properties of Ni(cycC) in acidic media; it was hypothesised that protonation of the complex to form the carboxylic acid could provide a local proton source. Figure 11 shows the CVs under a CO_2 atmosphere at a range of decreasing pH values, adjusted by adding aliquots of either $HClO_4$ 1 M or NaOH 1 M to the prepurged solution of the complex until the desired pH value was reached. The catalytic curve retains the same shape for pHs >3. At values lower than 3 a new irreversible wave appears with a peak potential of -0.99 V_{NHE}, which increases in

current density with decreasing pH. At pH 2 the peak at -1.2 V_{NHE} is no longer distinguishable due to the overlap with the new feature.

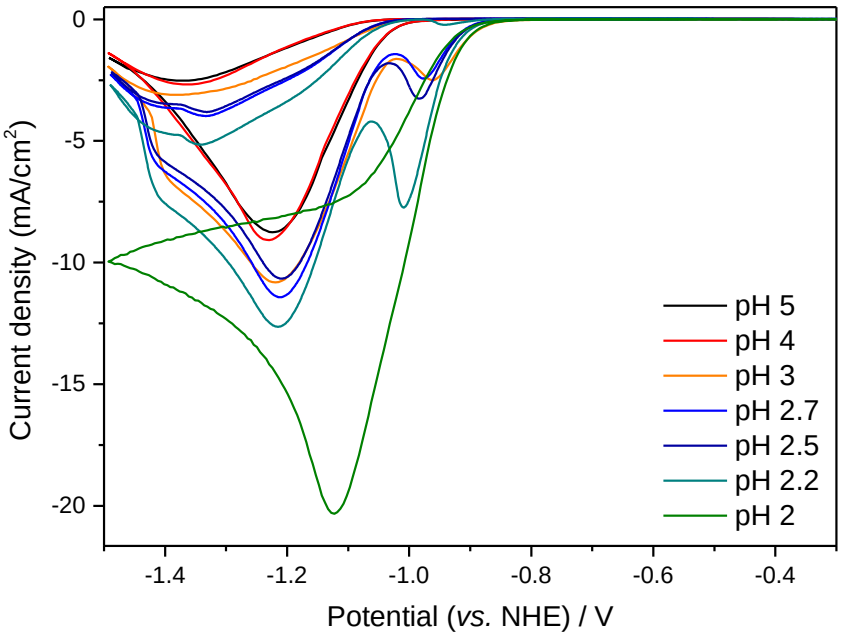

Figure 11 - CVs of Ni(cycC) (1 mM) at a range of pH values under CO_2, recorded in 0.1 M $NaClO_4$, scan rate 100 mVs^{-1}.

The same behaviour is not observed in the CVs for Ni(cyc) in the same conditions, with the current density at -0.99 V_{NHE} remaining approximately constant throughout all the pH values of interest (Figure 12(a)). A slight shift in the onset potential to less negative values is observed in the CV for Ni(cyc) under CO_2 at pH 2, and this can be attributed to the shift in the overpotential for the reaction brought about by the change in pH ($E^0_{CO_2/CO,NHE}$ = -0.12-0.059·pH). Remarkably, the onset potential shift observed in the CVs for Ni(cycC) is much larger, implying that there is a step change in the catalytic activity of Ni(cycC) at pH 2 compared to Ni(cyc). The traces under argon show very little contribution from proton reduction at potentials >-1.1 V_{NHE}, indicating by first approximation that Ni(cycC) is an excellent catalyst at pH 2.

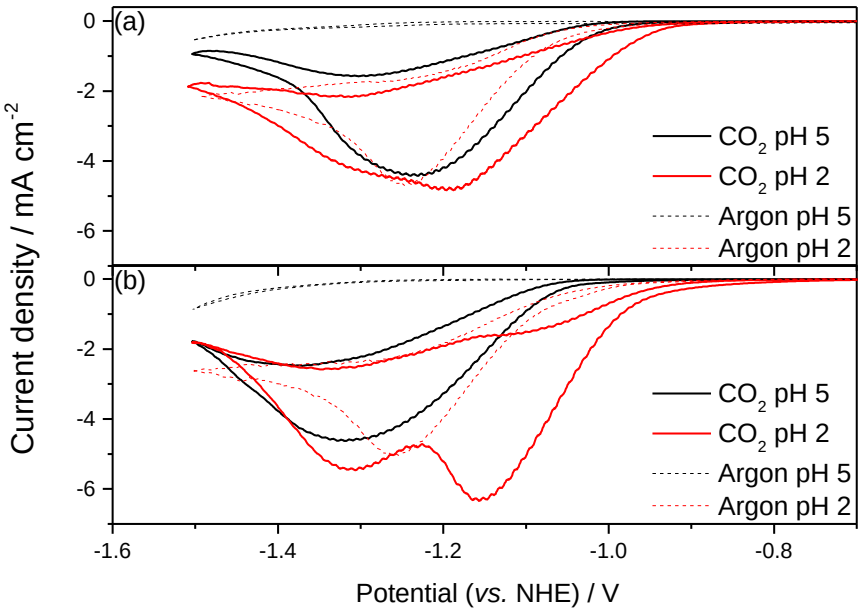

Figure 12 - CVs of (a) Ni(cyc) and (b) Ni(cycC) (1mM) under CO_2 (solid lines) and Ar (dashed), at pH 5 (black) and 2 (red), 0.1 M $NaClO_4$, 100 mV s^{-1} using a Hg-Au amalgam electrode.

As it is well known that nickel macrocycle complexes lose selectivity at pH < 4, the selectivity of both complexes was examined by carrying out bulk electrolysis experiments. As expected from the CVs, the charge passed in an hour by Ni(cycC) was much higher than Ni(cyc) (Figure 13(a)). Furthermore, at this pH Ni(cyc) produces mainly hydrogen, in agreement with the past reports for this complex (0.2:1 CO:H_2; FE: total = 86%, H_2 = 73 ± 16%, CO = 13 ± 10%, with errors being the result of 3 experiments). In contrast, Ni(cycC) shows a remarkable retention of selectivity. Electrolysis of unstirred solutions yielded after an hour a selectivity of > 4:1 (CO:H_2), with a total FE of 81% (calculated on the total FEs for H_2 and CO, H_2 = 15 ± 5%, CO = 66 ± 9%). These results correspond to a TON for CO of 591 compared to the value of *ca.* 49 for Ni(cyc), calculated by considering the concentration of catalyst in the bulk solution. As explained above, the species adsorbed at the surface have been shown to be the primary active complex on mercury electrodes, thus the bulk TON calculated here is but a lower limit of the real value. A TON for CO calculated using the surface coverage values obtained during DPSC measurements (*vide infra*) would give a higher TON of 65,000. This value represents the upper limit for the TON, as it is obtained by

assuming that no catalyst exchange from solution to the electrode during the time the CPE is carried out. A more accurate evaluation of the catalytic activity of the catalyst will be provided in the following sections with Tafel plot analysis and RDE measurements.

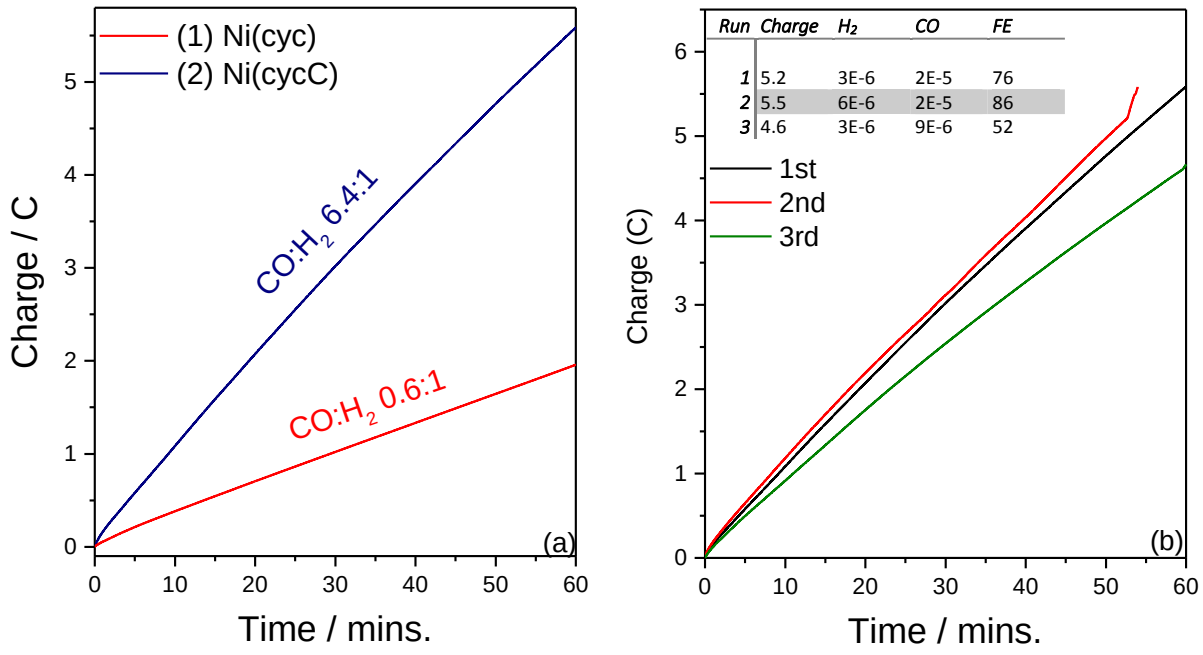

Figure 13 – (a) Charge passed vs. *time for CO_2-purged, $3x10^{-6}$ M solutions of Ni(cyc) (red) and Ni(cycC) (blue), $CO:H_2$ ratios are for the individual experiments. (b) Consecutive charge vs. time plots for a CO_2-purged, $3x10^{-6}$ M solution of Ni(cycC). The CPE experiments were carried out on a custom made Hg pool electrochemical cell at -0.99 V_{NHE}, 0.1 M $NaClO_4$, pH = 2.*

The stability of the complex was evaluated at first by running consecutive bulk electrolysis experiments on the same solution of the complex, which was repurged with CO_2 after every run (Figure 13(b)), to ensure sufficient CO_2 was present. There is little deviation in the charge *vs.* time plots for the first two runs, with a more significant deviation from linearity and lower selectivity and FE measured for the third run. This is likely due to the build-up of CO in the unstirred mercury pool cell, which is known to lead to catalyst inhibition and precipitation of the insoluble inactive species on the surface of the electrode.[26,27] Experiments run for longer time periods (7.5hours), on a constant stream of CO_2 to avoid significant substrate consumption and to agitate the solution, show reasonable

stability, with a FE for CO = 52 % and H_2 = 31 % being obtained in the final 0.5 of an hour (Figure 14).

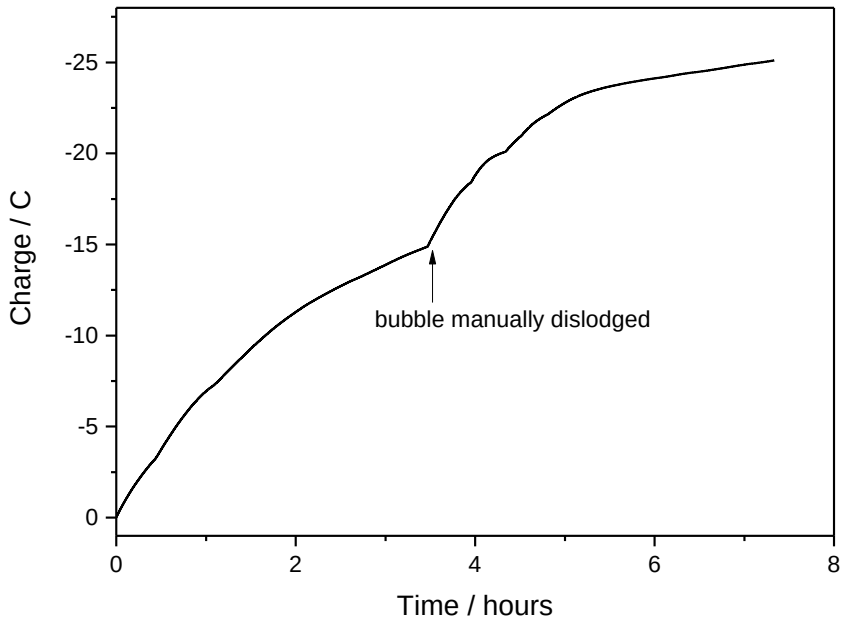

Figure 14 - Prolonged electrolysis of Ni(cycC) carried out using a Hg pool electrochemical cell (-0.99 V_{NHE}) on a constant CO_2 purge, 0.1 M $NaClO_4$, pH = 2. During the final 30 minutes the cell was sealed to allow for the product ratio to be measured. Despite the presence of a constant CO_2 purge large bubbles still formed on the Hg pool electrode during electrolysis.

From the electrochemistry data shown above, it is apparent that Ni(cycC) is an extremely active catalyst for the reduction of CO_2 to CO at pH 2. It is hypothesised that the step change in catalytic activity is due to the opening of a different mechanism pathway to the one that has been demonstrated for the unmodified complex. The analysis of the rate constants in this case would be revealing, however the unusual nature of the active species makes a thorough kinetic analysis complicated. A Tafel analysis was carried out at pH 5 and 2, and it is shown in Figure 15 and Figure 16.

The Tafel plot is a useful tool for evaluating rate constants for the region where linearity of the log(*j*) *vs.* the overpotential is maintained. In this potential range the catalytic reaction can be considered non-hindered by substrate consumption, and the apparent first order rate constant (k_{obs}) can be calculated with equation (1):

$$i_{cat} = nF\Gamma Ak_{obs} \quad (1)$$

Where i_{cat} is the current of the catalytic curve, n is the number of electrons, F is Faraday's constant, Γ is the surface coverage and A is the area of the electrode. This type of analysis is convenient here because it is based only on the measured current densities (i.e. the actual number of electrons transferred), and does not require a detailed knowledge of the catalytic mechanism. The overpotential was based on literature reported reduction potentials for the reduction of CO_2 to CO at pH 5.[35] A change in solubility of CO_2 and CO will change the overpotential, according to the Nernst equation. As the CO_2 reduction to CO is a proton-assisted reaction, the change in the overpotential here was calculated using the Nernst relationship ($E_{CO2/CO}$ = -0.117 – 0.059•pH). Furthermore, as discussed in chapter 1, at low pH values the concentration of CO_2 can be approximated to remain the same.

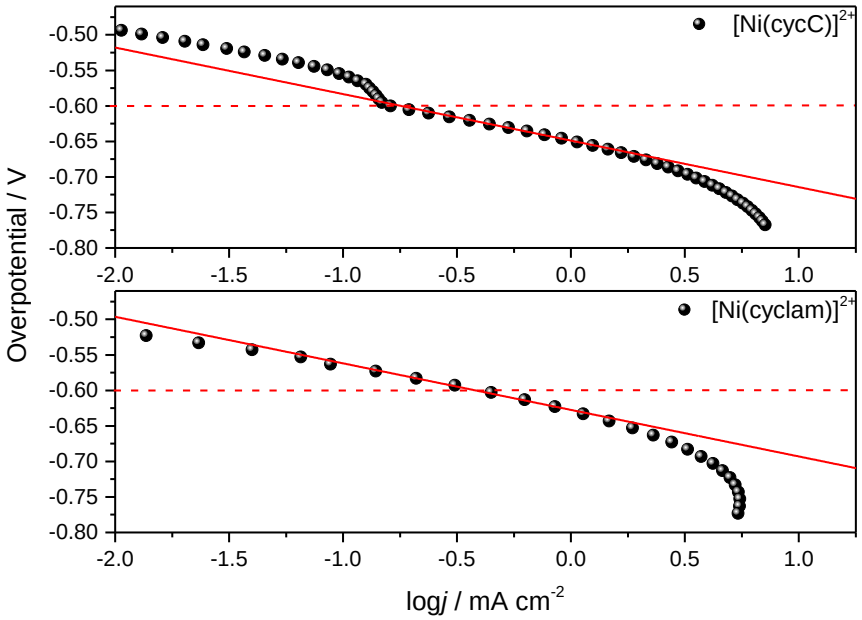

Figure 15 - Plots of CO_2 reduction overpotential (pH = 5) vs. log of current density for Ni(cycC) and Ni(cyc) at pH 5; calculated from LSVs at 100 mV s^{-1} in 0.1 M $NaClO_4$ electrolyte containing 1 x 10^{-4} M catalyst.

The Tafel plot for Ni(cyc) at pH 5 has been reported,[25] and the one obtained in this work is in agreement with the literature data. The red full line shows the linear fit of the overpotential-current data, while the red dotted lines in the figures represent the potential at which bulk electrolysis at pH

2 was carried out (-0.99 V_{NHE}), which is also a potential where the Tafel plot is linear. According to equation (1), and using the values for the surface coverage (see below) we obtained a k_{obs} = 4.6 s^{-1} for Ni(cycC) and k_{obs} = 7 s^{-1} for Ni(cyc) at pH 5 and at an overpotential of -0.6 V (-0.99 V_{NHE}, the potential at which the CPE experiments at pH 2 have been carried out).

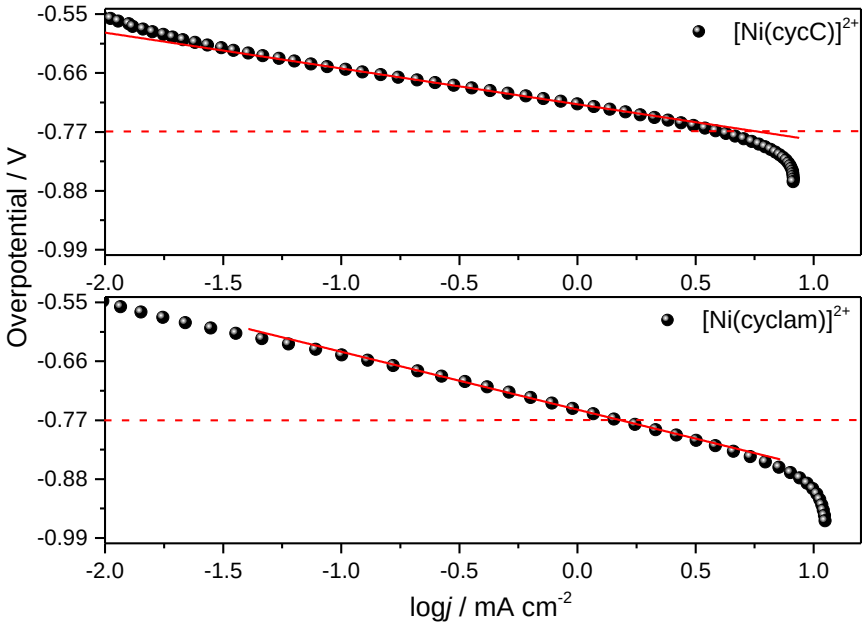

Figure 16 - Plots of CO_2 reduction overpotential vs. log of current density for Ni(cycC) and Ni(cyc) at pH 2; calculated from LSVs at 100 mV s^{-1} in 0.1 M $NaClO_4$ electrolyte containing 1 x 10^{-4} M catalyst.

For the catalysis at pH 2 we have obtained a k_{obs} of 54 and 230 s^{-1} for Ni(cyc) and Ni(cycC) respectively. It is apparent that Ni(cycC) turns over at least five times faster than Ni(cyc) under these conditions and over 25 times faster than Ni(cyc) at pH 5 at -0.99 V_{NHE}. In contrast to Ni(cycC), which has a remarkable selectivity towards CO_2 at this low pH, Ni(cyc) primarily produces H_2 in bulk electrolysis experiments and it is likely that the k_{obs} for Ni(cyc) at pH 2 towards CO_2 is actually a significant overestimate.

Whilst the Tafel plots provide a measure of the catalytic rate constant at the foot of the wave they do not offer insights into the potential dependence of the k_{obs} at higher driving forces. The variation of the catalytic rates with the potential has been measured by carrying out rotating disc electrode voltammetry. This technique allows us to eliminate substrate diffusion problems which are encountered in static electrochemical methods[34]. The experiments were carried out using an Au-Hg amalgam electrode, which was prepared by dipping a gold rotating disc electrode in mercury followed by drying for at least two hours. The experiments proved somewhat challenging, due to the nature of the set-up for the RDE voltammetry. The nature of the amalgam material made the electrode preparation key to the success of the experiment. Even when prepared with the utmost care, the surface area varied due to the difficulties in polishing the electrode without removing the mercury layer; for the current densities calculation, the geometric surface area of the electrode has been considered. To give a fair comparison, only sets of data carried out with the same electrode are presented. For the electrode to be able to move freely when mounted on the rotating shaft, the electrochemical cell needed to be kept open to air on the main port; to circumvent this problem all the experiments were carried out while bubbling the solution with the gas in analysis, so that a positive pressure was maintained throughout the experiment. Care was taken to ensure the purging needle was as far away from the rotating electrode as possible, so not to disrupt the flow to the electrode. It was found that the amalgam is extremely sensitive to the rotation speed of the electrode; bare gold was visible on the electrode after experiments where a rotation of > 900 RPM (rotations per minute) was maintained. Therefore, only rotation speeds lower than this value were considered for analysis. Experiments were carried out at a constant temperature using a water bath kept at 26°C.

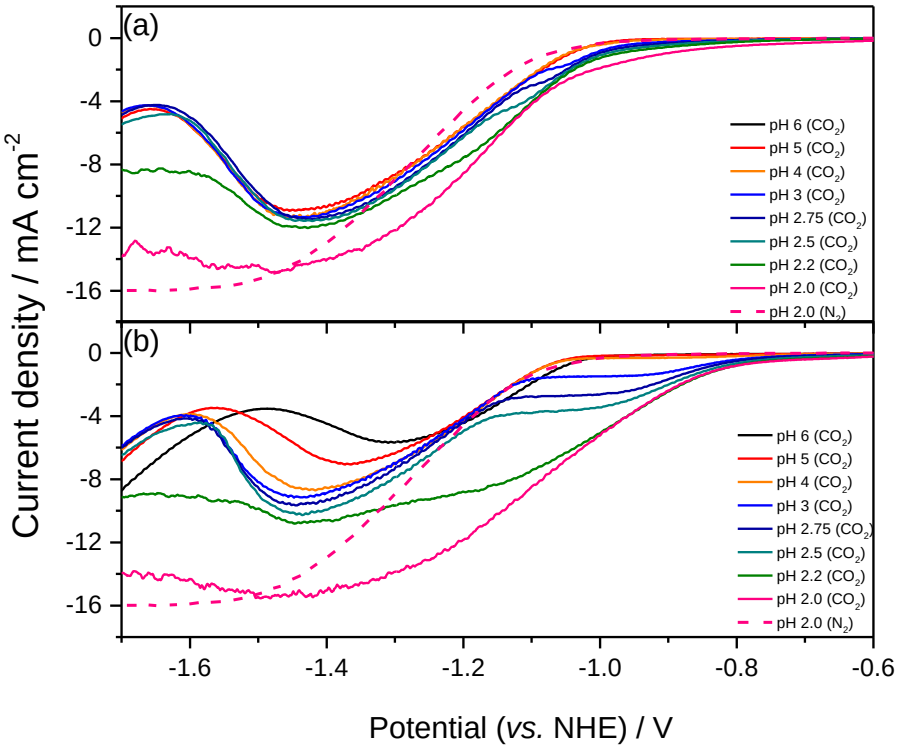

Figure 17 - RDE voltammetry of (a) Ni(cyc) and (b) Ni(cycC) (0.1 mM) under CO_2 (solid lines) and Ar (dashed) recorded at 800 rpm at the pH indicated. All experiments are recorded using a Hg–Au amalgam electrode in 0.1 M $NaClO_4$.

Figure 17 shows the pH dependence on the RDE at 800 RPM. There is very little change for complex Ni(cyc) throughout all the pH values examined, save for a small anodic shift in the onset potential, likely due to the increased proton reduction, as shown by the CPE experiments. On the other hand, while the plateau current increases only slightly for complex Ni(cycC) at the pH values 6-4, a new reductive feature is noted at pH 3 and below, with the current density at the corresponding potential (*ca.* -0.95 V_{NHE}) increasing dramatically between pH 2.5 and 2.2, and plateauing at pH 2. The voltammetry under nitrogen at the same pH values show very little change, apart from an increase in current density plateau at very negative potentials, due to the increase in proton reduction at low pHs (Figure 18(a)).

The rate constants at different potentials can be obtained with RDE voltammetry by varying the rotation speed, Figure 18(a). Koutecký-Levich plots can be obtained by plotting the inverse of the plateau current *vs.* the inverse of the square of thr rotation speed expressed in radians (ω):

$$1/i_{lim} = 1/i_k + 1/0.62nFAD^{2/3}\omega^{1/2}\nu^{-1/6}C \qquad (2)$$

The intercept of this linear plot, $1/i_k$, represents the inverse of the limiting current at infinite rotation speed, which will be determined by the apparent rate constant according to the following relationship:

$$i_k = nF\Gamma A k_{obs} \qquad (3)$$

The Koutecký-Levich analysis holds value only if the plots of the inverse current *vs.* the inverse of the rotation speed are linear. A representative example is shown in Figure 18(b).

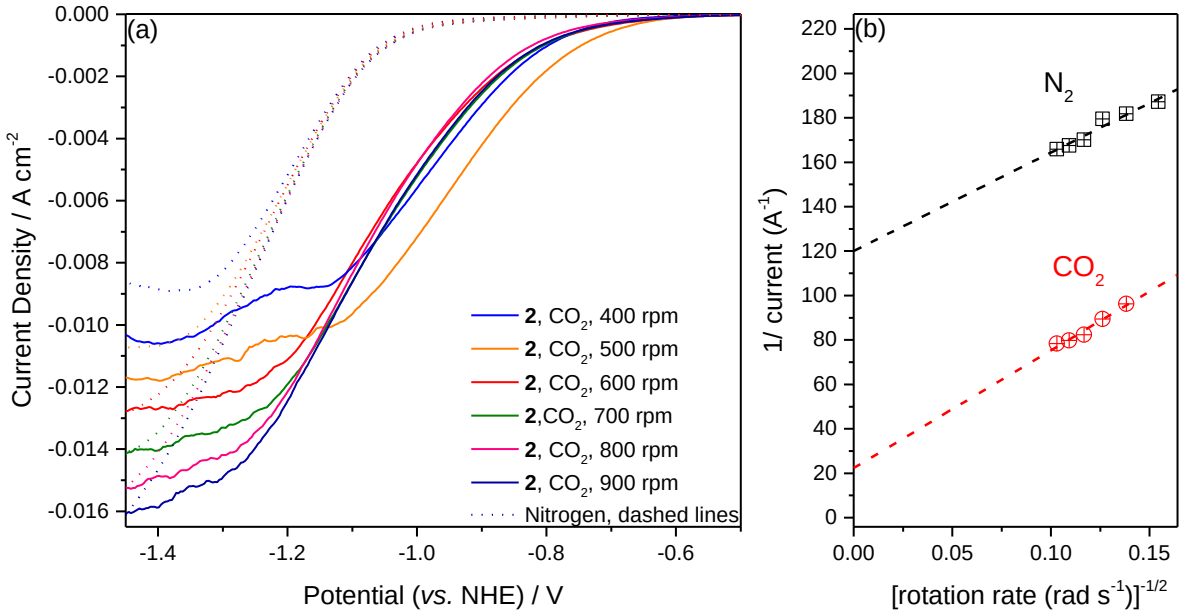

Figure 18 – (a) RDE voltammetry of Ni(cycC) (0.1 mM) under nitrogen (dashed) and CO_2 (solid lines), 100 mV s^{-1}, 0.1 M $NaClO_4$, pH 2, recorded using a Hg-Au amalgam electrode. (b) Example of a Koutecký-Levich plot for Ni(cycC), under argon and CO_2, calculated at -1.25 V_{NHE}.

The Koutecký-Levich analysis has been applied to a series of potentials for the RDE voltammetry of Ni(cyc) and Ni(cycC) at pH 5 and 2. The rate constants have been calculated as the average of three

independent measurements, and reported in Figure 19 and Table 3. Since the currents under CO_2 are well resolved from the currents under N_2 for Ni(cycC) it can be assumed that the k_{obs} measured will be independent of proton reduction. There is very good agreement between the rate constant calculated with the Tafel plot and RDE methods at -0.99 V_{NHE}, with a value of 3.5 (±1.0) x 10^1 s^{-1} for Ni(cyc) and 1.9 (±0.2) x 10^2 s^{-1} for Ni(cycC), confirming that Ni(cycC) turns over *ca.* five times faster than Ni(cyc) at this potential. Furthermore, as Ni(cyc) has been shown above to mainly produce H_2, it is likely that the k_{obs} value found is a significant overestimate. At the plateau current we obtain a very high value for k_{obs} = 3.4 (±1.0) x 10^3 s^{-1}. We have not calculated the k_{obs} for Ni(cyc) at potentials lower than -1.1 V_{NHe} as there is minimal difference between the currents under CO_2 and N_2.

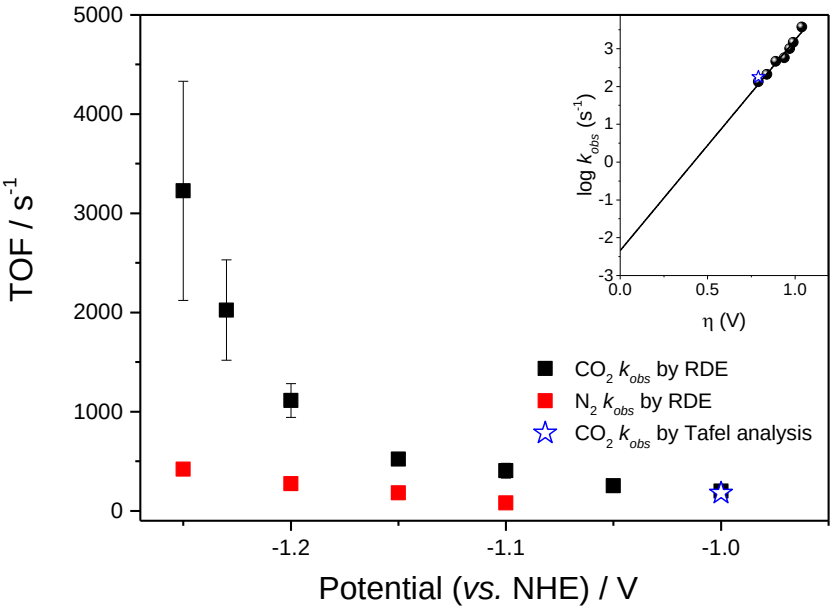

Figure 19 - Plot of k_{obs} of Ni(cycC), calculated from the intercepts of Koutecký-Levich plots, vs. potential at pH 2. Error bars are the result of 3 independent measurements. The blue star indicates the TOF of Ni(cycC) calculated from the Tafel plot, Figure 16. Inset: log(TOF) vs. overpotential under CO_2.

Table 3 - k_{obs} for catalysts Ni(cyc) and Ni(cycC) at different potentials, calculated from Koutecký-Levich plots, and relative errors. At potential below -1.1 V_{NHE} using Ni(cycC) the value of k_{obs} measured under N_2 was found to be very low, on the order of the experimental error.

V_{NHE}	k_{obs} CO_2 (s^{-1}) x10^2	Error ± (s^{-1}) x10^2	k_{obs} N_2 (s^{-1}) x10^2	Error ± (s^{-1}) x10^2
Ni(cycC)				
-0.99	2.02	0.28	NA	
-1.05	2.54	0.27	NA	
-1.10	4.05	0.25	0.81	0.16
-1.15	5.23	0.45	1.81	0.14
-1.20	11.39	1.75	2.34	0.16
-1.23	20.30	4.80		
-1.25	34.39	10.02	3.38	0.38
Ni(cyc)				
-0.99	0.35	0.10	0.04	0.01
-1.10	1.39	0.45	0.53	0.05

The k_{obs} calculated here is the observed rate constant for the overall CO_2 reduction process. The exact reaction mechanism is not known, however the results presented until now indicate the presence of two different mechanisms for the CO_2 reduction, which are activated at different pH values to different degrees. The value obtained for k_{obs} at -1.25 V_{NHE} is amongst the highest ever reported for a CO_2 reduction catalyst, and exceeds most catalysts operating in aqueous solutions. To our knowledge, only one other catalyst with higher rate constant and selectivity in water has been reported[33], WSCAT (an Fe complex with 5,10,15,20-tetrakis(4'-trimethylammoniumphenyl) porphyrin), however we note that the complex shows good activity at pH values close to neutral, and it rapidly loses selectivity when the pH decreases. Nevertheless, the authors report a turnover

frequency (TOF) calculated through the FOWA (Foot-of-the-Wave Analysis) of 10^7 s^{-1}, although the calculations were showed only for the catalyst in DMF (dimethylformamide) with added phenol as the proton source.

Comparison between catalysts operating in different solvents (where CO_2 solubility varies) is usually achieved using a second order rate constant, by dividing the k_{obs} by the concentration of CO_2 used during the experiment. Here, we attempted to carry out RDE experiments at different concentrations (Figure 20) of CO_2, however as highlighted previously the nature of the RDE cell makes it necessary to continuously purge solutions, complicating the measurements. Our tentative data indicates that the reaction order with respect to $CO_2 \leq 1$, and therefore the calculation of the 2nd order rate constant is non trivial, therefore benchmarking of Ni(cycC) using a recently proposed method of calculating the rate constants by extrapolation from CVs, in the same solvent systems used in other studies, will be presented separately in section 2.2.5.

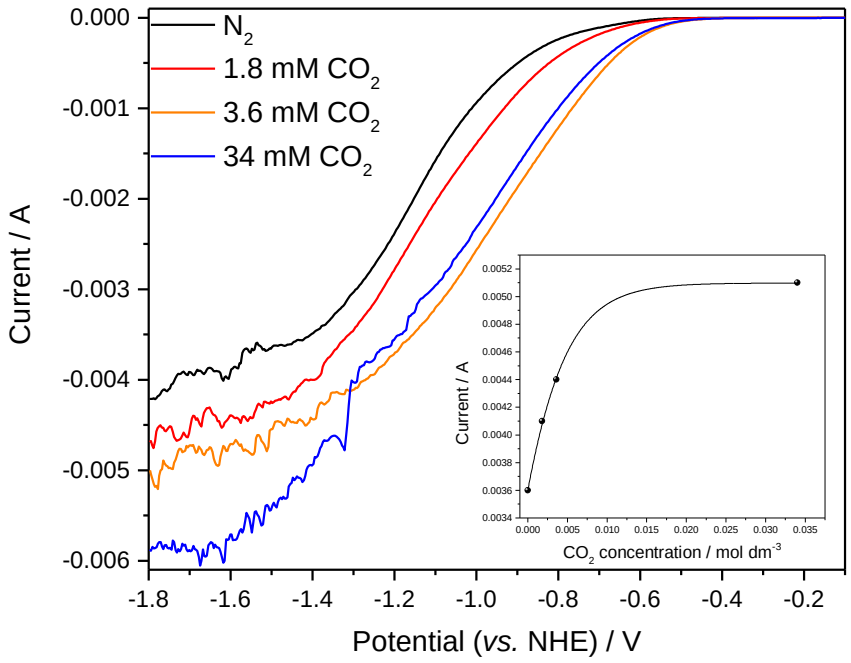

Figure 20 - RDE voltammetry of 0.1 mM solutions of Ni(cycC) at different CO_2 concentration, 900 rpm, scan rate 100 mV s^{-1}, 0.1 M $NaClO_4$, pH 2, recorded using a Hg-Au amalgam electrode. The inset shows the non-linear dependence of the current with increasing CO_2 concentration, calculated at -1.45 V_{NHE}.

The reasons behind the enhanced catalytic activity at pH 2 were investigated. Firstly, it was of importance to determine whether Ni(cycC) adsorbs on the surface of the mercury electrode in a manner previously shown for Ni(cyc), and if so whether the adsorption is affected by the change in pH. This measurement might give some mechanistic insights, and more importantly will yield an accurate surface coverage, useful to calculate the upper limit of the TON for the catalytic reaction (above). To verify that Ni(cycC) adsorbs on mercury in a similar manner to Ni(cyc), the CVs for low concentration solutions of the catalysts on GCE and HMDE were compared (Figure 21). When the concentration is decreased by one order of magnitude the complex shows trivial currents under CO_2 on GCE compared to the argon trace (the $Ni^{II/I}$ is not visible on GCE because of the reduced potential window in aqueous solutions), while on the HMDE the catalytic current is very similar for both concentrations. This behaviour confirms that only a small fraction of the complex present in the starting solution is responsible for catalysis on the mercury surface, but that high concentrations are required on GCE for catalytic activity to be maintained.

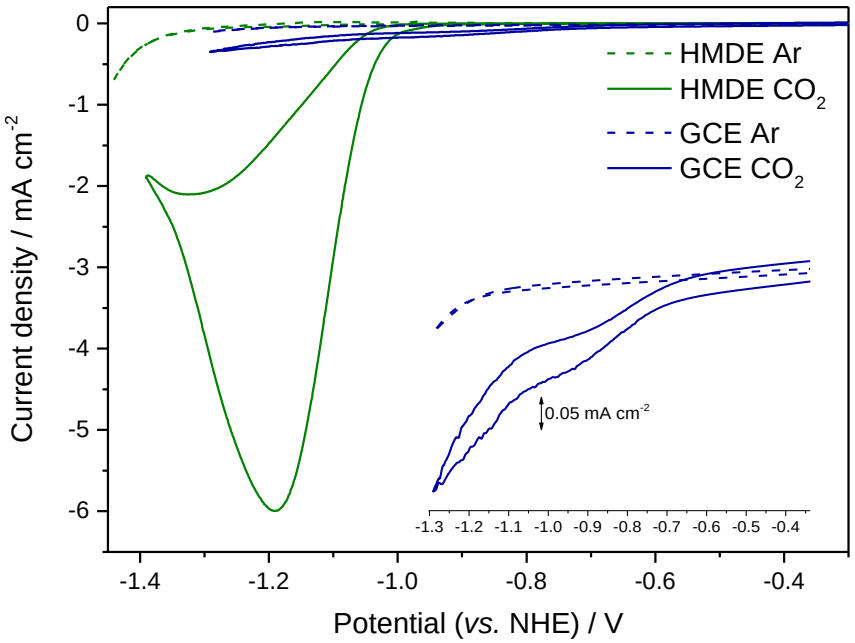

Figure 21 - CVs of 0.1 mM solutions of Ni(cycC) recorded with GCE (blue) and a HMDE (green), under Ar (dashed lines) and CO_2 (solid lines), 0.1 M KCl, 100 mV s^{-1}. The inset shows an expansion of the GCE data.

The adsorption of Ni(cyc) on mercury electrodes can also be measured and quantified[36] using a technique called double-potential step chronocoulometry (DPSC). The technique, developed by Anson and co-workers,[37,38] is well suited in this case as it has been shown that only the reduced species $[Ni^{I}(cyc)]^{+}$ adsorbs on the electrode surface. A detailed discussion of the DPSC measurement to calculate the surface coverage of adsorbed species is reported elsewhere,[37–39] however briefly we report the key points here. In the experiment the working electrode potential is kept at a value where adsorption is expected, and then rapidly stepped to a value where desorption is expected to occur and which is known to be free of other redox reactions. The charge passed during the potential step can be split into three components:

$$Q = \frac{2nFAD_R^{1/2}C_R^*}{\pi^{1/2}} t^{1/2} + nFA\Gamma + Q_{d.l.} \quad (4)$$

Where Q is the charge passed during the step, *n* is the number of electrons, F is the Faraday's constant, A is the area of the electrode, D is the diffusion coefficient of the species, C_R* is the concentration of the species in the bulk, *t* is the time, Γ is the surface coverage and $Q_{d.l.}$ is the charge due to the double layer.

The term $\frac{2nFAD_R^{1/2}C_R^*}{\pi^{1/2}} t^{1/2}$ arises from the faradaic charge generated by any redox process of diffusing species. The term $nFA\Gamma$ is generated by any adsorbed species being re-oxidised, and the $Q_{d.l.}$ is the capacitive charge required to charge the double layer during the potential step. The two latter terms are time independent as they occur at a much greater rate compared to the slow accumulation of the diffusional component, making them essentially instantaneous on the measurement timescale (ms-s).

Therefore plotting the charge passed *vs.* $t^{1/2}$ yields a linear plot with a slope equal to $\frac{2nFAD_R^{1/2}C_R^*}{\pi^{1/2}}$ (the faradaic term from diffusing redox species) and an intercept that is the sum of $Q_{d.l.}$and the charge for the oxidative desorption. To calculate the capacitive charge and hence the surface coverage, one could measure the charge passed in the absence of the analyte and subtract the intercept obtained for the *Q*

vs. $t^{1/2}$ plot. This method is called single-step chronocoulometry. This calculation however does not take into account the changes to the interfacial capacitance brought about by the presence of the redox species. A more elegant solution is to apply a second potential step after the first, going back to the initial potential (Figure 22).

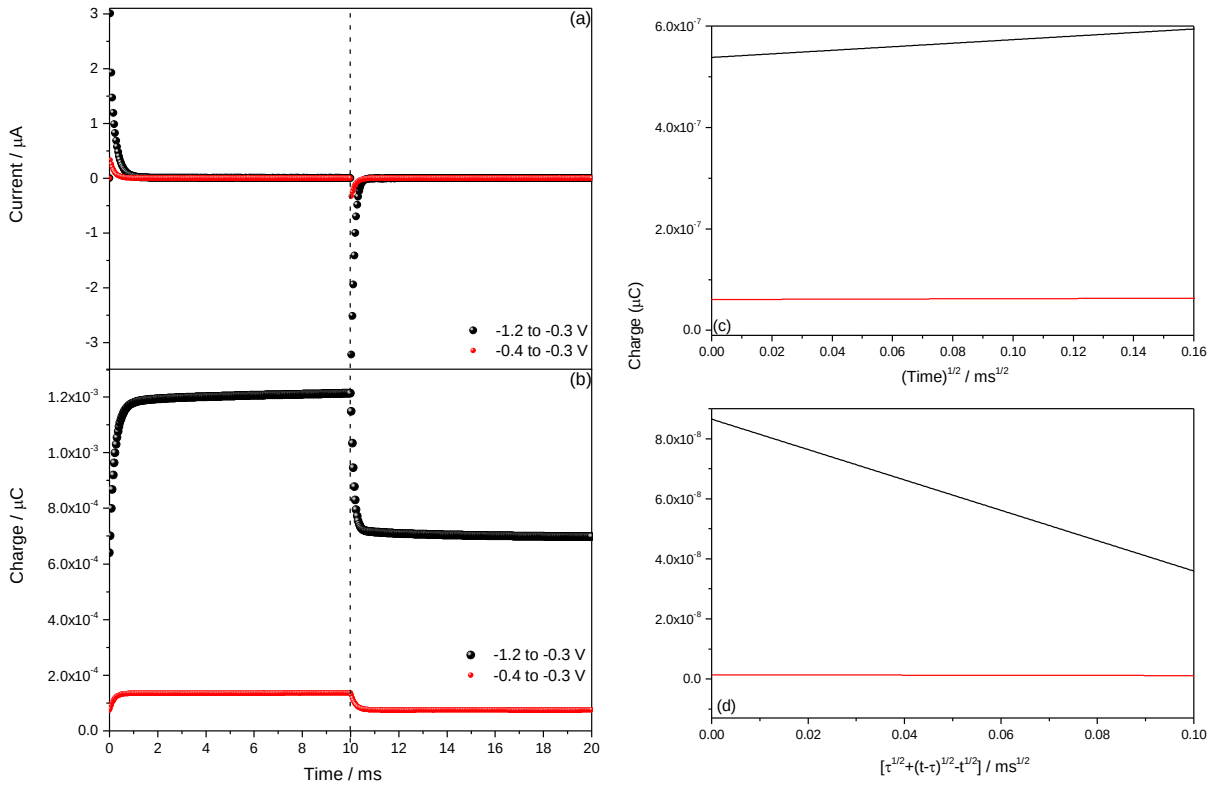

Figure 22 – Representative DPSC experiment; (a) current plot, (b) charge plot, (c) relationship between charge and time for the first step and (d) relationship between charge and time for the second step.

In this case as the oxidised Ni^{II} complex is not anticipated to adsorb and the only "instantaneous" charge will be generated by the double layer capacitance, the overall charge for the second step will be equal to:

$$Q_r(t > \tau) = \frac{2nFAD_O^{1/2}C_O^*}{\pi^{1/2}}\left[\tau^{1/2} + (t-\tau)^{1/2} - t^{1/2}\right] + Q_{d.l.} \qquad (5)$$

Where t is the time after the first step, and τ is the time after the second step. Therefore a plot of $Q_r(t > \tau)$ *vs.* $[\tau^{1/2}+(t-\tau)^{1/2}-t^{1/2}]$ will be linear, and the intercept will correspond to the charge due to the

double layer charging in the presence of the redox species. The surface coverage (mol cm^{-1}) can be calculated using Eq. (6):

$$Q = nFA\Gamma \quad (6)$$

Since this experiment requires an electrochemically fast (ms) time resolution, the time constants for the electrochemical cell have to be taken into consideration. The cell resistance has to be reduced as much as possible. A platinum wire has been used as the counter electrode, placed very close to the mercury drop. A Ag wire reference is also employed as the resistance of the Vycor® tip of a commercial Ag/AgCl electrode was found to be too large, leading to significant errors in the measurements. The *quasi* reference Ag wire potential was referenced using the $Ni^{II/I}$ couple potential of the solution as an internal standard. Prior to each experiment, a new mercury drop was used for every double potential step, in order to prevent fouling from the potential presence of residual adsorbed complex from the previous measurement. Finally, an argon blanket was maintained throughout the experiment to avoid side reactions caused by the presence of trace amounts of oxygen in the cell.

The potential dependence of the adsorption of both Ni(cyc) and Ni(cycC) has been measured under argon, and the results have been found to be comparable with Ni(cyc)[22] at pH 5 (Figure 23). In line with past reports for Ni(cyc), adsorption of Ni(cycC) has been found to occur at potentials significantly more positive than the formal reduction potential of the $Ni^{II/I}$ couple in solution, indicating a significant stabilisation of Ni^{I} on a Hg electrode.

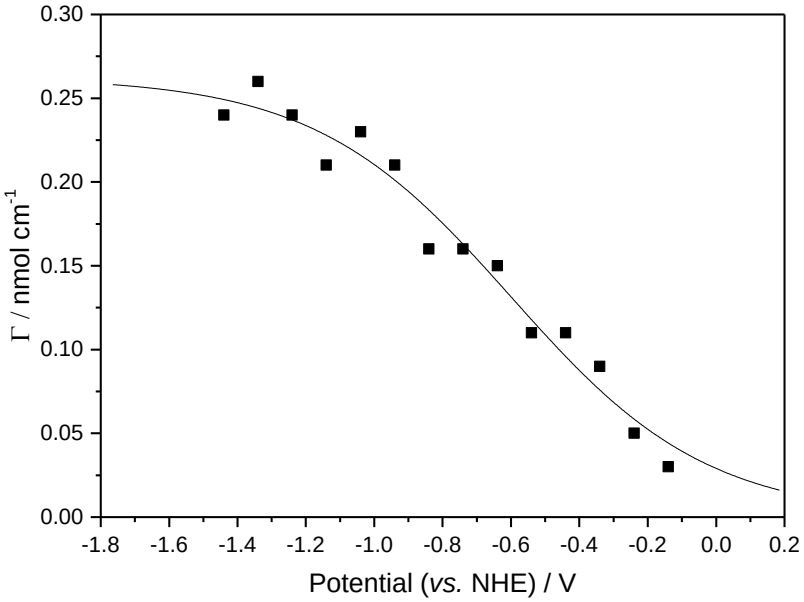

Figure 23 - Dependence of the surface coverage of Ni(cycC) with the potential for 0.1 mM solutions of Ni(cycC), 0.1 M $NaClO_4$, pH 5. The potential was referenced using the $Ni^{II/I}$ couple as an internal standard, and converted to NHE.

At pH 2 and 5 the adsorption of Ni(cyc) takes place in two main stages as the potential is stepped at more negative values, with a sharp rise at *ca.* -1 V_{NHE} corresponding to a monolayer of reduced complex on the surface. This step-like adsorption has been attributed to a structural rearrangement of the complex to allow the formation of a monolayer, together with a change in the capacitive properties of the double layer, causing the step change at -1 V_{NHE}. Ni(cycC) doesn't show such a defined trend at pH 5, however similar values are calculated for the surface coverage at the different potentials compared to Ni(cyc) and a the formation of a full monolayer is observed at -1.04 V_{NHE}. DPSC measurements were also carried out for both complexes at pH 2. The results are shown in Figure 24.

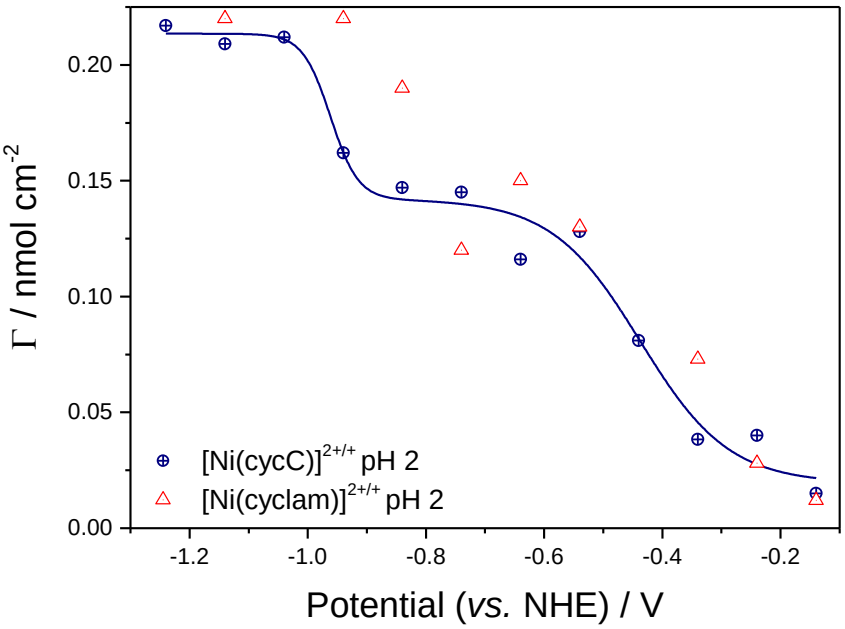

Figure 24 – Dependence of the surface coverage of Ni(cycC) with the potential for 0.1 mM solutions of catalyst, 0.1 M $NaClO_4$, pH 2. The potential was referenced using the $Ni^{II/I}$ couple.

It is clear from the plot of surface coverage *vs.* potential that the two complexes have the same adsorption characteristic at this pH value, indicating that a different mechanism of adsorption is not the cause for the observed different CO_2 catalytic behaviour of the two complexes. Interestingly, at pH 2 Ni(cycC) shows a two stage adsorption, much like its unmodified counterpart at pH 5. This, as mentioned above is attributed to a sudden increase in adsorption caused by a structural rearrangement made easier by the increasing driving force at more negative potentials.

The effects of pH on redox couples are usually illustrated with electrochemical Pourbaix diagrams. This type of analysis shows the stability of a certain redox species as a function of pH and potential. Figure 25 shows the pH dependence of the $Ni^{II/I}$ couple under argon for Ni(cyc) and Ni(cycC), and the experimental Pourbaix diagram for Ni(cycC).

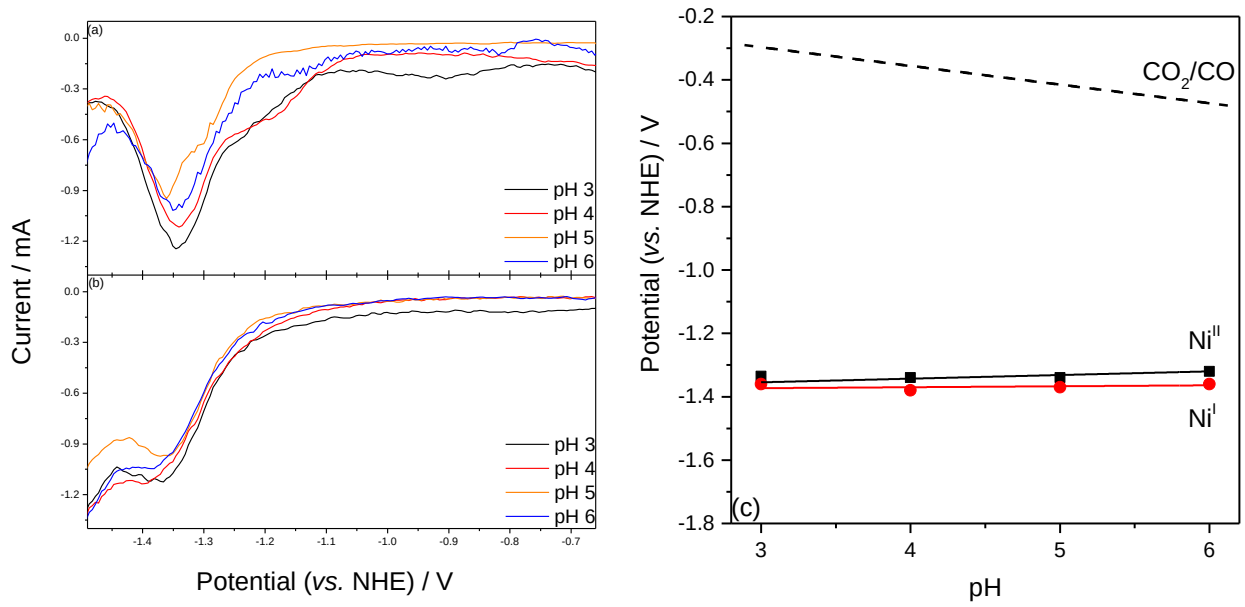

Figure 25 – (a) Differential pulse voltammetry of 1 mM solutions of Ni(cyc) and (b) Ni(cycC) in Ar purged 0.1 M $NaClO_4$ on a gold amalgam electrode at the pHs indicated recorded at 100 mV s^{-1}. (c) Experimental Pourbaix diagram for the $Ni^{II/I}$ couple of Ni(cycC).

Due to the large catalytic wave at pH values lower than 3 due to proton reduction it was not possible to include this value in the diagram. The analysis is based on the CVs and differential pulse voltammograms, and therefore probes the behaviour of the complex present in the bulk of the solution, which is controlled by slow diffusion at the electrode. It is clear from the data available that there is no substantial effect on the redox couple with decreasing pH for the bulk $Ni^{II/I}$ couple. This result indicates that the bulk of the complex in solution has the same redox properties at all pH values, and the increase in catalytic activity is not due to the diffusion controlled species cooperating with the surface adsorbed one.

Finally, we have also monitored the UV-vis spectra of Ni(cycC) at pH = 2 in the absence and presence of CO_2 in order to evaluate whether the protonated catalyst is able to interact directly with CO_2 (Figure 26). It has been suggested that the mechanism of CO_2 reduction by Ni(cyc) is EC'EC', where the first reduction happens prior to CO_2 binding to the metal centre. As UV-vis spectra of the complex in

argon and CO_2-purged solutions at pH 2 showed no changes in the coordination mode from square planar to octahedral, which would be expected if CO_2 were able to interact with Ni^{II}, it was concluded that reduction of the nickel centre occurs prior to CO_2 binding.

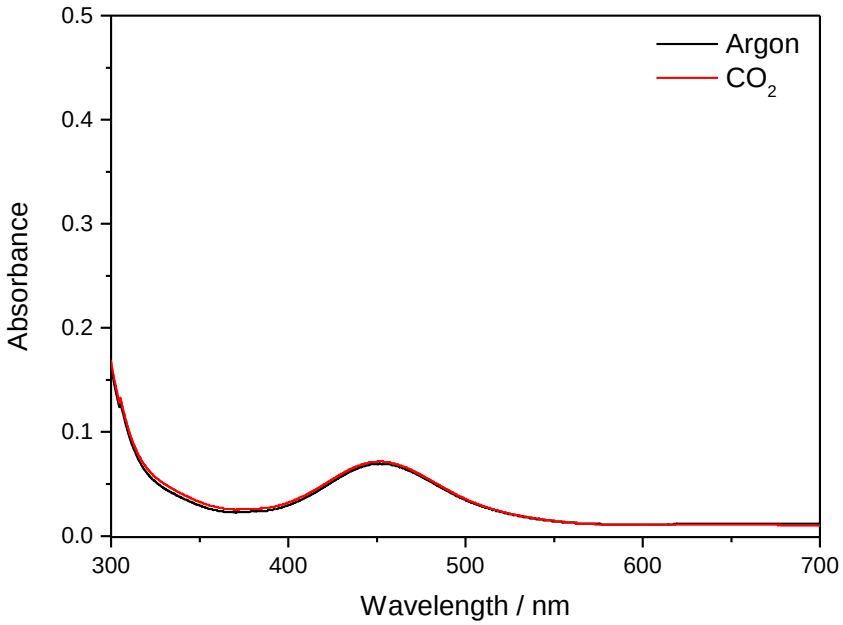

Figure 26 - UV-vis spectra of Ni(cycC) (3 mM) at pH 2 under argon (black) and CO_2 (red), 0.1 M $NaClO_4$.

The pKa of the carboxylic acid was measured *via* Fourier-Transform Infrared (FTIR) spectroscopy titration (Figure 27)[40]. The complex was dissolved in D_2O, to prevent the δ(HOH) modes from masking the carbonyl region of interest, and the pH was varied using a DCl solution in D_2O. The synthesis of the complex is carried out in basic solutions, and in its powder form it exists as the carboxylate form, as shown by the ATR-FTIR spectrum in Figure 6. The starting pD of the solution (0.05 M) was found to be 9.87, and the FTIR spectrum showed the expected band at 1575 cm^{-1} due to the $\nu_{as}(CO_2^-)$, with a shoulder at 1627 cm^{-1} which as discussed may be due to a coordinated carboxylate. The cyclam structure is extremely flexible, and the possibility for a functional group to coordinate one of the axial binding sites of the metal centre has been shown for derivatives of Co(cycC),[18,41] so it is feasible that a fraction of the complex in solution is present in a conformation

where the carboxylate could bind to the nickel. There was little change in the spectrum for pHs >5.5, save for a slight decrease in intensity of the shoulder at 1627 cm^{-1}. At this value the shoulder disappeared, and the main peak at 1575 cm^{-1} started to decrease in intensity as well. At the same value, a new feature started to appear at 1706 $cm^{-1}$and this was assigned to the carbonyl group of the protonated carboxylic acid. As the pH was lowered further, this new peak increased while the carboxylate steadily decreased, until at a value of pH = 1.75 it was not visible anymore. In addition to the peak at 1706 cm^{-1} a peak at 1653 cm^{-1} appeared with the decrease of the pH. This is tentatively assigned to the carboxylic acid which has been deuterated. The raising baseline is due to the presence of notable quantities of H_2O in the DCl stock solution, causing the DOH modes slowly increasing as more acid was added.

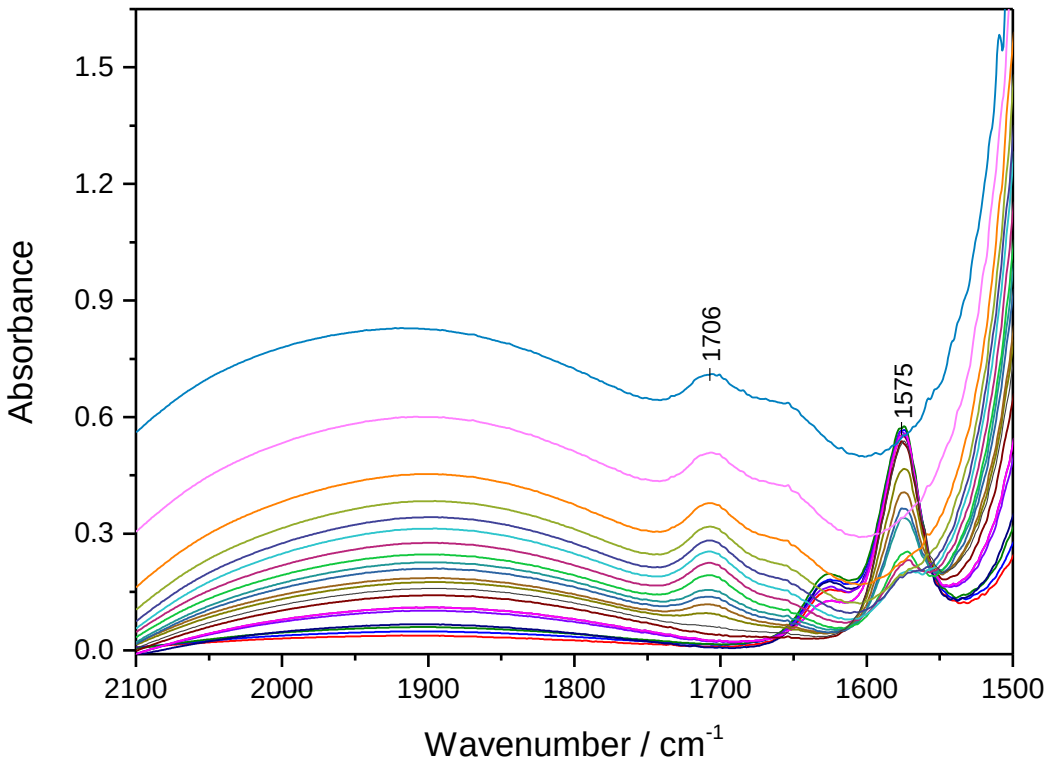

Figure 27 - A series of FTIR spectra for a 0.1 M solution of Ni(cycC) in D_2O at decreasing pD values, recorded in a 0.1 mm path length CaF_2 IR cell.

The intensities of the carboxylate and carboxylic acid peak were plotted versus the pH (Figure 28). The two curves have the aspect of a traditional titration curve. However, while for the latter the equivalence point represents the point at which an acid or a base has been completely consumed by the base/acid, and the pKa is given by the plateau region, here the point at which the two curves cross can be interpreted by the pH value at which both species, carboxylate and carboxylic acid, are present in equimolar amounts, which can be directly translated to the pKa value for the carboxylic acid, which after applying the well-known conversion from pD to pH[42] was calculated to be 2.6.

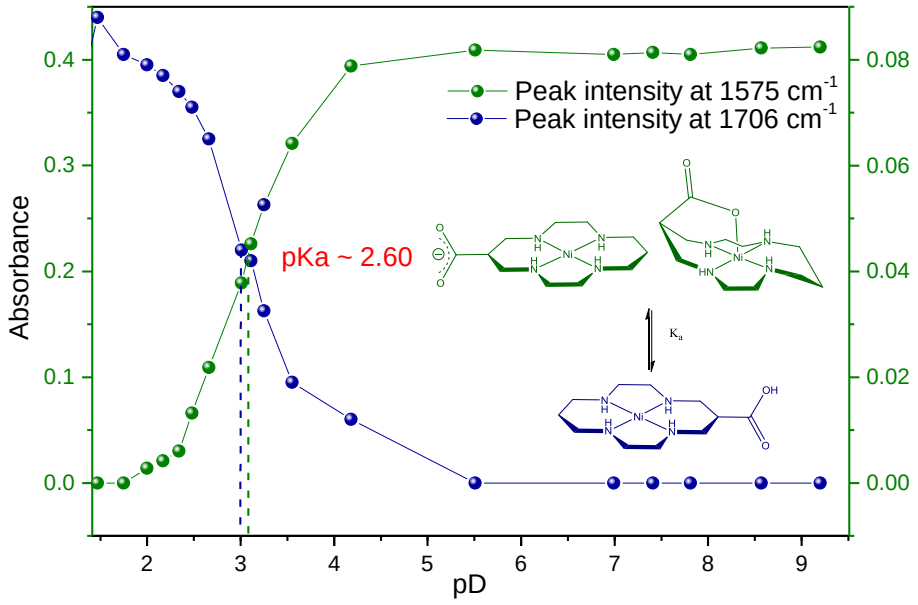

Figure 28 - pD titration curves obtained by plotting the IR intensity of the peaks of the carboxylic acid (1706 cm^{-1}, blue) and carboxylate (1575 cm^{-1}, green).

Literature pKa values for carboxylic acids are very varied, but most are within the range 2-6. The obtained value is then lower than expected for an aliphatic carboxylic acid group. The protonation constants of the ligand are not reported in the literature, however they have been measured for a similar compound[43] *via* a potentiometric titration and were found to be 10.52, 9.70, 6.54, 3.19 and <1. The carboxylate protonation constant was determined to be the third (6.54) on account of the difficulty in protonating the last two amines in the macrocycle cavity. The unmodified complex has

been shown to form a Ni-H complex with pKa of 1.8 (estimated by pulse radiolysis studies),[25] and the formation of the hydride is considered the reason for the drop in selectivity observed at lower pH for Ni(cyc). Here, we hypothesise that the protonation of the carboxylic acid prevents the subsequent formation of the hydride by stabilising the CO_2 adduct, and this prevents the mechanism pathway that would lead to proton reduction.

Remarkably, there is a close correlation between the plot of increasing intensity of the carboxylic acid and the current density of the RDE voltammograms with decreasing pH, Figure 29, which leads to the conclusion that the availability of the proton on the carboxylic group correlates to the enhancement in catalytic activity with low pH values.

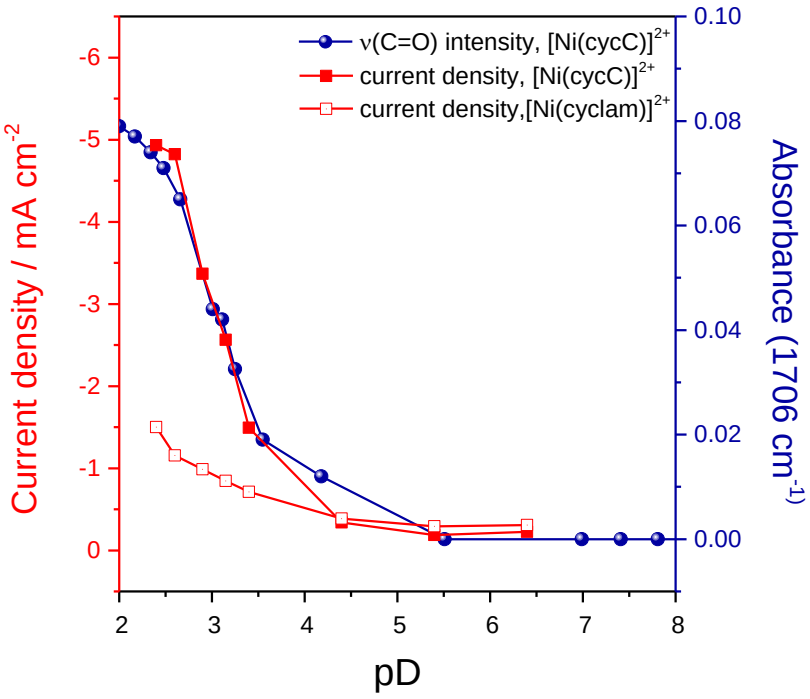

Figure 29 - Relationship between CO_2 reduction current measured at 0.99 V_{NHE} of Ni(cycC) (filled squares) by RDE voltammetry (800 rpm, 100 mV s^{-1}), relative concentration of carboxylic acid (given by the ν_{as}(CO) at 1706 cm^{-1} , blue circles) and pD. The current density of Ni(cyc)under CO_2 with pH is also shown (open squares). pD = pH + 0.4.

From the electrochemical and spectroscopic evidence presented above, it is evident that there is a change in the mechanism of CO_2 reduction by Ni(cycC) at low pH values. The protonation of the carboxylate has been shown to be essential for the increase in catalytic activity. We also rule out that

the change in catalytic activity of Ni(cycC) compared to Ni(cyc) at low pH is due to a change in surface coverage on the mercury electrode or due to a change in the $Ni^{II/I}$ couple prior to CO_2 reduction. The kinetic selectivity and high TOF found at pH values lower than the pKa suggest that the carboxylic acid might act as an internal proton source, as reported previously for other complexes[29,31,32]. It is remarkable that such an effect occurs in water. In addition, the acidic proton might stabilise binding of CO_2 reduction to the metal centre through hydrogen bonding. Cobalt analogues of Ni(cycC) have been reported for use in dye-sensitized solar cells with binding of the $-CO_2H$ group directly to the metal centre, [18,41] suggesting that an intra-molecular interaction is geometrically feasible. On the basis of the available data, and the recent literature, which suggests that protonation of the CO_2 adduct is the rate limiting step,[27] we have hypothesised a mechanism for the catalysis at pH 2, Scheme 15.

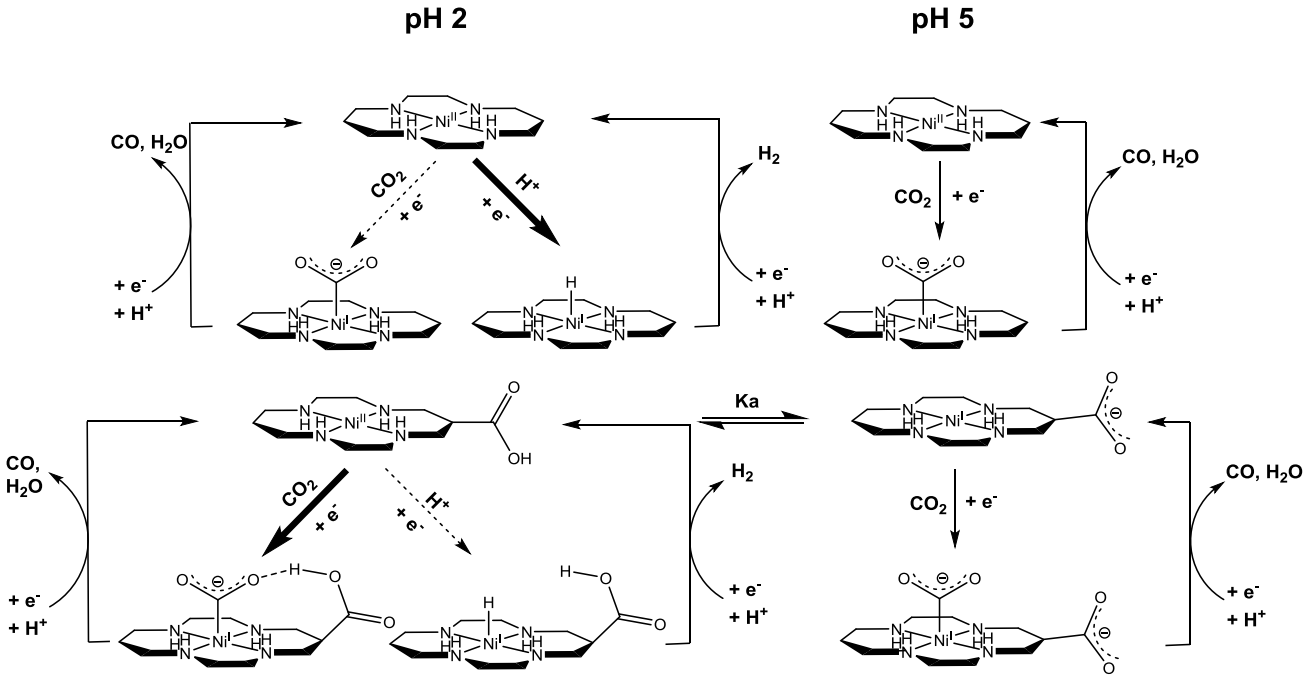

Scheme 15 – Proposed mechanism for CO_2 and H^+ reduction at pH 2 (left) and 5 (right) for Ni(cyc) (top) and Ni(cycC) (bottom).

2.2.5 Homogenous CO_2 reduction by Ni(cycC) on GCE

Recently, some studies by Kubiak *et al.*[3,44] have shown that Ni(cyc) is also a homogeneous CO_2 reduction catalyst on a GCE both in water and in acetonitrile (MeCN) solutions doped with water. The use of non-aqueous or solutions doped with a low water content allowed for the potential window of GCE to be sufficient for the electrochemical analysis, and allowed for some interesting observations on the properties of the complex. GCE is an inert electrode, where the complex cannot adsorb, and it is anticipated that it will be a useful tool to assess the behaviour of Ni(cycC) as an homogeneous catalyst. In this section, we will analyse the properties of Ni(cycC) on a GCE, and through the application of a recently proposed method for extrapolating the kinetics of homogeneous catalysts from the CVs we will also attempt to benchmark the complex with the existing catalysts for CO_2 reduction in aprotic solutions.

The use of GCE also allowed the analysis of the complex at positive potentials, Figure 30. The CVs under argon show the appearance of the $Ni^{III/II}$ couple at +1.04 V *vs. NHE*. The i_{pa}/i_{pc} is close to unity, and the peak current density shows a linear dependence on the square root of the scan rate, indicating the reversibility of the process.

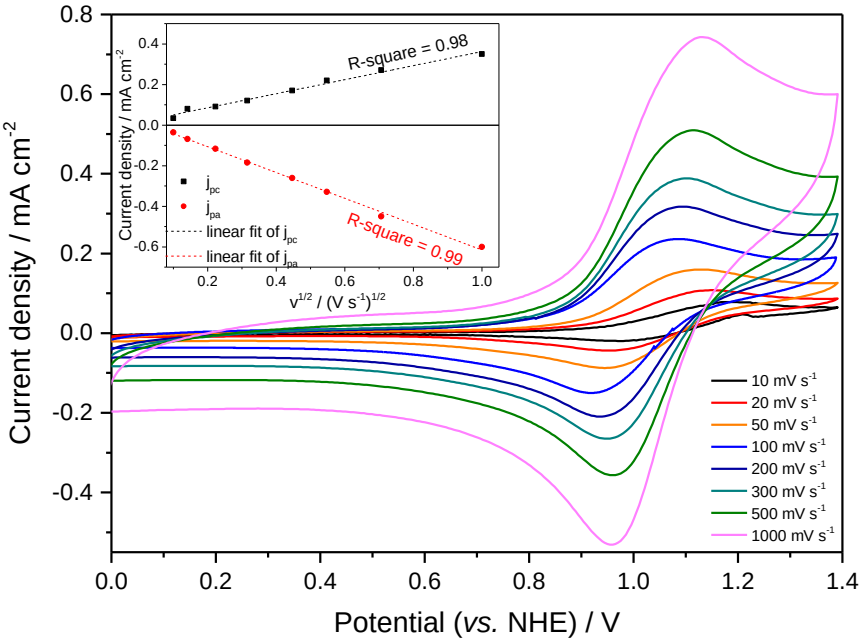

Figure 30 - CVs at positive potentials for an Argon-purged 1 mM solution of Ni(cycC) in MeCN doped with 10 % water, using 0.1 M $TBAPF_6$ as the supporting electrolyte and a GCE. The inset shows the dependence of the peak current with the square root of the scan rate.

In addition, the peak-to-peak separation is constant with the scan rate. Although this value is > 0.059 V/n for this redox couple, which might indicate slow electron transfer kinetics, the higher peak-to-peak separation is more likely to be due to uncompensated cell resistance, as the same values are obtained for the ferrocene/ferrocenium redox couple in the same conditions.

Under argon at -1.33 V_{NHE} Ni(cycC) shows a quasi-reversible redox couple (Figure 31), assigned to the $Ni^{II/I}$ couple. The non-reversible behaviour of the redox couple could be attributed to the complex acting as a weak proton reduction catalyst under argon, as reported for similar compounds.[22] The CV response under CO_2 is quite similar to that of the parent complex under the same conditions.[3] The large increase in current density at potentials close to the $Ni^{II/I}$ couple under CO_2 indicates that catalytic CO_2 reduction is occurring.

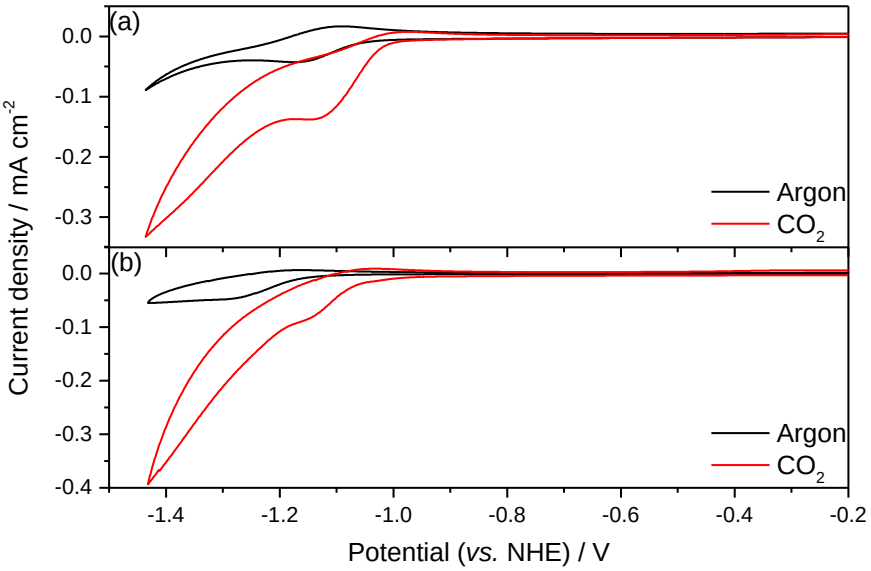

Figure 31 - CVs of 1 mM (a) Ni(cyc) and (b) Ni(cycC)in MeCN with 10 % added water, using 0.1 M $TBAPF_6$ as the supporting electrolyte and a GCE (surface area = 0.717 cm^2), under both argon and CO_2.

The most effective method for benchmarking homogenous electrocatalysts is a widely debated topic in the literature.[45–48] Historically bulk electrolysis experiments have been employed, where the TON (defined as the ratio between moles of product and moles of catalyst present in the reaction), FE (the efficiency of charge transfer between the electrode and the substrate) and TOF (defined as the TON per unit of time) are the figures of merit used to define the activity of a catalyst. However several authors have recently noted that any kinetic values extrapolated from these figures will be highly dependent on the rate of substrate diffusion to the electrode, and thus from the reactor geometry,[46] complicating catalyst benchmarking.

One other common method is to use the ratio i_c/i_p, where i_c is the peak current of the catalytic wave and i_p is the peak current of the catalyst in the absence of substrate, as a measure of the catalytic efficiency[3,26,49]. With this ratio it is possible to calculate the observed rate constant for the catalytic reaction, providing that a clear plateau in the current-voltage plot under catalytic conditions is observed, i.e. that the catalytic current reaches a steady state value. In the case of the two electron reduction of CO_2 to CO it is often assumed that the concentration of CO_2 in the solution is sufficiently

high that it remains substantially unchanged throughout the reaction and that electron transfer is fast. In these conditions, i_c is given by[25,44,50–52]:

$$i_c = nFA[cat]\sqrt{Dk_{obs}} \quad (6)$$

Where n is the number of electrons involved in the catalytic reaction, F is Faraday's constant, A is the area of the electrode, D is the diffusion coefficient of the catalyst and k is the rate constant.

The i_p for a reversible 1 electron reduction is given by the Randles-Sevcik equation:

$$i_p = 0.4463FA[cat]\sqrt{{Fv D}/{RT}} \quad (7)$$

Where v is the scan rate. Therefore the ratio between equations (6) and (7) yields:

$$\frac{i_c}{i_P} = \frac{n}{0.4463}\sqrt{\frac{RTk_{obs}}{Fv}} \quad (8)$$

For Ni(cycC) the i_c/i_p ratio in MeCN + 10% H_2O on a GCE (calculated from the CVs in Figure 31) is equal to 2, while the value found for Ni(cyc) with the same electrode material was found to be 4.[3]

These i_c/i_p values give observed rate constants of 0.8 s^{-1} for Ni(cycC) in MeCN with 10% H_2O, compared to 3.4 s^{-1} for Ni(cyc) in the same conditions. While this method can give an accurate rate constant, it is often difficult to obtain a clear plateau in the catalytic current due to the possibility of catalyst inhibition and the limitations of substrate diffusion. Moreover, the i_c/i_p ratio can be calculated only for one potential value across the CV, and k_{obs} away from the plateau region cannot be reported.

Recently, a more elegant method for benchmarking homogeneous catalysts has been proposed by Savéant and co-workers[46,48,53,54]. The FOWA examines the dependence of the TOF on the overpotential η for the reaction considered, in a region of the CV where catalysis is slow, and thus not affected by side phenomena, which are the cause of the deviation from the purely kinetic S-shape of the voltammogram (such as substrate consumption, catalyst deactivation, inhibition from the reaction products, Scheme 16). From the value of the rate constant obtained at the foot of the catalytic

wave it is then possible to extrapolate the TOF at every value of the overpotential, obtaining the intrinsic catalytic activity for a particular catalyst.

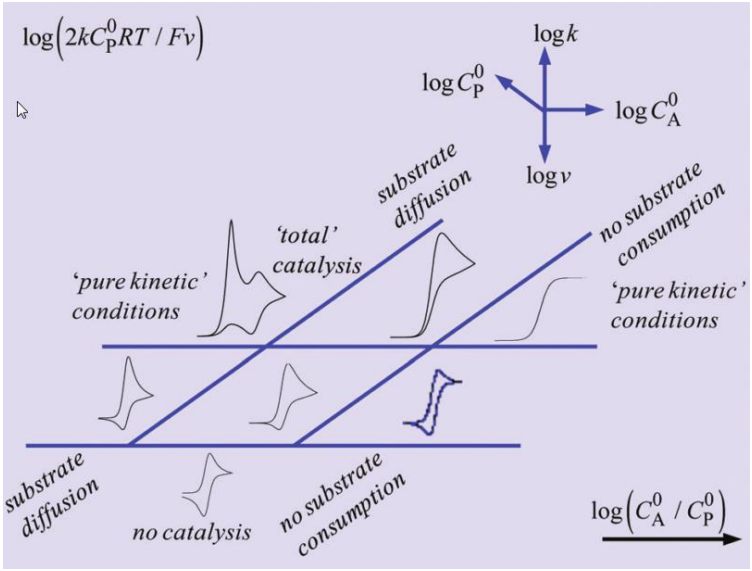

Scheme 16 – Characteristic shapes showed by a homogeneous catalyst in different regimes, reproduced from ref.[46]

This particular type of analysis can be applied to most homogeneous catalysts, which makes it possible to compare the efficiencies of different systems even when the conditions (solvent, proton source, electrode material) vary substantially. If the system behaves in pure kinetic conditions, the CV will have a pure S-shape, however in most cases side phenomena become more significant the more the potential is scanned to more cathodic values. The FOWA examines the behaviour of the system at a point where these effects are negligible and extrapolates this behaviour to the entire CV, obtaining idealised kinetic values. Savéant and co-workers have applied the FOWA to the most prominent molecular catalysts for CO_2 reduction in non-aqueous solutions.[46] However, they note that the analysis they presented for Ni(cyc) will not be accurate as the data they used for the FOWA was obtained on a mercury electrode, where catalysis is not strictly homogeneous as Ni(cyc) is an active catalyst only when it adsorbs on the mercury surface. Here, the FOWA analysis has been carried out for Ni(cycC) and Ni(cyc) for comparison on a GCE in acetonitrile solutions. The analysis was thought appropriate here as the catalysis is carried on a GCE electrode, where the two complexes are thought

to behave as homogeneous catalysts. Taking into account an EC'EC' mechanism, as has been previously proposed for Ni(cyc):[27]

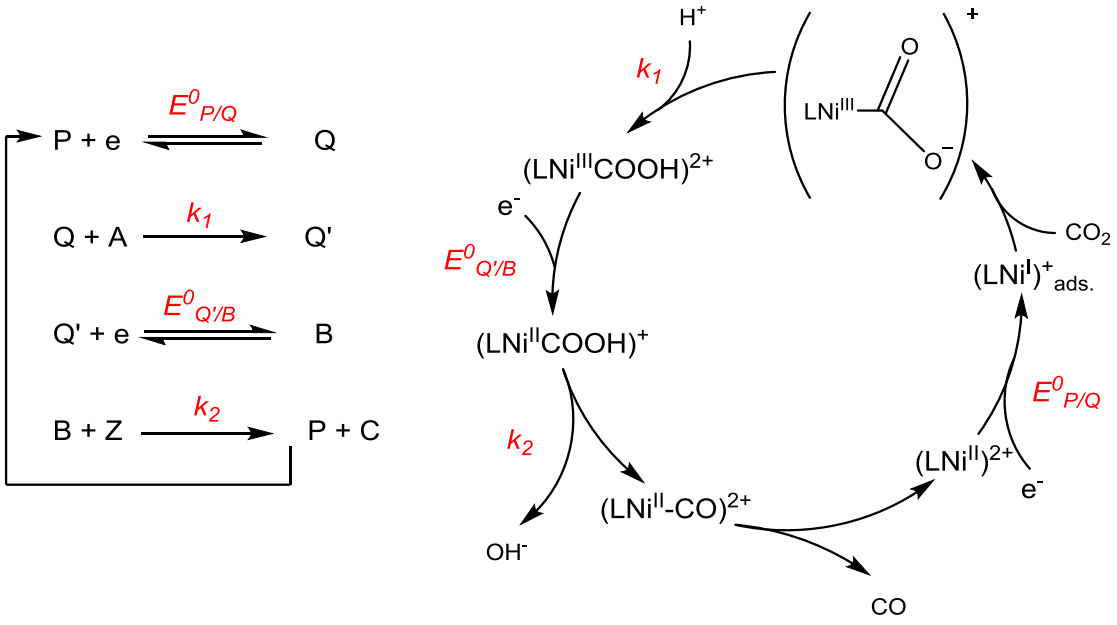

Scheme 17 – General scheme for an EC'EC' reaction, and proposed mechanism for CO_2 reduction by Ni(cyc).[27]

Where P is the catalyst, A is the substrate, Q' is the active species, B is an intermediate of the reaction, C is the final product, $E^0_{P/Q}$ is the redox potential for the reduction of P to Q, k_1 is the rate for the first chemical step, $E^0_{Q'/B}$ is the potential of the second electron transfer, and k_2 is the rate of the second chemical step.

For the homogenous reduction of CO_2 by Ni(cyc) the rate-limiting step has been determined to be the protonation of the adduct of the reduced complex with CO_2. According to the model reported by Dempsey *et al.*[54], in the case where the first chemical step of an EC'EC' mechanism is the rate determining one, that is to say, when $k_2 C_Z^0 \gg k_1 C_A^0$ and $E_{cat}/2 = E_{redox}$ the catalytic current is given by Eq. (4):

$$i = \frac{nFAC_p^0\sqrt{Dn'k_{obs}}}{1 + exp\left[\frac{nF}{RT}(E - E_{redox})\right]} \quad (9)$$

Normalisation *versus* i_p (the catalyst current on the absence of the substrate) yields Eq (10):

$$\frac{i}{i_p} = \frac{2.24\sqrt{\frac{RT}{nFv}}\sqrt{n'k_{obs}}}{1 + \exp\left[\frac{nF}{RT}(E - E_{redox})\right]} \quad (10)$$

In the case of a system where no side phenomena were affecting catalysis, plotting i/i_p *vs.* $\{1+\exp[nF/RT\,(E-E_{redox})]\}^{-1}$ would give a straight line. Side effect will cause a curvature, however, a linear extrapolation can be obtained at the foot of the wave (Figure 32(a)). The slope obtained from the extrapolation is equal to: $[2.24(2k_{obs}C_{sub}/fv)^{1/2}]$, where k_{obs} is the observed rate constant, C_{sub} the concentration of the substrate, f = RT/F and v is the scan rate. The concentration of CO_2 in the conditions at which the experiment was carried out (10% H_2O in MeCN, saturated with CO_2) has been taken from literature values (190 mM).[44] From this value it is now possible to calculate the TOF, defined as the moles of product per unit of time per mole of catalyst contained in the diffusion layer, and not in the bulk solution. Plotting the TOF *vs.* the overpotential of the reaction (Figure 32(b)) gives a measure of the intrinsic catalyst performance at a given potential and in absence of side phenomena. The overpotential is calculated by taking the standard potential for CO_2 ($E^0_{CO_2/CO} = -0.65\ V_{NHE}$) in acetonitrile with 10% water, which has been calculated previously.[29] The y intercept of the plot in Figure 32 will be a measure of the rate at zero overpotential (TOF_0), while the plateau corresponds to k_{obs} (also called TOF_{max}).

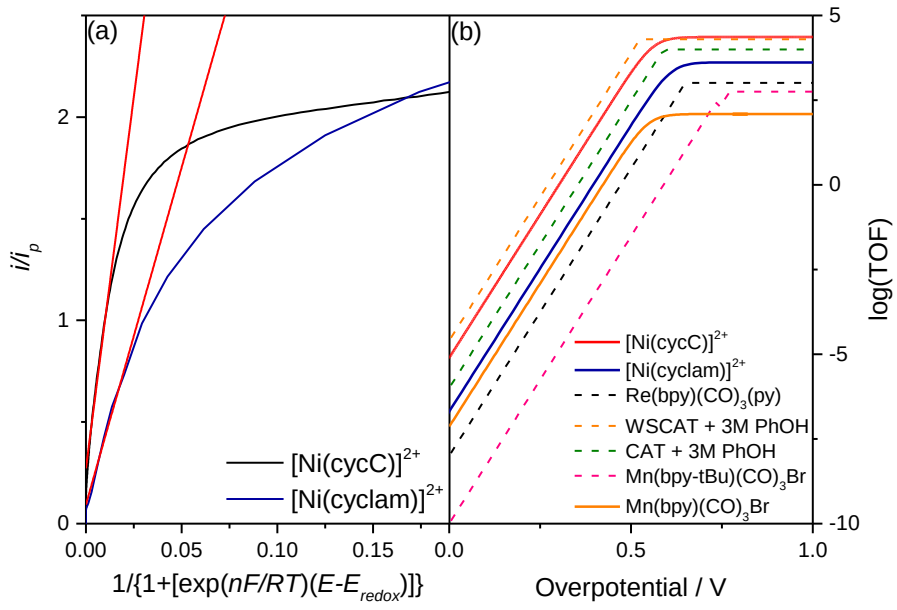

Figure 32 – FOWA analysis for homogenoeous catalysts Ni(cyc), Ni(cycC) and literature catalysts[30,33,55,56] (data is given for catalysis carried out in MeCN doped with 10% H_2O, where available, or at the solutions indicated) and some representative electrocatalysts for CO_2 reduction. The straight lines represent curves obtained by experimental measurements, the dashed lines are data reproduced from the literature.

Figure 32(b) shows the FOWA analysis for Ni(cyc) and Ni(cycC), calculated from the CVs in Figure 31, alongside the same analysis for some of the most prominent electrocatalysts for CO_2 reduction found in the literature. The data for these catalysts has been calculated by Savéant and co-workers[33], and here we report a reproduction of those plots. The CVs for [Mn(bpy)$(CO)_3$Br] have been measured in our lab, and therefore the FOWA for this catalyst is calculated from our own data. Visually, a "good" catalyst will sit in the top left of the graph (low overpotential and high TOF_{max}), while a "bad" one will sit in the bottom right; comparison between catalysts is therefore intuitive. In acetonitrile doped with water, Ni(cycC), with a TOF_{max} of 2.3 x 10^4 s^{-1}, appears to be a better catalyst than most of the well-known electrocatalysts found in the literature, such as [Re(bpy)$(CO)_3$(py)]$^+$ (TOF_{max} ~ 790 s^{-1}, MeCN + 0.8 M CF_3CH_2OH), [Mn(bpy^{t}Bu)$(CO)_3$Br] (TOF_{max} ~ 630 s^{-1}, MeCN + 1.4 M CF_3CH_2OH), [Ru(tpy$^-$)(bpy$^-$)] (TOF_{max} ~ 8 s^{-1}, MeCN) and Mn(bpy)$(CO)_3$Br (TOF_{max} = 123 s^{-1}, MeCN + 10% H_2O), and is comparable to the highly active WSCAT porphyrin (TOF_{max} ~ 2 x 10^4 s^-

[1], DMF + 3 M PhOH) reported recently,[33] although we note that this value is obtained at a considerably lower overpotential than Ni(cycC).

Where the *ic/ip* ratio calculation suggests that Ni(cycC) is a worse catalyst than Ni(cyc), the FOWA for the two complexes suggests the opposite, with a log(TOF) at 0.55 V (the overpotential at which CPE was carried out) of 4 for Ni(cycC) compared to 2.65 obtained for Ni(cyc). The contrasting results show the differences between the two methods; from the FOWA analysis one could easily conclude that the new Ni(cycC) is a much better catalyst for CO_2 reduction than Ni(cyc). The comparison with the i_c/i_p data however paints a slightly different picture, which is in agreement with the bulk electrolysis data, although it should be noted that the i_c/i_p analysis may not be appropriate as no clear plateau current was observed. Together, the contrasting values suggest that while Ni(cycC) might have intrinsically better catalytic properties than Ni(cyc), the new complex might be more susceptible to inhibition from reaction products, which may limit its practical use.

2.2.6 Immobilisation on semiconductor surfaces.

The functionalisation of cyclam with a carboxylic acid was targeted primarily for its ability to react with semiconductor oxide surfaces. Carboxylic acid derivatives have been widely used in the dye-sensitised solar cell literature as a convenient and stable group for surface immobilisation and functionalisation[57,58]. Here, we have attempted the immobilisation of Ni(cycC) on semiconductor oxides (namely, nc-TiO_2 and $Ti_{0.8}Zr_{0.2}O_2$ mesoporous thin films) and we have studied the properties of this heterogeneous system as a photoelectrode for CO_2 reduction.

2.2.6.1 Immobilisation of Ni(cycC) on nc-TiO_2 and $Ti_{0.8}Zr_{0.2}O_2$ thin films.

For this study nc-TiO_2 (nc = nanocrystalline) and $Ti_{0.8}Zr_{0.2}O_2$ mesoporous film have been chosen as the semiconductor material as it was hypothesised that by careful control of the solvent the conduction band edge of these materials would sit at a negative enough potential to be able to drive the electron transfer from the semiconductor to the complex efficiently. The mesoporous films were made in-house by the doctor blading technique[59] using a nc-TiO_2 or $Ti_{0.8}Zr_{0.2}O_2$ paste synthesised according

to literature procedures by our collaborators at Imperial College London (particle sizes of 20 nm on average)[60,61]. The pastes were doctor bladed on fluorine-doped tin oxide (FTO) on glass which had previously been coated with a bulk TiO_2 blocking layer to prevent degradation of the FTO layer at the negative potentials required for the electron transfer to occur, see section 2.3.1 for experimental details. The thickness of the films was measured by profilometry, and an average value of 3 μm was obtained.

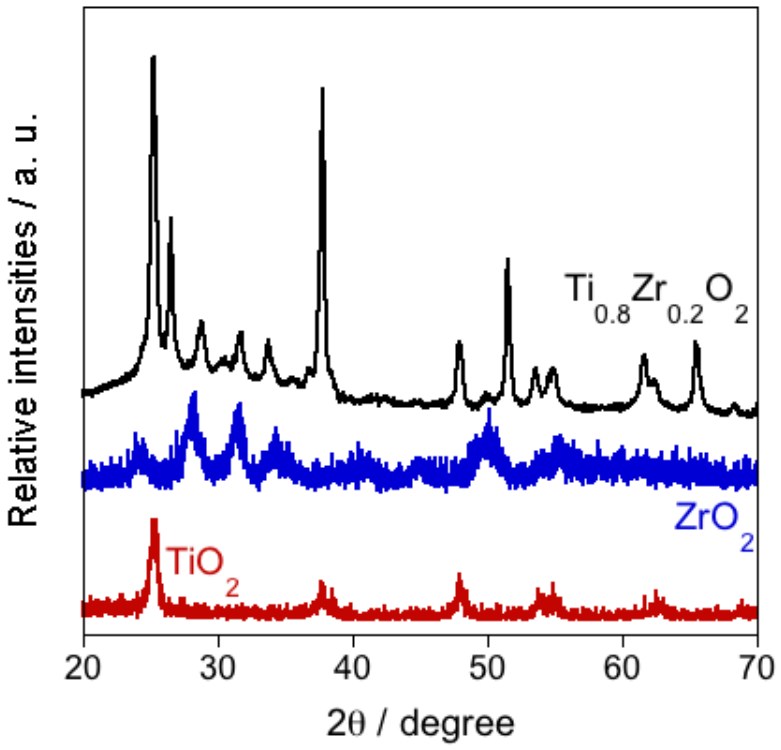

Figure 33 - X-ray diffraction (XRD) patterns of nc-TiO_2 (red trace), ZrO_2 (blue trace) and $Ti_{0.8}Zr_{0.2}O_2$ (black trace) films. Recorded by Dr Anna Reynal, Imperial College London.

The films were characterised by X-ray powder diffraction (Figure 33). The diffraction spectrum for nc-TiO_2 is in agreement with that previously reported for this material. $Ti_{1-x}Zr_xO_2$ materials are known to behave as solid solutions only for certain values of x, that is only until values at which Zr is not soluble in nc-TiO_2 anymore and any extra zirconium is present as ZrO_2. The threshold values reported in the literature for x vary from 0.08 to 0.35[62,63]. The value of x for the material used in this study[61] is 0.2, below one of the reported threshold. However, the diffraction spectrum shows peaks belonging

to ZrO_2 (shown in blue for comparison), indicating only partial solubility of zirconium in nc-TiO_2 and the system is not a phase pure solid solution. Nonetheless the conduction band edge of $Ti_{0.8}Zr_{0.2}O_2$ was shown to be modified, as measured by spectroelectrochemical (SEC) measurements, Figure 34.

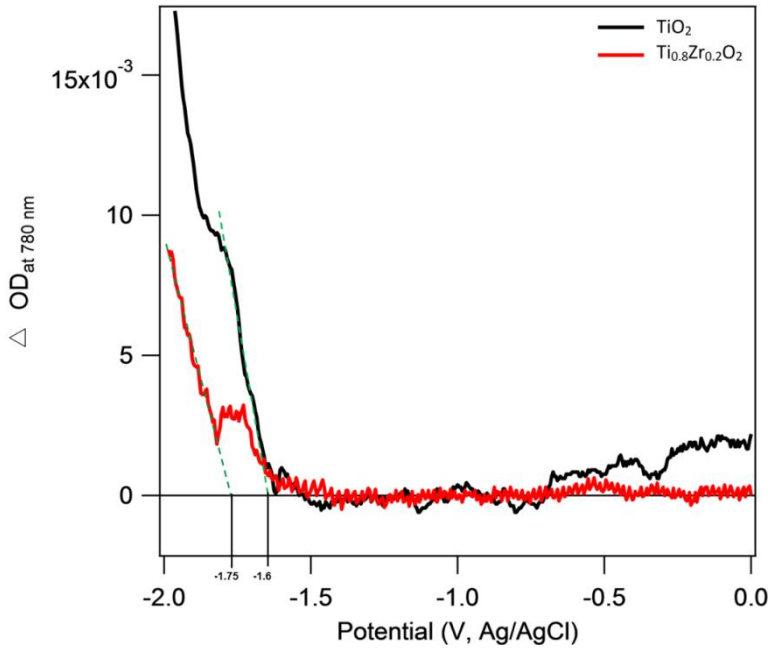

Figure 34 – ΔO.D. at 780 nm as a function of applied potential for nc-TiO_2 and $Ti_{0.8}Zr_{0.2}O_2$ electrodes, in MeCN with $TBAPF_6$ 0.1 M as the supporting electrolyte. Recorded by Dr Anna Reynal, Imperial College London.

The excited electrons in the conduction band and trap states of nc-TiO_2 are known to absorb at 780 nm; the absorbance at 780 nm was measured as a function of the applied potential. When the potential is swept negative enough, electrons will be injected directly into the conduction band and into trap states. Measuring the intercept of the potential *vs.* $O.D._{780\ nm}$ plot can therefore give an estimate of the conduction band edge. The conduction band edge found for nc-TiO_2 is more positive than what was expected for this material in thoroughly dried MeCN[64]. The conduction band edge for nc-TiO_2 has been shown to be highly dependent of both solvent and supporting electrolyte,[64] and in particular water is known to shift the conduction band edge on nc-TiO_2 to more anodic potentials due to the establishment of a proton adsorption-desorption equilibrium, and the shift to more positive potential found here (*ca.* 400 mV)[64] is attributed to the presence of residual water either in the solvent or the

electrolyte, which was not thoroughly dried. In agreement with past reports, the shift in CB edge potential for the mixed oxide material is *ca.* 150 mV negative of the CB edge potential of nc-TiO_2. From these results it is expected that both materials have sufficient driving force for electron transfer to Ni(cycC) ($E(Ni^{II/I})$ = -1.53 $V_{Ag/AgCl}$, in MeCN with 10% H_2O), with the mixed oxide system being able to drive the electron transfer faster and more efficiently.

The immobilisation of the complex was achieved by dip coating the films in 2 mM solutions of Ni(cycC) in ethanol. The concentration of the soaking solutions was chosen on account of the low extinction coefficient for the complex; lower concentrations made the estimation of catalyst uptake on the semiconductor difficult to measure. Although the quantification of the catalyst immobilised on the films was initially calculated by measuring the difference in absorbance of the soaking solution before and after the soaking, this method was quickly discarded as it provides a large overestimate of the complex on the semiconductor; when the film is rinsed after the soaking this removes any complex molecule which is not strongly immobilised (e.g. physisorbed or non-monolayer molecules), which is however taken into account when measuring the decrease in absorbance for the soaking solution. Instead, a large film (6 x 1 cm) modified with the complex has been soaked in 1 M NaOH solution for 4 hours, as a way of desorbing the complex molecules on the surface, the UV-vis of this solution was measured, in the same way as reported in a recent paper[65] and compared to a 2 mM solution of Ni(cycC) in 1 M NaOH to give a more accurate measure.

With this method it was estimated that 1.7 x 10^{17} molecules were adsorbed on the film. It was then possible to calculate the surface coverage by considering the volume of the particles (average radius = 10 nm) and the volume of the film (average thickness = 3 μm).

The volume of one particle is: $\frac{4}{3}\pi(10x10^{-9})^3 = 4.2x10^{-24}m^3$

The volume of the film is $A_{film} \cdot L_{film} \cdot (1 - P_{film}) = 6x10^{-4}m^2 \cdot 3x10^{-6}m \cdot (1 - 0.6) = 7.2x10^{-10}m^3$

The total number of particles in a film will be given by the ratios of the two values above: $\#_{particles} = \frac{7.2x10^{-10}}{4.2x10^{-24}} = 1.7x10^{14}$

The surface coverage is given by the total number of molecules adsorbed divided by the total number of nanoparticles in the film: $\frac{1.7x10^{17}}{1.7x10^{14}} = 1000\ molecules/nanoparticle$.

This result is in line with past reports of molecular catalysts immobilised on semiconductor surfaces[65]. Considering the area of a single Ni(cycC) molecule as 6.4 x 10^{-15} cm^2 (based on geometric considerations extrapolated from the complex crystal structure), and the average surface area of a nc-TiO_2 nanoparticle as 1.25 x 10^{-11} cm^2, this value would correspond roughly to half a monolayer.

The nature of the complex immobilised on the oxide surface was investigated by FTIR spectroscopy (Figure 35). To have a suitable window, a TiO_2 film was doctor-bladed on CaF_2 window from a commercial TiO_2 paste (Dyesol) and placed in a muffle furnace at 400°C for 30 minutes, and subsequently modified with Ni(cycC) following the standard procedure.

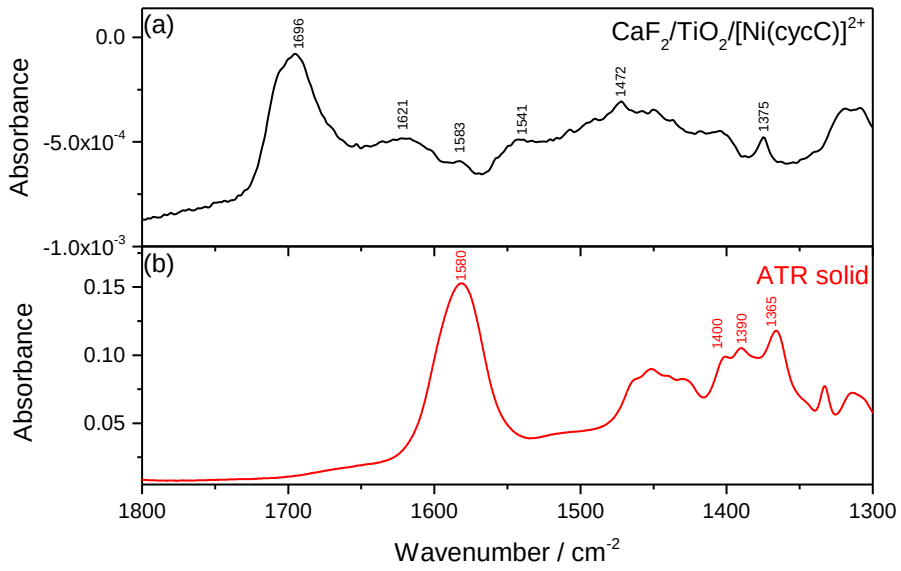

Figure 35 - (a) FTIR absorbance spectrum for a TiO_2 film on a CaF_2 slide modified with Ni(cycC); (b) ATR-FTIR absorbance spectrum of Ni(cycC) (powder).

The FTIR spectrum can be used to assess how the complex is bound to the surface. An empirical rule has been proposed[66–68], according to which the difference in energy between the antisymmetric and symmetric stretching modes of the carboxylate group gives information about the binding mode of the carboxylate to a metal oxide surface, with $\Delta\nu_{as\text{-}s}$(unidentate) > $\Delta\nu_{as\text{-}s}$(isolated) > $\Delta\nu_{as\text{-}s}$(bidentate). Here, the main features in the spectrum are peaks at 1696, 1583 and 1375 cm^{-1}. These are assigned to a ν_s(C=O), $\nu_{as}(CO_2^-)$ and $\nu_s(CO_2^-)$, respectively. The band splitting is therefore 209 cm^{-1}, larger than the 197 cm^{-1} found for the free complex, implying a monodentate surface coordination. This result would explain the presence of a C=O stretching mode in addition to the carboxylate ones.

2.2.6.2 Dark electrochemistry

The electrochemical properties of the nc-TiO_2-Ni(cycC) films have been investigated. TiO_2 nanocrystalline films have been studied as working electrodes for reductive electrochemistry.[69] The behaviour of a semiconductor is different than conventional conductive electrodes, in that the redox species of interest can be observed only once the conduction band has been filled at least partially (potentials close to the conduction band edge). The electrochemistry of bare nc-TiO_2 films has been investigated in MeCN with $TBAPF_6$ as the electrolyte, Figure 36. The CVs show the charge and discharge behaviour that is due to the progressive filling of surface trap-states with electrons as the potential is scanned more and more negative. This is in agreement for past reports of similar semiconductor electrodes.[70–74]

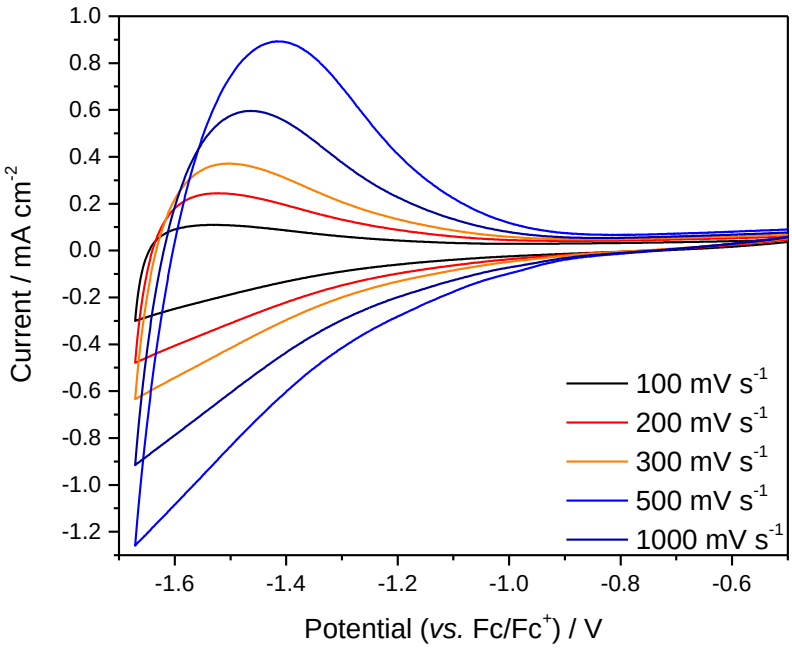

Figure 36 - CVs of a nc-TiO_2 electrode in MeCN, 0.1 M $TBAPF_6$, at different scan rates.

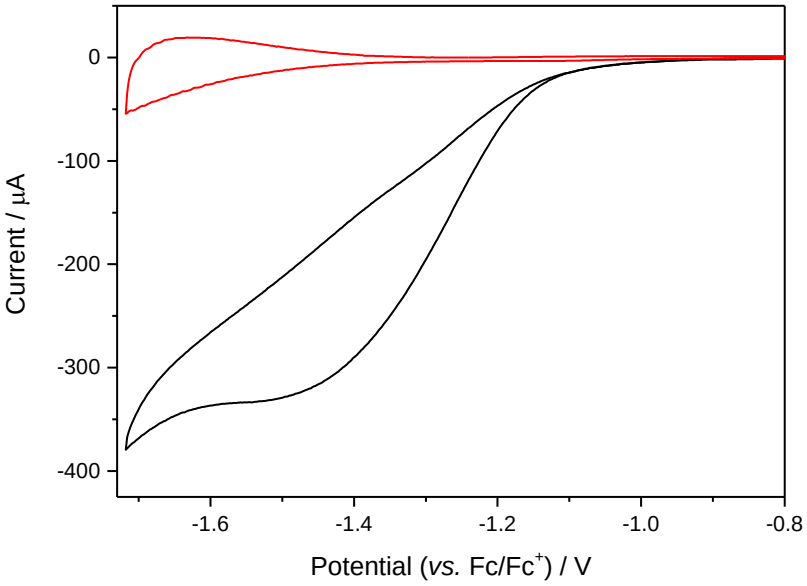

Figure 37 - CVs of nc-TiO_2 (red) and nc-TiO_2–cat (black) under argon in 0.1 M $TBAPF_6$/MeCN. v = 100 mV s^{-1}.

In contrast, the nc-TiO_2-cat film in the same electrolyte shows different behaviour (Figure 37), with the appearance of a reductive feature not typical of the charging and discharging of the electrode. This is assigned to the irreversible $Ni^{II/I}$ redox couple of the bound Ni(cycC). The immobilised nature

of the complex is confirmed by the linear dependence of the observed peak with the scan rate (Figure 38), in line with a bound species without diffusion components. The redox couple loses the reversibility that it has on other electrode materials (e.g. GCE, HMDE). Interestingly, the reduction potential of the $Ni^{II/I}$ redox couple (-1.4 *vs.* Fc/Fc^{+}, *ca.* -1.1 V *vs.* Ag/AgCl) is found at more positive potentials than the complex on mercury at pH 5 (-1.5 V *vs.* Ag/AgCl), indicating that the immobilisation stabilises the Ni^{I} species.

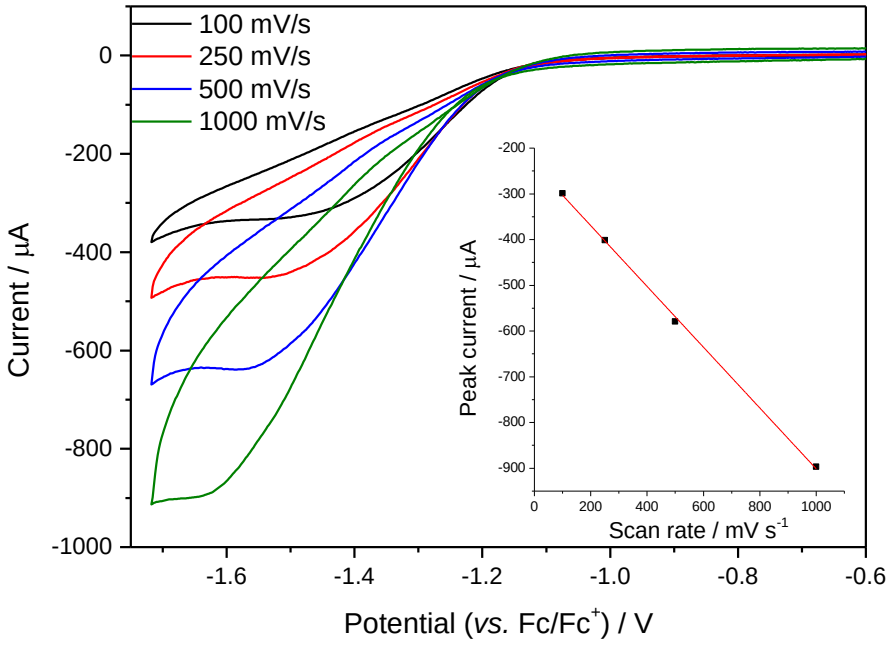

Figure 38 - Scan rate dependence of Ni(cycC) on a nc-TiO_2 electrode in Argon-purged MeCN/0.1 M $TBAPF_6$. Inset: dependence of the peak current on the scan rate, showing a linear relationship.

Control experiments were carried out with blank nc-TiO_2 films immersed in solutions of Ni(cyc) or Ni(cycC) in millimolar concentrations (Figure 39) to assess the role of surface immobilisation in enabling electron transfer to the nickel centre. The control with Ni(cyc) was carried out as this complex does not have a functional group suitable for covalent binding to the metal oxide surface. Due to solubility issues, both complexes had to be studied in a MeCN/1% H_2O mixed solvent. Therefore blank experiments were carried out in acetonitrile, and subsequently the complex in water was added to give the desired concentration of catalyst and ratio of solvents (99% MeCN, 1% H_2O).

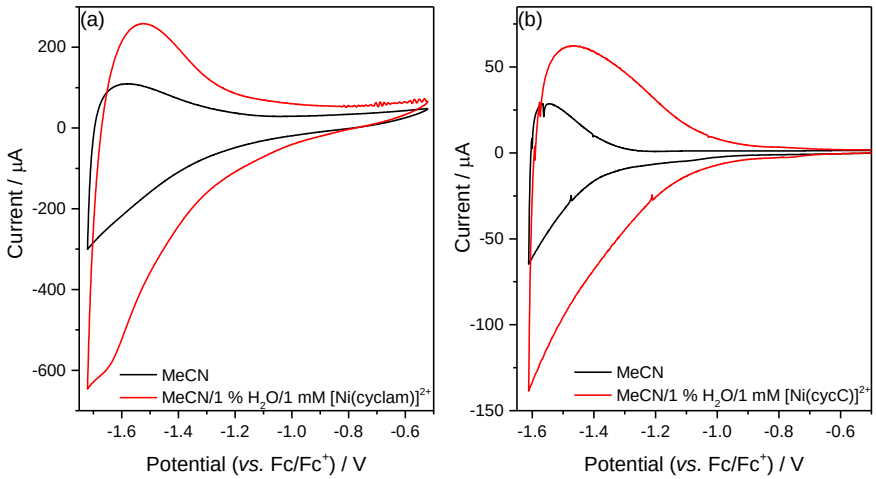

Figure 39 - CVs of a TiO_2 electrode in blank MeCN (black) and following addition of Ni(cyc) in H_2O ((a),red) or Ni(cycC) ((b), red) to make a 1 mM solution in MeCN/1 % water, 0.1 M $TBAPF_6$.

The addition of either Ni(cyc) or Ni(cycC) to the solution (Figure 39) led to no redox features observed that are assignable to the catalyst being reduced. The only difference that is noted is the earlier onset of the pseudocapacitive current and its increase in magnitude. This is due to the increased proton concentration in 1% water, which shifts the conduction band edge to more positive potentials, in line with previous studies.[64] The absence of a clear redox couple for both complexes in solution shows that there is minimal electron transfer from the electrode to the catalysts when they are not anchored on the electrode surface.

The electrochemistry of Ni(cycC) immobilised on TiO_2 in CO_2 purged solutions was investigated, Figure 40. The first CV scan under CO_2 shows an earlier onset for the reduction feature, associated with the Ni(cycC) reduction, and a slight increase in the current density. This could be attributed to CO_2 reduction, however another possibility is that the change in shape is due to the presence of residual water in the CO_2 line. Indeed by the second scan the CV loses all features and more closely resembles the CV of a blank nc-TiO_2 film. This indicates poor stability of the bound complex under CO_2, suggesting that a carboxylic acid may not be a suitable binding group to enable coupling of a cyclam catalyst to a light absorber for photocatalytic CO_2 reduction in water.

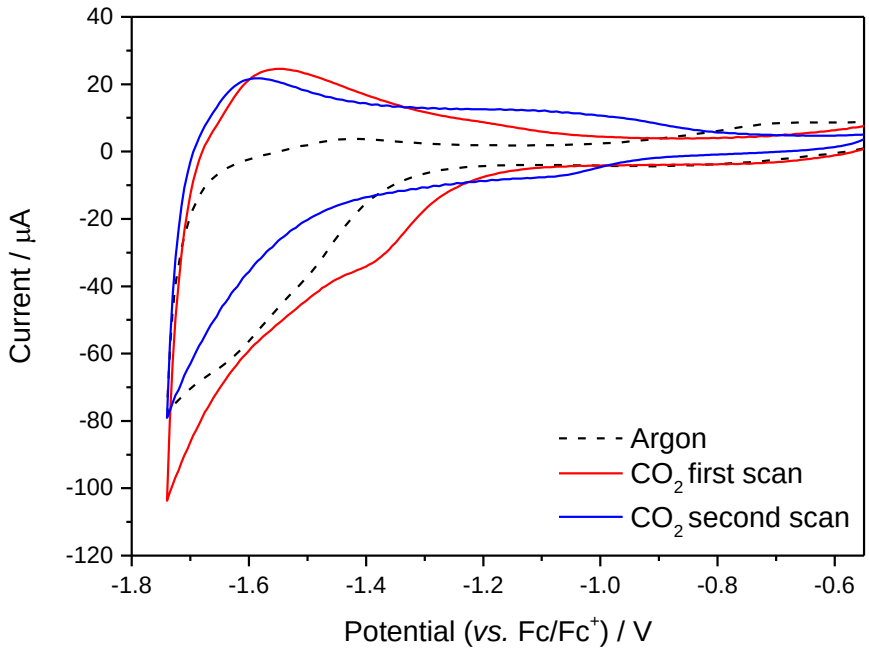

Figure 40 - CVs of a TiO_2-Ni(cycC)electrode in MeCN under argon (black) and CO_2 (red, first scan; blue, second scan), 0.1 M $TBAPF_6$.

2.2.6.3 Charge carrier dynamics

Although the carboxylic acid group does not provide a stable system for catalysis it does offer an opportunity to carry out a study of the electron transfer dynamics of the complex-semiconductor system to assess if immobilisation aids charge transfer. We have focused on the role of the thermodynamic driving force on the rate of electron transfer by carrying out TAS on the modified TiO_2 and $Ti_{0.8}Zr_{0.2}O_2$ films. TAS is a widely used technique for the study of charge carrier in semiconductors[75]. A more detailed review of the TAS technique has been provided in the first chapter. Briefly, TAS is a pump-probe technique which monitors the change in optical density of a sample following excitation from ultrafast to slow time scales. It is expected that a negative shift in the potential of the conduction band edge will cause faster electron transfer from the semiconductor to the catalyst.

The dynamics of photoelectrons and photoholes in TiO_2 have been extensively studied with this technique[76]. It is well known[77–79] that electrons in the conduction band show an absorption feature at

wavelengths greater than 800 nm. The lifetime of the excited electrons has been monitored in blank and modified TiO_2 films in the presence of triethanolamine as a hole scavenger to prevent electron recombination, (Figure 41). Furthermore, a control was carried out with a blank TiO_2 film and Ni(cyc) in solution.

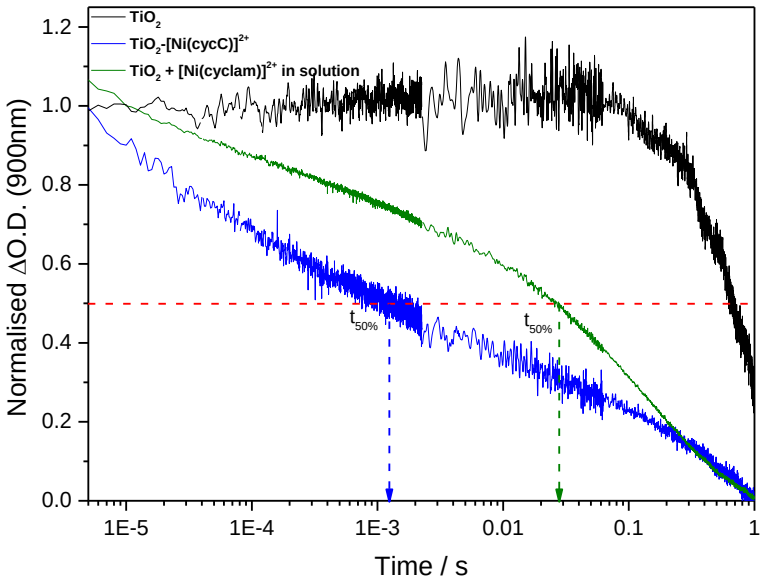

Figure 41 - Transient absorption decays of unmodified TiO_2 (black), TiO_2–cat (blue) and TiO_2 with $1x10^{-4}$ M in solution Ni(cyc) (green), measured in MeCN with 0.1 M TEOA, N_2.

The samples were excited at 355 nm (350 μJ cm^{-2}) and the absorption change at 900 nm was measured. In the absence of the catalyst, the TiO_2 film shows a very long-lived signal at this wavelength, assigned to photoelectrons in TiO_2. The long lifetime is due to the presence of the hole scavenger, preventing electron-hole recombination. A useful value for this type of measurements is $t_{50\%}$, which represents the time at which the photoelectron concentration has dropped by half compared to the beginning of the measurement. For the bare TiO_2, we obtained a $t_{50\%}$ = 0.8 s, and it is proposed that photogenerated electrons are reacting with residual protons or O_2 in the MeCN solution. In the presence of Ni(cycC) bound on the TiO_2 surface, the signal at 900 nm shows a faster decay, with a $t_{50\%}$ = 1.2 ms, which is over two orders of magnitude faster than the signal shown by

blank TiO_2. With the TEOA rapidly scavenging the holes and preventing recombination, the rapid decay is assigned to photoelectron transfer from the semiconductor to the catalyst. This is in agreement with the electrochemistry in the dark under argon, which showed that electron transfer from the TiO_2 conduction band to Ni(cycC) could occur.

The control experiment with Ni(cyc) in solution does show a faster decay of the signal at 900 nm with respect to the blank TiO_2 control ($t_{50\%}$ = 20 ms), however the electron transfer is still one order of magnitude slower than for the immobilised complex, confirming that covalent binding on the semiconductor surface improves considerably the kinetics of electron transfer to the metal centre, in line with past reports of similar hybrid systems.[65,80,81]

While the dynamics of the photogenerated carriers are well-known for TiO_2, this is less true for mixed oxides such as the $Ti_{0.8}Zr_{0.2}O_2$ used here. Experiments carried out at Imperial college showed that in the presence of methanol (see Experimental section), the spectrum of $Ti_{0.8}Zr_{0.2}O_2$ shows a broad absorption feature with a long lifetime at wavelengths >800 nm, and this is assigned to photogenerated electrons. On the other hand, in the presence of an electron scavenger the spectrum shows a less broad absorption which is long-lived at low wavelengths (460-500 nm), but decays rapidly at higher wavelengths. This is assigned to the photoholes. Knowing the main absorption features of the charge carriers in $Ti_{0.8}Zr_{0.2}O_2$ allows us to monitor the kinetics of the photoelectron transfer to the nickel catalyst. The kinetics of the blank and modified $Ti_{0.8}Zr_{0.2}O_2$ were monitored, in a similar manner as for the TiO_2 films (Figure 42). Again, the blank $Ti_{0.8}Zr_{0.2}O_2$ shows the presence of long-lived photoelectrons due to the rapid scavenging of holes by the TEOA, with a $t_{50\%}$ = 500 ms, slightly faster than the value found for TiO_2. In the presence of the Ni(cycC) immobilised complex on the surface, the decay is much faster than in the blank $Ti_{0.8}Zr_{0.2}O_2$, and significantly faster than for the complex immobilised on TiO_2 ($t_{50\%}$ = 800 μs, compared to 1.2 ms for TiO_2). This confirms the hypothesis that a more negative potential of the conduction band edge provides a higher thermodynamic driving force for electron transfer.

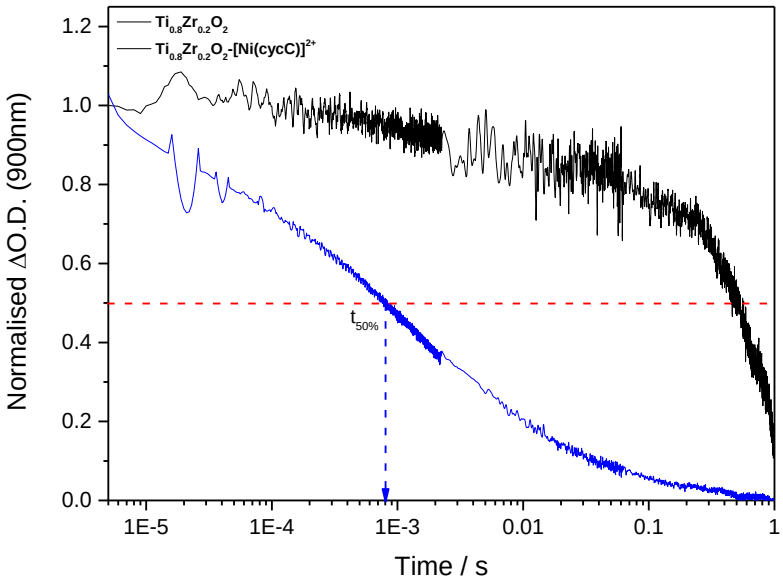

Figure 42 - Transient absorption decays of unmodified $Ti_{0.8}Zr_{0.2}O_2$ (black) and $Ti_{0.8}Zr_{0.2}O_2$–cat (blue), measured in MeCN with 0.1 M TEOA, under N_2. Recorded by Dr Anna Reynal, Imperial College London.

The results obtained for the two different semiconductor oxides are summarised in Table 4. While the experiments under CO_2 could not be carried out due to the instability of the complex on the semiconductor surface, the studies under argon provide some interesting insights for the future design of more stable and efficient semiconductor/molecular catalyst systems.

Table 4 - Potentials of electron transfer processes. [a] Estimated from the onset of the 780 nm absorption edge by spectroelectrochemistry in MeCN/$TBAPF_6$. [b] Assuming that the reduction potential of Ni(cycC) is not significantly altered upon binding to $TiO_{0.8}Zr_{0.2}O_2$ when compared to TiO_2. [c] Rate of photoelectron transfer from semiconductor to molecular catalyst, measured by TAS.

Semiconductor	Conduction Band Edge[a] (V_{Fc/Fc^+})	TiO_2/2 $Ni^{II/I}$ (V_{Fc/Fc^+})	ΔG (eV, *estimated*[b])	$t_{50\%}$ (s)[c]
nc-TiO_2	-2.0	-1.5	0.5	$1.2x10^{-3}$
$TiO_{0.8}Zr_{0.2}$	-2.15	-1.5	0.65	$0.8x10^{-3}$

The faster electron transfer observed for the immobilised complex compared to the unmodified Ni(cyc) in solution shows the advantages of immobilised systems over homogeneous ones. The approach therefore has merits, provided that more stable binding groups to the metal oxide surface are employed. Towards this effort, the second chapter will explore the properties of a Ni(cyc) derivative which has been modified with a phosphonic acid pendant arm, with the aim of obtaining a more durable heterogeneous system.

2.2.7 Conclusions

The development of selective, efficient and scalable molecular catalysts is critical in making electrocatalytic CO_2 reduction in water a feasible process for the production of fuels. The well-known electrocatalyst Ni(cyc) has been modified with a carboxylic acid pendant arm and its properties for the electrocatalytic CO_2 reduction both in organic and aqueous electrolytes have been tested. Furthermore, the ability of the complex to bind on semiconductor metal oxides has been explored, and the electron transfer dynamics have been studied using electrochemical and spectroscopic methods.

Unlike most past reports, where modification of the ligand framework brought about a decrease in the activity of the metal complex in solution, the complex shows retention of the catalytic current density and selectivity for CO over H_2. Studies in mixed acetonitrile/water solutions on a GCE showed catalytic properties similar to the few past reports for Ni(cyc) available for this electrode material. A FOWA analysis of the complex in this solvent revealed that in pure kinetic condition Ni(cycC) is a faster catalyst than the parent complex. This is in contrast with a kinetic analysis based

on the peak of the catalytic current. These disagreeing results might indicate that Ni(cycC) has a better intrinsic ability to reduce CO_2 than Ni(cyc), however it is also more easily affected by external complications such as substrate consumption and catalyst deactivation.

When the catalytic activity of Ni(cycC) was analysed on a HMDE electrode in aqueous solutions, the catalytic response was in line with past reports for similar complexes which show that this class of catalysts has a particular affinity to mercury. The modification of the framework seems to affect catalysis very little. At pH 5 Ni(cycC) behaves similarly to Ni(cyc), with a selectivity of 100:1 ($CO:H_2$, -1.2 V_{NHE}) and a FE of 88%. Double potential-step chronocoulometry experiments proved that Ni(cycC) reductively adsorbs on the surface of the electrode at potentials more positive than the formal redox potential for the $Ni^{II/I}$ couple, and comparison with other electrode materials demonstrated that the adsorbed species is the real catalyst.

More interestingly, electrochemical experiments carried out at different pH values on the HMDE showed that Ni(cycC) is a very efficient catalyst in acidic media, in contrast with the unmodified complex, which loses its catalytic properties at low pH values. Selectivity is maintained despite the much increased concentration of protons (6.4:1 $CO:H_2$, -0.99 V_{NHE}), with high TONs at potentials much more positive than at pH 5 (TON_{bulk} = 591 at -0.99 V_{NHE} at pH =2, TON_{bulk} = 5.3 at -1.2 V_{NHE} at pH = 5). The kinetics of the catalysis at pH 2 have been investigated using RDE voltammetry, and a k_{obs} = 3.4 (±1) x 10^3 s^{-1} was found at plateau currents. Moreover, the RDE CVs suggested that the improvement in catalytic activity is due to a sudden change in the mechanism at low pH values. Spectroscopic studies showed an excellent correlation between current density and protonation of the carboxylate functional group. These results lead to the hypothesis that a new mechanism pathway is opened upon protonation of the carboxylate, wherein the mobile carboxylic acid proton aids CO_2 reduction by stabilising the metal-CO_2 adduct, and acting as an internal proton source, as previously shown for several other classes of CO_2 reduction catalysts. Ni(cycC) is based on a low cost metal centre and is able to use a pendant acid group to achieve excellent selectivity and activity towards

CO_2 even at the very low pH value of 2; we are aware of no other molecular catalysts for CO_2 reduction that retains activity and selectively at this pH, making this catalyst a first in class.

The immobilisation of Ni(cycC) on nc-TiO_2 and $Ti_{0.8}Zr_{0.2}O_2$ mesoporous thin films was readily achieved by dip-coating the oxide films in ethanolic solutions of the complex. The surface coverage has been estimated *via* UV-vis spectroscopy, and found to be on the order of half a monolayer, and the binding mode of the carboxylic acid on the oxide surface has been found to be monodentate. The electrochemistry of modified nc-TiO_2 films under argon shows the appearance of the $Ni^{II/I}$ redox couple, demonstrating that electron transfer from the semiconductor to the complex is achievable. The hybrid system however is unstable under a CO_2 atmosphere, and therefore detailed catalytic studies were not carried out. The light-driven electron transfer was studied using TA spectroscopy. Faster decay of the photoelectron signal on the modified oxides compared to the blank materials in the presence of a hole scavenger were assigned to electron transfer from the semiconductor to the catalyst. The $t_{50\%}$ were found to be 1.2 ms for the complex immobilised on TiO_2 and 800 μs for the complex immobilised on $Ti_{0.8}Zr_{0.2}O_2$. These values show how a higher thermodynamic driving force causes faster electron transfer. Furthermore, the immobilised complex shows faster electron transfer than the unmodified complex in solution, demonstrating the advantages of this approach.

2.3 Materials and methods

2.3.1 Materials

Cyc (1,4,8,11-tetraazacyclotetradecane, Sigma) cycC (1,4,8,11-tetraazacyclotetradecane-6-carboxylic acid, Chematech) and $NiCl_2{\cdot}H_2O$ (Sigma) were used as received. $[Ni(cyclam)]Cl_2$ was prepared according to literature procedures[82]. Milli-Q water (18.2 MΩ) was used throughout. All electrolyte salts and solvents were purchased from Sigma Aldrich or VWR and used without further purification. Ar, N_2 and CO_2 were purchased from BOC at CP or higher grade. The pH of aqueous

solutions was adjusted by adding 1 M $HClO_4$ or NaOH to the pre-purged solution until the desired value was reached, measuring with a Hannah pH probe, which was calibrated daily.

[Ni(cycC)]Cl_2: cycC (130 mg, 0.5 mmol) was dissolved in water (40 ml, 10 mM) at room temperature, and $NaHCO_3$ (250 mg, 3 mmol) was added. When gas evolution stopped, $NiCl_2 \cdot H_2O$ (130 mg, 0.55 mmol) was added portionwise over the course of one hour. Within the first few minutes from the first addition the solution turned orange. Stirring at room temperature was maintained for two hours. The $Ni(OH)_2$ and nickel carbonates that precipitated as a result of the side reaction with $NaHCO_3$ were filtered, and the solution was rotary evaporated to dryness, taking care that the water of the bath never exceeded 50°C. Above this temperature a brown solid forms. The pink powder that results was dissolved in ethanol, to yield a pink solution and a white solid (NaCl, by-product of the reaction, and $NaHCO_3$ which is added in great excess). The solid was filtered and the ethanol removed by rotary evaporation. This step was repeated several times, until no white powder precipitated upon addition of more ethanol. The crystalline solid that was obtained was dried under vacuum overnight. Single crystals suitable for X-ray diffractometry were obtained by slow vapour diffusion of hexane in ethanol. Obtained: 83 mg, yield 45 %; **ATR-IR**: 3184 (br), 2915, 2856, 1580 (s), 1451, 1400, 1390, 1365, 1090, 945, 879 cm^{-1}; **ESI-MS**: 301 [M^+-2Cl]; **CHN microanalysis**: Anal. calcd. for $C_{11}H_{24}Cl_2N_4NiO_2 \cdot 1.75C_2H_5O$: C, 35.50; H, 6.88; N, 14.28. Found: C, 35.45; H, 6.68; N, 14.03.

Table 5 - Crystal data and structure refinement for [Ni(cycC)]Cl_2

Empirical formula	$C_{11}H_{26}Cl_2N_4NiO_3$
Formula weight	391.97
Temperature/K	173
Crystal system	N/A
Space group	$P2_1/n$
a/Å	6.66207(9)
b/Å	17.0552(2)
c/Å	15.01109(19)
α/°	90
β/°	102.4162(13)
γ/°	90
Volume/$Å^3$	1665.71(4)

Z	4
ρ_{calc}g/cm^3	1.563
μ/mm^{-1}	4.767
F(000)	824
Crystal size/mm^3	0.24 × 0.19 × 0.19
Radiation	CuKα (λ = 1.54184)
2Θ range for data collection/°	7.96 to 144.72
Index ranges	$-7 \leq h \leq 8$, $-21 \leq k \leq 17$, $-18 \leq l \leq 17$
Reflections collected	14185
Independent reflections	3260 [R_{int} = 0.0239, R_{sigma} = N/A]
Data/restraints/parameters	3260/7/219
Goodness-of-fit on F^2	1.062
Final R indexes [I>=2σ (I)]	R_1 = 0.0365, wR_2 = 0.1001
Final R indexes [all data]	R_1 = 0.0404, wR_2 = 0.1031
Largest diff. peak/hole / e Å^{-3}	0.94/-0.67

Table 6 - Fractional Atomic Coordinates (×104) and Equivalent Isotropic Displacement Parameters (Å2×103) for [Ni(cycC)]Cl2. Ueq is defined as 1/3 of of the trace of the orthogonalised UIJ tensor.

Atom	x	y	z	U(eq)
Ni	6985.5(5)	3776.3(2)	2290.6(2)	25.58(14)
Cl1	10142.7(8)	2996.9(3)	3016.6(4)	34.63(16)
Cl2	3792.8(8)	4570.0(3)	1637.8(4)	33.17(16)
N1	5086(3)	3030.4(11)	2801.7(14)	30.3(4)
C2	5543(4)	2910.8(15)	3791.5(17)	37.6(5)
C3	5587(4)	3692.5(15)	4299.4(17)	37.7(5)
C4	7495(4)	4204.8(16)	4294.6(16)	37.6(5)
N5	7424(3)	4540.5(11)	3383.5(13)	30.0(4)
C6	9236(4)	5017.8(14)	3318.7(17)	35.9(5)
C7	9111(4)	5232.9(13)	2326.0(17)	34.3(5)
N8	8858(3)	4516.7(11)	1767.6(13)	29.4(4)
C9	8210(4)	4682.1(15)	778.8(17)	37.3(5)
C10	8062(4)	3937.3(17)	214.2(17)	42.1(6)
C11	6280(4)	3396.0(16)	273.1(17)	40.1(6)
N12	6552(3)	3028.0(11)	1185.5(14)	33.2(4)
C13	4851(4)	2507.7(15)	1276.2(18)	40.1(6)

C14	5038(4)	2300.1(13)	2269.9(19)	38.0(5)
C15	5317(4)	3531.9(18)	5262.9(18)	44.4(6)
O15	4818(5)	2901.9(16)	5516.0(17)	77.5(8)
O16	5830(5)	4110.0(14)	5826.7(16)	71.9(7)
O20	5303(3)	3778.0(11)	7449.0(14)	48.6(5)

Table 7 - Anisotropic Displacement Parameters ($Å^2×10^3$) for [Ni(cycC)]Cl_2. The Anisotropic displacement factor exponent takes the form: $-2\pi^2[h^2a^{*2}U_{11}+2hka^*b^*U_{12}+...]$.

Atom	U_{11}	U_{22}	U_{33}	U_{23}	U_{13}	U_{12}
Ni	21.8(2)	23.5(2)	32.0(2)	0.37(14)	7.24(15)	-1.52(13)
Cl1	25.0(3)	33.4(3)	45.4(3)	6.8(2)	7.5(2)	3.7(2)
Cl2	24.7(3)	32.7(3)	41.9(3)	5.2(2)	6.5(2)	3.45(19)
N1	22.5(9)	28.5(9)	40.2(10)	4.8(8)	7.3(8)	0.1(7)
C2	29.8(12)	40.2(13)	43.5(13)	11.7(10)	9.8(10)	-1.4(10)
C3	32.0(12)	47.4(14)	35.0(12)	6.2(10)	9.9(10)	0.3(10)
C4	35.8(13)	46.1(14)	30.6(11)	1.4(10)	6.7(9)	-3.4(10)
N5	27.5(9)	30.5(10)	32.0(9)	-0.5(7)	6.2(7)	-0.8(7)
C6	31.0(12)	33.8(12)	42.8(13)	-6(1)	7.8(10)	-7.9(9)
C7	31.6(12)	26.9(11)	47.7(13)	-0.9(10)	15.7(10)	-4.9(9)
N8	25.1(9)	27.6(9)	36.6(10)	1.8(7)	9.3(8)	0.8(7)
C9	37.6(13)	39.1(13)	37.6(12)	10.3(10)	13.4(10)	1.5(10)
C10	44.9(14)	49.1(14)	34.7(12)	2.4(11)	14.0(11)	2.7(11)
C11	41.6(14)	44.3(14)	32.8(12)	-4.1(10)	4.5(10)	1.0(11)
N12	27.9(10)	32(1)	39.6(10)	-3.9(8)	6.9(8)	1.4(8)
C13	35.2(13)	32.5(12)	51.8(15)	-9.2(11)	7.4(11)	-6.9(10)
C14	30.6(12)	24.5(11)	60.1(15)	-0.4(10)	12.5(11)	-5.0(9)
C15	40.2(14)	53.9(16)	41.0(13)	4.0(12)	12.7(11)	-5.7(12)
O15	106(2)	80.0(17)	53.1(13)	-1.0(12)	30.7(13)	-39.8(16)
O16	124(2)	52.0(13)	50.6(12)	-2.5(10)	43.5(14)	-12.2(14)
O20	66.0(13)	39.4(11)	44.8(10)	-1.0(8)	21.6(9)	3.6(9)

Table 8 - Bond Lengths for [Ni(cycC)]Cl_2

Atom	Atom	Length/Å
Ni	N8	2.0465(18)
Ni	N1	2.0555(18)
Ni	N12	2.063(2)
Ni	N5	2.0662(19)

Ni	Cl1	2.5284(6)
Ni	Cl2	2.5340(6)
N1	C2	1.465(3)
N1	C14	1.476(3)
C2	C3	1.533(4)
C3	C15	1.520(3)
C3	C4	1.544(3)
C4	N5	1.474(3)
N5	C6	1.476(3)
C6	C7	1.519(3)
C7	N8	1.471(3)
N8	C9	1.481(3)
C9	C10	1.518(4)
C10	C11	1.522(4)
C11	N12	1.482(3)
N12	C13	1.468(3)
C13	C14	1.512(4)
C15	O15	1.210(4)
C15	O16	1.297(4)

Table 9 - Bond Angles for [Ni(cycC)]Cl_2

Atom	Atom	Atom	Angle/°
N8	Ni	N1	179.37(8)
N8	Ni	N12	93.71(8)
N1	Ni	N12	85.77(8)
N8	Ni	N5	85.51(8)
N1	Ni	N5	95.01(8)
N12	Ni	N5	179.08(8)
N8	Ni	Cl1	88.32(5)
N1	Ni	Cl1	92.04(5)
N12	Ni	Cl1	88.92(6)
N5	Ni	Cl1	91.54(6)
N8	Ni	Cl2	92.99(5)
N1	Ni	Cl2	86.68(5)
N12	Ni	Cl2	93.36(6)
N5	Ni	Cl2	86.19(6)
Cl1	Ni	Cl2	177.29(2)
C2	N1	C14	113.99(19)
C2	N1	Ni	117.03(15)
C14	N1	Ni	105.31(14)

N1	C2	C3	111.2(2)
C15	C3	C2	108.8(2)
C15	C3	C4	111.9(2)
C2	C3	C4	114.7(2)
N5	C4	C3	111.22(19)
C4	N5	C6	114.31(18)
C4	N5	Ni	117.55(15)
C6	N5	Ni	105.88(14)
N5	C6	C7	108.95(19)
N8	C7	C6	109.51(19)
C7	N8	C9	112.71(19)
C7	N8	Ni	107.37(13)
C9	N8	Ni	115.58(14)
N8	C9	C10	111.7(2)
C9	C10	C11	115.6(2)
N12	C11	C10	111.6(2)
C13	N12	C11	113.5(2)
C13	N12	Ni	106.07(15)
C11	N12	Ni	116.70(15)
N12	C13	C14	109.4(2)
N1	C14	C13	108.88(19)
O15	C15	O16	121.5(3)
O15	C15	C3	123.7(3)
O16	C15	C3	114.5(2)

Table 10 - Hydrogen Atom Coordinates ($Å \times 10^4$) and Isotropic Displacement Parameters ($Å^2 \times 10^3$) for [Ni(cycC)]Cl_2

Atom	x	y	z	U(eq)
H1	3861(18)	3274(13)	2669(17)	28(6)
H2A	6891	2647	3981	45
H2B	4485	2565	3956	45
H3A	4359	3999	3984	45
H4A	7561	4634	4743	45
H4B	8752	3883	4479	45
H5	6300(30)	4841(14)	3189(18)	37(7)
H6A	10509	4717	3556	43
H6B	9268	5500	3689	43
H7A	7932	5589	2112	41
H7B	10381	5509	2265	41
H8	10070(20)	4266(15)	1885(19)	42(8)
H9A	9212	5043	594	45
H9B	6855	4946	657	45

H10A	9360	3640	409	50
H10B	7947	4086	-432	50
H11A	4983	3700	144	48
H11B	6173	2981	-196	48
H12	7710(30)	2739(15)	1321(19)	41(8)
H13A	4895	2024	915	48
H13B	3522	2773	1039	48
H14A	3853	1974	2342	46
H14B	6312	1996	2494	46
H16	5500(60)	3940(20)	6347(14)	68(11)
H20A	5320(50)	3283(7)	7660(20)	54(9)
H20B	5690(50)	4155(15)	7870(18)	61(10)

Semiconductor films for electrochemistry: Anatase TiO_2 films were prepared by depositing TiO_2 colloidal paste (average particle diameter = 20 nm) on fluorine-doped tin oxide (FTO) glass slides. The slides were sonicated in ethanol for 20 minutes before the deposition. The paste was deposited on the films and spread with a glass rod. The thickness was controlled by using scotch tape and was measured *via* profilometry to be an average of 3 μm. The films were allowed to dry before the slides were heated at 450°C for 30 minutes. The slides were cut so that the geometric surface area of the TiO_2 films was 1 cm^2.

Semiconductor films for TAS: the films for TAS analysis were prepared by Dr Anna Reynal, Imperial College London. Anatase TiO_2 and $Ti_{0.8}Zr_{0.2}O_2$ films were deposited onto microscope or fluorine-doped tin oxide (FTO) coated glass by the Doctor blading technique from their respective colloidal pastes and calcined in a furnace at 450 °C for 30 min. The anatase TiO_2 paste was prepared as described in the literature.[60] $Ti_{0.8}Zr_{0.2}O_2$ colloidal paste was prepared as follows: Acetic acid (2.4 g) and titanium isopropoxide ($Ti(iPrO)_4$, 10.53 mL), were mixed under nitrogen upon vigorous stirring (700 rpm) until a pale yellow colour appeared. Then, $Zr(iPrO)_4$ ($Zr(iPrO)_4$–IPA, 3.45 g) pre-dissolved in 16 mL anhydrous isopropanol solution was added. After stirring for 10 min, the mixture was poured into a conical flask containing 63 mL of 0.1 M HNO_3 solution at room temperature. The

resulting milky mixed oxide suspension was subsequently stirred at 80 °C for 8 h. Finally, the mixture was poured into a Teflon inlet inside a stainless steel reactor and heated at 240 °C for 12 h. Polyethylene glycol (PEG) 20,000 (50% of TiO_2 by weight) was added to the above colloidal solution to prevent subsequent film cracking during heat treatment and to enhance film porosity.

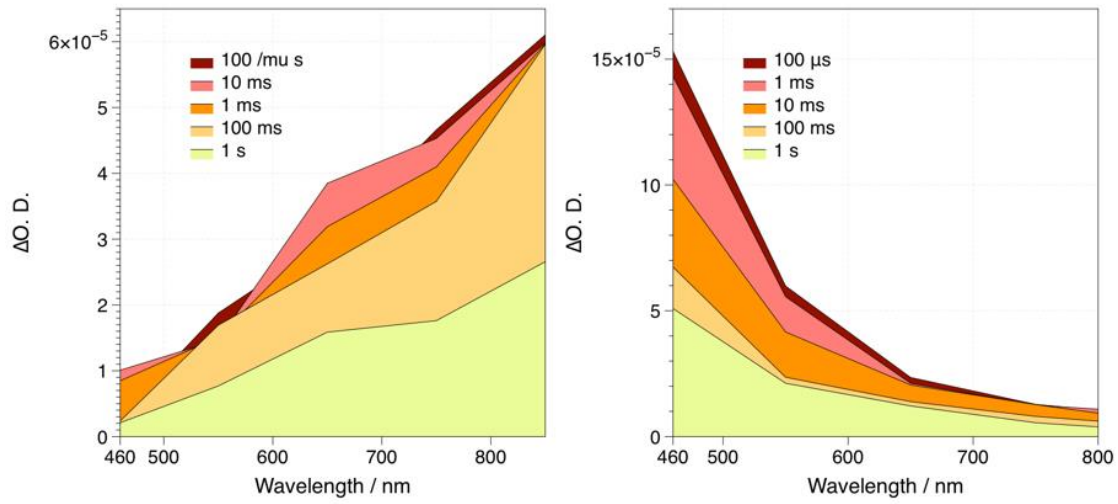

Figure 43 - Transient absorption spectra of (a) photoexcited electrons in a $Ti_{0.8}Zr_{0.2}O_2$ film using methanol as the hole scavenger, and (b) $Ti_{0.8}Zr_{0.2}O_2$ holes, when employing a 10^{-3} M $AgNO_3$ aqueous solution as the electron scavenger. The samples were excited at 355 nm with a laser intensity of 350 μJ cm^{-1} and a repetition rate of 1 Hz. Recorded by Dr Anna Reynal, Imperial College London.

2.3.2 Electrochemistry

All electrochemical experiments except chronocoulometry and RDE were carried out using either a Palmsens[1], Palmsens[3] or Emstat potentiostats (Alvatek). Static electrochemistry was carried out in a 4-neck pear-shaped flask, with a three electrode set-up. The counter electrode was either a platinum basket, platinum gauze or platinum coiled wire. The working electrode for the non-aqueous electrochemistry was a GCE, which has been hand polished to mirror finish using decreasing sizes of diamond (15, 6 and 1 μm) and alumina (0.5 μm) slurry before every experiment. For the aqueous electrochemistry a Hanging Mercury Drop Electrode WK2 was used. This was filled in the laboratory with triply distilled mercury (Fisher); the area of a drop was 0.023 cm^2, measured by weighing and averaging a large amount of drops. A silver wire *quasi*reference electrode was used as the reference electrode for non-aqueous electrochemistry. The potential was referenced by measuring the ferrocene

redox couple at the end of each experiment. A Ag/AgCl/3.5 M NaCl reference electrode (BASi, IJ Cambria or home-made) was used for aqueous electrochemistry.

Bulk electrolysis experiments were carried out either using a gold-mercury amalgam as the working electrode (geometric surface area ≈ 2.5 cm^2), or a custom-made mercury pool cell (surface area ≈ 4.15 cm^2). For these experiments, the counter electrode was separated from the main compartment of the cell by a glass double junction with a porous frit to avoid reoxidation of the reaction products. The nature of the reaction products was verified by gas chromatography. The instrument used was an Agilent 6890N with helium N6 (BOC) as the carrier gas (5 mol min^{-1}), equipped with a 5 Å molecular sieve column (ValcoPLOT, 30 m length, 0.53 mm ID) and a pulsed discharge detector (D-3-I-HP, Valco Vici). The peak areas for H_2 and CO were quantified by calibration with a custom-ordered calibrant gas containing 500 ppm of H_2 and 200 ppm of methane and CO. Calibrations were carried out daily.

Chronocoulometry experiments used a Whistonbrook DF63 potentiostat and Labview software (National Instruments), HMDE working electrode, platinum wire counter and a silver wire quasi-reference electrode. The cell was purged with argon (30 mins) before the experiments and kept under a blanket of argon throughout. A fresh mercury drop was used with every potential step.

RDE measurements were carried out in a 5-neck, pear-shaped flask using a Pine AFMSRCE and Bio-Logic SP-200 potentiostat. The electrode was prepared by dipping a polished gold disc (Pine) in mercury for 1-2 minutes, shaking the excess mercury off and drying for at least two hours. Best quality electrodes are obtained by polishing the gold to a mirror finish before the amalgamation process and leaving to dry for longer periods of time. Lightly polishing the amalgam with an alumina slurry (0.5 μm diameter) provides more reproducible surface areas (measured by comparing the non-faradaic currents of each electrode at multiple scan rates in aqueous electrolyte), however the lifespan of the electrode decreases significantly. After each experiment, the mercury is removed by dipping the electrode in concentrated HNO_3 for 15-30 seconds, followed by copious rinsing with water.

2.3.3 Spectroscopic characterisation

ESI-MS and elemental analyses were performed by the University of Liverpool analytical services. FTIR samples were prepared by depositing a TiO_2 film (*vide infra*) on a CaF_2 slide followed by dipping in a 2 mM solution of Ni(cycC) in ethanol for 48 hours. Spectra were recorded with a Bruker Vertex 70V Fourier-transform infrared spectrometer, using a MIR globar source, KBr beamsplitter and a liquid nitrogen-cooled HgCdTe detector, at a resolution of 2 cm^{-1}. ATR-FTIR measurements of the powder and FTIR titration were carried out on a Bruker Vertex instrument. Profilometry was measured using an Ambios Technology XP200. UV-Vis spectra were recorded on a Shimadzu UV-2600 spectrophotometer.

Spectro-electrochemical measurements were carried out by Dr Anna Reynal in Imperial College London, and were performed in a homemade PTFE cell with quartz windows, using an Autolab potentiostat (PGSTAT12) to apply a voltage while measuring the absorption of the sample with a Perkin Elmer Lambda 35 UV/vis spectrophotometer. A three-electrode configuration was employed, with a nanostructured film deposited onto FTO as working electrode, a Pt wire as counter electrode and a Ag/AgCl/sat KCl. The absorption of the semiconductors as a function of the voltage applied was monitored at λ_{abs} = 780 nm, corresponding to the absorption of electrons in the conduction band of TiO_2 and $Ti_{0.8}Zr_{0.2}O_2$.

Scanning electron microscopy (SEM) images were obtained with a Philips XL-30 field emission gun scanning electron microscope. Samples were coated with Au (2 nm) prior to observation. SEM was used to determine the morphology of the $Ti_{0.8}Zr_{0.2}O_2$ particles and films. The thickness of the mesoporous nanostructured films was 3 μm, measured by profilometry (Tencor Instruments). The $Ti_{0.8}Zr_{0.2}O_2$ particles had a diameter of ~ 20 nm.

X-Ray diffraction (XRD) measurements were made on a Philips PW1710 diffractometer with mono-chromated Cu radiation.

The microsecond-second transient absorption decays were measured at Imperial College using a Nd:YAG laser (Big Sky Laser Technologies Ultra CFR Nd:YAG laser system, 6 ns pulse width). The third harmonic of the laser, corresponding to 355 nm, at a frequency of 1 Hz, was used as the excitation pulse. Typical excitation densities of 350 $\mu J/cm^2$ were used, unless otherwise stated. A liquid light guide with a diameter of 0.5 cm was used to transmit the laser pulse to the sample. The probe light source was a tungsten lamp (Bentham IL1 tungsten lamp) and the probing wavelength was selected by using a monochromator OBB-2001 dual grating, Photon Technology International) placed prior to the sample. Transient absorption data were collected with a Si photodiode (Hamamatsu S3071). The information was passed through an amplifier box (Costronics) and recorded using a Tektronics TDS 2012c oscilloscope (microsecond to millisecond timescale) and a National Instruments (NI USB-6211) DAQ card (millisecond to second timescale). The decays observed are the average of between 500 and 1000 laser pulses. The data was processed using home-built software based on Labview.

2.4 References

1. M. Beley, J.-P. Collin, R. Ruppert, and J.-P. Sauvage, *J. Chem. Soc. Chem. Commun.*, 1984, **2**, 1315–1316.

2. J. Schneider, H. Jia, K. Kobiro, D. E. Cabelli, J. T. Muckerman, and E. Fujita, *Energy Environ. Sci.*, 2012, 5, 9502.

3. J. D. Froehlich and C. P. Kubiak, *Inorg. Chem.*, 2012, **51**, 3932–3934.

4. A. Jarzębińska, P. Rowiński, I. Zawisza, R. Bilewicz, L. Siegfried, and T. Kaden, *Anal. Chim. Acta*, 1999, **396**, 1–12.

5. M. Beley, J. P. Collin, J. P. Sauvage, J. P. Petit, and P. Chartier, *J. Electroanal. Chem.*, 1986, **206**, 333–339.

6. C. Herrero, A. Quaranta, S. El Ghachtouli, B. Vauzeilles, W. Leibl, and A. Aukauloo, *Phys. Chem. Chem. Phys.*, 2014, **16**, 12067.

7. J. L. Grant, K. Goswami, L. O. Spreer, J. W. Otvos, and M. Calvin, *J. Chem. Soc., Dalton Trans.*, 1987, 2105–2109.

8. H. Tian, *ChemSusChem*, 2015, **8**, 3746–3759.

9. K. Bujno, R. Bilewicz, L. Siegfried, and T. A. Kaden, *J. Electroanal. Chem.*, 1998, **445**, 47–53.

10. R. D. Hancock, R. J. Motekaitis, J. Mashishi, I. Cukrowski, J. H. Reibenspies, and A. E. Martell, *J. Chem. Soc. Perkin Trans. 2*, 1996, 1925.

11. P. J. C. and E. J. Billo, *Inorg. Chem.*, 1987, **26**, 3224–3226.

12. E. Joseph Billo, P. J. Connolly, D. J. Sardella, J. P. Jasinski, and R. J. Butcher, *Inorganica Chim. Acta*, 1995, **230**, 19–28.

13. D. T. Pierce, T. L. Hatfield, E. J. Billo EJ and, and Y. Ping, *Inorg. Chem.*, 1997, **36**, 2950–2955.

14. L. Sabatini and L. Fabbrizzi, *Inorg. Chem.*, 1979, **18**, 438–444.

15. M. Boiocchi, L. Fabbrizzi, F. Foti, and M. Vazquez, *Dalton Trans.*, 2004, 2616–2620.

16. A. Anichini, L. Fabbrizzi, P. Paoletti, and R. M. Clay, *Inorg. Chim. Acta*, 1977, **24**, L21–L23.

17. A. Evers and R. D. Hancock, *Inorg. Chim. Acta*, 1989, **160**, 245–248.

18. T. W. Hambley, G. A. Lawrance, M. Maeder, and E. N. Wilkes, *J. Chem. Soc. Dalton Trans.*, 1992, 1283–1289.

19. P. V. Bernhardt and G. A. Lawrance, *Coord. Chem. Rev.*, 1990, **104**, 297–343.

20. A. J. Bard, L. R. Faulkner, N. York, W. Brisbane, and S. E. Toronto, *ELECTROCHEMICAL METHODS Fundamentals and Applications*, 1944.

21. P. Jacquinot and P. C. Hauser, *Electroanalysis*, 2003, **15**, 1437–1444.

22. G. B. Balazs, California Institute of Technology, 1993.

23. M. Beley, J.-P. Collin, R. Ruppert, and J.-P. Sauvage, *J. Chem. Soc. Chem. Commun.*, 1984, 1315.

24. M. Fujihira, Y. Hirata, and K. Suga, *J. Electroanal. Chem. Interfacial Electrochem.*, 1990, **292**, 199–215.

25. J. Schneider, H. Jia, K. Kobiro, D. E. Cabelli, J. T. Muckerman, and E. Fujita, *Energy Environ. Sci.*, 2012, **5**, 9502.

26. G. B. Balazs and F. C. Anson, *J. Electroanal. Chem.*, 1993, **361**, 149–157.

27. J. D. Froehlich and C. P. Kubiak, *J. Am. Chem. Soc.*, 2015, **137**, 3565–3573.

28. M. Beley, J. P. Collin, R. Ruppert, and J. P. Sauvage, *J. Am. Chem. Soc.*, 1986, **108**, 7461–7467.

29. C. Costentin, S. Drouet, M. Robert, and J.-M. Saveant, *Science (80-.).*, 2012, **338**, 90–94.

30. C. Costentin, G. Passard, M. Robert, and J.-M. Savéant, *Proc. Natl. Acad. Sci.*, 2014, **111**, 14990–14994.

31. J. Agarwal, T. W. Shaw, H. F. Schaefer, and A. B. Bocarsly, *Inorg. Chem.*, 2015, **54**, 5285–5294.

32. F. Franco, C. Cometto, F. Ferrero Vallana, F. Sordello, E. Priola, C. Minero, C. Nervi, and R. Gobetto, *Chem. Commun.*, 2014, **50**, 14670–14673.

33. C. Costentin, M. Robert, J.-M. Savéant, and A. Tatin, *Proc. Natl. Acad. Sci.*, 2015, **112**, 6882–6886.

34. B. P. (B. P. Sullivan, K. Krist, and H. E. Guard, *Electrochemical and electrocatalytic reactions of carbon dioxide*, Elsevier, 1993.

35. J. Schneider, H. Jia, K. Kobiro, D. E. Cabelli, J. T. Muckerman, and E. Fujita, *Energy Environ. Sci.*, 2012, **5**, 9502–9510.

36. G. B. Balazs and F. C. Anson, *J. Electroanal. Chem.*, 1992, 322, 325–345.

37. J. H. Christie, G. Lauer, R. a. Osteryoung, and F. C. Anson, *Anal. Chem.*, 1963, **35**, 1979–1979.

38. F. Anson and R. Osteryoung, *J. Chem. Educ.*, 1983, **60**, 293–296.

39. J. H. Christie, R. a. Osteryoung, and F. C. Anson, *Electroanal. Chem. Interfacial Electrochem.*, 1967, **13**, 236–244.

40. O. Gershevitz and C. N. Sukenik, *J. Am. Chem. Soc.*, 2004, **126**, 482–483.

41. P. V. Bernhardt, G. K. Boschloo, F. Bozoglian, A. Hagfeldt, M. Martínez, and B. Sienra, *New J. Chem.*, 2008, **32**, 705.

42. P. K. Glasoe and F. A. Long, *J. Phys. Chem.*, 1960, **64**, 188–190.

43. Y. Baran, G. A. Lawrance, and E. N. Wilkes, *Polyhedron*, 1997, **16**, 599–602.

44. J. D. Froehlich and C. P. Kubiak, *J. Am. Chem. Soc.*, 2015, **137**, 3565–3573.

45. J.-M. Savéant, *Chem. Rev.*, 2008, **108**, 2348–78.

46. C. Costentin, M. Robert, and J.-M. Savéant, *Chem. Soc. Rev.*, 2013, **42**, 2423–2436.

47. H. Takeda, C. Cometto, O. Ishitani, and M. Robert, *ACS Catal.*, 2016, 70–88.

48. C. Costentin, S. Drouet, M. Robert, and J. M. Savéant, *J. Am. Chem. Soc.*, 2012, **134**, 11235–11242.

49. J.-M. Savéant, *Chem. Rev.*, 2008, **108**, 2348–2378.

50. J. M. Savéant and E. Vianello, *Electrochim. Acta*, 1967, **12**, 629–646.

51. J. M. Saveant and E. Vianello, *Electrochim. Acta*, 1965, **10**, 905–920.

52. A. D. Wilson, R. H. Newell, M. J. McNevin, J. T. Muckerman, M. Rakowski DuBois, and D. L. DuBois, *J. Am. Chem. Soc.*, 2006, **128**, 358–366.

53. C. Costentin and J.-M. Savéant, *ChemElectroChem*, 2014, **1**, 1226–1236.

54. E. S. Rountree, B. D. McCarthy, T. T. Eisenhart, and J. L. Dempsey, *Inorg. Chem.*, 2014, **53**, 9983–10002.

55. J. M. Smieja, M. D. Sampson, K. a. Grice, E. E. Benson, J. D. Froehlich, and C. P. Kubiak,

Inorg. Chem., 2013, **52**, 2484–2491.

56. K.-Y. Wong, W.-H. Chung, and C.-P. Lau, *J. Electroanal. Chem.*, 1998, **453**, 161–170.

57. B. O'Regan and M. Grätzel, *Nature*, 1991, **353**, 737–740.

58. M. Grätzel, *Prog. Photovoltaics Res. Appl.*, 2000, **8**, 171–185.

59. A. Berni, M. Mennig, and H. Schmidt, in *Sol-Gel Technologies for Glass Producers and Users*, eds. M. A. Aegerter and M. Mennig, Springer US, Boston, MA, 2004, pp. 89–92.

60. S. Ito, T. N. Murakami, P. Comte, P. Liska, C. Grätzel, M. K. Nazeeruddin, and M. Grätzel, *Thin Solid Films*, 2008, **516**, 4613–4619.

61. M. Dürr, S. Rosselli, A. Yasuda, and G. Nelles, *J. Phys. Chem. B*, 2006, **110**, 21899–21902.

62. J. C. Yu, J. Lin, and R. W. M. Kwok, *J. Phys. Chem. B*, 1998, **102**, 5094–5098.

63. B.-F. Gao, Y. Ma, Y.-A. Cao, Z.-J. Gu, G.-J. Zhang, and J.-N. Yao, *Chinese J. Chem.*, 2007, **25**, 484–489.

64. G. Redmond and D. Fitzmaurice, *J. Phys. Chem.*, 1993, **97**, 1426–1430.

65. A. Reynal, J. Willkomm, N. M. Muresan, F. Lakadamyali, M. Planells, E. Reisner, and J. R. Durrant, *Chem. Commun.*, 2014, **50**, 12768–12771.

66. G. Deacon and R. J. Phillips, *Coord. Chem. Rev.*, 1980, **33**, 227–250.

67. M. Nara, H. Torii, and M. Tasumi, *J. Phys. Chem.*, 1996, **100**, 19812–19817.

68. C. Bauer, G. Boschloo, E. Mukhtar, and A. Hagfeldt, *J. Phys. Chem. B*, 2002, **106**, 12693–12704.

69. S. N. Frank and A. J. Bard, *J. Am. Chem. Soc.*, 1975, **97**, 7427–7433.

70. E. Topoglidis, Y. Astuti, F. Duriaux, M. Grätzel, and J. R. Durrant, *Langmuir*, 2003, **19**, 6894–6900.

71. E. Topoglidis, A. E. . Cass, B. O'Regan, and J. R. Durrant, *J. Electroanal. Chem.*, 2001, **517**, 20–27.

72. G. Rothenberger, D. Fitzmaurice, and M. Griitzel, *J. Phys. Chem*, 1992, **96**, 5983–5986.

73. G. Boschloo and D. Fitzmaurice, *J. Electrochem. Soc.*, 2000, **147**, 1117–1123.

74. G. Boschloo and D. Fitzmaurice, *J. Phys. Chem. B*, 1999, **103**, 2228–2231.

75. C. Czekelius, M. Hilgendorff, L. Spanhel, I. Bedja, M. Lerch, G. Muller, U. Bloeck, D. S. Su, and M. Giersig, *Adv. Mater.*, 1999, **11**, 643–+.

76. D. Bahnemann, A. Henglein, J. Lilie, and L. Spanhel, *J. Phys. Chem.*, 1984, **88**, 709–711.

77. J. Tang, J. R. Durrant, and D. R. Klug, *J. Am. Chem. Soc.*, 2008, **130**, 13885–13891.

78. T. Yoshihara, Y. Tamaki, A. Furube, M. Murai, K. Hara, and R. Katoh, *Chem. Phys. Lett.*, 2007, **438**, 268–273.

79. T. Yoshihara, R. Katoh, A. Furube, Y. Tamaki, M. Murai, K. Hara, S. Murata, H. Arakawa, and M. Tachiya, *J. Phys. Chem. B*, 2004, **108**, 3817–3823.

80. F. Lakadamyali, A. Reynal, M. Kato, J. R. Durrant, and E. Reisner, *Chemistry*, 2012, **18**, 15464–75.

81. M. A. Gross, A. Reynal, J. R. Durrant, and E. Reisner, *J. Am. Chem. Soc.*, 2014, **136**, 356–366.

82. B. Bosnich, M. L. Tobe, and G. A. Webb, *Inorg. Chem.*, 1965, **4**, 1109–1112.

“Felix qui potest rerum cognoscere causas”

“Fortunate is he, who is able to know the causes of things”

-Virgilio

3

CO_2 reduction by Ni(cycP):

synthesis and solution electrocatalysis

3.1 Scope of the chapter

In the previous chapter the ability of the newly synthesised complex Ni(cycC) (cycC = 1,4,8,11-tetraazacyclotetradecane-6-carboxylic acid) to bind to semiconductor surfaces was investigated. It was found that the complex bound to TiO_2 and $Ti_{0.8}Zr_{0.2}O_2$, likely in a bidentate manner, and electron transfer from the excited semiconductor to the catalyst under argon occurred, significantly faster than when the complex was in solution. However, the binding mode of the complex was found to be unstable under CO_2. The carboxylic acid functionality was introduced in the ligand framework as extensive studies on dye-sensitised solar cells have shown that they give the fastest electron transfer rates, together with cyanoacrylate groups.[1,2] Phosphonate groups have been used as alternatives to carboxylic acids and cyanoacrylates on account of their much higher stability in wet environments, at a wide range of pH values, however the formation of stronger bonds comes at the cost of a slower electron transfer.[1] The slower electron injection rates have been attributed to the tetrahedral geometry of the phosphorus centre and loss of conjugation when compared to carboxylic acids[3–5] (Scheme 18).

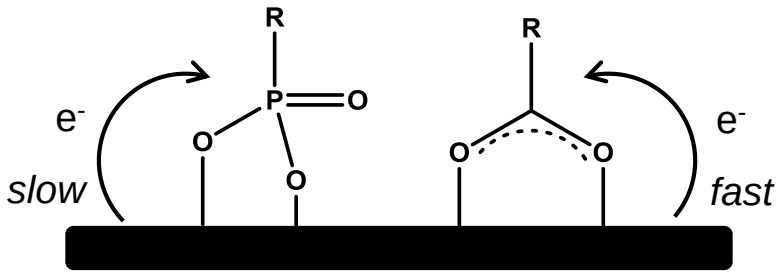

Scheme 18 – Phosphonate vs. carboxylate binding group; the electron transfer in phosphonates has been found to be slower than in carboxylates due to the loss of conjugation and tetrahedral structure of the phosphonate.

Nevertheless, the slow electron transfer is largely considered a necessary compromise in order to increase the stability of immobilised complexes, and the use of this functional group is slowly replacing the use of carboxylic acids.

This chapter will describe the synthesis of a Ni(cyc) (cyclam = 1,4,8,11-tetraazacyclotetradecane) complex functionalised with a phosphonic acid binding group, Ni(cycP) (cycP = {[(1,4,8,11-

tetraazacyclotetradecan-1-yl)methyl]phosphonic acid}) to allow for higher stability of the complex on semiconductor surfaces. The complex of the modified ligand with nickel has never been reported, and therefore its catalytic activity towards the electroreduction of CO_2 was investigated. Furthermore, the binding, electrochemistry and electron transfer of the complex on nc-TiO_2 and ZrO_2 thin films will be analysed.

3.2 Results and Discussion

3.2.1 Synthesis and characterisation

The cyclam backbone can be modified in three different positions, (Scheme 19).

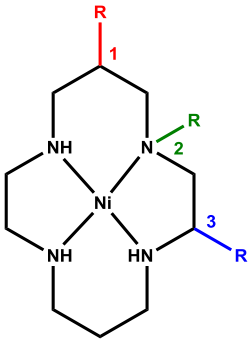

Scheme 19 - Three possible functionalisation sites on the cyclam ligand.

As shown in the previous chapter, functionalisation of the framework with a carboxylic group in position 1 (Scheme 19, red) retains and can improve CO_2 reduction activity. Ideally functionalisation with the phosphonic acid group would be carried out at position 1. There is one example in the literature of a versatile method to functionalise position 1[6], starting from a linear tetraamine which is cyclised by condensation with a 2-functionalised 1,3-dibromopropane. This synthetic strategy has been attempted in our lab as a way to obtain cyc-C in-house and a hydroxyl substituted ligand, however every attempt has failed, and the synthesis is still under optimisation. Functionalisation in position 2 (Scheme 19, green) was explored, as a more facile route to obtain mono-, bis-or tetra-substituted alkyl phosphonate derivatives of cyclam[7–9], and their metal complexes of Cu[9,10], have

been reported. We were aware that modifying even only one of the secondary amines would most likely affect catalysis in solution in a negative manner. The effect of N-methylation of Ni(cyc) on the electrochemical properties of the complex has been the focus of several studies.[11–14] Figure 44 shows the difference in reduction potentials for the $Ni^{II/I}$ couple of increasingly substituted complexes under argon, and the CVs obtained under CO_2, reproduced from a study by Kaden *et al.*[13] The study showed that increasing methylation of the amines caused the reduction potential to shift anodically, and this was attributed to a higher stability of the Ni^{I} compared to the less substituted complexes, in agreement with other studies on the matter.[12] The same anodic shift was not noted in the cyclic voltammetry under CO_2. In contrast, the onset potential for CO_2 reduction remained unchanged for $[Ni(MMC)]^{2+}$ and $[Ni(DMC)]^{2+}$ (Figure 44), with the catalytic current decreasing as the number of methyl groups increased. $[Ni(TRMC)]^{2+}$ and $[Ni(TMC)]^{2+}$ showed very little catalysis. Several factors have been proposed to be the cause for the decrease in catalytic activity, primarily the reduced availability of amine protons, which have been shown to assist CO_2 binding to the metal centre *via* H-bonding, and the different adsorption behaviour shown by N-methylated complexes.

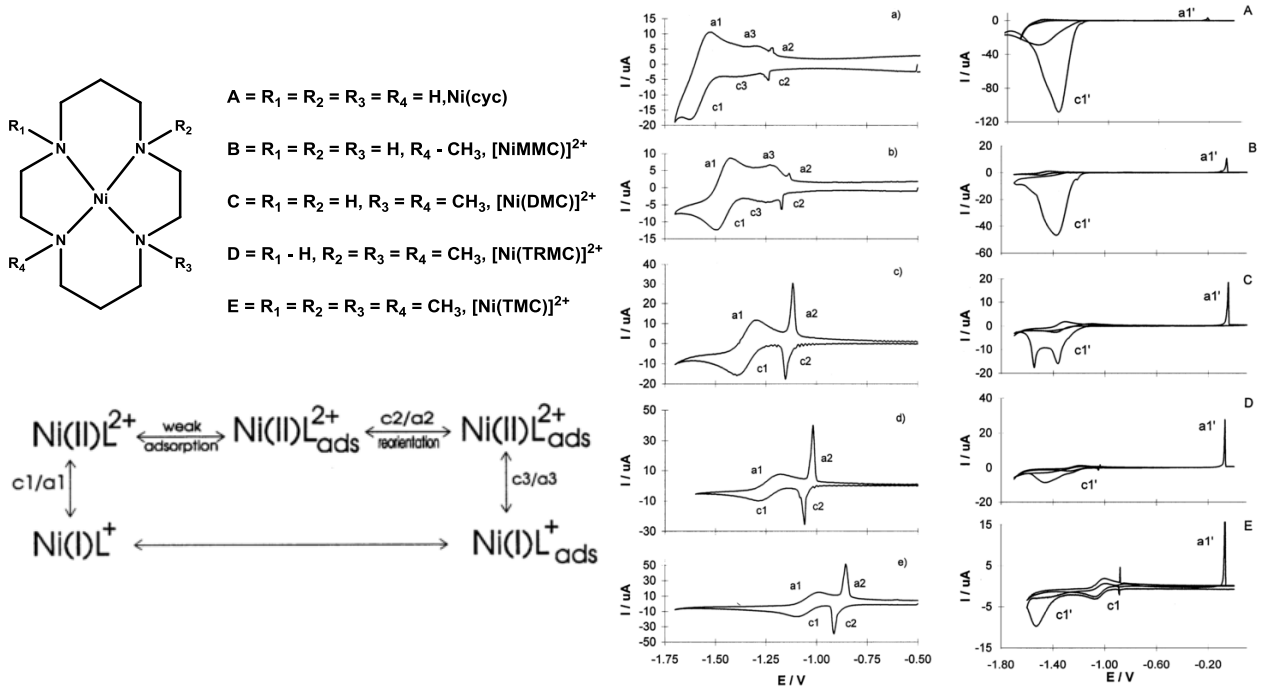

Figure 44 – Ni(cyc) was N-methylated to various degrees and the electrochemical behaviour of the methylated complexes was studied under argon and CO_2. The letters in the CVs correspond to the differently substitute complexes, on the left. Figure reproduced from ref. [13]

In the study shown here, it was hypothesised that the main difference in adsorption behaviour was due to the unsubstituted complex being able to adsorb on the surface of the electrode prior to reduction of the nickel metal centre, and that adsorbed Ni^{II} complex was able to be reduced to Ni^{I}, as shown in the scheme in Figure 44. A subsequent study[14,15] showed that the adsorption of Ni^{II}(cyc) doesn't occur, but instead that the complex undergoes a reductive adsorption even at very positive potentials. This last hypothesis would explain why the voltammogram of the unsubstituted complex showed a current spike before the diffusion controlled reduction, the area of which does not correspond to a full monolayer: the reduced adsorbed complex is already largely present on the electrode surface at these potentials. In contrast, the intensity of the spike increases with increased N-substitution, indicating that the complex adsorbs in a single step, instead of gradually with scanning the potential. This difference in behaviour has been attributed to a higher rigidity of the methylated complexes, which would prevent reorganisation of the structure, needed for adsorption, at low potentials. Here,

the potential negative effects of N-functionalisation on the CO_2 reduction efficiency in order to obtain a phosphonate derivative of Ni(cyc) were taken into account, however it was envisaged that functionalisation of only one of the four amines would not completely turn off catalysis.

There are several methods[16] for obtaining differentiated, or selectively protected cyclams. The first involves direct reaction of cyclam with the chosen protecting agent using stoichiometric[17], pH[18] and temperature control to yield differentially protected ligands. This method is hindered by low yields and the formation of under- and over-protected side-products, which are removed through intense purification procedures.[19] Another approach is to temporarily protect three of the four amino groups using metal-tricarbonyl[20], boron[21] or phosphorus[22] containing moieties. These procedures have considerable drawbacks, such as the use of air-sensitive reagents and undesirable solvents. It has been recently found[23] that ethyl trifluoroacetate (EtOTFA), a mild acetylating agent for amine protection,[24] reacts selectively with only three of the four nitrogen atoms of cyclam and other tetraaza-macrocycles, with high yields (>90%) and in mild conditions, even when it is present in the reaction mixture in excess. The reaction proceeds at room temperature in 4 hours, and the product has a very different R_f (retention factor) to the starting material, making purification facile. The reaction (Scheme 20) was carried out in anhydrous conditions, using methanol as the solvent, and the tri-protected cyclam (**2**) was purified by passing the crude transparent oil through a silica gel plug by eluting with ethyl acetate (full synthetic details are in the materials and methods section), and was obtained with a 94% yield.

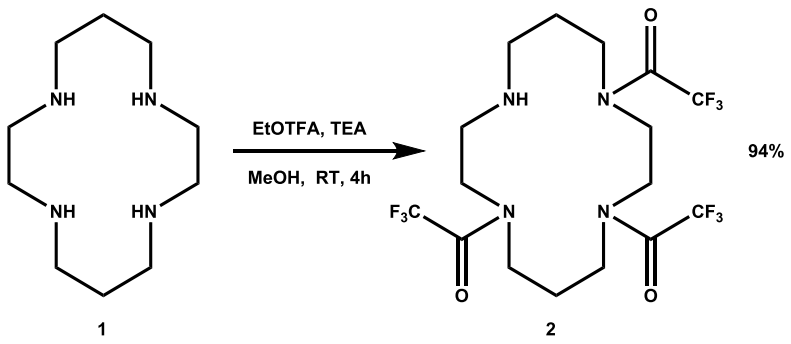

Scheme 20 – Selective protection of the amine groups.

The free amine was functionalised with the alkyl phosphonate *via* the Mannich reaction between the protected macrocyclic amine, formaldehyde and triethyl phosphite, which was also used as the reaction solvent. The reaction was run at 40 °C for three days, and the crude product was used for the next step without any purification apart from the removal of the solvent (Scheme 21). Boiling the residue in 6 M HCl for three days afforded crude compound **5**. As the final hydrolysis step is carried out in concentrated acid the final product is represented as the hydrochloric acid form (·nHCl). Elemental analysis was not carried out (due to difficulties in the purification, see below), therefore the precise amount of HCl molecules could not be determined.

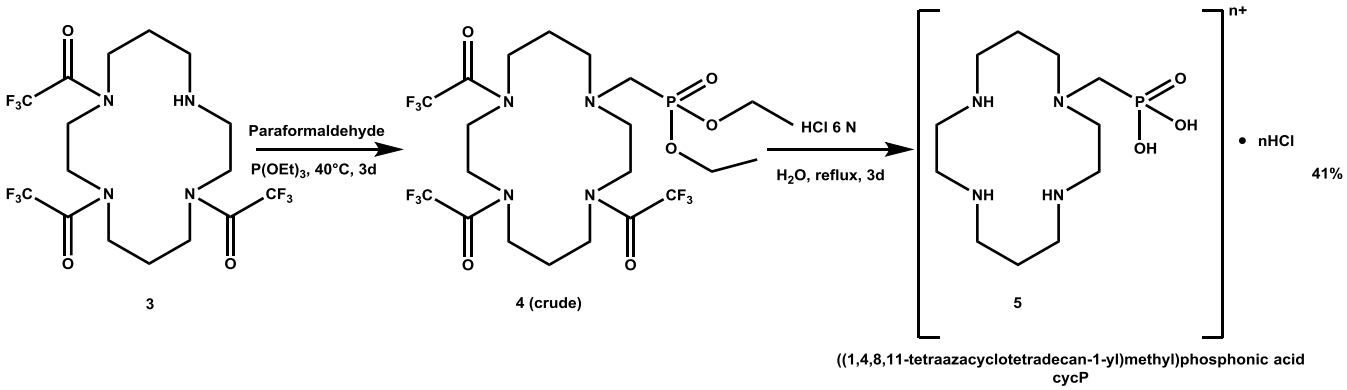

Scheme 21 - Mannich reaction between triethyl phosphite and the protected cyclam and hydrolysis.

The purification of the final ligand proved to be challenging. The major impurities in the crude product (verified by proton nuclear magnetic resonance, ^{1}H-NMR) are by-products of the reaction between formaldehyde and triethyl phosphite such as HO-CH_2-P(O)$(OEt)_2$ and HO-CH_2-P(O)$(OH)_2$ (1.16, 3.61, 3.82 and 4.03 ppm). In addition, multi-substituted products of cyclam can form, albeit in smaller amounts, due to formaldehyde and triethyl phosphite being present in large excess and functionalising more than one amine on the same molecule, in spite of the positions being initially protected. These are observed in the proton NMR as smaller impurities, complicating the aliphatic region (Figure 45). Removal of the non-macrocyclic impurities was achieved by running the crude product through a column loaded with a strong acid cation exchange resin (Dowex 50W, H^{+}-form). The triethyl phosphite by-products were washed with water to neutral reaction of the eluate, and the

product was collected by eluting with aqueous HCl (6 M). After removal of the excess HCl, the yellowish oil was loaded onto a weakly acidic ion-exchange resin (Amberlite CG50, H^+-form), with the aim of removing the macrocyclic derivatives bearing multiple phosphonic acid pendant arms by eluting them with water, and subsequently obtaining the product by elution with 10% aqueous acetic acid. NMR and mass spectrometry were used to investigate the outcome of the purification steps.

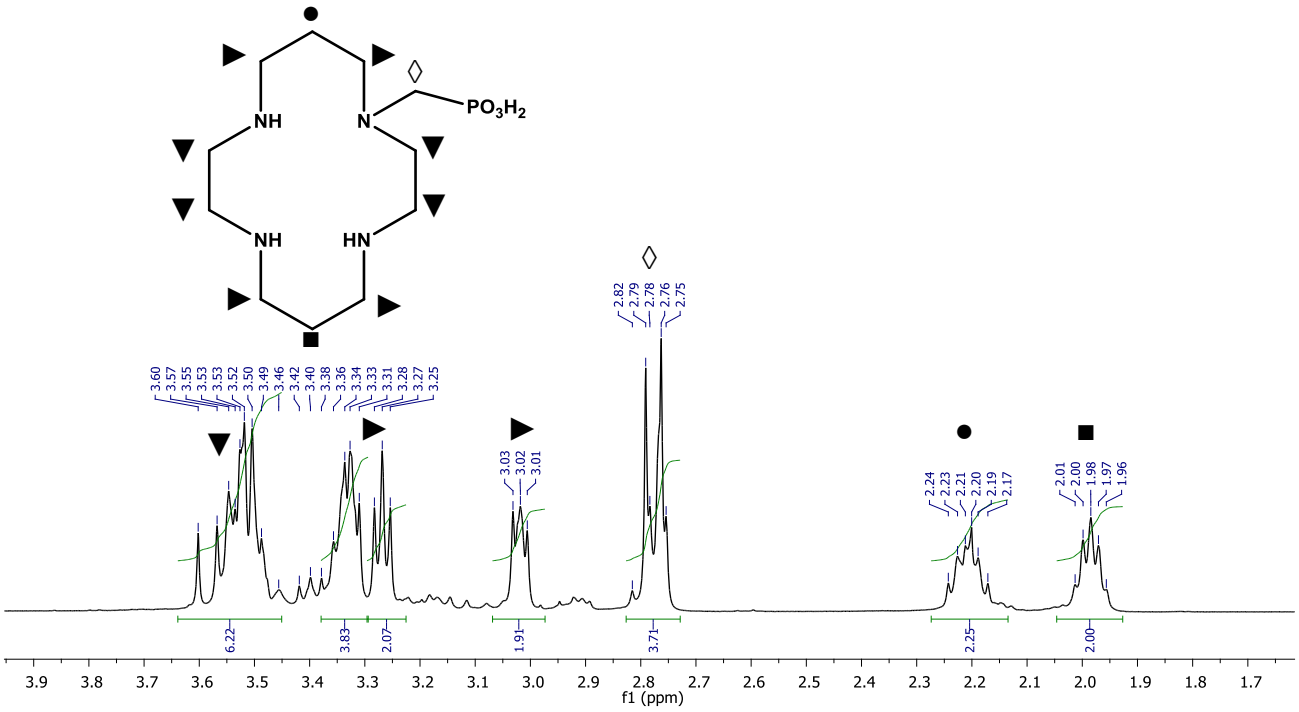

Figure 45 – ^{1}H-NMR spectrum of the cycP ligand in D_2O, showing the peaks corresponding to the product, after the purification steps with Dowex resin and Amberlite resin, and the respective assignment, based on previous literature reports;[8,9] macrocycles bearing multiple methyl-phosphonic acid groups were not successfully removed.

All attempts at replicating this literature derived[8,9] purification procedure for similar macrocyclic ligands were unsatisfactory. While the triethyl phosphite by-products were readily removed with the Dowex purification step, after eluting the product through Amberlite resin no improvements in the purity of the product were noted. Electrospray Ionisation Mass Spectrometry (ESI-MS) of samples carried out before and after elution through Amberlite showed a single molecular ion peak at m/z = 295 ($[M+H]^+$), however the ^{1}H-NMR spectrum in D_2O (Figure 45) indicated that impurities consisting of macrocycles which have been substituted in more than one amine position were present

(it should be noted that mass spectrometry does not provide quantitative analysis, and its results are dependent on the ionisation technique used). The conditions for the Amberlite column have been varied in several ways (e.g. increasing the amount of Amberlite loaded in the column and eluting with acidity gradient) without success.

Other purification methods have been attempted. Flash column chromatography (EtOH:H_2O:NH_3aq 5:5:1) resulted in reasonably pure product (>85%), however the column conditions were deemed too wasteful, since most of the product was retained on the silica gel (the yield after the column was ~ 10%). Similarly, decolourisation of the crude product with activated charcoal and subsequent precipitation with HBr, as per the literature procedure for the final step[9] did not result in the desired pure product. A series of washings with organic solvents (MeOH, $CHCl_3$) was attempted next, but this did not improve the purity.

With the intention of purifying the final compound at a later stage, the impure ligand obtained after the Dowex column was used to attempt complexation. The reaction was tested in various solvent mixtures and using different bases to deprotonate the macrocycle amines, which were present as the HCl salt following the final synthetic step. The best results were obtained using neat water as the solvent and $NaHCO_3$ as the base (Scheme 22), in a similar way as described for the synthesis of [Ni(cycC)]Cl_2 in the previous chapter.

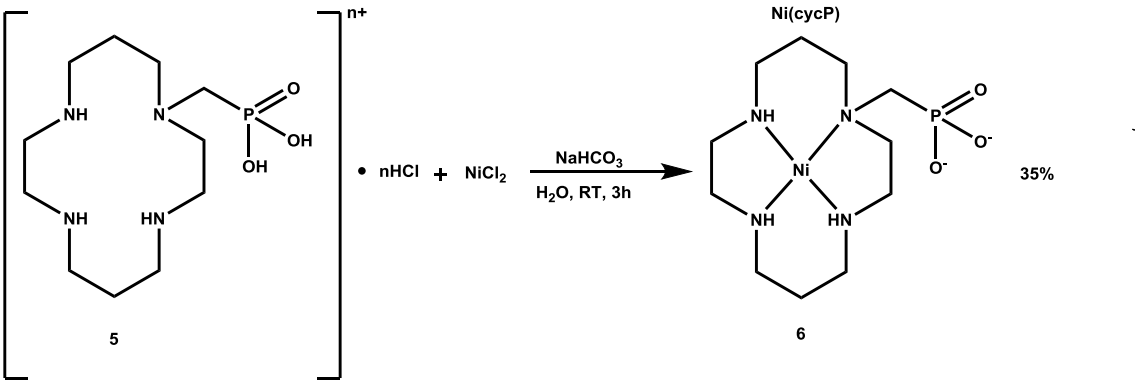

Scheme 22 - Synthetic scheme for complexation of the modified ligand with nickel to obtain Ni(cycP).

The reaction between the phosphonic acid cyclam and $NiCl_2 \cdot H_2O$ was carried out at room temperature, and a colour change from green ($NiCl_2$) to lilac, indicating the successful complexation, was noticed in the first minutes after addition of $NiCl_2$. The reaction was followed to completion *via* UV-Vis spectroscopy until the peak corresponding to $NiCl_2$ (393 nm) disappeared completely (3 hours). The target compound was purified via flash column chromatography (MeOH:NH_{3aq} 9:1), affording a crystalline lilac powder, thus avoiding the need to initially purify the ligand. Elemental analysis indicated that the complex as prepared is in the form [Ni(((1,4,8,11-tetraazacyclotetradecan-1-yl)methyl)phosphonate)]$\cdot 0.3H_2O$, hereafter labelled Ni(cycP). The complex was further characterised using ESI-MS, UV-vis and FTIR (Fourier Transform Infrared) spectroscopies, and X-ray crystal diffractometry.

Suitable crystals for X-ray crystal diffraction were obtained by slow evaporation of a solution of the complex in water (Figure 46). Ni(cycP) crystallises in a polymeric structure (denoted [Ni(CycP)]n) with supporting lattice waters; the chains propagate diagonally along the *c*-axis. The phosphonates form a bridge between each unit by binding to two adjacent nickel centres in the axial positions, while the lattice waters form a hydrogen bonding network which link neighbouring chains together. The chains appear to form a *pseudo* closed packed structure. The crystal structure shows a slightly distorted octahedral coordination of the metal centre (N-Ni-N *cis* angles in the range 84.92(18)° to 94.66(18)°, N-Ni-O angles 90.99(16)° and 94.20(16)°), with the nitrogen atoms occupying the equatorial sites. The nickel metal centre is coordinated in the axial positions by oxygens of the phosphonate groups. The bond lengths of the Ni-O indicate no substantial difference between the Ni-O relative to the intramolecular coordination (2.119(3) Å) and the Ni-O relative to the intermolecular coordination (2.065(3) Å), and these are similar to the Ni-N bond lengths as well (2.065(4) Å - 2.124(4) Å). There is therefore a striking difference between this complex and the previously studied $[Ni(cycC)]Cl_2$, where the bond lengths of the Ni-Cl were found to be elongated with respect to the

Ni-N bond lengths. Full crystallographic data, including bond lengths and bond angles, can be found in section 3.3.1.

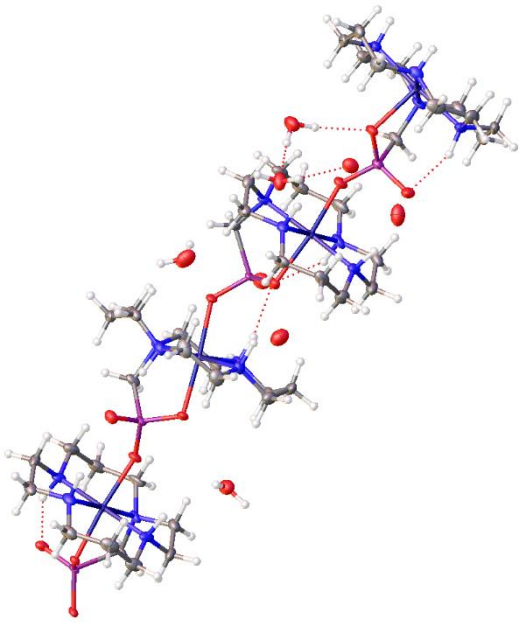

Figure 46 – ORTEP diagram of the crystal structure of $[Ni(cycP)]_n$.

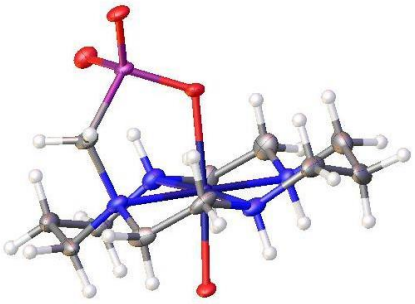

Figure 47 - ORTEP diagram of a single molecule unit in $[Ni(cycP)]_n$, to clarify the conformation of the complex.

The behaviour of the new complex in solution is different from other cyclam complexes of nickel, including Ni(cyc) and Ni(cycC). The latter exists in an equilibrium of square planar and octahedral coordination geometries, with the square planar being the most abundant in non-coordinating solvents; in contrast, Ni(cycP) forms purple solutions even in water, with a UV-vis spectrum (Figure 48) characterised by two absorption peaks, at 344 nm (ε = 24 $M^{-1}cm^{-1}$) and at 533 nm (ε = 12 $M^{-1}cm^{-}$

[1]), suggesting an octahedral structure,[25] in line with the crystal structure. Furthermore, obtaining a [1]H-NMR spectrum of the complex was not possible, suggesting the complex is paramagnetic, in line with an octahedral geometry.

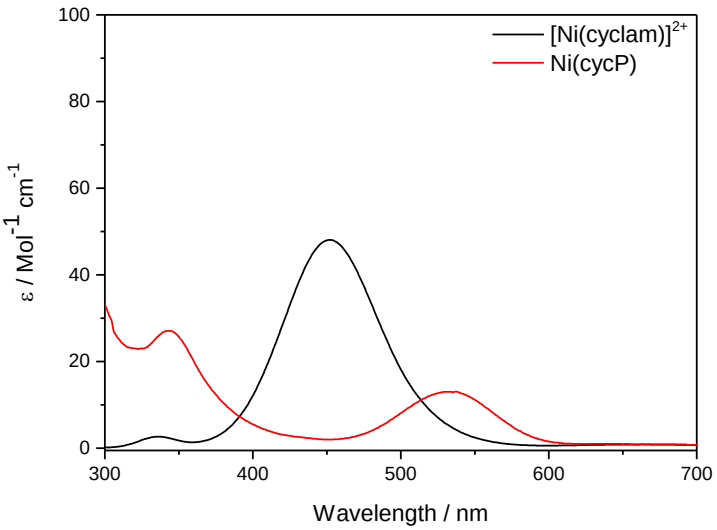

Figure 48 - Solution UV-Vis spectra of Ni(cyc) and Ni(cycP) (10 mM in water, 1 cm pathlength).

Based on the crystal structure and on reports of similar complexes with pendant arms (often referred to as scorpiand complexes)[9,26–28] we hypothesise that in solution the phosphonic acid arm remains strongly coordinated to the metal centre in an intramolecular manner, maintaining the octahedral structure. Any attempt to force the geometry to a square planar one, by changing solvents or adding strongly coordinating electrolytes in high concentrations failed.

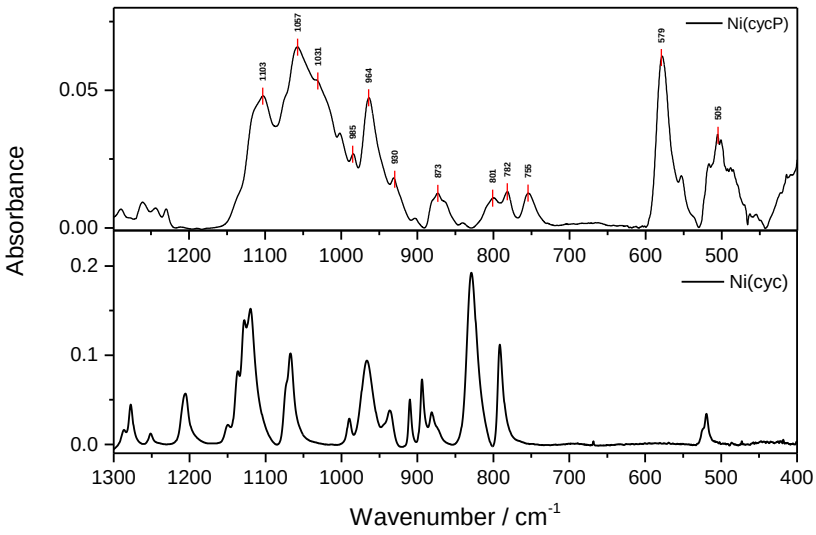

Figure 49 – ATR-FTIR spectrum of powder [Ni(cycP)]$_n$ (top) and the cyc (bottom).

The ATR-FTIR (Attenuated Total Reflectance Fourier Transform Infrared Spectroscopy) spectrum of the Ni(cycP) powder (Figure 49, shown with the ATR spectrum of cyc for reference) has been assigned on the basis of values found in literature for phosphonic acids in solution and coordinated to metal centres.[29–33] The sharp bands between 1300-1200 cm^{-1} are due to the P-C stretching modes.[34] The absence of a broad peak between 1200 and 1150 cm^{-1}, typical of P-O-H bonds, suggests the absence of hydroxyl groups, in agreement with the crystal structure. The peak at 1103 cm^{-1} is assigned to the ν(PO), while the peaks at 1057 and 1031 cm^{-1} are assigned to the ν_s(PO$_2$) and νa_s(PO$_2$), respectively. The narrow region of the spectrum where these modes appear indicate coordination of the phosphonate to the metal centre.[29] The bands at 982 and 970 cm^{-1} are assigned to the ν_{as}(P-O-Ni) and ν_s(P-O-Ni), respectively. Finally, the strong peaks at 579 and 505 cm^{-1} are assigned to the bending modes δ(PO) coordinated to the metal centre.[33]

In light of the strong pH dependence on catalysis shown by Ni(cycC) with respect to CO_2 reduction a pH titration was carried out to measure the pK_a of the phosphonic acid protons. A solution of the complex in water (0.05 M) has a pH of 7.74. The change in pH of the solution upon addition of small aliquots of concentrated acid (0.1 M HCl) was plotted *vs* the volume of acid added, Figure 50. The

two equivalence points are found at pH values of 6.7 and 3.2 and the half equivalence points will give the pK_a values. The first pK_a is thus calculated to be 4.95. The absence of a third equivalence point makes the calculation of the second pK_a less precise, however in these cases the pKa is calculated with the values of the first pK_a and the equivalence point, according to the relationship: $pH_{equivalence} = (pK_{a1} + pK_{a2})/2$.

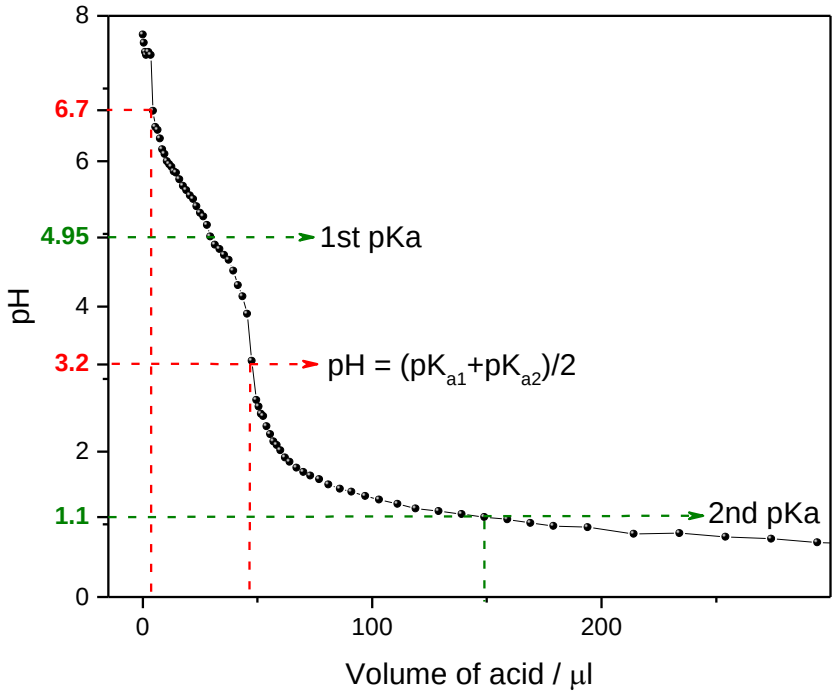

Figure 50 – pH titration for Ni(cycP), obtained by adding 0.1 M HCl to a 0.5 M solution of Ni(cycP) in water.

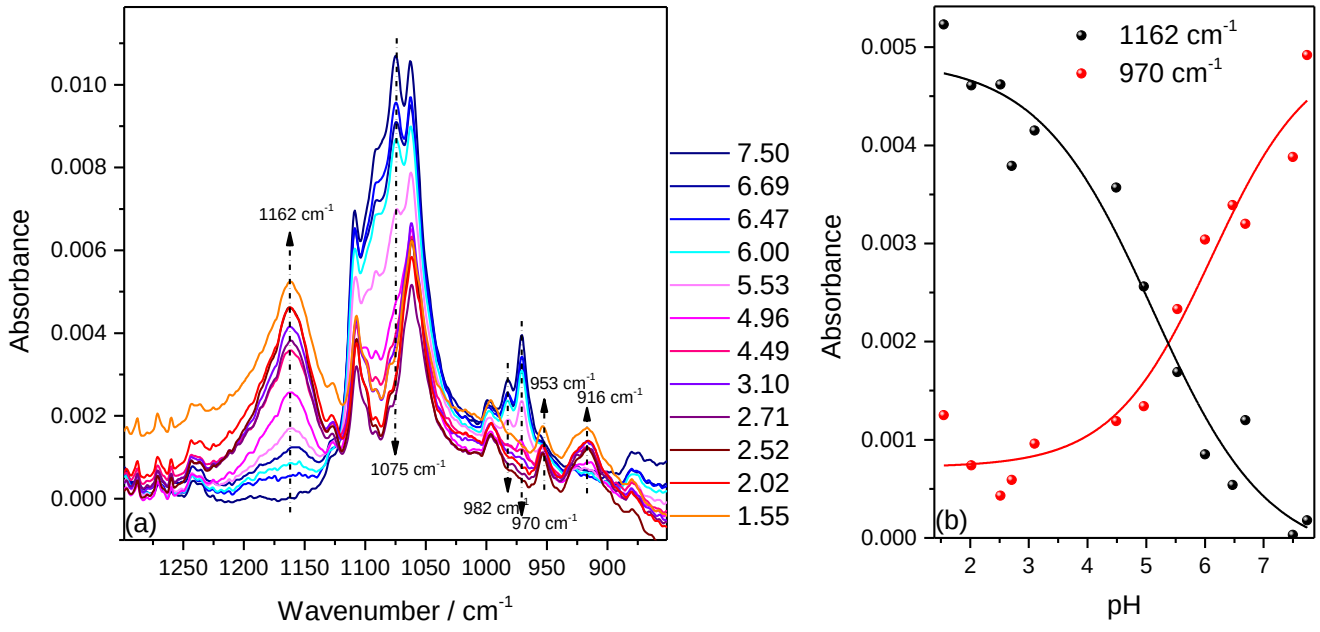

Figure 51 – (a) Variation in the ATR-FTIR spectrum of Ni(cycP) (0.1 M in H_2O) with decreasing pH, varied by additions of 0.1 M HCl. The change in the baseline is attributed to the change in concentration of the complex upon addition of acid. (b) Absorbance of peaks at 1162 cm^{-1} (P-O-H) and 970 cm^{-1} (P-O-Ni) vs. pH.

The IR spectrum of the complex, recorded using ATR-FTIR, in aqueous solution at the starting pH (7.74) shows the same features as the solid, Figure 51. The most evident change upon lowering the pH is the gradual appearance of a broad peak at 1162 cm^{-1}, assigned to a P-O-H mode, indicating that protonation is occurring. In addition to this, the peak at 1075 cm^{-1}, previously assigned to the $\nu_{as}(PO_3)$, disappears. The peaks corresponding to the ν_{as}(P-O-Ni) and ν_s(P-O-Ni) (982 and 970 cm^{-1}) are replaced by peaks at 916 and 953 cm^{-1}. The first is tentatively assigned to the ν_{as}(P-OH) of the newly protonated phosphonate, and the second to a shift in the P-O-Ni stretching mode due to protonation of the other oxygen. The first pK_a of the phosphonic acid was extrapolated by plotting the normalised intensity of the relevant peaks *vs.* the pH, (Figure 51(b)). At pH ~ 5 the plot shows an intersection point, indicating the value at which both species are present at the same concentration. The second pK_a could not be identified at the pH values examined, due to the restriction of the ATR accessory with regards to the pH stability. No change in the coordination geometry was found when the UV-vis dependence on the pH was investigated (Figure 52), indicating that either (a) when protonated the

PO_3H_2 group is able to act as a ligand to the Ni^{2+} centre, or (b) that H_3O^+ is a potential ligand for axial coordination to the Ni^{II} centre.

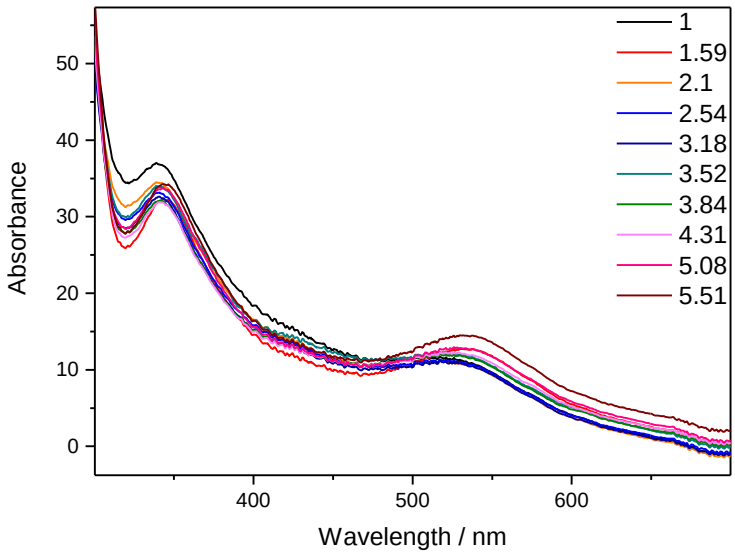

Figure 52 – UV-vis spectra at different pH values for a solution of Ni(cycP) (1 mM in water). The pH was varied by adding 1 M HCl.

3.2.2 CO_2 reduction by Ni(cycP) on mercury electrodes

As for Ni(cycC) the electrochemical properties of Ni(cycP) have been analysed on the HMDE (Hanging Mercury Drop Electrode) in aqueous solutions. Figure 53 shows the cyclic voltammograms (CVs) for the complex under argon and CO_2 on the HMDE, with the data compared to Ni(cyc) and Ni(cycC).

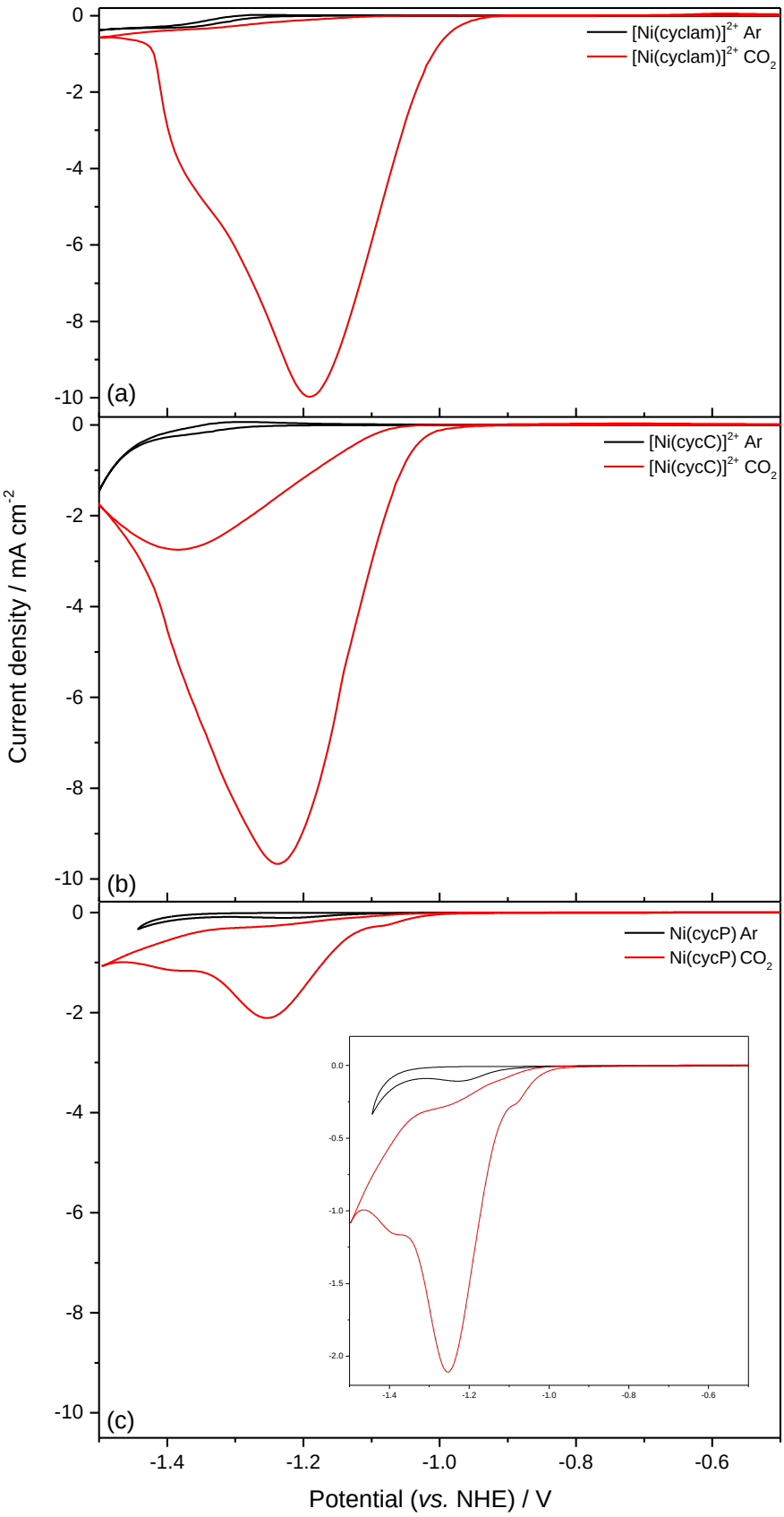

Figure 53 - CV of 1 mM solutions of (a) Ni(cyc), (b) Ni(cycC)and (c) Ni(cycP) recorded in 0.1 M $NaClO_4$ at pH 5 purged with either argon (black line) or CO_2 (red line) recorded at 100 mV s^{-1} using a HMDE electrode (0.023 cm^2). The inset in (c) shows an expansion of the CV in (c).

Under argon an irreversible wave with cathodic peak position E_{pc} = -1.23 V_{NHE} is assigned to the reduction of the Ni^{II} of Ni(cycP). This potential is *ca.* 100 mV more positive than what found for the $Ni^{II/I}$ couple in solution of Ni(cyc) and Ni(cycC). Past reports on N-functionalised nickel macrocycles have showed that the reduction potential is shifted anodically with increasing N-substitution (such as in the N-methylated complexes $[Ni(MMC)]^{2+}$, $[Ni(DMC)]^{2+}$, $[Ni(TRMC)]^{2+}$ and $[Ni(TMC)]^{2+}$), due to stabilisation of the Ni^{I}. The stabilisation effect has been assigned primarily to the effect of the N-alkylation on the solvation energies of the complexes; N-alkylation increases the radius of the complex due to the steric hindrance of the bulky methyl groups, thus decreasing the solvation energy and stabilising the larger Ni^{I} ion.[35,36] Nickel macrocycle complexes usually show reversible $Ni^{II/I}$ redox couples. Here, reversibility is lost even at high scan rates (2 V/s). This might indicate a very short-lived Ni^{I}(cycP), which following reduction undergoes a chemical step, similarly to what was found for a Ni(cyc) modified with four methylene-carboxylic acid groups bound to the amines.[35]

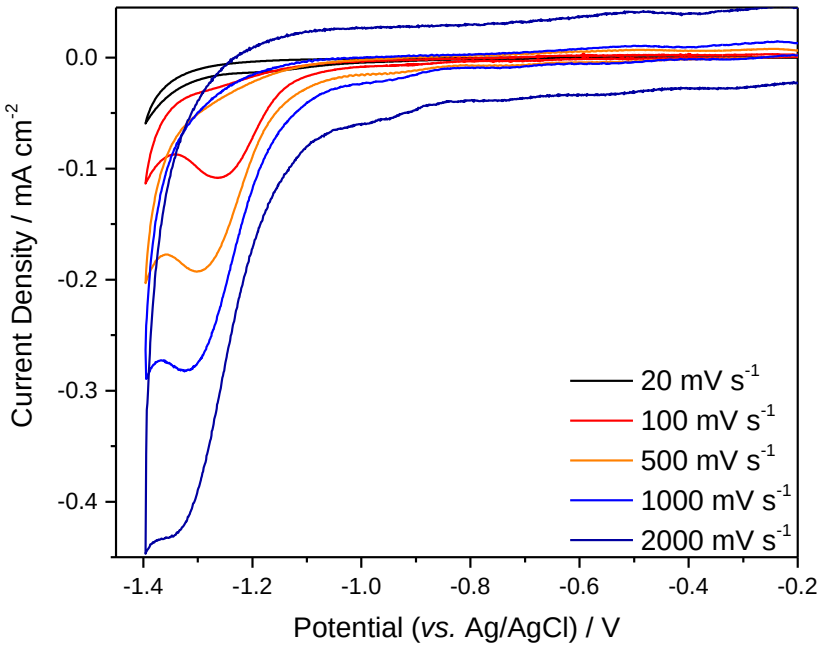

Figure 54 - CVs of 1 mM [Ni(cycP)] in Ar-purged H_2O containing 0.1 M $NaClO_4$ on a HMDE working electrode at increasing scan rates.

Under CO_2 the irreversible $Ni^{II/I}$ reduction of Ni(cycP) is shifted to more anodic potentials, and a large increase in current is observed, assigned to CO_2 reduction (Figure 53(c)). Under the same conditions the onset potential for catalysis is *ca.* 50 mV more cathodic than for Ni(cycC), and *ca.* 100 mV more cathodic than for Ni(cyc)**.** Furthermore, the catalytic current density is much lower (Ni(cycC): i_c/i_p ~ 48, Ni(cyc): i_c/i_p ~ 31, Ni(cycP): i_c/i_p ~ 19. This response is not surprising, considering past reports on modified macrocyclic complexes of Ni, which consistently show lower activities for CO_2 reduction than the parent Ni(cyc) on mercury electrodes.[13] The decrease in activity upon modification of the amines has been attributed in the past[37,38] to the decreased availability of the amine protons, which are thought to stabilise CO_2 binding (Scheme 23). Furthermore, the presence of bulky substituents on the macrocyclic nitrogen atoms causes steric hindrance to the axial site of the metal centre, thus preventing CO_2 binding.

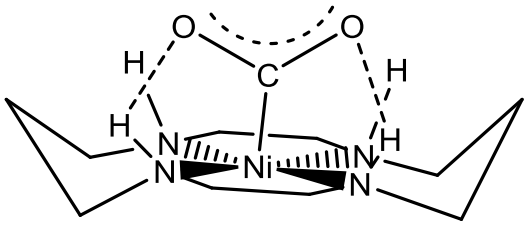

Scheme 23 – (a) Free amine protons on the cyclam backbone are proposed to stabilise the interaction between the CO_2 and the metal centre by hydrogen bonding.[15,37] Functionalisation of the amine group is anticipated to decrease the strength of the CO_2 interaction with the complex.

Controlled potential electrolysis (CPE) experiments show the selectivity is 1:1 CO:H_2. Furthermore, the charge passed in five hours is only slightly higher than the charge passed by Ni(cyc) in one hour, in agreement with the lower current observed in the CVs.

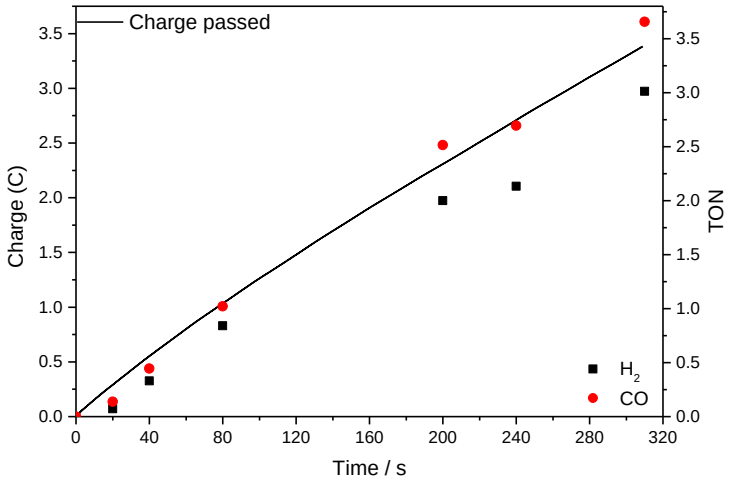

Figure 55 - CPE of a 1 x 10^{-4} M solution of Ni(cycP) containing 0.1 M $NaClO_4$, pH 5 (black line), yield of H_2 (black squares) and CO (red circles) expressed in turnover numbers. The potential was kept at -1.2 V_{NHE} for 5 hours using an Au-Hg amalgam electrode.

The FTIR titration in Figure 51 showed some interesting results regarding the protonation of the phosphonic acid moiety; the possibility of a similar catalytic enhancement to what has been found for Ni(cycC) due to the presence of labile protons led us to carry out a pH study under CO_2 (Figure 56).

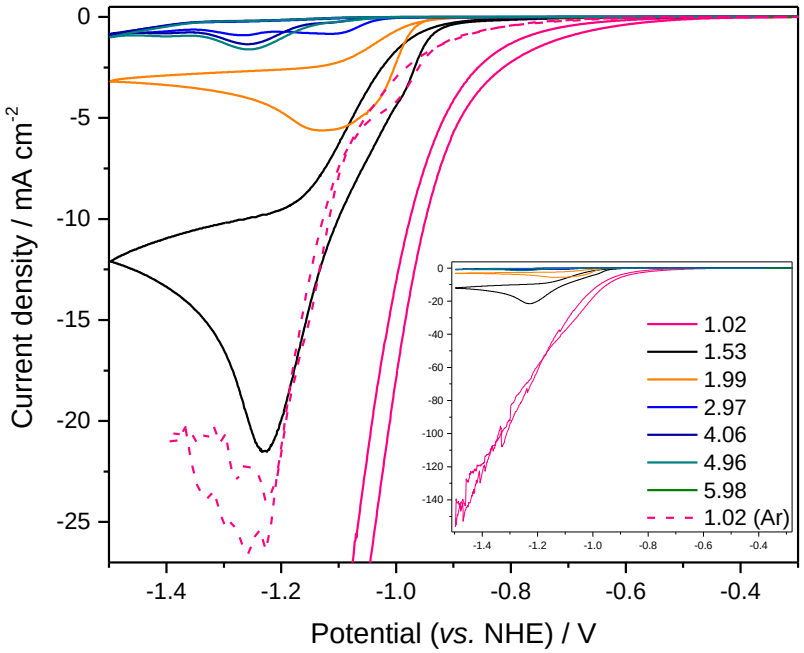

Figure 56 - CVs of 1mM Ni(cycP) at a range of pH values under CO_2, recorded in 0.1 M $NaClO_4$, scan rate 100 mVs^{-1}. The inset shows an expansion of the CV. The noise at high current densities is due to large bubbles forming on the surface of the mercury drop.

The CVs showed a similar behaviour of Ni(cycP) compared to Ni(cycC); the current density remained low for pH values > 3. No change in the CV was noted for values on either side of the first pK_a. At pH 3 a new curve was observed at -1.1 V_{NHE}. At pH 2, a large increase in current density and shift in onset potential to more positive values (*ca.* 200 mV) was observed. At this value, the current density was comparable to the values obtained by Ni(cyc) and Ni(cycC) at pH 5. While the current density for Ni(cycC) started to plateau at pH ≤ 2, here the current density continued to increase. At pH 1.5 the current density at -1 V_{NHE} reached the same value observed for Ni(cycC) at the same potential at pH 2, and at pH 1 (lower than the value of the second pK_a) the current is more than triple compared to pH 1.5. This result was encouraging, as the same trend of increased current with protonation state of the acidic moiety found for Ni(cyc) was observed for this complex. A series of CPE experiments were carried out at both pH = 1.5 and pH = 1 (Table 11) and at different potentials under CO_2, however mainly hydrogen was detected, with very small amounts of CO. We note however that due to the high current densities under CO_2, and the static nature of our CPE experiments, it is possible that the CO_2 present locally is being consumed within the first few minutes of the bulk electrolysis, after which proton reduction would dominate due to the high concentration of protons at pH = 1.

Table 11 – CPE experiments for 1 mM solutions of Ni(cycP), using 0.1 M $NaClO_4$ as the supporting electrolyte, Au-Hg amalgam working electrode. The potential was kept at the indicated pH value for 30 mins.

Experiment *vs.* NHE	**moles H_2**	**moles CO**	**Charge (C)**	**Moles e^-**	**Selectivity H_2:CO**
pH 1 -0.9 V	3.3×10^{-6}	3.1×10^{-9}	1.18	1.2×10^{-5}	1100:1
pH 1 -0.95 V	5.2×10^{-6}	1.5×10^{-8}	2.4	2.5×10^{-5}	323:1
pH 1 -1.1 V	6.8×10^{-5}	1.1×10^{-7}	25	2.6×10^{-4}	662:1
pH 1.5 -1.0 V	1.1×10^{-5}	8.9×10^{-8}	2.5	2.6×10^{-5}	133:1
pH 5 -1.2 V	4.63×10^{-7}	6.23×10^{-7}	0.55	5.7×10^{-6}	1:1

The adsorption of the complex on the mercury surface has been analysed, much like for Ni(cycC). It has been reported that differently substituted Ni(cyc) complexes have different adsorption behaviour, and it has been suggested that this difference is partly the cause of the differences in catalytic activity.[14] The dependence of the surface coverage with the potential has been measured using DPSC (Double Potential-Step Chronocoulometry) (Figure 57), with the method described in section 2.2.4.

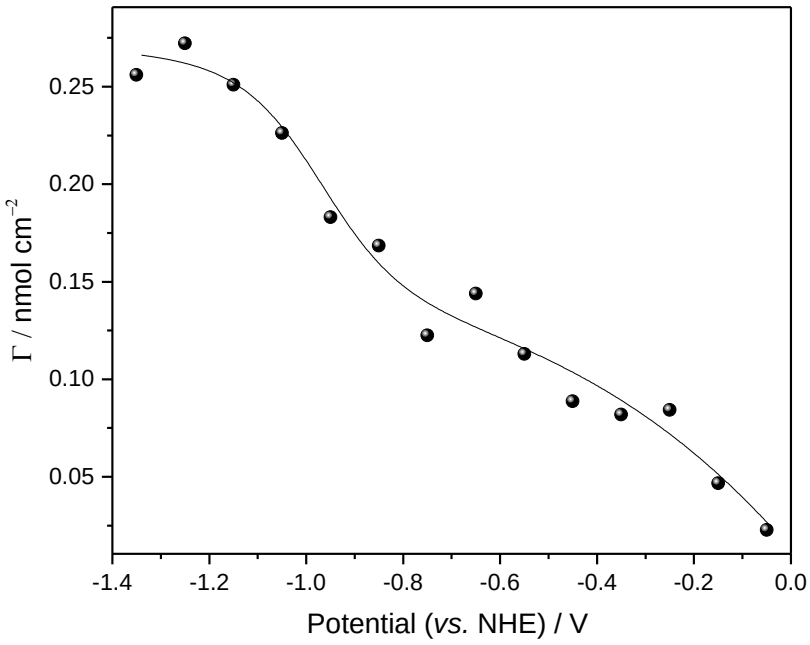

Figure 57 - Dependence of the surface coverage of Ni(cycP) with the potential for 0.1 mM solutions of catalyst, 0.1 M $NaClO_4$, pH 5. The potential was referenced using the $Ni^{II/I}$ couple as an internal standard.

The data points to an adsorption profile very similar to that of Ni(cyc). This is in contrast with past reports of N-methylated Ni(cyc) complexes such as in Figure 44, which showed adsorption on the electrode surface only at potentials close to and negative of the $Ni^{II/I}$ reduction potential (Figure 44).[13–15] This behaviour was believed to be caused by two main factors, (a) the steric hindrance of the methyl groups interfering with a close interaction of the nickel centre with the mercury surface and (b) the hindered interconversion between conformational isomers, which requires deprotonation of the amines in the cyclam ring[39,40]. Here it is hypothesised that (a) the phosphonate is bound to one of the nickel axial sites, leaving the other site free to interact with the electrode surface without any major

steric effect and (b) interconversion may still be allowed by the availability of the remaining free nitrogens to deprotonate. Given the low Faradaic efficiencies (FEs) obtained by bulk electrolysis at low pHs the adsorption mechanism was not investigated further.

From the electrochemical data presented above, it is apparent that the new modified complex is a poor catalyst for CO_2 reduction in solution. A complete kinetic analysis using RDE (Rotating Disc Voltammetry) was deemed unnecessary considering the small activity shown by Ni(cycP); the rate constant has been calculated by using the Tafel analysis method, as outlined in section 2.2.4 of Chapter 2. A k_{obs} calculated through the Tafel analysis (Figure 58) for the pH = 5 solution, using equation (1) in the previous chapter and the values for the surface coverage obtained through DPSC analysis, gives a value of 0.45 s^{-1} at -1 V_{NHE} (η = 0.6 V), one order of magnitude lower than that obtained for the other two complexes studied. However we note that at this overpotential the linear sweep is still in the region of the prewave, and therefore cannot be strictly considered a linear region of the plot. A k_{obs} calculated at the potential where CPE was carried out (-1.2 V_{NHE}, η = 0.8 V) gives a value of 11.5 s^{-1}. A Tafel analysis at lower pH values was not carried out on the account of the poor selectivity shown by the complex.

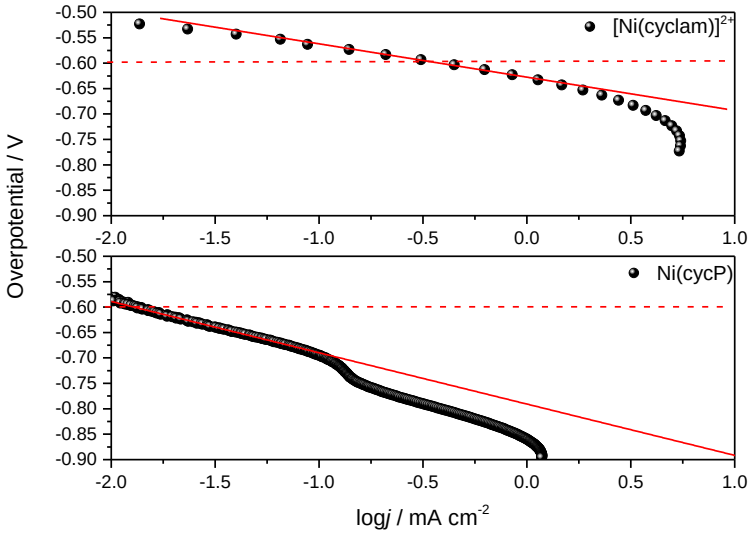

Figure 58 - Plots of CO_2 reduction overpotential (pH = 5) vs. log of current density for Ni(cyc) and Ni(cycP) at pH 5 Calculated from LSVs at 100 mV s^{-1} in 0.1 M $NaClO_4$ electrolyte containing 1 x 10^{-4} M catalyst.

The poor performances displayed by Ni(cycP) (low selectivities and yields of CO in all the conditions studied) are most likely a result of the geometric structure of the complex. As shown by the chronocoulometry experiment, adsorption on mercury is however not hindered by the new functional group; we speculate that this could be due to the phosphonic acid occupying one of the axial sites, leaving the other free to interact with the electrode. If this was to be the case, then the nickel centre would be extremely hindered by the presence of the mercury on one side and the bulky phosphonic acid on the other, limiting CO_2 binding.

In the next section we will explore the binding of Ni(cycP) on TiO_2 surfaces in order to test the stability of the new binding group. It was envisaged that the interaction of the phosphonic acid with the semiconductor surface might weaken the bond with the nickel centre and improve the catalytic activity of the complex towards CO_2 reduction.

3.2.3 Immobilisation of Ni(cycP) on semiconductor oxides

The behaviour of the complex when immobilised on semiconductor surfaces was examined by anchoring the catalyst on nc-TiO_2 films and carrying out electrochemical and TAS measurements. The complex was immobilised by dipping the films in ethanolic solutions of the complex (1 mM) for 48 hours, followed by rinsing and drying (see section 3.3.1 for experimental details). The UV-vis of the soaking solutions proved to be uninformative for verifying the presence of the complex on the semiconductor surface on the account of the very low extinction coefficients for the complex in solution ($\varepsilon_{533\ nm}$ = 12 $M^{-1}cm^{-1}$). ATR-FTIR spectroscopy of the modified TiO_2 powder revealed the characteristic phosphonate bands at 1200-1000 cm^{-1} (Figure 59).

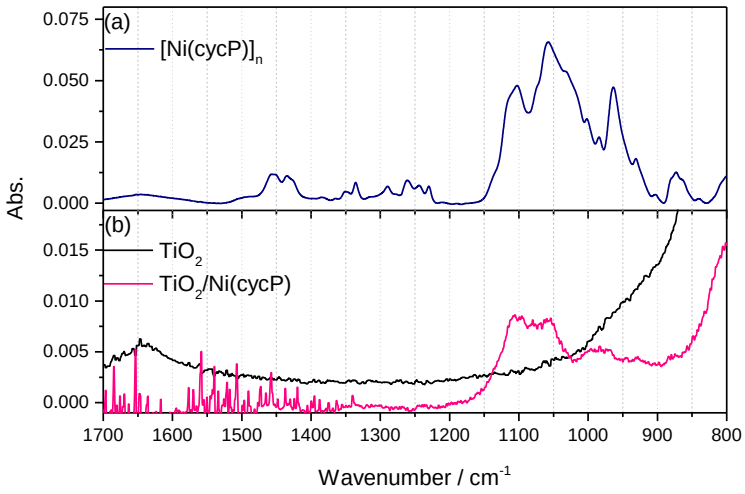

Figure 59 - a) ATR-FTIR spectrum of powder $[Ni(cycP)]_n$ and (b) ATR-FTIR spectrum of blank TiO_2 (black) and TiO_2 soaked in 0.1 mM Ni(cycP) in ethanol for 48 hours (pink).

The interpretation of the spectrum is made difficult by the broadness of the peaks (likely indicating a mixture of different binding modes on the TiO_2 surface) and the strong absorption of TiO_2 close to the region of interest, however it is notable that the strong band at 963 cm^{-1} present in the powder ATR-FTIR spectrum, and previously assigned to a Ni-O-P stretching mode, is absent in the TiO_2-catalyst system, possibly indicating that the phosphonic acid is no longer coordinating to the nickel centre. Intriguingly, we did not observe any clear spectral feature that can be assigned to the formation of a P-O-H mode (*ca.* 1150 cm^{-1}).[31]

The films were used as the working electrode in acetonitrile (MeCN) solutions using $TBAPF_6$ (tetrabutyl ammonium hexafluorophosphate) as the supporting electrolyte. The CV at 10 mVs^{-1} is shown in Figure 60, together with the integration, to give the charge passed, and the differentiation of the current/voltage plot, to aid identification of redox features.

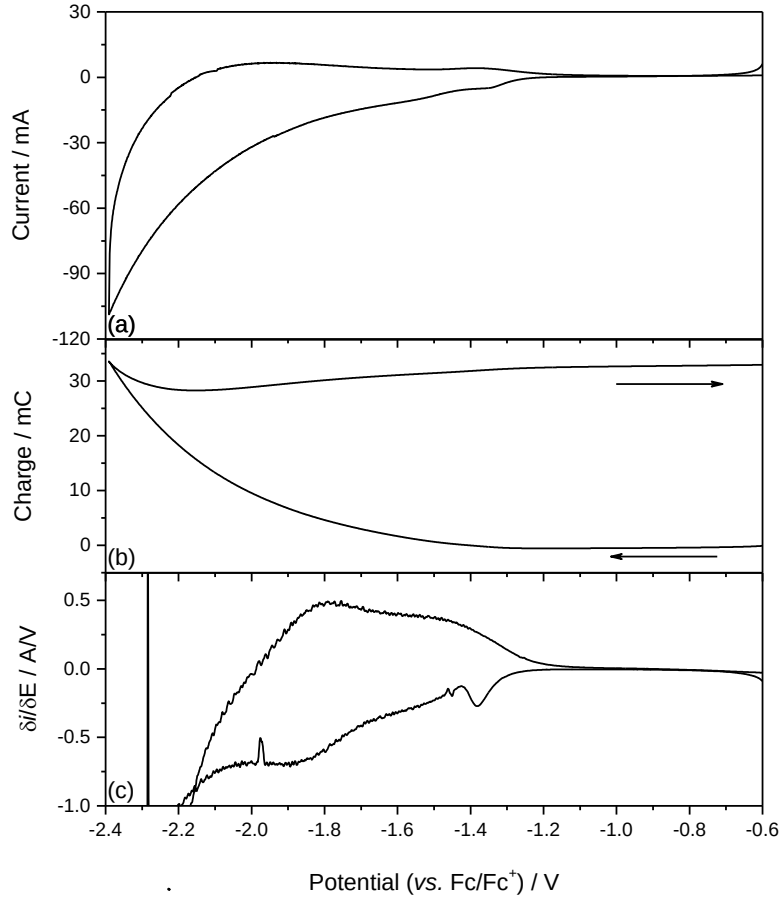

Figure 60 - (a) CV of nc-TiO_2-Ni(cycP)(10 mVs^{-1}, 0.1 M $TBAPF_6$ in MeCN), (b) Charge vs. Potential plot, obtained by integrating the CV and (c) 1st order derivative of the current for the CV in (a).

The shape of the voltammogram, which is missing the distinctive discharge wave typical of bare TiO_2 electrodes, is a first indication that there is one other electrochemical process apart from the capacitive behaviour of a unmodified TiO_2 film, see section 2.2.6.2. This is confirmed by integrating the CV; the charge *vs.* potential plot indeed shows that only part of the charge injected in the electrode is transferred back in the reverse sweep. If the only process on the CV was the injection of electrons in the conduction band of the TiO_2 electrode, then this process would be entirely reversible and the total charge passed during a CV measurement would be zero. Although the CV does not show a distinguishable redox process, the 1st order derivative of the current reveals the presence of a feature at -1.85 $V_{Fc/Fc+}$ (*ca.* -1.25 V_{NHE}) which is assigned to the $Ni^{II/I}$ couple, based on the similar reduction

potential observed for the complex in solution. The small response obtained, compared to the very clear redox couple observed for Ni(cycC) on the same electrode (see Chapter 2), is surprising, as it was anticipated from the CVs of the complex in solution under argon that the alignment of the TiO_2 conduction band in MeCN with the $Ni^{II/I}$ couple of Ni(cycP) would enable electron transfer. The efficiency of electron transfer from semiconductor to metal complexes, and the differences between different binding groups to the surface have been widely studied.[3–5] When comparing carboxylic acids to phosphonic acids it has been generally reported that while the latter offer a much higher stability on the surface of the metal oxide, and faster uptake, the electron transfer is slowed, compared to carboxylic acids,[3–5] which allow electronic coupling between the dye and semiconductor (Scheme 18). It is envisaged that the phosphonic acid moiety on the nickel complex hinders electron transfer from the TiO_2 electrode to the catalyst, giving rise to the small response obtained in the CV of a TiO_2/Ni(cycP) electrode. A more in-depth investigation of the electron transfer kinetics has been carried out using Transient Absorption Spectroscopy (TAS) of the modified films (Figure 61), by monitoring the decay of the photoelectrons at 900 nm.

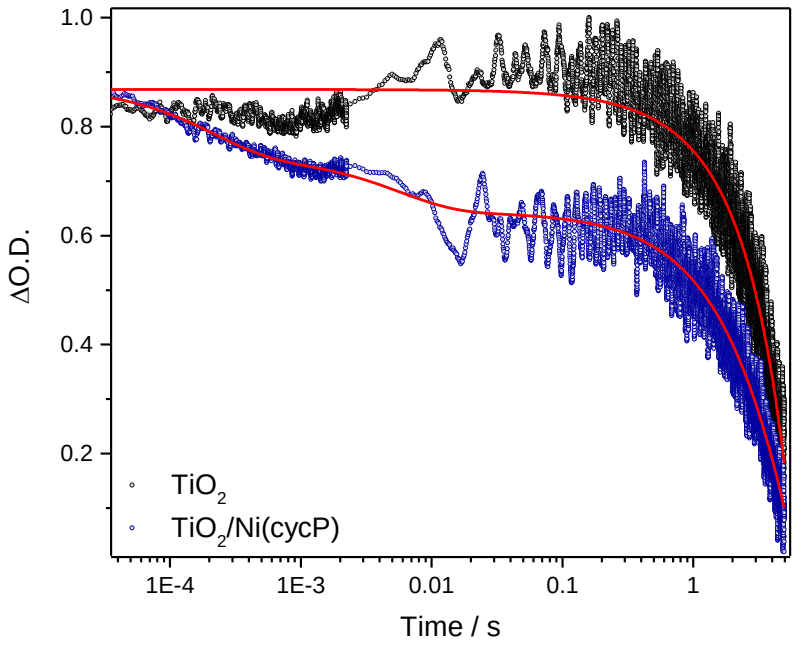

Figure 61 - Transient absorption decays of unmodified TiO_2 (black) and TiO_2/Ni(cycP) (blue), measured in MeCN with 0.1 M TEOA, Ar.

As expected, the unmodified TiO_2 in MeCN with 0.1 M TEOA (Triethanolamine) under argon shows a long-lived signal at 900 nm, following band gap excitation of the TiO_2 (355 nm). This is due to the presence of the hole scavenger, yielding long lived photoelectrons. The experimental trace at 900 nm is well fitted to a single exponential decay function with a lifetime τ = 10.00 ± 0.24 s, Figure 61. When the catalyst is immobilised on the surface, a faster decay is observed, showing that electron transfer is occurring from the TiO_2 conduction band to Ni(cycP). The data is fitted to a tri-exponential function, characterised by a fast component ($\tau_1 = 2.07 \times 10^{-4} \pm 2.1 \times 10^{-5}$ s), a millisecond component ($\tau_2 = 5.6 \times 10^{-3} \pm 4 \times 10^{-4}$ s) and a slow component (τ_3 = 13.5 ± 0.4 s). We assign the two faster components to electron transfer of photoelectrons in the TiO_2 conduction band to the anchored Ni(cycP), with the slower component being the recombination of the non-transferred electrons with residual species in solution, such as O_2 or $TEOA^{+\cdot}$, formed through reaction of TEOA with the photogenerated holes. In line with what was previously observed for phosphonic acid anchoring groups, and with the dark electrochemistry, the electron transfer is much slower than that observed for the carboxylic acid system TiO_2/Ni(cycC) (section 2.2.63), with a $\tau_1 = 1.73 \times 10^{-3}$ s. Interestingly, the observation of two different lifetimes for charge transfer from the TiO_2 conduction band to Ni(cycP) is in line with the FTIR studies which showed broad IR bands, indicating multiple Ni(cycP) binding modes (Figure 59).

The electrochemical behaviour of the complex when immobilised on ZrO_2 electrodes was also investigated, Figure 63. Nanocrystalline ZrO_2 films (Ø ~ 10-30 nm) were modified with Ni(cycP) by dipping the films in ethanolic solutions of the complex (10 mM) for 48 hours, followed by rinsing with ethanol and drying (see section 3.3.1 for full experimental details). The ATR-FTIR spectra of the ZrO_2 powder modified with Ni(cycP) are shown in Figure 62.

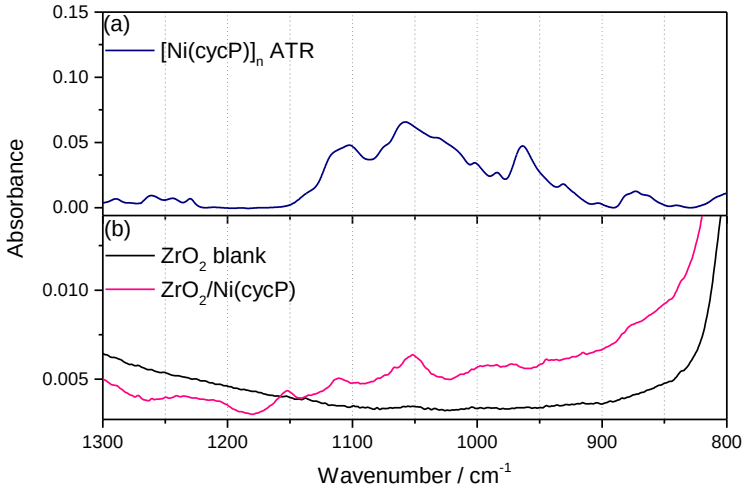

Figure 62 – (a) ATR-FTIR spectrum of powder $[Ni(cycP)]_n$ and (b) ATR-FTIR spectrum of blank ZrO_2 (black) and ZrO_2 soaked in 0.1 mM Ni(cycP)in ethanol for 48 hours.

Interestingly, the IR spectrum of Ni(cycP) bound to ZrO_2 showed a different phosphonate region with respect to the modified TiO_2 nanoparticles. The disappearance of the sharp peak at 963 cm^{-1} upon immobilisation on ZrO_2, previously assigned to a Ni-O-P stretching mode, would indicate at least partial de-coordination of the phosphonate group from the nickel centre, in a similar manner to TiO_2/Ni(cycP), however the appearance of a peak at 1152 cm^{-1}, the region where P-O-H modes usually appear, is also noted, indicating a different binding mode of the phosphonate to the ZrO_2 with respect to TiO_2. The CVs of an unmodified ZrO_2 electrode in MeCN with 10% water under argon (Figure 63) showed a current onsetting at *ca.* -0.8 V_{NHE}. This is attributed to proton reduction by the ZrO_2 film. The presence of a reductive current at potentials *ca.* 0.5 V positive of the conduction band edge (*ca.* -1.2 V_{NHE}[41]) indicates the presence of accessible trap states, in line with past reports,[41] which make the film non-insulating at these potentials. In contrast to our findings on TiO_2 electrodes, the cyclic voltammetry of modified ZrO_2 electrodes showed the appearance of a clear reduction feature under argon at *ca.* -0.9 $V_{NHE,}$ which was not present in the unmodified ZrO_2 and this is assigned to the $Ni^{II/I}$ redox couple. The potential for the reduction wave shifted to -0.8 V_{NHE} under CO_2 (Figure 63). The presence of the complex on the voltammogram under CO_2 shows the validity of modifying

the cyclam framework with a phosphonic acid moiety, as the nickel complex clearly shows a higher stability on semiconductor surfaces than shown by Ni(cycC) in Chapter 2.

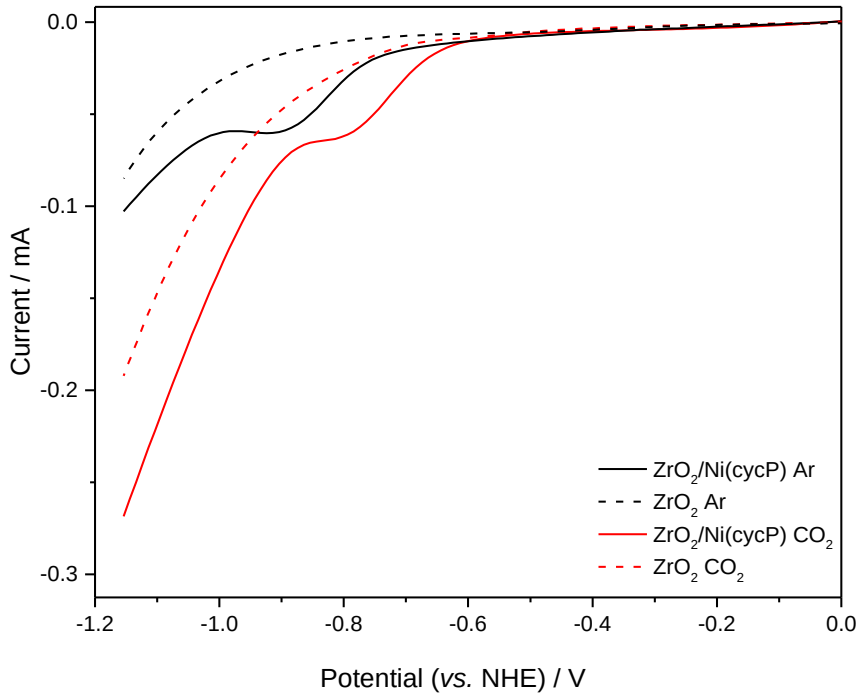

Figure 63 – Linear sweep voltammetry of ZrO_2 electrodes (dashed lines) and ZrO_2/Ni(cycP) electrodes (solid lines) under argon (black) and CO_2 (red), MeCN:H_2O 9:1, 0.1 M $TBAPF_6$, scan rate = 100 mV s^{-1}.

We note that the potential for the nickel reduction here is shifted anodically compared to what observed on the HMDE (E_{pc} = -1.23 V_{NHE}) for the $Ni^{II/I}$ couple in solution and on TiO_2 (E_{pc} = *ca.* -1.25 V_{NHE}), but is in line with the potentials at which the Ni^{II} reduction occurs on a mercury surface. We propose that the reduction potential of the nickel metal centre for Ni(cycP) is strongly dependent on the interaction of the complex with the electrode material. It is apparent that the differences in the FTIR spectra between ZrO_2/Ni(cycP) and TiO_2/Ni(cycP) correlate with the differences in the electrochemical behaviour, leading to the conclusion that on ZrO_2 the binding mode of the phosphonate on ZrO_2 is more favourable to electron transfer than in the case of the TiO_2.

3.2.4 Conclusions

With the aim of finding a stable binding group for anchoring to semiconductor surfaces in aqueous solvents, the cyclam ligand was modified with an alkyl phosphonic acid group at an amine position, yielding the ligand cycP. Its complex with nickel was synthesised for the first time, and it was found that unlike the previously studied (Ni(cycC) the new complex Ni(cycP) in solution is present solely in its octahedral high-spin geometry.

The properties of Ni(cycP) with respect to the electrochemical reduction of CO_2 in aqueous solutions have been investigated on a mercury electrode. The complex shows some activity towards the reduction of CO_2 to CO, however the current densities are low, and the selectivity for CO poor (1.2:1 CO:H_2). This decrease in activity compared to the other nickel macrocycles is likely due to the functionalisation of one of the amines, which has been previously shown to affect catalysis in a negative way. Furthermore, even though the new catalyst shows a similar dependence of the current density with the pH to Ni(cycC), bulk electrolysis experiments revealed the increase to be caused by increasing amounts of hydrogen being produced.

The immobilisation of the complex on TiO_2 electrodes coupled with TAS experiments showed that the new binding group slowed electron transfer from the conduction band of the TiO_2 to the complex when compared to Ni(cycC). This is in line with past reports for various complexes modified with binding groups, which consistently show slower electron transfer when the complex is modified with a phosphonic acid rather than a carboxylic acid.[3–5] Interestingly, the electron transfer has been found to be controlled by the different interaction of Ni(cycP) with different electrode materials: when immobilised on ZrO_2 the $Ni^{II/I}$ redox couple appears notably shifted towards anodic potentials. Furthermore, the redox couple appears to be stable under CO_2 as well as under argon, in the presence of MeCN doped with water, demonstrating that the intended higher stability was achieved.

In the next chapter the properties of Ni(cycP) towards the photocatalytic CO_2 reduction in aqueous environments will be shown, exploring two different ways of driving the reduction of the catalyst

with either a ruthenium dye, which was co-immobilised with the catalyst on an inert support, or by immobilising Ni(cycP) onto semiconductor quantum dots.

3.3 Materials and methods

3.3.1 Materials

The starting materials and solvents for the synthesis were purchased by Sigma Aldrich, Fisher Scientific or VWR, and used without further purification unless otherwise specified. Milli-Q water (18.2 MΩ) was used throughout. All electrolyte salts and solvents were purchased from Sigma Aldrich or VWR and used without further purification. Ar, N_2 and CO_2 were purchased from BOC at CP or higher grade. The pH of aqueous solutions was adjusted by adding 1 M $HClO_4$ or NaOH to the pre-purged solution until the desired value was reached, measuring with a Hannah pH probe, which was calibrated daily.

Tri-trifluoroacetate cyclam (2)

In a 100 ml round-bottomed flask equipped with a magnetic stirring bar cyclam (2 g, 1 eq.) is dissolved, under an Ar atmosphere, in 15 ml of dry methanol, and the temperature is brought to 0°C by means of an ice bath. Triethylamine (0.6 ml, 1 eq.) and ethyl trifluoroacetate (4.0 ml, 3.3 eq.) are added, and the mixture is stirred for five hours at room temperature. The solvent is evaporated to dryness, and the crude is purified *via* flash column chromatography (silica gel) using EtOAC as the eluent. The fractions containing the product are combined, and the solvent is removed, affording a white foam. Obtained: 4.6 g, yield 94%. ***m/z*** **(ESI):** 489 $(M+H)^+$, 511 $(M+Na)^+$; **^{1}H NMR** (400 MHz, CHLOROFORM-*d*) δ ppm 1.64 - 1.86 (m, 2 H) 2.03 - 2.16 (m, 1 H) 2.52 - 2.69 (m, 2 H) 2.80 - 2.93 (m, 2 H) 3.34 - 3.78 (m, 12 H); **^{13}C NMR** (101 MHz, CHLOROFORM-*d*) δ ppm 25, 32, 42, 54, 114, 116, 117, 119, 155, 161.

cycP - [(1,4,8,11-tetraazacyclotetradecan-1-yl)methyl]phosphonic acid (5)

In a 50 ml round-bottomed flask equipped with a magnetic stirring bar, compound **2** (700 mg, 1 eq.) is dissolved in triethyl phosphite (2.5 ml), and paraformaldehyde (170 mg, 4 eq.) is added. The mixture is heated at 40°C for three days. The mixture is then allowed to cool to room temperature

and the solvent is removed by repeated co-distillation with toluene. The crude colourless oil is dissolved in 15 ml of 6 M HCl in water and refluxed for three days. The mixture is allowed to cool to room temperature, and the solvent is removed by co-distillation with water. The yellow oil is dissolved in the minimum amount of water and loaded on a freshly activated Dowex® resin (50W, H^+, strongly acidic) column. The non-macrocyclic impurities are eluted with water to pH neutral, and the product is collected by washing the resin with a 6 M HCl aqueous solution. The fractions containing the product **5** are combined, and the solvent is evaporated. Pale yellow vitreous solid; obtained: 172 mg (yield = 41%); ***m/z*** **(ESI):** 295 $(M+H)^+$; **^{1}H NMR** (400 MHz, DEUTERIUM OXIDE) δ ppm 3.64 – 3.45 (m, 6H), 3.38 – 3.29 (m, 4H), 3.27 (t, *J* = 5.8 Hz, 2H), 3.07 – 2.97 (m, 2H), 2.83 – 2.73 (m, 4H), 2.21 (td, *J* = 12.1, 6.9 Hz, 2H), 2.05 – 1.93 (m, 2H); **^{31}P NMR** (162 MHz, DEUTERIUM OXIDE) δ ppm 20.59; **^{13}C NMR** (101 MHz, DEUTERIUM OXIDE) δ ppm 19.82 (s, 1 C) 19.94 (s, 1 C) 38.63 (s, 1 C) 38.84 (s, 1 C) 39.63 (s, 1 C) 39.78 (s, 1 C) 41.87 (s, 1 C) 42.33 (s, 1 C) 42.53 (s, 1 C) 48.87 (s, 1 C) 52.03 (br. s., 1 C).

$[Ni(cycP)]_n$ - $[Ni([(1,4,8,11\text{-tetraazacyclotetradecan-1-yl})methyl]phosphonic\ acid)]_n$ (6)

In a 50 ml round-bottomed flask equipped with a magnetic stirring bar the ligand **5** (733 mg, 1.1 eq., calculated considering 4 molecules of HCl in the salt) is dissolved in water. Sodium bicarbonate (850 mg, 6 eq.) is added. Gas is evolved. $NiCl_2 \cdot 6H_2O$ (440 mg, 1 eq.) is added. The solution changes colour from green to purple within the first 15 minutes and it becomes cloudy after 30 minutes. The mixture is left stirring at room temperature for three hours. The precipitate is filtered off, and the solvent is rotary evaporated to dryness. The remaining lilac powder is dissolved in methanol, the undissolved solid is filtered off and the solvent is evaporated. Product **6** is then purified by loading the crude on a silica gel column and eluting with a MeOH:NH_3 9:1 mixture as the mobile phase. Lilac crystalline powder; obtained: 267 mg, yield = 35%; $C_{11}H_{25}N_4NiO_3P \cdot 0.3H_2O$ (350.1): calcd. N 15.72, H 7.24, C 37.07; found N 15.46, H 7.46, C 37.32; ***m/z*** **(ESI):** 351.1 $(M+H)^+$; 373.1 $(M+Na)^+$; ATR-FTIR (ν,

cm^{-1}): 3384 (br.), 3146 (br.), 2914, 2840, 1651, 1459, 1454, 1436, 1102 (st.), 1055 (v.st.), 967 (st.), 874.

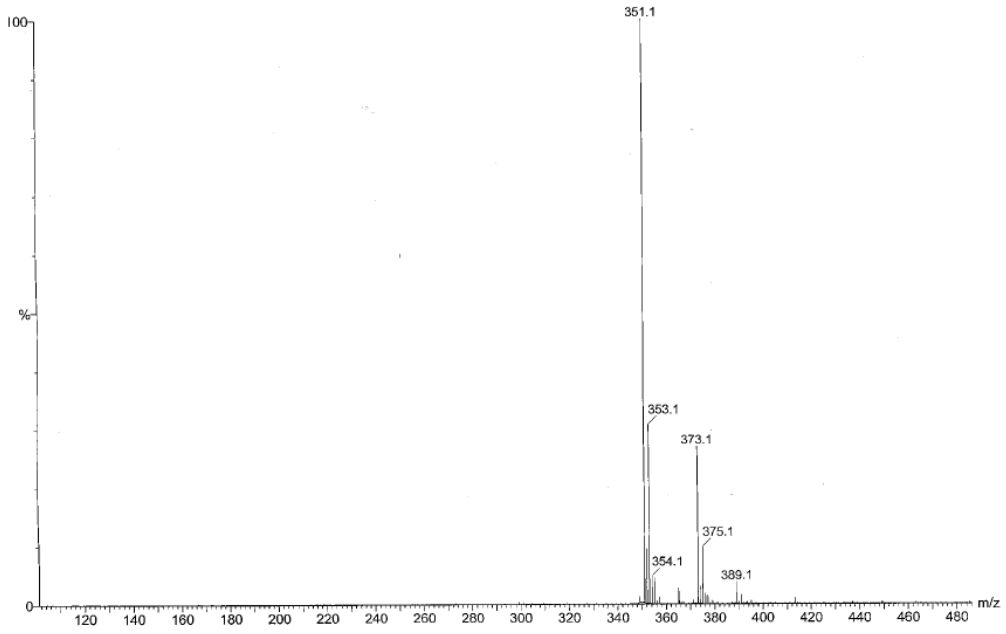

Figure 64 – ESI-MS spectrum of a Ni(cycP) in methanol.

Table 12 - Crystal data and structure refinement for[Ni(cycP)]$_n$.

Empirical formula	$C_{22}H_{54}N_8Ni_2O_{10.01}P_2$
Formula weight	770.25
Temperature/K	100
Crystal system	triclinic
Space group	P-1
a/Å	10.3977(3)
b/Å	14.1488(4)
c/Å	22.4532(7)
α/°	90.0930(10)
β/°	90.5310(11)
γ/°	90.0970(10)
Volume/$Å^3$	3303.05(17)
Z	4
$\rho_{calc}g/cm^3$	1.549
μ/mm^{-1}	1.299
F(000)	1632
Crystal size/mm^3	0.198 × 0.092 × 0.054

Radiation	MoKα (λ = 0.71073)
2Θ range for data collection/°	4.628 to 52.744
Index ranges	$-12 \leq h \leq 12$, $-17 \leq k \leq 17$, $-28 \leq l \leq 28$
Reflections collected	137618
Independent reflections	13486 [R_{int} = 0.0826, R_{sigma} = 0.0419]
Data/restraints/parameters	13486/289/805
Goodness-of-fit on F^2	1.116
Final R indexes [I>=2σ (I)]	R_1 = 0.0640, wR_2 = 0.1399
Final R indexes [all data]	R_1 = 0.0762, wR_2 = 0.1443
Largest diff. peak/hole / e $Å^{-3}$	1.03/-0.64

Table 13 - Fractional Atomic Coordinates (×104) and Equivalent Isotropic Displacement Parameters (Å2×103) for [Ni(cycP)]$_n$. Ueq is defined as 1/3 of of the trace of the orthogonalised UIJ tensor.

Atom	x	y	z	U(eq)
Ni3	6420.6(6)	7853.0(4)	3602.5(3)	10.84(13)
Ni4	3778.4(6)	7711.6(4)	1002.6(3)	11.40(14)
Ni2	8729.1(6)	7310.5(4)	6015.0(3)	11.81(14)
P4	3600.8(12)	7296.1(9)	-317.3(5)	13.0(3)
P2	8472.8(12)	7828.3(9)	4717.5(5)	13.9(3)
P3	5077.7(12)	8154.4(9)	2398.9(5)	14.3(3)
P1	10107.0(13)	6925.9(10)	7406.8(6)	17.0(3)
O5	7679(3)	8342(2)	4250.1(15)	16.9(7)
O4	7665(3)	7385(2)	5209.0(14)	13.4(7)
O10	2728(3)	7565(2)	204.8(14)	13.4(7)
O7	5185(3)	7422(2)	2896.8(15)	17.4(7)
O6	9415(4)	7136(3)	4458.1(15)	20.9(8)
O11	2893(3)	6734(2)	-794.9(15)	16.2(7)
O8	4852(3)	7723(3)	1792.5(15)	19.5(8)
O9	4138(4)	8947(3)	2543.5(16)	22.5(8)
O1	10077(3)	7587(3)	7951.6(15)	18.8(8)
O12	4327(3)	8149(3)	-562.2(15)	19.5(8)
O2	9393(4)	6010(3)	7519.8(17)	25.6(9)
O3	9728(4)	7398(3)	6829.1(16)	22.7(8)
O20	4135(4)	5616(3)	2549(2)	32.2(10)
O15	6346(4)	9158(3)	7604.9(18)	29.2(9)
N10	7396(4)	8677(3)	2957.9(18)	17.6(9)
O19	11509(4)	5770(3)	2696(2)	37.9(11)
O14	6947(5)	6258(3)	8036(2)	38.6(11)
O13	6353(4)	8060(3)	8648.2(18)	29.9(9)
N11	7715(4)	6795(3)	3397.3(19)	20.1(9)
O16	9016(4)	9400(3)	7647(2)	33(1)
O18	11723(5)	8797(3)	2987(2)	38.1(11)
O17	11261(4)	7065(3)	3606.2(18)	31.6(10)

N3	10581(5)	5853(3)	8748(2)	23.2(10)
N12	5471(4)	7070(3)	4238(2)	20.3(9)
N8	7811(5)	6082(3)	6253(2)	23(1)
N1	12356(4)	8478(3)	8530.6(19)	20.3(9)
N14	5099(4)	6714(3)	641.4(19)	19.9(9)
N13	4763(4)	8858(3)	647.1(19)	21.5(9)
N6	9647(4)	8575(3)	5734.9(19)	20.9(9)
N15	2821(5)	6563(3)	1352(2)	23.9(10)
N4	10346(4)	7625(3)	9327(2)	23.8(10)
N5	7375(4)	8187(3)	6408.6(19)	19.2(9)
N16	2496(5)	8700(3)	1322.6(19)	22.4(9)
N7	10090(5)	6430(3)	5624(2)	24.2(10)
C33	6679(5)	8693(4)	2374(2)	20.8(11)
N9	5172(4)	8942(3)	3848(2)	22.5(9)
N2	12579(4)	6706(3)	7894.8(19)	21.8(9)
C4	12989(6)	8434(4)	7953(2)	26.1(12)
C25	7635(5)	9660(4)	3185(2)	21.8(11)
C30	5303(6)	6046(4)	4095(3)	27.2(12)
C41	6463(5)	7050(4)	716(2)	25.7(12)
C14	6021(5)	7872(4)	6344(3)	23.4(11)
C17	11049(5)	8527(4)	5832(2)	25.6(12)
C27	8350(5)	7126(4)	2842(2)	24.1(12)
C5	13578(5)	7474(4)	7879(2)	26.7(12)
C32	4508(6)	8588(4)	4389(3)	30.7(13)
C26	8613(5)	8170(4)	2892(2)	23.3(11)
C16	9057(6)	9290(4)	6138(2)	24.3(12)
C29	6580(6)	5565(4)	3961(3)	28.6(13)
C9	9939(6)	5921(4)	9323(3)	28.9(13)
C23	5791(6)	9854(4)	3926(2)	23.2(11)
C24	6434(6)	10192(4)	3364(3)	23.9(12)
C19	11467(6)	6735(5)	5685(3)	30.5(13)
C2	10885(6)	9301(4)	9224(3)	27.8(12)
C34	1421(6)	6596(5)	1314(3)	29.6(13)
C13	5824(6)	6880(4)	6569(3)	27.7(12)
C1	9824(6)	8579(4)	9290(3)	28.9(13)
C7	12202(6)	5014(4)	8124(3)	28.2(13)
C10	9332(6)	6879(5)	9378(3)	32.8(14)
C22	9326(5)	8797(4)	5099(2)	21.8(11)
C6	13162(6)	5783(4)	8006(2)	25.4(12)
C21	8392(6)	5334(4)	5868(3)	29.8(13)
C36	1120(6)	8403(5)	1306(3)	30.7(13)
C43	3401(6)	5725(4)	1058(3)	28.7(13)
C37	2755(6)	9572(4)	988(3)	28.6(13)
C12	6405(6)	6093(4)	6215(3)	28.1(12)
C39	6166(5)	8849(4)	702(3)	27.3(12)
C40	6752(6)	7985(5)	426(3)	30.7(13)
C8	11507(6)	5053(4)	8719(3)	25.6(12)
C18	11705(6)	7745(5)	5491(3)	29.9(13)
C38	4176(6)	9698(4)	936(2)	27.1(12)
C15	7623(6)	9137(4)	6176(3)	24.2(12)

C28	7189(6)	5836(4)	3382(3)	27.4(12)
C3	11548(6)	9324(4)	8623(3)	25.7(12)
C11	11847(5)	6699(4)	7318(2)	25.3(12)
C35	889(6)	7454(5)	1613(3)	32.3(14)
C20	9822(6)	5483(4)	5845(3)	31.7(13)
C42	4833(6)	5879(4)	1014(3)	26.4(12)
C44	4802(5)	6497(4)	1(2)	21.2(11)
C31	4249(6)	7551(4)	4333(3)	28.4(13)
Ni1	11448.1(6)	7174.5(4)	8618.5(3)	11.32(14)

*Table 14 - Anisotropic Displacement Parameters (Å2×103) for [Ni(cycP)]$_n$. The Anisotropic displacement factor exponent takes the form: -2π2[h2a*2U11+2hka*b*U12+...].*

Atom	U_{11}	U_{22}	U_{33}	U_{23}	U_{13}	U_{12}
Ni3	10.9(3)	12.8(3)	8.8(3)	-1.0(2)	-1.7(2)	0.5(2)
Ni4	12.6(3)	13.7(3)	7.9(3)	-0.2(2)	-2.6(2)	-0.8(2)
Ni2	12.6(3)	14.6(3)	8.2(3)	0.2(2)	-2.0(2)	1.1(2)
P4	14.1(6)	16.9(6)	8.0(6)	-0.7(5)	-4.1(5)	2.6(5)
P2	15.2(6)	18.0(6)	8.3(6)	1.5(5)	-4.4(5)	-3.8(5)
P3	13.2(6)	19.9(6)	9.7(6)	-0.3(5)	-2.8(5)	-0.7(5)
P1	17.0(7)	21.9(7)	12.0(6)	-0.5(5)	-3.3(5)	1.0(5)
O5	21.9(19)	17.9(18)	10.9(16)	-1.3(13)	-6.4(14)	-2.1(14)
O4	13.6(17)	15.2(17)	11.5(16)	-1.1(13)	-3.0(13)	0.6(13)
O10	13.4(17)	16.4(17)	10.3(16)	1.7(13)	-3.0(13)	-0.1(13)
O7	15.4(18)	19.0(18)	17.5(17)	0.8(14)	-7.3(14)	-2.6(14)
O6	21.0(19)	30(2)	11.7(17)	-0.7(15)	-2.8(14)	5.0(16)
O11	22.9(19)	15.5(17)	10.2(16)	0.1(13)	-6.9(14)	2.9(14)
O8	19.4(19)	27(2)	12.2(17)	-0.1(14)	-6.2(14)	0.1(15)
O9	22(2)	27(2)	18.5(19)	0.4(15)	-1.2(15)	5.1(16)
O1	18.9(18)	22.3(19)	15.0(17)	-1.8(14)	-5.9(14)	3.7(15)
O12	17.3(18)	29(2)	12.0(17)	2.2(15)	-1.8(14)	-6.7(15)
O2	32(2)	25(2)	18.8(19)	1.1(16)	-8.0(17)	-8.2(17)
O3	24(2)	31(2)	13.1(17)	2.9(15)	-5.7(15)	-2.2(16)
O20	35(2)	30(2)	32(2)	-3.4(19)	-4.0(19)	2.0(19)
O15	38(2)	26(2)	24(2)	3.5(17)	6.4(18)	7.9(19)
N10	14(2)	26(2)	13(2)	2.7(17)	-1.5(16)	0.9(17)
O19	40(3)	34(2)	40(3)	-3(2)	8(2)	-8(2)
O14	44(3)	36(3)	36(3)	11(2)	15(2)	10(2)
O13	25(2)	39(2)	26(2)	3.1(18)	2.1(17)	-4.0(18)
N11	23(2)	24(2)	13(2)	-4.2(17)	-4.7(17)	6.2(18)
O16	31(2)	36(2)	32(2)	-1(2)	-9(2)	6.3(19)
O18	32(2)	35(3)	48(3)	-5(2)	15(2)	-7(2)
O17	25(2)	42(3)	28(2)	-4.0(19)	4.9(18)	4.6(19)
N3	27(3)	23(2)	19(2)	4.7(18)	-8.9(18)	-8.9(18)
N12	19(2)	23(2)	19(2)	5.0(18)	-2.1(17)	-0.9(17)
N8	28(2)	25(2)	16(2)	4.9(18)	-7.4(18)	-8.1(19)
N1	24(2)	21(2)	16(2)	2.3(17)	-8.3(18)	-1.9(18)
N14	25(2)	23(2)	11(2)	-1.8(17)	-5.9(17)	10.5(18)
N13	26(2)	27(2)	11(2)	0.7(17)	-4.3(18)	-8.3(18)

N6	20(2)	31(2)	12(2)	1.9(17)	-5.3(17)	-9.3(18)
N15	30(2)	29(2)	12(2)	2.2(18)	-3.4(18)	-12.6(19)
N4	20(2)	34(2)	18(2)	-2.4(19)	1.0(18)	4.8(19)
N5	26(2)	20(2)	12(2)	-3.5(17)	-2.0(17)	2.3(17)
N16	27(2)	27(2)	13(2)	-6.7(18)	-3.0(18)	7.6(19)
N7	25(2)	34(3)	14(2)	-0.3(19)	-5.1(18)	11.8(19)
C33	19(3)	34(3)	10(2)	4(2)	-1.0(19)	-2(2)
N9	23(2)	25(2)	19(2)	-0.6(18)	-2.6(18)	5.2(18)
N2	23(2)	32(2)	10(2)	-1.8(18)	-6.9(17)	5.7(19)
C4	27(3)	35(3)	16(3)	5(2)	-3(2)	-7(2)
C25	28(3)	23(3)	14(2)	3(2)	-5(2)	-10(2)
C30	32(3)	26(3)	24(3)	3(2)	0(2)	-9(2)
C41	17(3)	40(3)	20(3)	-7(2)	-10(2)	12(2)
C14	15(2)	30(3)	25(3)	-6(2)	-3(2)	5(2)
C17	22(3)	39(3)	16(3)	1(2)	-5(2)	-10(2)
C27	21(3)	36(3)	15(3)	-1(2)	-3(2)	15(2)
C5	19(3)	48(3)	13(3)	0(2)	1(2)	-9(2)
C32	28(3)	40(3)	24(3)	4(3)	9(2)	14(3)
C26	14(3)	43(3)	13(3)	-1(2)	3(2)	0(2)
C16	39(3)	20(3)	15(3)	0(2)	1(2)	-2(2)
C29	31(3)	14(3)	41(3)	0(2)	-12(3)	-2(2)
C9	29(3)	31(3)	27(3)	8(2)	0(2)	-12(2)
C23	28(3)	23(3)	19(3)	-3(2)	-7(2)	8(2)
C24	28(3)	17(3)	26(3)	1(2)	-9(2)	0(2)
C19	23(3)	44(3)	25(3)	-7(3)	-7(2)	13(2)
C2	34(3)	22(3)	27(3)	-3(2)	-8(2)	10(2)
C34	26(3)	46(3)	17(3)	3(2)	2(2)	-12(3)
C13	19(3)	40(3)	24(3)	11(2)	0(2)	-5(2)
C1	25(3)	33(3)	29(3)	-6(2)	3(2)	7(2)
C7	38(3)	24(3)	22(3)	-1(2)	-11(2)	11(2)
C10	24(3)	54(4)	21(3)	0(3)	7(2)	-8(3)
C22	26(3)	23(3)	16(2)	5(2)	-9(2)	-9(2)
C6	30(3)	31(3)	15(3)	-4(2)	-6(2)	7(2)
C21	51(4)	18(3)	20(3)	1(2)	-8(3)	0(2)
C36	24(3)	44(3)	24(3)	-7(3)	-5(2)	11(2)
C43	52(4)	13(2)	21(3)	3(2)	-7(3)	-5(2)
C37	45(3)	23(3)	18(3)	-5(2)	-9(2)	9(2)
C12	28(3)	30(3)	27(3)	5(2)	-1(2)	-9(2)
C39	24(3)	40(3)	18(3)	3(2)	-5(2)	-11(2)
C40	18(3)	52(4)	23(3)	3(3)	-6(2)	-5(2)
C8	32(3)	16(2)	29(3)	6(2)	-11(2)	-2(2)
C18	17(3)	49(4)	24(3)	0(3)	-6(2)	0(2)
C38	51(4)	14(2)	16(3)	0(2)	-6(3)	-4(2)
C15	29(3)	21(3)	23(3)	-5(2)	-6(2)	3(2)
C28	35(3)	19(3)	28(3)	-6(2)	-12(2)	6(2)
C3	29(3)	16(3)	31(3)	4(2)	-10(2)	2(2)
C11	24(3)	36(3)	16(3)	-1(2)	-5(2)	10(2)
C35	19(3)	53(4)	24(3)	1(3)	3(2)	-5(3)
C20	47(3)	31(3)	17(3)	-2(2)	-9(3)	16(3)

C42	36(3)	24(3)	19(3)	0(2)	-9(2)	5(2)
C44	25(3)	26(3)	13(2)	-3(2)	-9(2)	12(2)
C31	25(3)	36(3)	24(3)	5(2)	8(2)	1(2)
Ni1	11.5(3)	12.4(3)	10.0(3)	0.7(2)	-2.2(2)	-0.2(2)

Table 15 - Bond Lengths for[Ni(cycP)]$_n$.

Atom	Atom	Length/Å
Ni3	O5	2.065(3)
Ni3	O7	2.119(3)
Ni3	N10	2.124(4)
Ni3	N11	2.069(4)
Ni3	N12	2.065(4)
Ni3	N9	2.093(5)
Ni4	O10	2.099(3)
Ni4	O8	2.087(3)
Ni4	N14	2.135(4)
Ni4	N13	2.081(5)
Ni4	N15	2.064(5)
Ni4	N16	2.067(4)
Ni2	O4	2.115(3)
Ni2	O3	2.097(4)
Ni2	N8	2.055(5)
Ni2	N6	2.126(5)
Ni2	N5	2.080(4)
Ni2	N7	2.086(5)
P4	O10	1.537(3)
P4	O11	1.518(3)
P4	O12	1.528(4)
P4	C44	1.828(5)
P2	O5	1.517(4)
P2	O4	1.528(4)
P2	O6	1.507(4)
P2	C22	1.838(5)
P3	O7	1.529(4)
P3	O8	1.507(4)
P3	O9	1.525(4)
P3	C33	1.832(5)
P1	O1	1.539(4)
P1	O2	1.516(4)
P1	O3	1.509(4)
P1	C11	1.850(6)
O11	Ni1	2.085(3)
O1	Ni1	2.141(3)
N10	C33	1.502(6)
N10	C25	1.501(7)
N10	C26	1.465(7)
N11	C27	1.492(7)
N11	C28	1.461(7)

N3	C9	1.462(7)
N3	C8	1.489(7)
N3	Ni1	2.096(4)
N12	C30	1.494(7)
N12	C31	1.459(7)
N8	C21	1.496(7)
N8	C12	1.463(7)
N1	C4	1.462(7)
N1	C3	1.479(7)
N1	Ni1	2.081(4)
N14	C41	1.503(7)
N14	C42	1.476(7)
N14	C44	1.500(6)
N13	C39	1.463(7)
N13	C38	1.489(7)
N6	C17	1.474(7)
N6	C16	1.492(7)
N6	C22	1.496(6)
N15	C34	1.459(7)
N15	C43	1.487(7)
N4	C1	1.458(7)
N4	C10	1.495(8)
N4	Ni1	2.069(4)
N5	C14	1.482(7)
N5	C15	1.466(7)
N16	C36	1.491(8)
N16	C37	1.471(7)
N7	C19	1.499(8)
N7	C20	1.458(8)
N9	C32	1.490(7)
N9	C23	1.451(7)
N2	C5	1.503(7)
N2	C6	1.461(7)
N2	C11	1.495(6)
N2	Ni1	2.121(5)
C4	C5	1.501(9)
C25	C24	1.516(8)
C30	C29	1.526(8)
C41	C40	1.506(9)
C14	C13	1.507(8)
C17	C18	1.510(8)
C27	C26	1.506(8)
C32	C31	1.496(9)
C16	C15	1.509(8)
C29	C28	1.501(9)
C9	C10	1.502(9)
C23	C24	1.511(8)
C19	C18	1.515(9)
C2	C1	1.511(9)
C2	C3	1.519(8)

C34	C35	1.496(9)
C13	C12	1.499(9)
C7	C6	1.502(9)
C7	C8	1.527(8)
C21	C20	1.503(9)
C36	C35	1.529(9)
C43	C42	1.509(9)
C37	C38	1.494(9)
C39	C40	1.503(9)
Ni1	O11	2.085(3)

Table 16 - Bond Angles for [Ni(cycP)]$_n$.

Atom	Atom	Atom	Angle/°
O5	Ni3	O7	175.98(14)
O5	Ni3	N10	89.64(15)
O5	Ni3	N11	89.38(16)
O5	Ni3	N12	89.75(16)
O5	Ni3	N9	87.66(16)
O7	Ni3	N10	86.40(15)
N11	Ni3	O7	90.99(16)
N11	Ni3	N10	86.01(18)
N11	Ni3	N9	177.01(18)
N12	Ni3	O7	94.20(16)
N12	Ni3	N10	179.08(18)
N12	Ni3	N11	94.66(18)
N12	Ni3	N9	84.92(18)
N9	Ni3	O7	91.99(16)
N9	Ni3	N10	94.37(18)
O10	Ni4	N14	86.75(15)
O8	Ni4	O10	174.70(14)
O8	Ni4	N14	89.17(15)
N13	Ni4	O10	90.11(15)
N13	Ni4	O8	93.46(16)
N13	Ni4	N14	92.83(19)
N15	Ni4	O10	89.97(15)
N15	Ni4	O8	86.41(16)
N15	Ni4	N14	86.42(19)
N15	Ni4	N13	179.2(2)
N15	Ni4	N16	94.9(2)
N16	Ni4	O10	91.71(16)
N16	Ni4	O8	92.45(16)
N16	Ni4	N14	177.94(18)
N16	Ni4	N13	85.81(19)
O4	Ni2	N6	86.31(15)
O3	Ni2	O4	173.48(14)
O3	Ni2	N6	89.44(16)
N8	Ni2	O4	91.48(16)
N8	Ni2	O3	92.81(16)

N8	Ni2	N6	177.74(17)
N8	Ni2	N5	94.38(19)
N8	Ni2	N7	85.6(2)
N5	Ni2	O4	88.95(15)
N5	Ni2	O3	85.83(16)
N5	Ni2	N6	86.03(18)
N5	Ni2	N7	179.74(18)
N7	Ni2	O4	91.30(15)
N7	Ni2	O3	93.91(16)
N7	Ni2	N6	94.02(19)
O10	P4	C44	105.2(2)
O11	P4	O10	112.4(2)
O11	P4	O12	113.3(2)
O11	P4	C44	106.1(2)
O12	P4	O10	112.1(2)
O12	P4	C44	107.0(2)
O5	P2	O4	113.5(2)
O5	P2	C22	102.8(2)
O4	P2	C22	103.6(2)
O6	P2	O5	113.4(2)
O6	P2	O4	112.1(2)
O6	P2	C22	110.6(2)
O7	P3	C33	104.1(2)
O8	P3	O7	113.3(2)
O8	P3	O9	113.2(2)
O8	P3	C33	105.8(2)
O9	P3	O7	112.8(2)
O9	P3	C33	106.6(2)
O1	P1	C11	102.6(2)
O2	P1	O1	111.8(2)
O2	P1	C11	110.4(3)
O3	P1	O1	114.0(2)
O3	P1	O2	113.5(2)
O3	P1	C11	103.5(2)
P2	O5	Ni3	131.6(2)
P2	O4	Ni2	110.66(18)
P4	O10	Ni4	111.62(18)
P3	O7	Ni3	113.09(19)
P4	O11	$Ni1^{1}$	129.1(2)
P3	O8	Ni4	147.9(2)
P1	O1	Ni1	111.75(19)
P1	O3	Ni2	147.9(2)
C33	N10	Ni3	111.6(3)
C25	N10	Ni3	110.8(3)
C25	N10	C33	111.1(4)
C26	N10	Ni3	102.5(3)
C26	N10	C33	110.1(4)
C26	N10	C25	110.4(4)
C27	N11	Ni3	104.6(3)
C28	N11	Ni3	115.7(4)

C28	N11	C27	116.1(4)
C9	N3	C8	112.8(4)
C9	N3	Ni1	105.4(3)
C8	N3	Ni1	113.2(3)
C30	N12	Ni3	115.3(3)
C31	N12	Ni3	105.8(3)
C31	N12	C30	112.6(4)
C21	N8	Ni2	104.9(3)
C12	N8	Ni2	116.2(4)
C12	N8	C21	112.5(4)
C4	N1	C3	114.9(4)
C4	N1	Ni1	104.8(3)
C3	N1	Ni1	116.4(4)
C41	N14	Ni4	111.0(3)
C42	N14	Ni4	101.0(3)
C42	N14	C41	111.7(4)
C42	N14	C44	110.0(4)
C44	N14	Ni4	111.8(3)
C44	N14	C41	110.9(4)
C39	N13	Ni4	117.0(4)
C39	N13	C38	112.6(4)
C38	N13	Ni4	104.5(3)
C17	N6	Ni2	111.2(4)
C17	N6	C16	110.8(4)
C17	N6	C22	111.2(4)
C16	N6	Ni2	101.7(3)
C16	N6	C22	110.2(4)
C22	N6	Ni2	111.3(3)
C34	N15	Ni4	115.8(4)
C34	N15	C43	114.2(5)
C43	N15	Ni4	105.0(3)
C1	N4	C10	113.2(5)
C1	N4	Ni1	116.7(4)
C10	N4	Ni1	103.8(3)
C14	N5	Ni2	115.2(3)
C15	N5	Ni2	105.9(3)
C15	N5	C14	114.2(4)
C36	N16	Ni4	115.0(3)
C37	N16	Ni4	105.6(3)
C37	N16	C36	113.8(5)
C19	N7	Ni2	116.2(4)
C20	N7	Ni2	105.9(4)
C20	N7	C19	114.7(5)
N10	C33	P3	114.2(3)
C32	N9	Ni3	105.1(3)
C23	N9	Ni3	114.3(3)
C23	N9	C32	114.2(5)
C5	N2	Ni1	100.4(3)
C6	N2	C5	111.3(5)
C6	N2	C11	110.5(4)
C6	N2	Ni1	112.4(3)

C11	N2	C5	109.3(4)
C11	N2	Ni1	112.5(3)
N1	C4	C5	108.9(4)
N10	C25	C24	114.6(4)
N12	C30	C29	112.1(5)
N14	C41	C40	114.9(4)
N5	C14	C13	112.2(4)
N6	C17	C18	114.4(5)
N11	C27	C26	109.1(4)
C4	C5	N2	111.6(5)
N9	C32	C31	110.3(5)
N10	C26	C27	109.4(4)
N6	C16	C15	110.5(4)
C28	C29	C30	115.6(5)
N3	C9	C10	109.1(5)
N9	C23	C24	112.4(4)
C23	C24	C25	115.8(5)
N7	C19	C18	113.7(5)
C1	C2	C3	116.1(5)
N15	C34	C35	112.0(5)
C12	C13	C14	117.2(5)
N4	C1	C2	111.1(5)
C6	C7	C8	116.7(5)
N4	C10	C9	109.4(5)
N6	C22	P2	113.0(4)
N2	C6	C7	113.7(5)
N8	C21	C20	109.1(5)
N16	C36	C35	113.0(5)
N15	C43	C42	108.7(4)
N16	C37	C38	109.0(5)
N8	C12	C13	112.7(5)
N13	C39	C40	112.4(5)
C39	C40	C41	117.0(5)
N3	C8	C7	112.2(4)
C17	C18	C19	118.0(5)
N13	C38	C37	110.5(4)
N5	C15	C16	109.1(4)
N11	C28	C29	112.2(5)
N1	C3	C2	111.7(4)
N2	C11	P1	113.4(4)
C34	C35	C36	116.8(5)
N7	C20	C21	109.4(5)
N14	C42	C43	109.9(4)
N14	C44	P4	112.5(3)
N12	C31	C32	108.3(5)
$O11^{2}$	Ni1	O1	174.77(14)
$O11^{2}$	Ni1	N3	87.27(16)
$O11^{2}$	Ni1	N2	89.35(15)
N3	Ni1	O1	93.30(16)
N3	Ni1	N2	94.03(19)

N1	Ni1	$O11^{2}$	90.09(16)
N1	Ni1	O1	89.43(16)
N1	Ni1	N3	177.14(17)
N1	Ni1	N2	87.06(19)
N4	Ni1	$O11^{2}$	90.46(16)
N4	Ni1	O1	94.77(16)
N4	Ni1	N3	85.72(19)
N4	Ni1	N1	93.19(19)
N4	Ni1	N2	179.69(19)
N2	Ni1	O1	85.42(15)

Table 17 - Torsion Angles for[Ni(cycP)]$_n$.

A	B	C	D	Angle/°
Ni3	N10	C33	P3	8.2(5)
Ni3	N10	C25	C24	-57.7(5)
Ni3	N10	C26	C27	45.3(4)
Ni3	N11	C27	C26	40.8(5)
Ni3	N11	C28	C29	-57.3(5)
Ni3	N12	C30	C29	55.0(6)
Ni3	N12	C31	C32	-45.5(5)
Ni3	N9	C32	C31	-37.0(5)
Ni3	N9	C23	C24	59.9(5)
Ni4	N14	C41	C40	-59.0(5)
Ni4	N14	C42	C43	46.6(5)
Ni4	N14	C44	P4	10.4(5)
Ni4	N13	C39	C40	57.2(5)
Ni4	N13	C38	C37	-39.5(5)
Ni4	N15	C34	C35	-57.4(6)
Ni4	N15	C43	C42	40.2(5)
Ni4	N16	C36	C35	53.3(6)
Ni4	N16	C37	C38	-42.1(5)
Ni2	N8	C21	C20	42.6(5)
Ni2	N8	C12	C13	-55.5(6)
Ni2	N6	C17	C18	61.2(5)
Ni2	N6	C16	C15	-44.5(5)
Ni2	N6	C22	P2	-9.5(5)
Ni2	N5	C14	C13	55.1(5)
Ni2	N5	C15	C16	-39.4(5)
Ni2	N7	C19	C18	-51.9(6)
Ni2	N7	C20	C21	39.6(5)
O5	P2	O4	Ni2	-151.41(18)
O5	P2	C22	N6	151.7(4)
O4	P2	O5	Ni3	-69.4(3)
O4	P2	C22	N6	33.3(4)
O10	P4	O11	$Ni1^{1}$	68.7(3)
O10	P4	C44	N14	-31.0(5)
O7	P3	O8	Ni4	130.5(4)

O7	P3	C33	N10	-27.9(4)
O6	P2	O5	Ni3	60.0(3)
O6	P2	O4	Ni2	78.5(2)
O6	P2	C22	N6	-86.9(4)
O11	P4	O10	Ni4	151.85(18)
O11	P4	C44	N14	-150.4(4)
O8	P3	O7	Ni3	148.9(2)
O8	P3	C33	N10	-147.6(4)
O9	P3	O7	Ni3	-80.8(3)
O9	P3	O8	Ni4	0.4(5)
O9	P3	C33	N10	91.5(4)
O1	P1	O3	Ni2	-139.5(4)
O1	P1	C11	N2	31.6(5)
O12	P4	O10	Ni4	-79.1(2)
O12	P4	O11	$Ni1^{1}$	-59.8(3)
O12	P4	C44	N14	88.4(4)
O2	P1	O1	Ni1	78.9(3)
O2	P1	O3	Ni2	-9.9(6)
O2	P1	C11	N2	-87.8(4)
O3	P1	O1	Ni1	-150.7(2)
O3	P1	C11	N2	150.4(4)
N10	C25	C24	C23	71.2(6)
N11	C27	C26	N10	-61.3(5)
N3	C9	C10	N4	-59.0(6)
N12	C30	C29	C28	-70.8(6)
N8	C21	C20	N7	-57.2(6)
N1	C4	C5	N2	61.0(6)
N14	C41	C40	C39	70.1(6)
N13	C39	C40	C41	-66.3(6)
N6	C17	C18	C19	-70.4(7)
N6	C16	C15	N5	59.8(6)
N15	C34	C35	C36	70.7(7)
N15	C43	C42	N14	-62.1(6)
N5	C14	C13	C12	-69.7(6)
N16	C36	C35	C34	-68.9(7)
N16	C37	C38	N13	56.9(6)
N7	C19	C18	C17	62.8(7)
C33	P3	O7	Ni3	34.4(3)
C33	P3	O8	Ni4	-116.0(4)
C33	N10	C25	C24	67.1(5)
C33	N10	C26	C27	-73.6(5)
N9	C32	C31	N12	57.2(6)
N9	C23	C24	C25	-70.8(6)
C4	N1	C3	C2	177.9(5)
C25	N10	C33	P3	-116.1(4)
C25	N10	C26	C27	163.4(4)
C30	N12	C31	C32	-172.3(5)
C30	C29	C28	N11	72.1(6)
C41	N14	C42	C43	164.7(4)
C41	N14	C44	P4	-114.1(4)

C14	N5	C15	C16	-167.2(4)
C14	C13	C12	N8	69.7(7)
C17	N6	C16	C15	-162.8(5)
C17	N6	C22	P2	115.1(4)
C27	N11	C28	C29	179.6(5)
C5	N2	C6	C7	170.7(4)
C5	N2	C11	P1	-119.2(4)
C32	N9	C23	C24	-179.1(5)
C26	N10	C33	P3	121.4(4)
C26	N10	C25	C24	-170.5(4)
C16	N6	C17	C18	173.5(5)
C16	N6	C22	P2	-121.6(4)
C9	N3	C8	C7	-178.0(5)
C23	N9	C32	C31	-163.0(5)
C19	N7	C20	C21	169.2(5)
C34	N15	C43	C42	168.1(5)
C1	N4	C10	C9	171.8(5)
C1	C2	C3	N1	-70.5(6)
C10	N4	C1	C2	-178.5(5)
C22	P2	O5	Ni3	179.4(3)
C22	P2	O4	Ni2	-40.7(3)
C22	N6	C17	C18	-63.5(6)
C22	N6	C16	C15	73.6(5)
C6	N2	C5	C4	-162.6(4)
C6	N2	C11	P1	118.0(5)
C6	C7	C8	N3	70.1(6)
C21	N8	C12	C13	-176.4(5)
C36	N16	C37	C38	-169.2(4)
C43	N15	C34	C35	-179.6(5)
C37	N16	C36	C35	175.3(5)
C12	N8	C21	C20	169.8(5)
C39	N13	C38	C37	-167.4(5)
C8	N3	C9	C10	163.9(5)
C8	C7	C6	N2	-71.2(6)
C38	N13	C39	C40	178.2(5)
C15	N5	C14	C13	178.0(5)
C28	N11	C27	C26	169.6(4)
C3	N1	C4	C5	-170.2(5)
C3	C2	C1	N4	72.0(6)
C11	P1	O1	Ni1	-39.5(3)
C11	P1	O3	Ni2	109.8(5)
C11	N2	C5	C4	75.0(5)
C11	N2	C6	C7	-67.7(6)
C20	N7	C19	C18	-176.1(5)
C42	N14	C41	C40	-170.9(5)
C42	N14	C44	P4	121.8(4)
C44	P4	O10	Ni4	36.8(3)
C44	P4	O11	$Ni1^{1}$	-176.9(3)
C44	N14	C41	C40	65.9(6)
C44	N14	C42	C43	-71.7(5)

C31	N12	C30	C29	176.6(5)
Ni1	N3	C9	C10	39.9(5)
Ni1	N3	C8	C7	-58.4(5)
Ni1	N1	C4	C5	-41.2(5)
Ni1	N1	C3	C2	54.9(5)
Ni1	N4	C1	C2	-58.1(6)
Ni1	N4	C10	C9	44.2(5)
Ni1	N2	C5	C4	-43.5(5)
Ni1	N2	C6	C7	59.0(5)
Ni1	N2	C11	P1	-8.5(5)

Preparation of TiO_2 films for electrochemical and TAS experiments

Anatase TiO_2 films were prepared by depositing TiO_2 colloidal paste (average particle diameter = 20 nm, 90T, Dye Sol) on fluorine-doped tin oxide (FTO) coated glass slides which had been protected by an insulating TiO_2 thin layer deposited by spray coating according to the following procedure: the FTO (sonicated in ethanol for 20 minutes before the coating) is placed on a hotplate at 500°C, and 10 layers of a 0.2 M solution of Titanium diisopropoxide bis(acetylacetonate) ($Ti(acac)_2$) in EtOH are sprayed onto the slides. The FTO is left on the hotplate for 1 hour, then placed in a muffle furnace and heated at 500°C for an additional hour. The TiO_2 paste was deposited on the films and spread with a glass rod. The thickness was controlled by using scotch tape and was measured *via* profilometry to be an average of 3 μm. The films were allowed to dry before the slides were heated at 450°C for 30 minutes in air. The slides were cut so that the geometric surface area of the TiO_2 films was 1 cm^2. The complex was deposited on the TiO_2 by placing the films in a 1 mM solution of Ni(cycP) in ethanol for 48 hours, followed by copious rinsing with ethanol and drying under a stream of nitrogen.

Preparation of ZrO_2 films for electrochemical and TAS experiments

ZrO_2 films were prepared by depositing ZrO_2 colloidal paste (average particle diameter = 20 nm) on fluorine-doped tin oxide (FTO) coated glass slides. The slides were sonicated in water for 20 minutes, then in ethanol for 20 minutes, and finally calcined in the furnace at 400°C for 30 minutes before the

deposition. The paste was deposited on the films and spread with a glass rod. The films were allowed to dry before the slides were heated at 450°C for 30 minutes. The films were placed in solutions of Ni(cycP) 10 mM in ethanol for 48 hours, then they were copiously rinsed with ethanol and dried with a stream of nitrogen.

3.3.2 Electrochemistry

All electrochemical experiments except chronocoulometry measurements were carried out using either a Palmsens[1], Palmsens[3] or Emstat potentiostats (Alvatek). Measurements were carried out in a 4-neck pear-shaped flask, with a three electrode set-up. The counter electrode was either a platinum basket, platinum gauze or platinum coiled wire. The working electrode for the non-aqueous electrochemistry was a TiO_2, TiO_2/Ni(cycP), ZrO_2 or ZrO_2/Ni(cycP) film. For the aqueous electrochemistry a Hanging Mercury Drop Electrode WK2 was used. This was filled in the laboratory with triply distilled mercury (Fisher); the area of a drop was 0.023 cm^2, measured by weighing and averaging multiple drops. A silver wire *quasi*reference electrode was used as the reference electrode for non-aqueous electrochemistry. The potential was referenced by measuring the ferrocene redox couple at the end of each experiment. A Ag/AgCl/3.5 M NaCl reference electrode (BASi, IJ Cambria or home-made) was used for aqueous electrochemistry.

Bulk electrolysis experiments were carried out using a gold-mercury amalgam as the working electrode (geometric surface area ≈ 2.5 cm^2). For these experiments, the counter electrode was separated from the main compartment of the cell by a glass double junction with a porous frit to avoid reoxidation of the reaction products. The nature of the reaction products was verified by gas chromatography. The instrument used was an Agilent 6890N with helium N6 (BOC) as the carrier gas (5 mol min^{-1}), equipped with a 5 Å molecular sieve column (ValcoPLOT, 30 m length, 0.53 mm ID) and a pulsed discharge detector (D-3-I-HP, Valco Vici). The peak areas for H_2 and CO were quantified by calibration with a custom-ordered calibrant gas containing 500 ppm of H_2 and 200 ppm of methane and CO. Calibrations were carried out daily.

Chronocoulometry experiments used a Whistonbrook DF63 potentiostat and Labview software (National Instruments), HMDE working electrode, platinum wire counter and a silver wire quasi-reference electrode. The cell was purged with argon (30 mins) before the experiments and kept under a blanket of argon throughout. A fresh mercury drop was used with every potential step. The potential was kept at the value of interest for 30 seconds, then stepped to -0.1 V_{NHE} for 10 ms and stepped to the initial potential.

3.3.3 Spectroscopic characterisation

ESI-MS and elemental analysis were carried out by the University of Liverpool analytical services. ICP analysis was carried out either by the University of Liverpool analytical services or the Centre for Chemical Instrumentation and Analytical Services in Sheffield. FTIR was carried out on a Bruker Vertex instrument. UV-Vis spectra were recorded on a Shimadzu UV-2600 spectrophotometer. ^{1}H, ^{13}C and ^{31}P NMR spectra were recorded on a Bruker 400 MHz spectrometer. Chemical shifts (δ) are reported in ppm relative to residual solvent signals for ^{1}H and ^{13}C NMR (^{1}H NMR: 7.26 ppm for $CDCl_3$, 4.79 ppm for D_2O. ^{13}C NMR: 77.1 ppm for $CDCl_3$). Coupling constants (J) are reported in Hz. Multiplicities are reported as follows: s, singlet, d, doublet, dd, doublet of doublets, ddd doublet of doublet of doublets, t triplet, dt, doublets of triplets, q, quartet, qdd, quartet of doublet of doublets m, multiplet, c, complex, and br, broad.

The microsecond-second transient absorption decays were measured using a Nd:YAG laser (Continuum, Surelite I-10, 355 nm, 4-6 ns pulse width). The third harmonic of the laser, corresponding to 355 nm, at a frequency of 0.33 Hz, was used as the excitation pulse. Typical excitation densities of 350 μJ/cm^2 were used, unless otherwise stated. A liquid light guide with a diameter of 0.5 cm was used to transmit the laser pulse to the sample. The probe light source was a 75 W Xe lamp (OBB Corp.) and the probing wavelength was selected using a monochromator (OBB Corp.) placed prior to the sample. The change in optical density of the sample is calculated by measuring the transmitted light with a Si Photodiode (Hamamatsu) and a homemade amplification

system coupled to both an oscilloscope (Textronix TDS 220) and data acquisition card (National Instruments NI-6221). The decays observed are the average of 250 laser pulses. The data was processed using home-built software built in Labview and with the Origin software.

3.4 References

1. L. Zhang and J. M. Cole, *ACS Appl. Mater. Interfaces*, 2015, **7**, 3427–3455.

2. J. Willkomm, K. L. Orchard, A. Reynal, E. Pastor, J. R. Durrant, and E. Reisner, *Chem. Soc. Rev. Chem. Soc. Rev*, 2016, **45**, 9–23.

3. K. Hanson, M. K. Brennaman, A. Ito, H. Luo, W. Song, K. A. Parker, R. Ghosh, M. R. Norris, C. R. K. Glasson, J. J. Concepcion, R. Lopez, and T. J. Meyer, *J. Phys. Chem. C*, 2012, **116**, 14837–14847.

4. K. Hanson, M. K. Brennaman, H. Luo, C. R. K. Glasson, J. J. Concepcion, W. Song, and T. J. Meyer, *ACS Appl. Mater. Interfaces*, 2012, **4**, 1462–1469.

5. D. G. Brown, P. A. Schauer, J. Borau-Garcia, B. R. Fancy, and C. P. Berlinguette, *J. Am. Chem. Soc.*, 2013, **135**, 1692–1695.

6. F. Boschetti, F. Denat, E. Espinosa, J.-M. Lagrange, and R. Guilard, *Chem. Commun.*, 2004, 588.

7. T. Vitha, J. Kotek, J. Rudovský, V. Kubíček, I. Císařová, P. Hermann, and I. Lukeš, *Collect. Czechoslov. Chem. Commun.*, 2006, **71**, 337–367.

8. J. Kotek, P. Vojtíšek, I. Císařová, P. Hermann, P. Jurečka, J. Rohovec, and I. Lukeš, *Collect. Czechoslov. Chem. Commun.*, 2000, **65**, 1289–1316.

9. S. Füzerová, J. Kotek, I. Císařová, P. Hermann, K. Binnemans, and I. Lukeš, *Dalt. Trans.*, 2005, 2908.

10. J. Kotek, P. Lubal, P. Hermann, I. Císařová, I. Lukeš, T. Godula, I. Svobodová, P. Táborský, and J. Havel, *Chem. - A Eur. J.*, 2003, **9**, 233–248.

11. N. Jubran, G. Ginzburg, H. Cohen, Y. Koresh, and D. Meyerstein, *Inorg. Chem.*, 1985, **24**,

251–258.

12. M. Ciampolini, L. Fabbrizzi, M. Licchelli, A. Perotti, F. Pezzini, and A. Poggi, *Inorg. Chem.*, 1986, **25**, 4131–4135.

13. K. Bujno, R. Bilewicz, L. Siegfried, and T. A. Kaden, *J. Electroanal. Chem.*, 1998, **445**, 47–53.

14. G. B. Balazs, California Institute of Technology, 1993.

15. G. B. Balazs and F. C. Anson, *J. Electroanal. Chem.*, 1992, 322, 325–345.

16. F. Denat, S. Brandes, R. Guilard, and N. Yamada, *Synlett*, 2000, 561–574.

17. S. BRANDES, C. GROS, F. DENAT, P. PULLUMBI, and R. GUILARD, *Bull. Soc. Chim. Fr.*, **133**, 65–73.

18. Z. Kovacs and A. D. Sherry, *Synthesis (Stuttg).*, 1997, **1997**, 759–763.

19. G. J. Bridger, R. T. Skerlj, S. Padmanabhan, S. A. Martellucci, G. W. Henson, M. J. Abrams, H. C. Joao, M. Witvrouw, K. De Vreese, R. Pauwels, and E. De Clercq, *J. Med. Chem.*, 1996, **39**, 109–119.

20. V. Patinec, J. J. Yaouanc, J. C. Clément, H. Handel, and H. des Abbayes, *Tetrahedron Lett.*, 1995, **36**, 79–82.

21. I. Gardinier, A. Roignant, N. Oget, H. Bernard, J. J. Yaouanc, and H. Handel, *Tetrahedron Lett.*, 1996, **37**, 7711–7714.

22. D. Guillaume and G. R. Marshall, *Synth. Commun.*, 1998, **28**, 2903–2906.

23. W. Yang, C. M. Giandomenico, M. Sartori, and D. a. Moore, *Tetrahedron Lett.*, 2003, **44**, 2481–2483.

24. D. Xu, K. Prasad, O. Repic, and T. J. Blacklock, *Tetrahedron Lett.*, 1995, **36**, 7357–7360.

25. B. Bosnich, M. L. Tobe, and G. A. Webb, *Inorg. Chem.*, 1965, **4**, 1109–1112.

26. K. V. Gobi, K. Tokuda, and T. Ohsaka, *Electrochim. Acta*, 1998, **43**, 1013–1022.

27. E. Kimura, T. Koike, K. Uenishi, M. Hediger, M. Kuramoto, S. Joko, Y. Arai, M. Kodama, and Y. Iitaka, *Inorg. Chem.*, 1987, **26**, 2975–2983.

28. P. V. Bernhardt and G. A. Lawrance, *Coord. Chem. Rev.*, 1990, **104**, 297–343.

29. A. G. Menke and F. Walmsley, *Inorganica Chim. Acta*, 1976, **17**, 193–197.

30. R. Luschtinetz, G. Seifert, E. Jaehne, and H.-J. P. Adler, *Macromol. Symp.*, 2007, **254**, 248–253.

31. M. C. Zenobi, C. V. Luengo, M. J. Avena, and E. H. Rueda, *Spectrochim. Acta - Part A Mol. Biomol. Spectrosc.*, 2008, **70**, 270–276.

32. K. D. Demadis and S. D. Katarachia, *Phosphorus. Sulfur. Silicon Relat. Elem.*, 2004, **179**, 627–648.

33. W. C. Grinonneau, P. L. Chapman, A. G. Menke, and F. Walmsley, *J. Inorg. Nucl. Chem.*, 1971, **33**, 3011–3017.

34. S. Bauer, T. Bein, and N. Stock, *Inorg. Chem.*, 2005, **44**, 5882–5889.

35. I. Zilbermann, M. Winnik, D. Sagiv, A. Rotman, H. Cohen, and D. Meyerstein, *Inorganica Chim. Acta*, 1995, **240**, 503–514.

36. G. Golub, I. Zilbermann, H. Cohen, and D. Meyerstein, *Supramol. Chem.*, 1996, **6**, 275–279.

37. M. Beley, J. P. Collin, R. Ruppert, and J. P. Sauvage, *J. Am. Chem. Soc.*, 1986, **108**, 7461–7467.

38. J. Schneider, H. Jia, J. T. Muckerman, and E. Fujita, *Chem. Soc. Rev.*, 2012, **41**, 2036–2051.

39. F. Wagner, M. T. Mocella, M. J. D'Aniello, A. H. J. Wang, and E. K. Barefield, *J. Am. Chem. Soc.*, 1974, **96**, 2625–2627.

40. M. J. D'Aniello, M. T. Mocella, F. Wagner, E. K. Barefield, and I. C. Paul, *J. Am. Chem. Soc.*, 1975, **97**, 192–194.

41. B. I. Lemon, F. Liu, and J. T. Hupp, *Coord. Chem. Rev.*, 2004, **248**, 1225–1230.

On the arid lands there will spring up industrial colonies without smoke and without smokestacks; forests of glass tubes will extend over the plains and glass buildings will rise everywhere; inside of these will take place the photochemical processes that hitherto have been the guarded secret of the plants, but that will have been mastered by human industry which will know how to make them bear even more abundant fruit than nature, for nature is not in a hurry and mankind is.

- *Giacomo Cimician, 1912*

4

The photochemical reduction of CO_2 by Ni(cycP) in water

4.1 Scope of the chapter

The previous chapter was focused on the synthesis and electrochemical properties of a Ni(cyc) catalyst modified with a phosphonic acid group. The results shown indicated that while the new complex retained some activity for CO_2 reduction at a mercury electrode, the performances of this catalyst were significantly decreased with respect to the unmodified complex. Ni(cycP) was synthesised primarily with the aim of obtaining a molecular catalyst for CO_2 reduction with a very stable binding group for immobilisation on semiconductor surfaces, to be coupled with a photosensitiser for the photochemical reduction of CO_2.

As outlined in Chapter 1, Ni(cyc) has been used in a completely photocatalytc system either in solution with a Ru dye (Scheme 24(a)) or in a supramolecular assembly (Scheme 24(b)), however it has never been reported in a heterogeneous photocatalytic system. The immobilisation of photosensitisers and catalyst on an inert support (Scheme 24(c)) has been proven efficient for the water splitting photocatalytic reaction,[1,2] however such an approach has not been reported for CO_2 reduction.

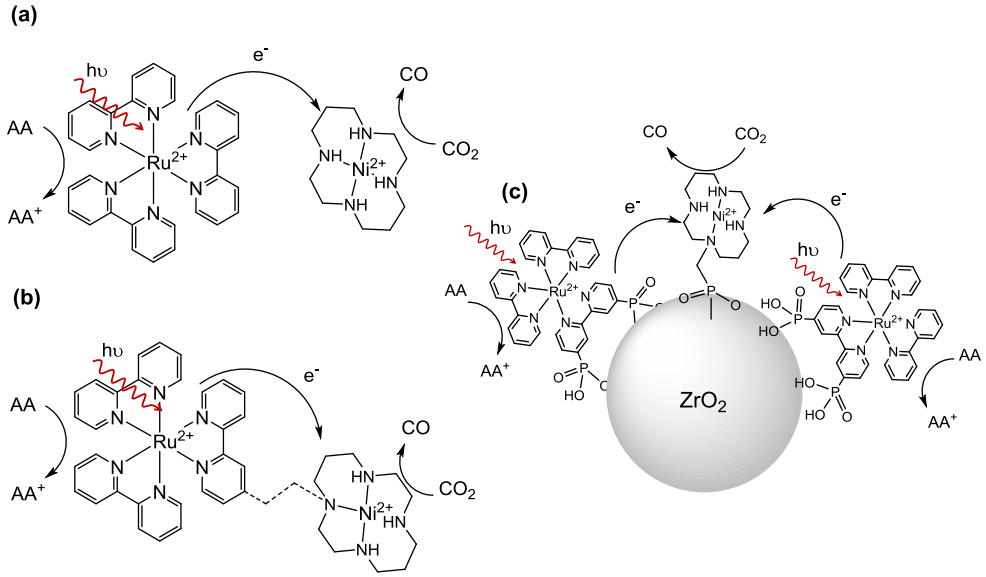

Scheme 24 – (a) Photocatalytic CO_2 reduction by Ni(cyc) sensitised by $Ru(bpy)_3$ in solution; (b) Ni(cyc) and $Ru(bpy)_3$ are covalently linked in a supramolecular complex (the dashed line represents an unspecified linker); (c) on-particle system which uses an inert scaffold as an easier and more economical way of forcing dye and catalyst close together.

The electrochemical behaviour of Ni(cycP) immobilised on ZrO_2 electrodes shown in the previous chapter indicated that the reduction of the nickel centre occurs at -0.8 V_{NHE} under CO_2. On the basis of this value we chose the well-known [Ru^{II}(2,2'-bipyridine)$_2$(2,2'-bipyridine-4,4'-diylbis(phosphonic acid)] (RuP from here onwards) as the photosensitiser, as we estimated RuP to have a sufficient driving force (*ca.* -0.3 eV under CO_2) for electron transfer to the CO_2 reduction catalyst ($E^0(RuP/RuP^-)$ = -1.1 V_{NHE}[2]). Moreover, it has been reported that electron injection from the excited RuP to the ZrO_2 conduction band does not take place,[3,4] due to the poor band alignment between RuP^- and the conduction band potential of ZrO_2 ($E_{CB} = -1.26$ V_{NHE} at pH 4.5[5,6]). Ruthenium polypyridyl complexes modified with anchoring groups are widely used in the DSSC field.[7] Amongst these, RuP has been found to be a very efficient sensitiser, mainly due to the high stability of the complex once it is bound to the surface. The presence of the phosphonic acid moieties has been studied and compared with other anchoring groups (carboxylic acids[8], alkyl phosphonic acids[9]). RuP was found to be a better sensitiser than the carboxylic acid-modified complexes on the account of the stability on the semiconductor surface. Compared to alkyl phosphonic drivatives, RuP has been found to have the same stability on the surface, but a higher photocurrent efficiency.[10]

In the first section of this chapter we will present the immobilisation of Ni(cycP) and RuP on commercial ZrO_2 nanoparticles and their characterisation. Following co-anchoring of the two complexes, the photocatalytic properties of the modified particles with respect to the catalytic CO_2 reduction will be analysed, in water with added ascorbate as a sacrificial electron donor. The differences in activity between the heterogeneous system and the homogeneous one have been rationalised through the use of transient absorption spectroscopy (TAS).

The second part of this chapter will focus on the ultrafast TAS of the complex Ni(cycP) immobilised on semiconductor nanocrystals of ZnSe. The system has been developed in collaboration with the University of Cambridge, where the ZnSe-QD were synthesised and the photocatalytic experiments carried out. We will briefly summarise the key results obtained by our collaborators, and subsequently

focus our discussion on the transient studies carried out at the University of Liverpool to build a kinetic model which would be consistent with the CO_2 reduction activity observed during photocatalysis.

4.2 Photocatalytic CO_2 reduction by Ni(cycP) and RuP anchored on ZrO_2

4.2.1 Binding studies

Preliminary binding studies of RuP have been carried out using a complex sample obtained from Dr Pau Farras, National University of Ireland, Galway. However, the sample was found to contain an impurity in the form of $Ru(bpy)_2Cl_2$. Although $Ru(bpy)_2Cl_2$ is unlikely to bind to ZrO_2 the dye was re-synthesised in-house, using a reported method.[9] Full details are in the materials and methods section, 4.4.1. RuP is prepared from diethyl 2,2'-bipyridine-4,4'-diphosphonate (**1**) and $Ru(bpy)_2Cl_2$ (**2**). **2** is readily obtained by reaction of $RuCl_3$ and a slight excess (2.5 eq.) of 2,2'-bipyridine in refluxing DMF (dimethylformamide) in the presence of LiCl to prevent complete conversion of $RuCl_3$ to $[Ru(bpy)_3]Cl_2$. The phopshonate ester of 2,2'-bipyridine is obtained by Pd-catalysed Hirao cross-coupling[11,12] of 4,4'-dibromo-2,2'-bipyridine and diethyl phosphite (Scheme 25).

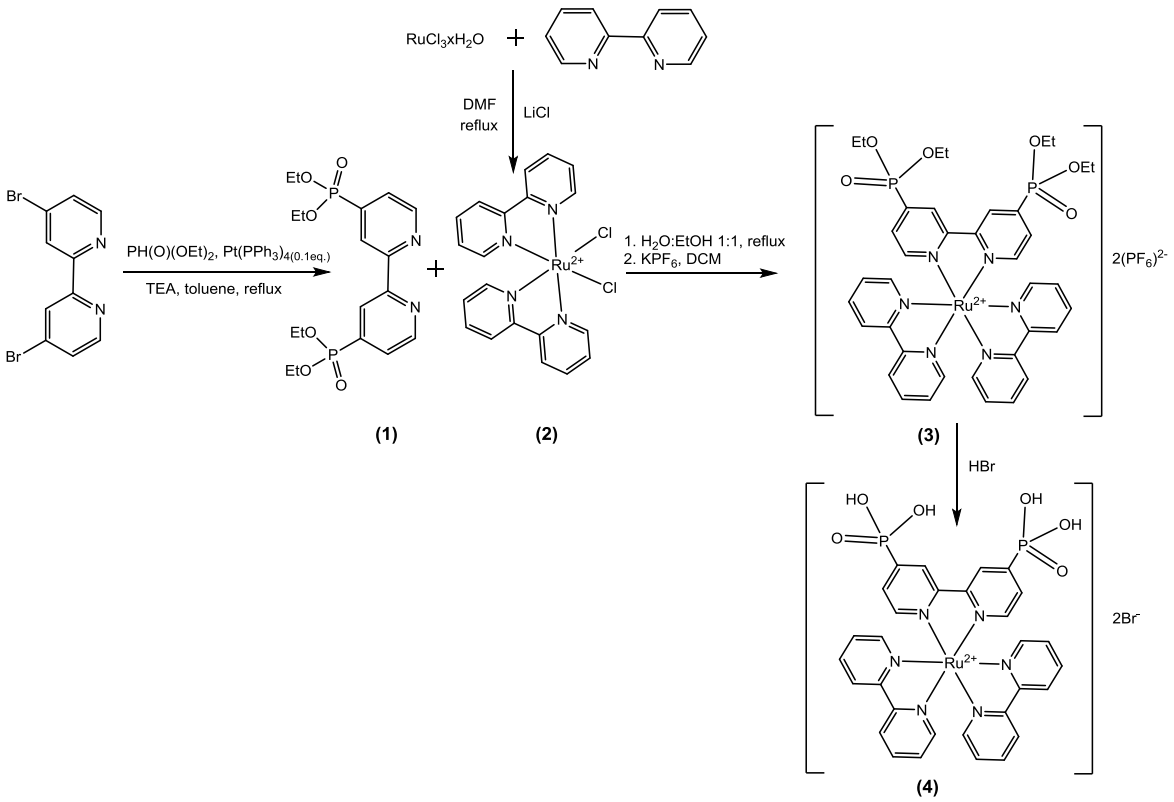

Scheme 25 – Synthetic pathway to obtain [Ru(bpy)$_2$(bpy-PO$_3$H$_2$)]Br$_2$ (RuP).

As the tetrakis(triphenylphosphine)palladium(0) catalyst is extremely air sensitive the reaction requires strictly anhydrous conditions. The pure product (**1**) is obtained *via* flash column chromatography, using a 9:1 mixture of $CHCl_3$:acetone as the mobile phase. The reaction between **1** and **2** is readily achieved by refluxing the two compounds in a mixed ethanol:water solvent for three hours, and the crude product is purified *via* column chromatography followed by ion exchange extraction to yield [Ru(bpy)$_2$(bpy-P(O)(OEt)$_2$](PF$_6$)$_2$ (**3**). Hydrolysis of the phosphonate ester (**3**) is achieved by refluxing in HBr overnight. The pure product [Ru(bpy)$_2$(bpy-PO$_3$H$_2$)]Br$_2$ (RuP, **4**) is then obtained by precipitation from methanol with diethyl ether, to give a red crystalline solid (λ_{max} = 455 nm in ethanol, in agreement with past reports). The product was found to be pure by comparison with the literature ^{1}H-NMR (NMR = nuclear magnetic resonance) and ^{31}P-NMR (Figure 65) spectra[9] and used without further purification.

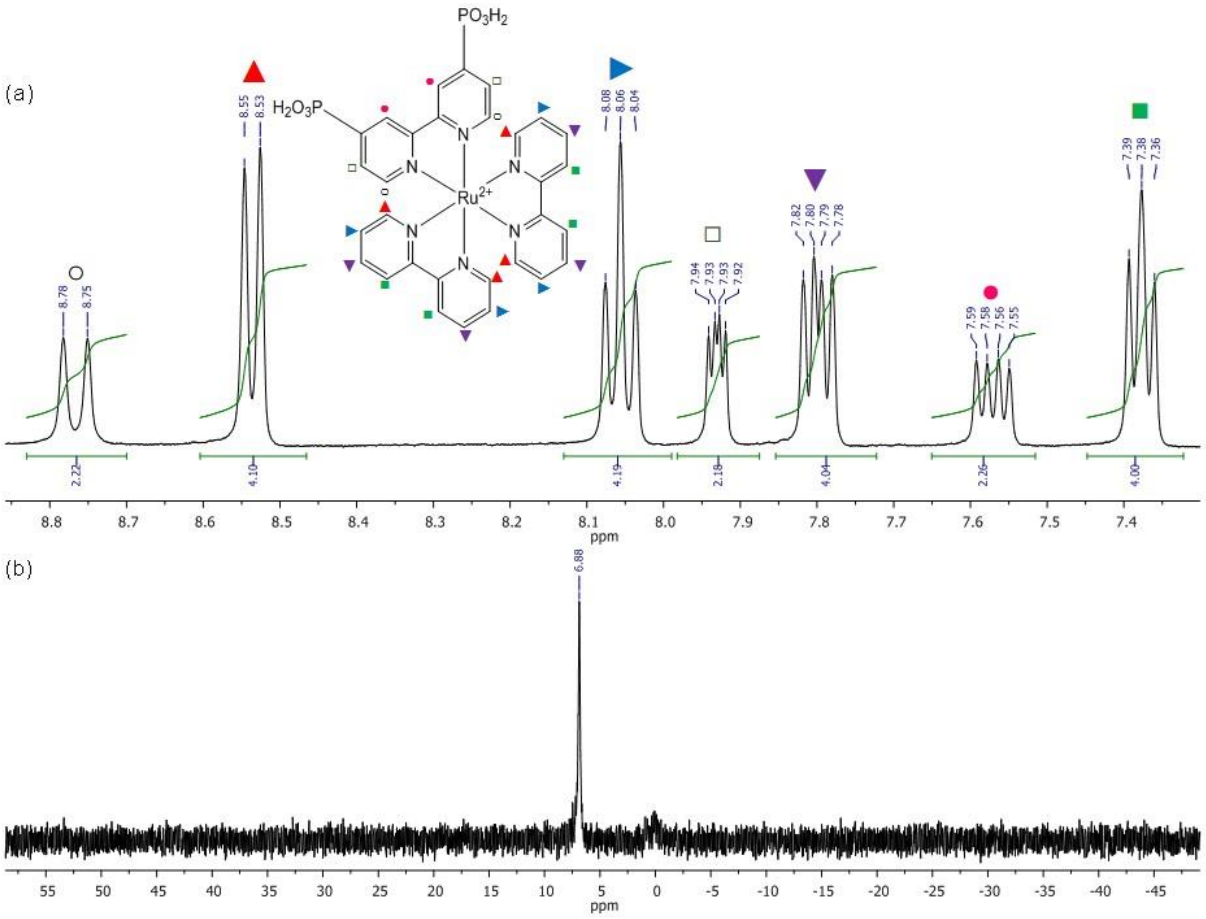

*Figure 65 – (a) ^{1}H-NMR and (b) ^{31}P-NMR of the final product RuP (**4**) in D_2O. The symbols represent the assignment of the spectrum.*

In Chapter 3 the binding of Ni(cycP) to ZrO_2 films was reported. FTIR (Fourier-Transform Infrared) spectroscopy confirmed the binding of Ni(cycP) to ZrO_2 but no attempt was made to quantify or study the stability of the ZrO_2/Ni(cycP). Here, the anchoring of RuP and Ni(cycP) to ZrO_2 nanoparticles in turn is examined in greater detail. Ethanolic solutions of Ni(cycP) (0.1 – 10 mM,) were used to soak ZrO_2 nanoparticles (Ø < 100 nm, BET surface area = 11.3 m^2/g) in a ratio of 10 mg of nanoparticles per ml of solution. The dependence of concentration of catalyst in solution can be followed during the soaking process by UV-vis spectroscopy to provide a quantification of surface binding (Figure 66).

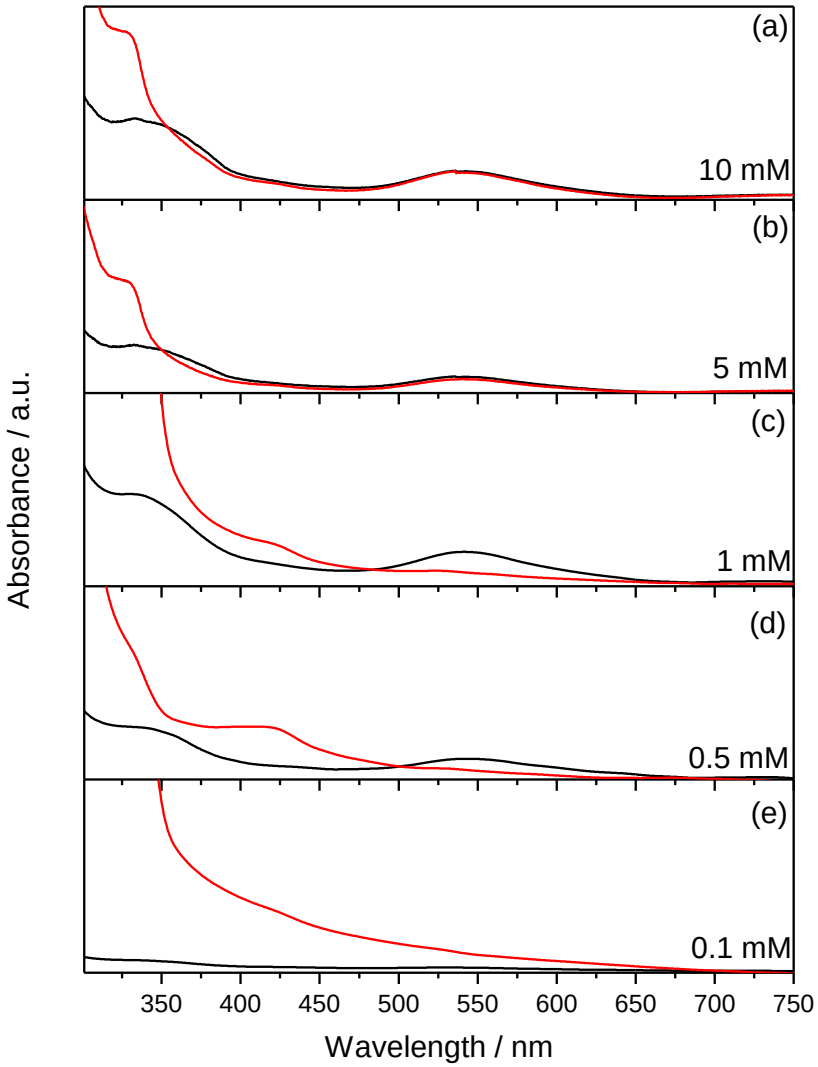

Figure 66 – UV-vis spectra of the ethanolic solutions used for immobilisation of Ni(cycP) on ZrO_2 before (black) and after (red) nanoparticles soaking, at different concentrations.

Immobilisation was attempted with Ni(cycP) concentrations of 0.1-10 mM. After 48 hours of soaking, the UV-vis absorbance of all the solutions showed a decrease, indicating that significant uptake was occurring, with the absorbance peaks at 344 and 533 nm, indicative of Ni(cycP), disappearing completely in the 0.5 and 0.1 mM solutions (Figure 66(d) and (e)). The appearance of the peak at 330 nm in the spectra can be attributed to the presence of residual ZrO_2 particles in the solution which were not successfully removed by centrifuging, while the presence of a peak at 420 nm in the 0.1, 0.5, and 1 mM soaking solutions may indicate the presence of square planar Ni(cycP), which is hypothesised to form upon adsorption of Ni(cycP) on ZrO_2 (see section 3.2.3). The presence of the

square planar complex in solution indicates the presence of an equilibrium between the complex on the surface and in solution. Assuming complete uptake of the catalyst for the 0.1 mM and 0.5 mM samples this corresponds to 5 x 10^{-5} mol/g and 1 x 10^{-5} mol/g of Ni(cycP) on the ZrO_2 nanoparticles. However this simple approach does not take into account the catalyst molecules that will not be covalently bound to the semiconductor surface, but will be physisorbed and will be removed with the ethanol washing which is carried out before drying the nanoparticles, and therefore the surface coverage calculated in this manner is not an accurate estimate. Diffuse reflectance (DR) UV-vis spectra of ZrO_2/Ni(cycP) did not show any new feature that could be assigned to the presence of the complex on the material (Figure 67), in line with the very low extinction coefficient of the complex in solution ($\varepsilon_{344\ nm}$ = 24 $M^{-1}cm^{-1}$ $\varepsilon_{533\ nm}$ = 12 $M^{-1}cm^{-1}$) and the studies of immobilisation of Ni(cycP) to ZrO_2 films, Chapter 3.2.3.

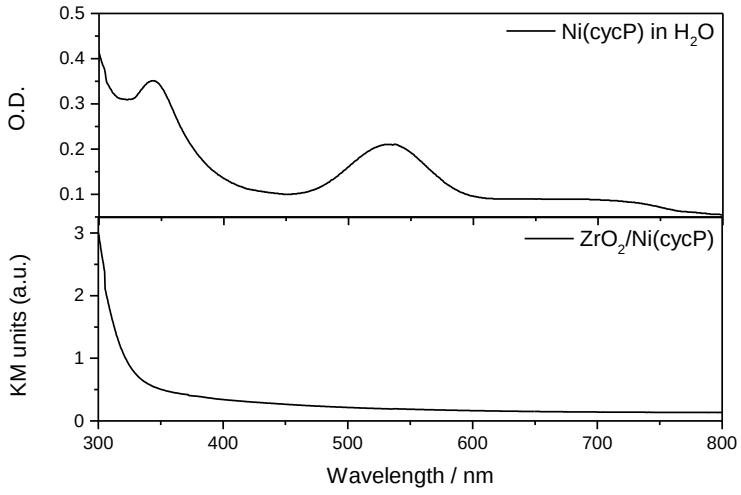

Figure 67 – UV-vis spectrum of Ni(cycP) 10 mM in water (top) and soaked nanoparticles reflectance spectrum (bottom, transformed using the Kubelka-Munk function).

The surface coverage of the catalyst on ZrO_2/Ni(cycP) nanoparticles was calculated by suspending the powder in 1 M NaOH overnight, to desorb the Ni(cycP). The resultant solution was centrifuged and Inductively Coupled Plasma Optical Emission Spectroscopy (ICP-OES) was carried out on the

resulting solution to measure the nickel content. The ZrO_2 nanoparticles commercial supplier states the average radius of the nanoparticles being 50 nm, therefore the surface area of one nanoparticle is:

$$4\pi(50x10^{-9})^2 = 3.14x10^{-14}m^2\ (3.14x10^{-10}cm^2)$$

And the volume is equal to:

$$4\pi((\frac{50x10^{-9})^3}{3}) = 5.24x10^{-22}m^3\ (5.24x10^{-16}cm^3)$$

In a typical experiment 5 mg of the ZrO_2/Ni(cycP) nanoparticles were suspended in 5 ml of 1 M NaOH, 6.5 x 10^{-8} moles of nickel were measured by ICP-OES. Considering the density of ZrO_2, d = 5.89 g cm^{-3}, the number of ZrO_2 particles in an ICP-OES experiment will be:

$$\frac{\left(\frac{5x10^{-3}}{5.89}\right)}{5.24x10^{-16}} = 1.62x10^{12}\ \text{particles}$$

With a total surface area of:

$$(1.62\ x\ 10^{12})\ x\ (3.14\ x\ 10^{-10}) = 508\ cm^2$$

The number of molecules of Ni(cycP) immobilised on the nanoparticles is given by multiplying the moles, found through ICP-OES analysis, by Avogadro's number: $(6.5x10^{-8}moles)x6.022x10^{23}\ {}^{molecules}/_{moles} = 3.9x10^{16}molecules$

Finally, the surface coverage is given by the total number of molecules adsorbed divided by the total number of nanoparticles:

$$\frac{3.9x10^{16}}{1.62x10^{12}} = 24074\ molecules/nanoparticle.$$

Considering the area of a single Ni(cycP) molecule as 8 x 10^{-15} cm^2 (based on geometric considerations extrapolated from the complex crystal structure), and the average surface area of a ZrO_2 nanoparticle as 3.14x10^{-10} cm^2, this value would correspond roughly to:

$$8x10^{-15}\ x\ 2.4x10^{4}/_{3.14x10^{-10}} = 0.61\ (61\%)$$

Which equates to over half a monolayer.

The binding of RuP to ZrO_2 has been studied elsewhere[2,9,13] and in line with past reports we observe that within 3 hours no further change in the concentration of RuP is observed for 0.1 mM solutions of the dye in ethanol in which ZrO_2 was suspended (in a ratio of 10 mg/ml), indicating rapid surface immobilisation (Figure 68).

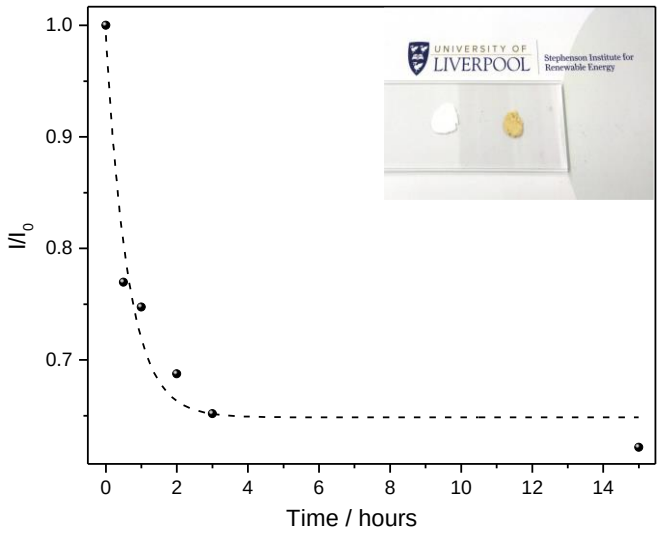

Figure 68 – Decrease in the absorbance intensity at ~460 nm for soaking solutions (starting concentration = 0.1 mM) of RuP in ethanol, recorded at different soaking times. The inset shows the ZrO_2 nanoparticles before (left) and after (right) soaking in RuP.

In a similar manner as for Ni(cycP), ICP-OES analysis of desorbed RuP was carried out by suspending the modified ZrO_2 in 1 M NaOH overnight and measuring the Ru content. For a standard sample (5 mg of ZrO_2/RuP in 5 ml of 1 M NaOH) 2.5 x 10^{-8} moles of ruthenium were found. These correspond to: $2.5x10^{-8} moles\ x\ 6.022x10^{23}\ molecules/_{moles} = 1.5x10^{16} molecules$, which in turn correspond to $\frac{1.5x10^{16}}{1.62x10^{12}} = 9259\ molecules/nanoparticle$. This result may appear much smaller than the one obtained for the nickel complex, however once the much larger size of the Ru

complex is taken into account (1.65 x 10^{-18} m^2)[2] the surface coverage results again in *ca.* half a monolayer. Studies on the coverage of RuP on semiconductor oxides usually report complete coverage after three hours,[14–16] in contrast to our results. However we note that the immobilisation *via* phosphonate linkers has been found extremely dependent on the conditions used for the anchoring, such as pH, solvent and temperature,[9,10,13] and we have made no attempt to optimise these.

The two complexes have been simultaneously immobilised on ZrO_2 by co-soaking solutions containing both RuP and Ni(cycP). The presence of both species on the surface of the nanoparticles was verified by UV-vis and ATR-FTIR spectroscopies, (Figure 69 and Figure 70). All characterisation is carried out for ZrO_2/RuP/Ni(cycP) samples prepared from a 5:1 ethanolic solution of RuP:Ni(cycP), and the rationale for the choice will be explained below.

DR-UV-vis spectra of ZrO_2/RuP and ZrO_2/RuP/Ni(cycP) are indistinguishable (Figure 69), indicating that the presence of the nickel complex does not prevent RuP binding, with the RuP band at 455 nm being the main feature of the spectrum.

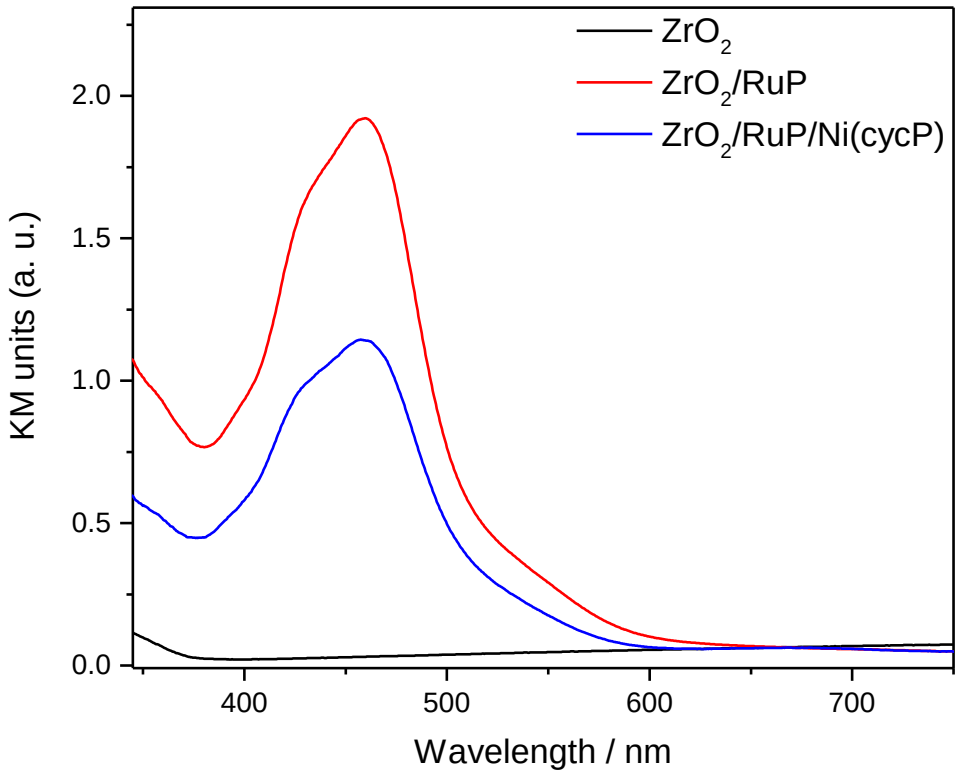

Figure 69 – Diffuse reflectance spectrum of ZrO_2 (black), ZrO_2/RuP (red), ZrO_2/RuP/Ni(cycP) (blue). The spectra have been transformed using the Kubelka-Munk function.

The ATR-FTIR (Attenuated Total Reflectance Fourier-Transform Infrared) spectrum of the RuP-ZrO_2-Ni(cycP) nanoparticles show a broadening of the bands in the phosphonate region (*ca.* 1250-900 cm^{-1}) observed in the ZrO_2-Ni(cycP) sample, Figure 70, likely due to the presence of the phosphonate bands of RuP heavily overlapping with the Ni(cycP) bands observed in the ZrO_2/Ni(cycP) sample.

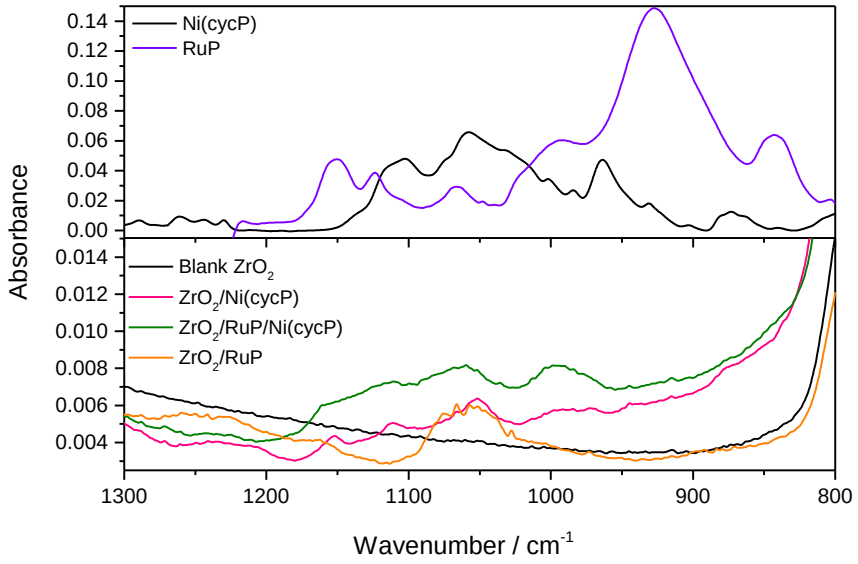

Figure 70 - (a) ATR-FTIR spectrum of powder $[Ni(cycP)]_n$ (black) and RuP (purple), (b) ATR-FTIR spectrum of blank ZrO_2 (black), RuP-ZrO_2 (orange), ZrO_2-Ni(cycP) (pink) and RuP-ZrO_2-Ni(cycP) (green).

The presence of the two complexes on the nanoparticles was instead studied by carrying out XPS spectroscopy, with the assistance of Dr Vin Danhak and Tom Whittles (Stephenson Institute for Renewable Energy). Because of the complexity of the signals under investigation, ZrO_2 samples modified with one complex, either Ni(cycP) or RuP, were initially studied to generate the fitting mode.

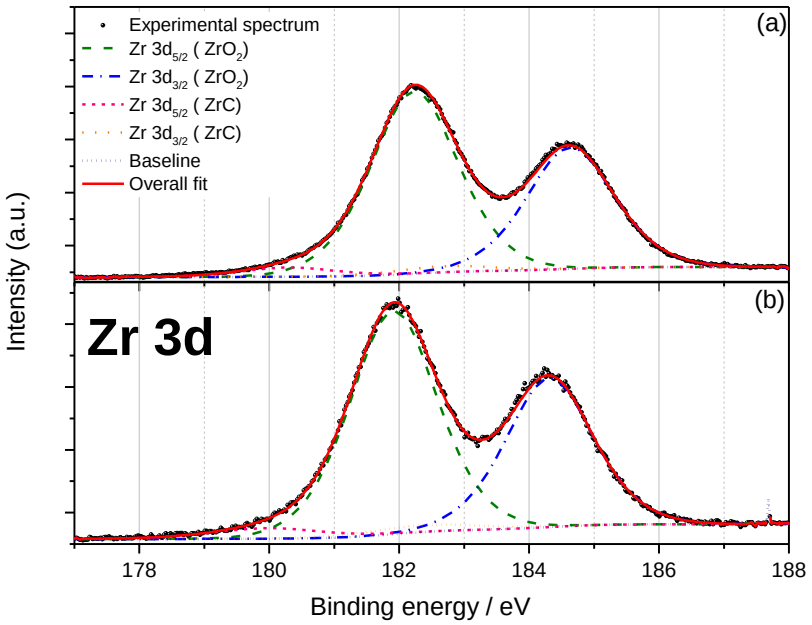

Figure 71 - Experimental and simulated XPS spectra of Zr 3d levels for a (a) ZrO_2 and (b) ZrO_2/RuP/Ni(cycP) sample.

The binding energies for Zr_{3d} in ZrO_2 nanoparticles (Figure 71(a)) show an agreement with literature values.[17–20] In addition to the peaks corresponding to the Zr $3d_{5/2}$ and Zr $3d_{3/2}$ for ZrO_2 another set of peaks at lower binding energy, which are much lower in intensity, are observed. The binding energy for these are in line with zirconium bonded to carbon, and the presence of a peak in the C 1s region, at low binding energies, further corroborates the assignment, and denotes the presence of carbon contaminant.[21] The slight shift in the binding energies for a ZrO_2/RuP/Ni(cycP) sample (Figure 71(b)) compared to a pure ZrO_2 sample is due to screening effects of the complexes on the surface.

The presence of the RuP complex on the nanoparticles was verified by analysing the Ru 3d peaks (Figure 72); these are heavily overlapped with the C 1s peaks, however the small concentration of complex on the surface prevents identification of other ruthenium peaks, which will have lower intensities. The binding energy of the Ru $3d_{5/2}$ peak is in agreement with past reports for a Ru^{2+} oxidation state,[22–24] with no noted difference between the spectra of ZrO_2/RuP (Figure 72(a)) and ZrO_2/RuP/Ni(cycP) (Figure 72(b)).

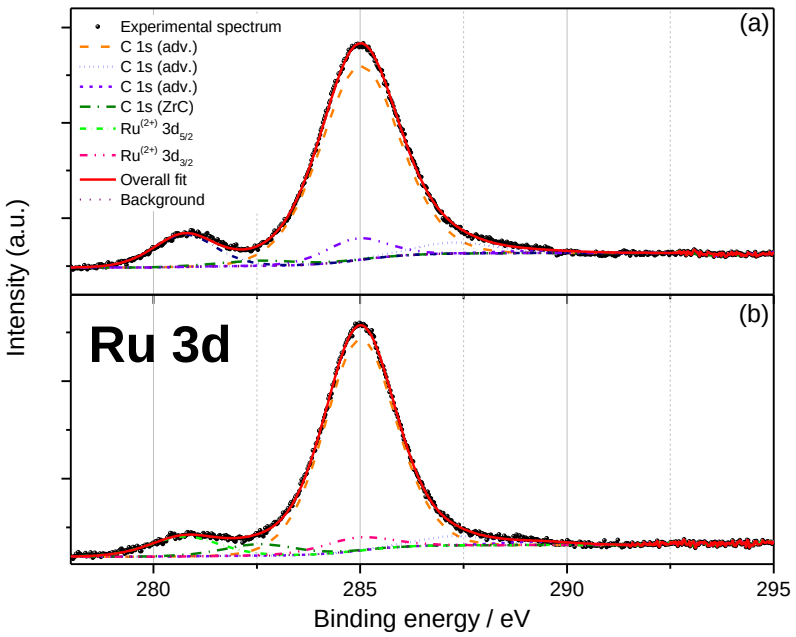

Figure 72 - Experimental and simulated XPS spectra of Ru 3d levels for a (a) ZrO_2/RuP and (b) ZrO_2/RuP/Ni(cycP) sample.

The XPS measurements were carried out by recording a survey scan of the whole spectral region, which is used to evaluate the main features present. The settings of the spectrometer are then changed to analyse the various regions of interest with a higher spectral resolution. It was noted that during the survey scan the peaks corresponding to the ruthenium appeared more intense. To further investigate this behaviour, a series of scans were recorded consecutively, Figure 73.

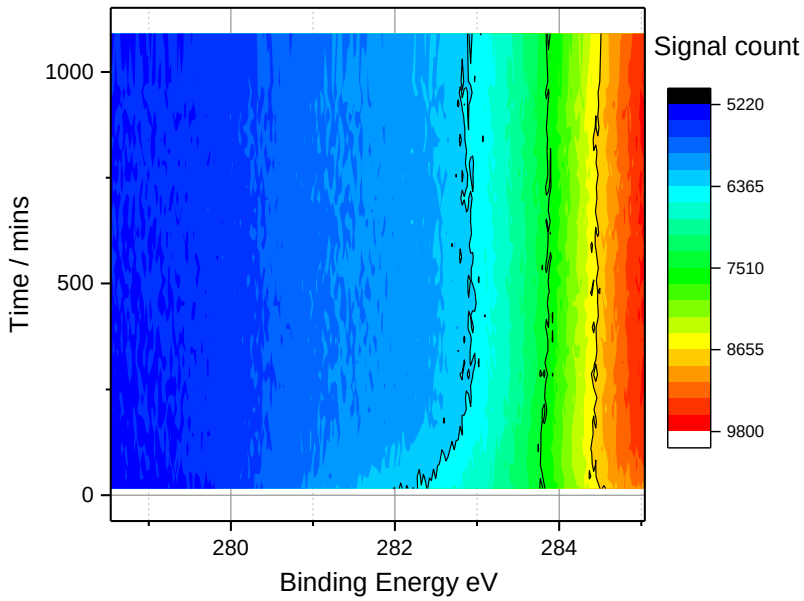

Figure 73 – High resolution XPS spectra of Ru 3d region, recorded repeatedly for a 3 h period to determine the stability of ZrO_2/RuP in the XPS experiment.

In the contour plot, red and yellow colours represent higher intensities, and blue colours represent lower intensities. The shoulder previously assigned to the Ru $3d_{5/2}$ peak clearly disappears with time, indicating that RuP is not stable during prolonged XPS measurements.

The Ni 2p peaks are regularly studied for nickel coordination complexes[25] as they provide the most intense XPS response, however they also show a complex structure involving multiplet satellites. The appearance of satellite peaks is a well-known occurrence in XPS spectroscopy,[26] and it occurs when an atom contains unpaired electrons, as is the case for a high spin nickel complex such as Ni(cycP). In these cases the core electron vacancies created during photoexcitation can be filled by coupling of the unpaired electrons in the core and in the outer shells, giving rise to a variety of states. This effect appears in the XPS as an envelope of peaks.[27]

Here, the Ni 2p was found to be extremely weak for ZrO_2/RuP/Ni(cycP), in line with expectations as the ZrO_2/RuP/Ni(cycP) sample studied is prepared with a 5:1 RuP:Ni(cycP) ethanolic solution. The XPS spectrum of Ni(cycP) alone was recorded to create a fitting model which could be propagated

to ZrO_2/RuP/Ni(cycP) and ZrO_2/Ni(cycP), Figure 74. A fitting model using one peak to fit the main core level and one peak as a satellite was used. The binding energy of the main peak on both samples corresponds to a Ni^{2+} oxidation state,[28–34] with the broadening of the bands in Figure 74(b) likely being caused by the presence of the zirconium together with the lower intensity of the nickel in this sample. The values for the binding energies calculated for all analysed samples are reported in Table 18.

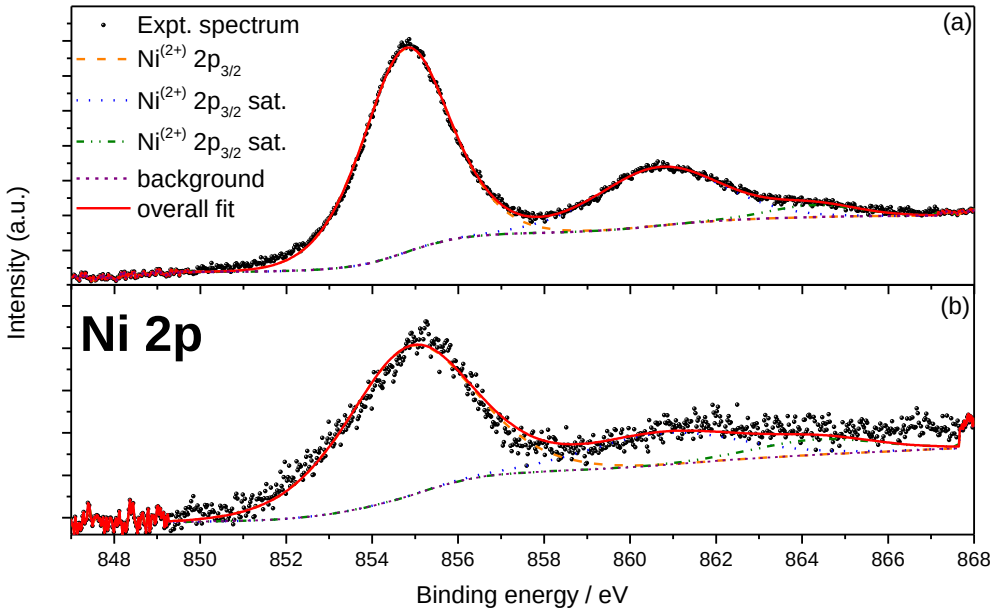

Figure 74 - Experimental and simulated high resolution XPS spectra of Ni 2p levels for (a) Ni(cycP) powder and (b) ZrO_2/RuP/Ni(cycP).

Table 18 – Binding energies values for the elements analysed with XPS spectroscopy (in eV).

Sample	Zr $3d_{5/2}$		O 1s			Ru	Ni	C 1s			
	ZrO_2	Zr-C	ZrO_2	Adv.	Ni/Ru-O	$3d_{5/2}$	$2p_{3/2}$	1	2	3	Zr-C
RuP/ZrO_2/Ni(cycP)	181.9	180.0	529.9	532.4	531.2	280.8	854.8	285.0	287.3	289.3	282.6
ZrO_2	182.2	180.3	530.2	532.4	--	--	--	285.0	287.3	289.3	282.6
ZrO_2/Ni(cycP)	181.8	179.9	529.8	532.4	531.1	--	854.8	285.0	287.3	289.3	282.6

ZrO_2/RuP	181.5	179.5	529.5	532.4	531.0	280.8	--	285.0	287.3	289.3	282.6
Ni(cycP)	--	--	--	--	--	--	854.8	--	--	--	--

4.2.2 CO_2 reduction by ZrO_2/RuP/Ni(cycP)

The ratio between the photosensitiser and the catalyst has been found to be crucial for catalytic activity in many studies.[2,35,36] In many reports the catalytic activity decreases over time due to degradation of the photosensitiser, which is very often light sensitive. Replenishing the sensitiser usually brings the activity to its initial level[37]. Having a higher ratio of light absorber molecules than catalyst would in this case improve the longevity of the photocatalytic system. In natural photosynthesis, the light harvesting process has been adapted to the low photon-flux conditions of sunlight by placing more than 30 molecules of chlorophyll (the light absorber in higher plants) surrounding the reaction centre.[38,39] This arrangement allows fast subsequent hole transfer to the reaction centre, circumventing the long timescales for light absorption in low photon-flux conditions (estimated at 1.6 photon per second[40]), and allowing the water oxidation reaction , which requires 4 electrons, to be carried out efficiently. In a similar manner it is envisaged that the presence of several light absorber molecules per catalyst molecule will provide higher light-harvesting capability in the system, allowing electron transfer from two different dye molecules to the same catalyst molecule, avoiding accumulation of highly reactive reduced species. Therefore photocatalytic studies were carried out to explore the activity of different RuP:Ni(cycP) surface concentrations.

A screening of different ratios of catalyst and photosensitiser was carried out by changing the concentration of RuP in the soaking solutions, while keeping the concentration of Ni(cycP) constant. Table 19 shows the ICP-OES results obtained for different soaking solutions. It is apparent from the ICP-OES results that the ratios of RuP and Ni(cycP) present in the soaking solutions don't reflect the ratios of Ru and Ni found on the ZrO_2 after the soaking, with the final values being lower than the

solution ratios, with the exception of the sample containing the highest concentration of ruthenium dye. This might indicate a higher affinity of Ni(cycP) with the semiconductor, rather than RuP.

Table 19 – Concentrations of Ru and Ni present in 5 mg of ZrO_2 nanoparticles soaked in solutions containing different ratios of RuP and Ni(cycP), measured by ICP-OES. [a]The concentration of Ni(cycP) was kept constant at 0.1 mM, and the RuP concentration was modified to reach the desired concentration ratio.

Sample[a]	**ICP concentration (mol l^{-1})**		**Achieved molar ratio on ZrO_2 (RuP:Ni(cycP))**
	Ru	Ni	
1:1	2.84×10^{-6}	5.00×10^{-6}	0.6
2.5:1	6.55×10^{-6}	2.69×10^{-6}	2.4
5:1	6.20×10^{-6}	2.65×10^{-6}	2.3
10:1	1.04×10^{-5}	7.24×10^{-6}	14.4

The photocatalysis was carried out by irradiating a nanoparticle sample suspended in ascorbate buffer (pH = 4, purged with CO_2 for 30 minutes), which acts as a sacrificial electron donor, with a 300 W xenon lamp (375 nm < λ < 795 nm, 40-50 mW cm^{-2}) under constant stirring, as previous studies indicated pH = 4 to be the best operating condition for Ni(cyc)[37]. The reaction products are analysed by carrying out GC of the cell headspace. Figure 75 shows the products obtained from initial screening experiments by irradiating 2 mg of each sample in 2 ml of ascorbate buffer solution at pH = 4 for a total of seven hours. Photocatalytic activity is typically reported with mass normalised rates, e.g. μmol g^{-1} hr^{-1}, where the mass is that of the photocatalyst. If the photocatalyst mass is taken to be that of the ZrO_2/RuP/Ni(cycP) we obtain a maximum CO evolution rate of 1.8 μmol g^{-1} hr^{-1}. In this approach however it is envisaged that the ZrO_2, which accounts for the largest amount of the material, is an inert scaffold, not taking part in the photocatalytic cycle. It was therefore considered more appropriate to report the results in moles per hour per gram of photoactive materials, by considering the total weight of Ru dye and Ni catalyst present in the photochemical cell, as measured by ICP-OES, while the Turnover Number (TON) is calculated by using the moles of Ni(cycP) present in the sample, and all future catalytic rates in this chapter will use this approach.

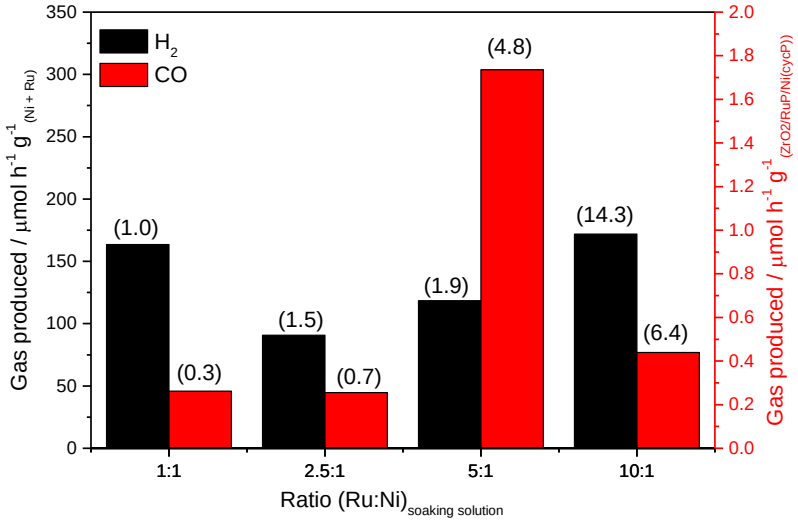

Figure 75 – Moles of gas produced by 2 mg of nanoparticles in 2 ml of ascorbate buffer at pH = 4, irradiated with 50 mW cm^{-2} of light intensity, 375 nm longpass filter, per hour of illumination per gram of active species (Ru + Ni). The y axis on the right indicates the rate in µmol g^{-1} hr^{-1} considering the powder as the active photocatalyst. The number in parenthesis is the TON after 7 hours. The Ru:Ni ratio refers to that of the original ethanolic soaking solution.

H_2 and CO are the only detected products of the photocatalytic reaction, with the ^{1}H-NMR of the post-reaction solution (Figure 76) showing only the ascorbate, with no trace of RuP desorbed from the particles, Ni(cycP) or of liquid products such as formate.

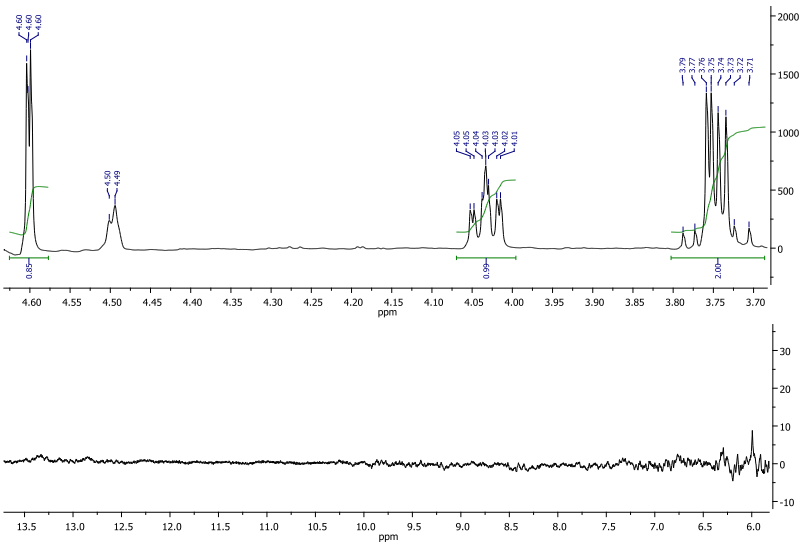

Figure 76 – ^{1}H-NMR of the post-catalysis solution, after centrifuging out the nanoparticles, with added 10% D_2O.

After 7 hours of illumination there was a marked difference in the yields of both H_2 and CO across the range of RuP:Ni(cycP) ratios examined. While proton reduction dominates for most of the samples, the 5:1 ratio showed CO to be the major product of the photocatalytic reaction. This was considered an extremely promising result, as very few CO_2 reduction photocatalysts in water are known. While it is noted that the 10:1 ratio gave a much higher TON_{CO} of 6.4 compared with the value of 4.8 obtained with the 5:1 ratio, the latter gave a higher overall yield of CO, and therefore we chose this as the main concentration for the rest of the photocatalytic experiments. Furthermore, it was initially thought that the 10:1 ratio gave poor selectivity, although it will be shown below that the H_2 yields are likely far greater than measured during the screening experiment.

During the optimisation of the photocatalytic system, a loss of selectivity was noted in repeat experiments. Intriguingly the CO yields were found to be constant and in line with Figure 75, however the H_2 levels increased. Initially, the inconsistencies were attributed to contaminations present in the quartz cell originally used for photocatalytic experiments, however this hypothesis was soon discarded, as using a new glass reaction vessel for each experiment did not bring the results to a comparable level with the initial data. Next, the aging of the nanoparticles was investigated as the cause for the poor activity, and several batches were prepared and tested at different lifetimes, however this hypothesis was disproven as well. As the CO production activity was found to be the same, there is a possibility that the initial screening experiments had significant leaks, giving an artificially high selectivity due to the higher leak rate of hydrogen. As the CO_2 → CO activity was retained across multiple experiments, including using different batches of ZrO_2/RuP/Ni(cycP) and ascorbate, and control experiments in the presence or absence of CO_2 continued to confirm that CO_2 reduction was occurring, it is concluded that the H_2 yields measured in Figure 75 were due to hydrogen leakage and don't represent the catalyst's intrinsic selectivity. For a 5:1 system repeated experiments gave a H_2 evolution rate of 1336 ± 160 μmol g^{-1} $h^{-1}_{(RuP+Ni(cycP))}$ and a CO evolution rate

of 322 ± 26 μmol g^{-1} $h^{-1}_{(RuP+Ni(cycP))}$, with a TON_{CO} of 4.8±0.38, calculated by considering the number of moles of Ni catalyst on the particles, being obtained after 7 hours of illumination.

A full set of controls was carried out to ensure that all the components of the system are necessary for CO_2 reduction to take place (Figure 77). At short timescales, the nanoparticles under argon showed *ca.* 20 times less CO than under CO_2. Removing one of the complexes (run 1 and 4) led to significantly reduced CO yields, especially when the sample did not contain any sensitiser; in the absence of nickel catalyst, some CO activity was observed, however it is likely that this was due to the increased availability of Ru, causing a faster photodegradation of the ascorbate scavenger (*vide infra*). Finally, a photocatalytic experiment without the ZrO_2 was carried out by irradiating a solution containing both RuP and Ni(cycP) in solution, with the concentration of Ru and Ni matching that in experiments 1-4, which showed only traces of CO compared to the immobilised complexes on the ZrO_2 scaffold (Figure 77, run 5, TON_{CO} = 0.2). Lastly, experiments using a 420 nm filter in place of the 375 nm show that CO production, while decreased and with reduced rate, is still occurring (Figure 77, runs 6 and 7).

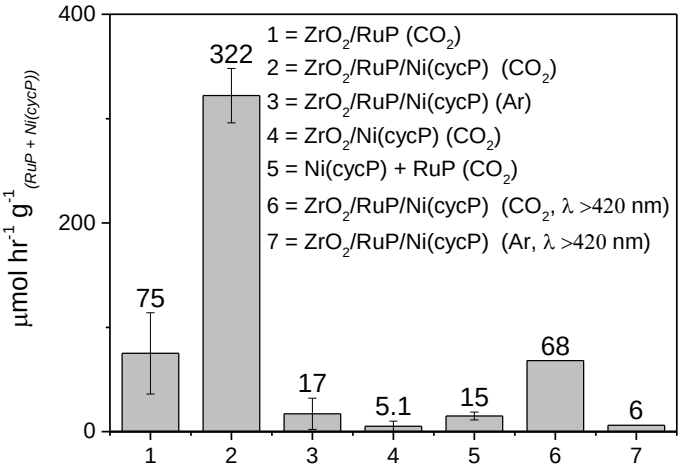

Figure 77 – CO produced during illumination for a series of different experiments. The samples for experiments 1-4 and 6-7 were prepared by suspending 2 mg of nanoparticles in 2 ml of ascorbate buffer (pH = 4), while experiment 5 was run by illuminating 2 ml of a solution that was 0.1 M in ascorbate buffer, 2.65 μM in Ni(cycP) and 6.2 μM in RuP, pH = 4, 40 mW cm^{-2}, 375 nm < λ < 795 nm (expt. 1-5) or 420 nm < λ < 795 nm (expt. 6-7).

Finally, we carried out isotopically labelled $^{13}CO_2$ experiments in order to verify that the detected CO originates from the reduction of CO_2 rather than decomposition of the components of the photocatalytic system. However, due to the lack of availability of a GC-MS, FTIR spectroscopy was used to determine whether ^{13}CO was produced. The experiment requires a substantial amount of ^{13}CO to be produced to have a high enough concentration for detection, therefore the $^{13}CO_2$ control was carried out by scaling up the sample (15 mg of the nanoparticles were suspended in 15 ml of ascorbate). The suspension was purged with $^{13}CO_2$, and the sample irradiated for 48 hours, to ensure that enough gas would be produced to allow detection. GC analysis revealed that 80 nanomoles of CO were evolved during the experiment. The headspace gas (1.5 ml) was injected in a custom-made FTIR gas cell, and the CO region of the FTIR spectrum was examined, Figure 78.

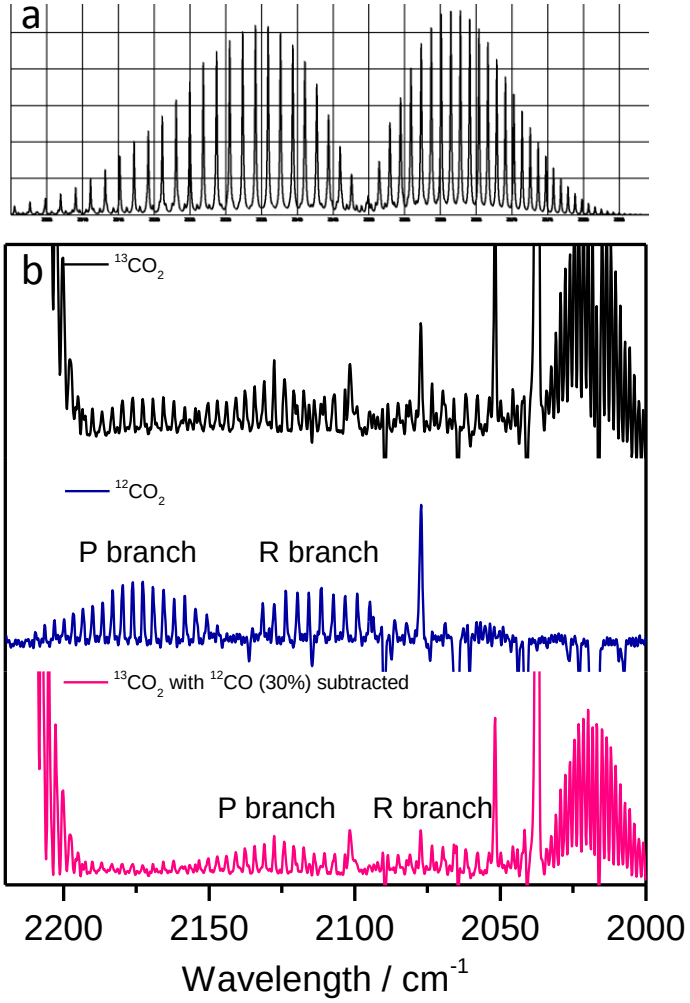

Figure 78 – a) rotovibrational spectrum of $^{12}CO_2$ at 1 atm; b) FTIR of the reaction headspace (black) for a $^{13}CO_2$ purged suspension of the modified nanoparticles after 48 hours of irradiation (40 mW cm^{-2}, 375 nm < λ < 800 nm) compared with the spectrum obtained after a $^{12}CO_2$ photocatalytic experiment (blue); the pink trace represents the top spectrum after a 30% subtraction of the blue trace.

The FTIR spectrum revealed the presence of a mixture of ^{12}CO and ^{13}CO (with the Q branch modes at 2141 cm^{-1} and 2098 cm^{-1}, respectively), with the ^{12}CO being *ca.* 30% of the total CO present in the cell (determined by subtraction of a pure ^{12}CO spectrum), showing that the majority of the product originates from the $^{13}CO_2$ dissolved in the solvent. This confirms that some photocatalytic CO_2 reduction is occurring, however the presence of ^{12}CO indicates that one of the components of the photocatalytic system is degrading during the experiment time. One other alternative is the contamination of the sample with an external carbon source (e.g. the particles were not completely dried after the ethanol washing). ICP-OES analysis of the post catalysis solution (obtained by

centrifuging the nanoparticles and diluting the remaining solution to 5 ml, the minimum amount required to carry out the analysis) shows no trace of either ruthenium or nickel in solution, suggesting that the complexes are stable on the surface of the nanoparticles within the time of the photocatalytic experiment. XPS of the nanoparticles after 48 hours of illumination was carried out. Although it was shown previously that RuP is unstable during the high resolution scans of the regions of interest, the survey scan at low resolution of the particles show the presence of the peak previously assigned to the Ru $3d_{5/2}$ level, Figure 79, indicating that RuP does not degrade during the photocatalysis, in line with the ICP-OES analysis of the solution over 48 hours.

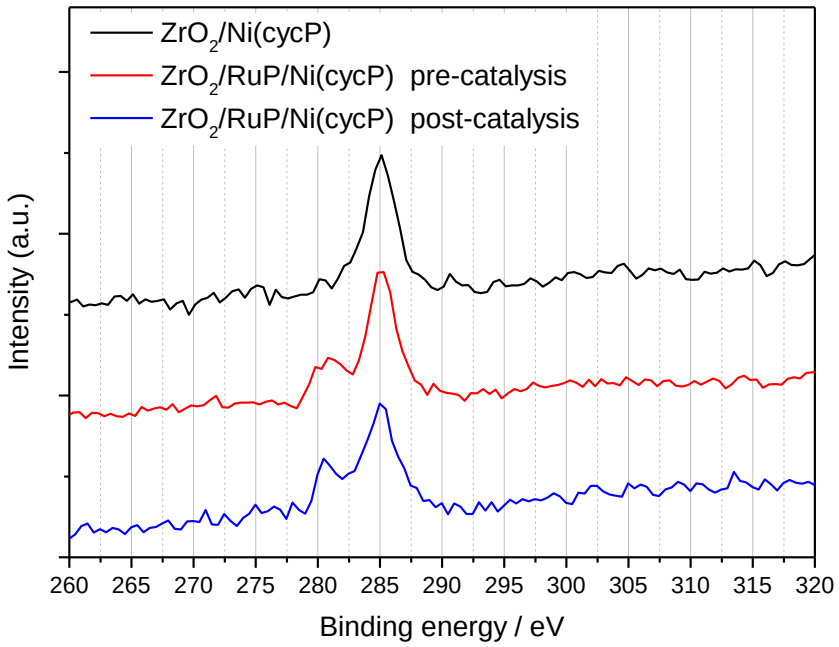

Figure 79 - Low resolution XPS spectra of the Ru 3d levels for ZrO_2/NiCycP (black), ZrO_2/NiCycP/RuP (red) and ZrO_2/NiCycP/RuP post catalysis (blue).

The XPS spectrum of the Ni 2p levels on the post catalysis nanoparticles was found to be complicated due to the high level of noise in the spectral region of interest (Figure 80), and was therefore considered inconclusive.

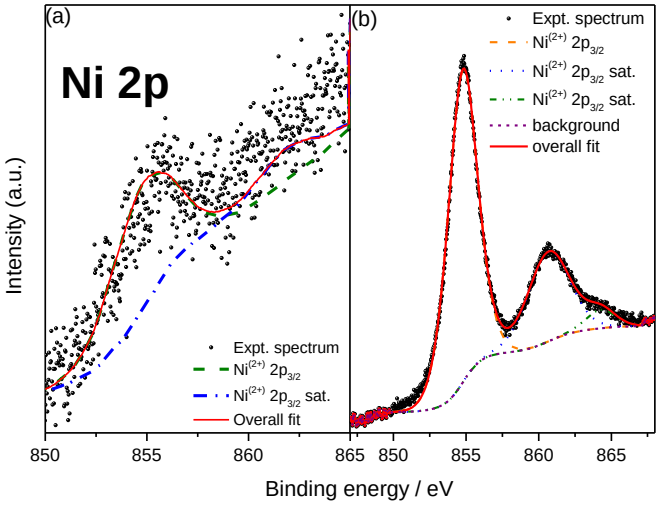

Figure 80 - Experimental and simulated XPS spectra of Ni 2p levels for (a) ZrO_2/RuP/Ni(cycP) after the photocatalysis experiment, and (b) Ni(cycP) powder.

We therefore decided to explore if the breakdown of the hole scavenger (AA) could be the cause of the additional ^{12}CO. Carrying out experiments under argon revealed that at short times (less than 20 hours) the amount of CO detected is negligible compared to the sample under CO_2 (Figure 81), again suggesting that the primary CO source is photocatalytic CO_2 reduction. However, the amount of CO at > 24 hours is significant, hence it is apparent that at prolonged periods decomposition of a component of the photocatalytic system is also giving rise to CO.

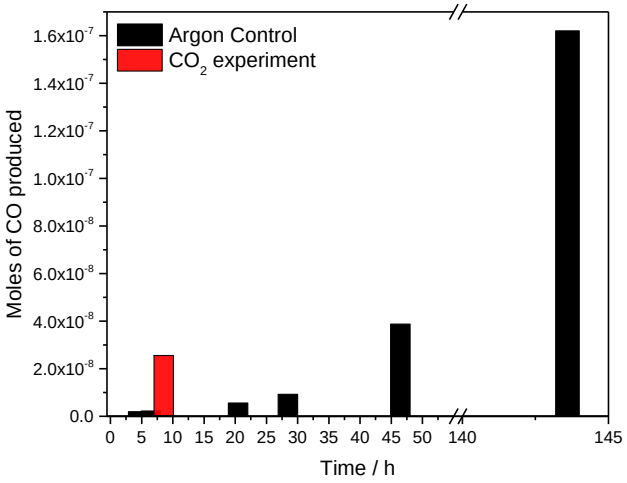

Figure 81 – Moles of CO produced during illumination (40 mW cm^{-2}, 375 nm < λ < 795 nm) of an argon purged photocatalytic sample (black). The red bar represents the typical amount of CO obtained after 7 hours of illumination of a CO_2 purged sample.

Ascorbate is well-known to degrade in the presence of light[41–43], heat[44,45] or oxygen[46–48] into a variety of products which can ultimately lead to CO being formed. As the XPS and ICP-OES analysis did not indicate significant degradation of either RuP or Ni(cycP), ascorbate break down appears the most likely source of the ^{12}CO in the labelled experiment and in the control under argon. While the $^{13}CO_2$ experiment did confirm that photocatalytic CO_2 reduction is occurring, it is important to recognise that at prolonged periods (> 20 hours) CO can also be produced *via* alternative pathways, thus CO yields measured during long experiments would be misleading. Unfortunately FTIR experiments for shorter periods did not give a sufficient signal-to-noise (S:N) ratio to determine if the ^{12}CO amount was significantly lower at <20 hours. As the control under argon showed minimal CO production for short experiment times, it was assumed that the ascorbate is stable within that timeframe, and therefore all other CO_2 reduction measurements were carried out for a maximum of 7 hours.

The data presented above shows that the on-particle approach used here has potential advantages over other systems using Ni(cyc) as a catalyst for the photochemical reduction of CO_2. The solution approach reported by Calvin *et al.*[37], which had both catalyst and sensitiser in solution, was characterised by low TONs (0.1 for CO and 0.7 for H_2) unless the sensitiser was replenished periodically, and the irradiation was sustained for long periods of time (TON = 4.8). Furthermore, the solutions for the photochemical experiments had to be quite concentrated (2×10^{-3}-10^{-4} M) to show significant amounts of gas. In line with this past study, our control experiment carried out by illuminating a solution of RuP and Ni(cycP) in solution in the absence of the ZrO_2 scaffold gave poor yields of products (*ca.* 30 times decrease in activity compared to the immobilised system), Figure 77. In addition, the same TONs ($TON_{CO} = 4.8$) were achieved within 7 hours of the suspension being illuminated, by using only a weak light source (150 or 300 W lamp, adjusted to give 40 mW cm^{-2}), compared to the 1000 W lamp used in the study. We note however, that in the best conditions, the selectivity of the solution sample was shown to be much higher than what was obtained here in repeat experiments.

The lower activity shown by the solution sample compared to the on-particle one is in line with the hypothesis that immobilising the components of the photocatalytic system would improve activity by increasing the electron transfer from the sensitiser to the catalyst. Towards the same aim a few studies have attempted to improve the yields of electron transfer by covalently binding the sensitiser to Ni(cyc) in supramolecular assemblies.[49–51] These systems do show higher stabilities when compared to the singular components in solution (in particular with regards to the Ru sensitiser), however the activities reported never showed higher activities than the solution system (the TONs reported are between 0.001 and 5).

Of particular relevance to this project was the study published by Aukauloo and co-workers[51] on a ruthenium-Ni(cyc) complex, where the authors carried out a thorough study of the kinetics of the photocatalytic reaction by the new complex. The authors used spectroscopic studies to demonstrate successful electron transfer from the Ru centre to the Ni, however they noted that recombination was still the major pathway, due to the very small driving force between the two metal centres. Furthermore, the CO_2 reduction to CO by the supramolecular complex in solution was shown, however the TON after 60 hours of illumination was only 5.2. Furthermore, the photocatalysis was carried out in acetonitrile only, while the system studied here is able to reduce CO_2 to CO in water. In the next section the kinetics of the on-particle systems will be studied with spectroscopic methods, in order to build a kinetic model and compare the immobilised system with the components in solution.

4.2.3 Transient spectroscopy

To explain the factors behind the greatly enhanced activity of ZrO_2/RuP/Ni(cycP) *versus* RuP and Ni(cycP) in solution we have carried out a series of spectroscopic studies to identify the kinetics of the key steps. The kinetic analysis was carried out on ZrO_2 thin films on glass rather than on the free nanoparticles, due to the experimental difficulties arising from a highly scattering sample such as a ZrO_2 suspension. ZrO_2 films were prepared in a similar way as outlined in the previous chapter, by

doctor blading a ZrO_2 paste made according to literature procedure on glass slides (see section 4.4.1). RuP and Ni(cycP) were immobilised on the films by soaking the films in ethanolic solutions of either RuP (0.5 mM) or RuP and Ni(cycP) (0.5 mM and 0.1 mM respectively) for 48 hours, followed by rinsing with ethanol and drying (see experimental section for more details). The films were characterised using UV-vis spectroscopy, which only showed the RuP MLCT band (Figure 82), due to the low extinction coefficient of Ni(cycP) ($\varepsilon_{533\ nm}$ = 12 M^{-1} cm^{-1}).

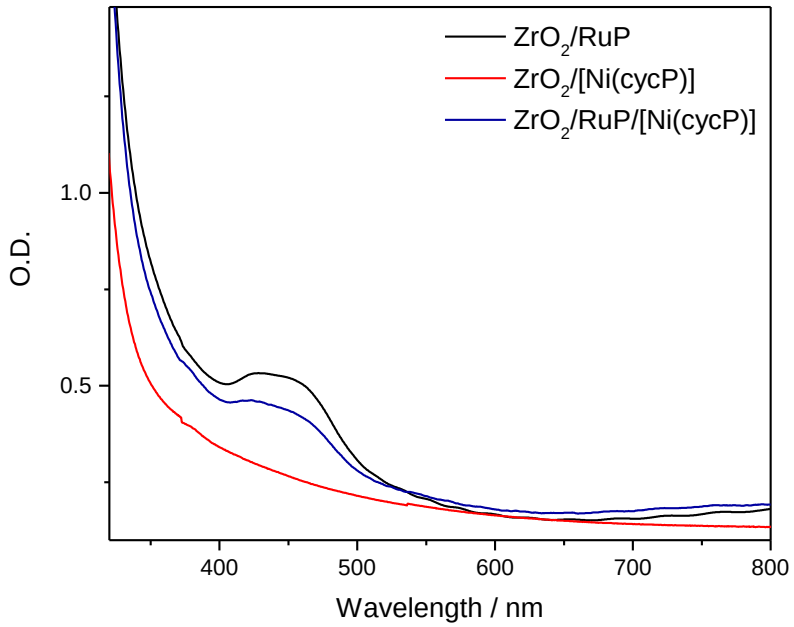

Figure 82 - UV/Vis spectra of ZrO_2/Ni(cycP), ZrO_2/RuP and ZrO_2/RuP/Ni(cycP) films.

The initial step in the photocatalytic cycle is proposed to be the excitation of RuP to an MLCT state RuP*, followed by reductive quenching by ascorbate to yield RuP^-. Steady-state emission spectroscopy of ZrO_2/RuP films in water at pH 4 (Figure 83) showed the formation of RuP* with an emission at 618 nm. The emission intensity decreased with increasing concentrations of ascorbate buffer, however it was not completely suppressed, and it remained approximately constant at concentrations of ascorbate > 0.1 M, indicating partial quenching of the emissive state.

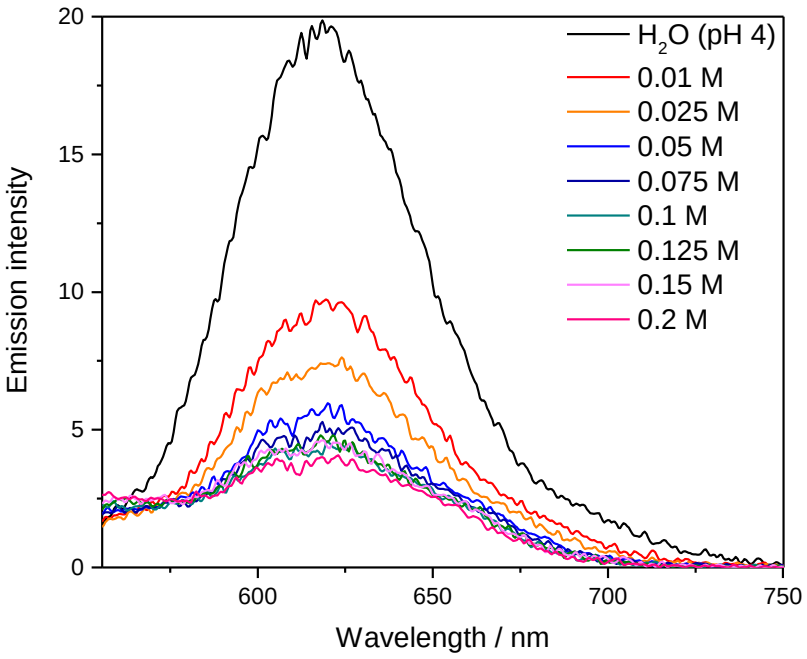

Figure 83 – Steady state emission for a ZrO_2/RuP film in argon purged solutions, recorded following excitation at 435 nm.

For freely diffusing species in solution, characterised by dynamic quenching, the relationship between the intensity of the emission and the concentration of scavenger is given by the Stern-Volmer equation:

$$F_0/F = 1 + k_q \tau_0 [Q] \quad (1)$$

Where F_0 is the emission intensity in the absence of the scavenger, k_q is the rate of quenching, τ_0 is the lifetime of emission in the absence of scavenger and [Q] is the concentration of scavenger. A plot of F_o/F should be linear, with an intercept of 1 and a slope that is equal to $k_q \tau_0$. If the emission lifetime is known it will then be possible to extrapolate the rate of emission quenching.

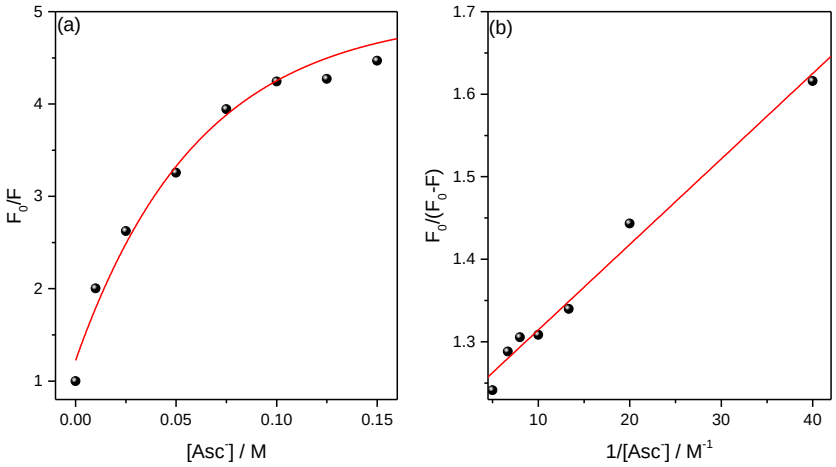

Figure 84 – (a) Classic Stern-Volmer analysis for a ZrO_2 film modified with RuP, obtained by plotting the decrease in steady-state emission with the concentration of ascorbate buffer (pH = 4), and (b) modified model accounting for immobilised RuP molecules that will be less accessible to the scavenger dissolved in solution.

The obtained relationship (Figure 84(a)) is not linear, indicating that the quenching is not completely dynamic. A similar trend in the fluorescence quenching was observed in systems with two different types of fluorophore in the system, one which is accessible to the quencher and one that has limited accessibility.[52,53] Here, it is feasible that the ruthenium dye molecules that are immobilised on ZrO_2 particles on the surface of the films are more accessible than the particles in the "bulk" of the films (Scheme 26), where diffusion of ascorbate molecules will be slower on the account of the porosity of the material, compared to the free diffusion in the solution.

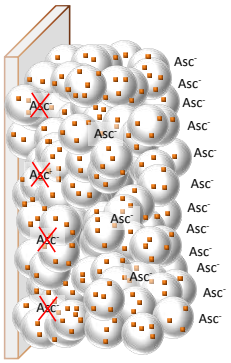

Scheme 26 – Simplified scheme showing how RuP molecules anchored on ZrO_2 particles within the film will be less accessible to ascorbate molecules, on the account of the slower diffusion through the pores in the films rather than in solution.

A modified Stern-Volmer analysis has been proposed for quenching in a system with restricted diffusion[53]:

$$F_0 = F_{0a} + F_{0i} \tag{2}$$

$$F = \frac{F_{0a}}{\left[1 + K[Q]\right] + F_{0i}} \tag{3}$$

$$\Delta F = F_0 - F = F_{0a}\left(\frac{K[Q]}{\left[1 + K[Q]\right]}\right) \tag{4}$$

$$\frac{F_0}{\Delta F} = \frac{1}{f_a K[Q]} + \frac{1}{f_a} \tag{5}$$

$$f_a = \frac{F_{0a}}{[F_{0a} + F_{0i}]} \tag{6}$$

Where F_{0a} is the emission intensity of the accessible dye, F_{0i} the emission intensity of the dye with limited accessibility, f_a is therefore the fraction of the emission intensity that is accessible to the quencher, and *K* is the Stern-Volmer constant for the quenching of the "accessible" MLCT states. A plot of $F_0/\Delta F$ *vs.* 1/[Q] should then be linear (Figure 84(b)), with the intercept being f_a^{-1} and the slope being $(f_a K)^{-1}$. Here, an intercept of 1.21 was obtained, with a slope of 7.78 x 10^{-3}, which indicates that 82% of the ruthenium is accessible to the ascorbate in solution. In order to calculate the rate constant for the quenching of RuP* by ascorbate, the emission lifetime was calculated by carrying out transient photoluminescence measurements (Figure 85). The emission decay was monitored at 650 nm following excitation with a laser pulse (355 nm, 40 μJ), taking extreme care in thoroughly purging the solution in order to avoid false values given by the presence of oxygen. In the absence of the scavenger the emission decay is well fitted to a single exponential function with a lifetime of 447 ± 6 ns. Measuring the change in emission decay upon addition of different concentrations of ascorbate would allow calculation of the rate of quenching of the excited state by the scavenger, however it is difficult to align the sample in the exact same position after each addition of ascorbate, making the

measurement challenging. A single point measurement was carried out at the concentration of ascorbate used during the photocatalytic experiments (Figure 85).

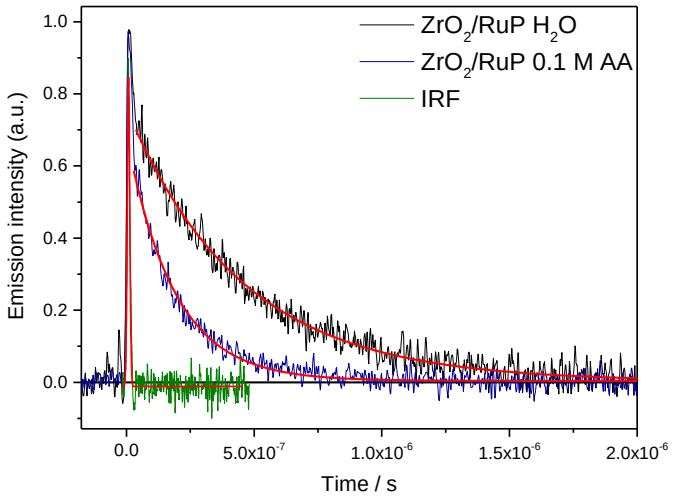

Figure 85 – Transient photoluminescence spectra of a ZrO_2 film modified with RuP in the absence and presence of ascorbate buffer (pH = 4). The sample was excited at 355 nm and the emission decay was monitored at 620 nm. The instrument response is reported for comparison.

Under these conditions the decay is much faster than for the film in the absence of the scavenger (the emission lifetime for the film in 0.1 M ascorbate was $\tau = 186 \pm 5$ ns, in line with past reports[2]), which indicates that the emission quenching is dynamic; if static quenching was the mechanism in action, the lifetime of emission would not change in the presence or the absence of the scavenger. Furthermore, in the case of a strong interaction between RuP and ascorbate, the MLCT band for RuP in the ground state UV-vis spectrum would be expected to shift in the presence of the scavenger, while this is not the case, Figure 86

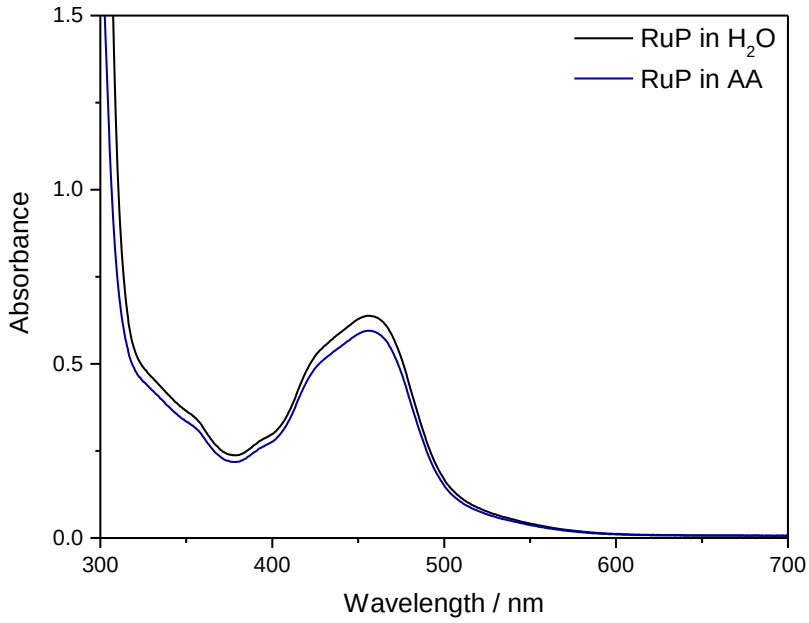

Figure 86 - UV-vis spectra of RuP in the absence and presence of ascorbate buffer (pH = 4).

The experimental trace is fitted to a single exponential function, similarly to the decay of emission in water. The calculated rate constant for the decay in presence of ascorbate was 5.48 x 10^6 s^{-1}, compared to the rate constant calculated for the film in water of 2.30 x 10^6 s^{-1}. If it is assumed that the decay in the presence of ascorbate occurs *via* a single competing pathway, the rate of quenching will be given by: (5.48 x 10^6 s^{-1})- (2.30 x 10^6 s^{-1}) = 3.18 x 10^{-6} s^{-1}, giving rise to a lifetime of *ca.* τ = 310 ns. The values calculated here indicate that *ca.* 60% of the emission is quenched by the ascorbate at this concentration, however they were extrapolated from a single point measurement. By using the emission lifetime value found here, it is possible to calculate a rate constant for quenching of RuP* by ascorbate, by dividing the Stern-Volmer constant (160 s^{-1} M^{-1}) calculated from the steady-state emission measurements (Figure 83 and Figure 84) by the emission lifetime (310 ns). This gives rise to a rate constant of 5.1 x 10^{10} M^{-1}. The value for the quenching rate constant here is higher than the limit for a diffusion-controlled process (10^9 M^{-1}), however we note that the model used to calculate the Stern-Vomer constant might not reflect the true nature of the quenching, and therefore the rate constant is an extrapolation. However, the emission lifetime value will be accurate, as it is calculated from a film in the same conditions as those used for photocatalytic experiments.

The model used here to examine the kinetics post RuP^- formation in more detail is based on the one used in the report by Aukauloo *et al.*[51] Excitation of RuP initially generates a ^{1}MLCT state, which rapidly decays to a long-lived ^{3}MLCT excited state (RuP*) This is quenched by ascorbate (AA) to generate the reduced RuP^- and oxidised ascorbate $AA^{+\cdot}$. RuP^- can then either react with Ni^{II}(cycP) to yield Ni^{I}(cycP) and RuP or undergo a back reaction with $AA^{-\cdot}$ (Scheme 27).

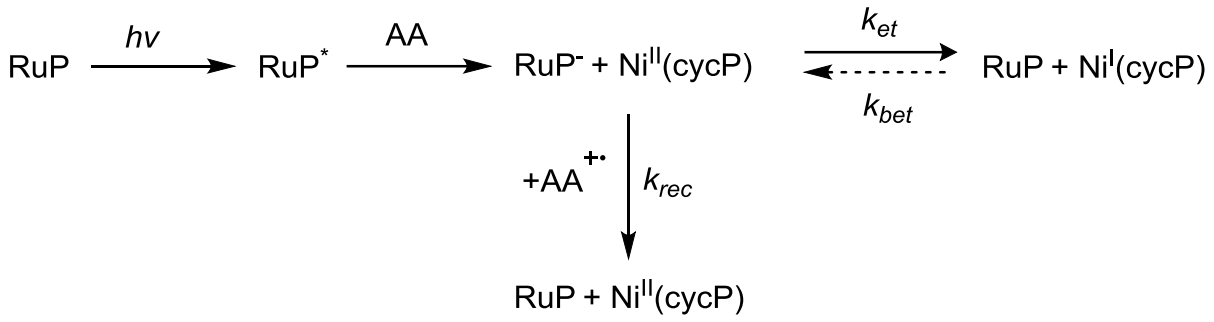

Scheme 27 – Proposed kinetic scheme for the photodriven reduction of Ni^{II}(cycP) by RuP, leading to CO_2 reduction, using the on-particle system described.

The transient absorption spectrum of a ZrO_2/RuP film in water shows an intense bleach which is partially overlapped with a positive feature at 650 nm, Figure 87. The positive peak is assigned to the MLCT state RuP → RuP^*. The negative signals arise from the ground state bleach at *ca.* 450 nm and the MLCT emission from 550 to 750 nm. It has been shown previously that RuP* is able to undergo reductive and oxidative quenching,[2] to yield either the reduced RuP^- or the oxidised RuP^+, respectively. The potentials for both species have been previously reported ($E(RuP^+ / RuP^*) = -0.95$ V_{NHE}, $E(RuP / RuP^-) = -1.1$ V_{NHE}),[54] and it is anticipated that electron injection from the RuP* or the RuP^- to the ZrO_2 conduction band edge (*ca.* -1.2 V_{NHE}[6]) cannot occur, in line with previous reports.[9,55,56] As anticipated, neither Figure 87 (a) or (b) show indication of electron injection from the excited RuP to ZrO_2, which would appear in the spectrum as a feature at *ca.* 700 nm,[9,55,56] characteristic of the formation of RuP^+. The spectrum of the film in the presence of ascorbate as the hole scavenger (0.1 M, pH = 4) shows partial quenching of the MLCT emission, with a decrease in intensity of the large bleach at 650 nm, and a new positive feature at 510 nm which is assigned to a

RuP^- species.[2] Electron injection from RuP^- has been shown not to occur[2], therefore the loss of RuP^- in the absence of Ni(cycP) is attributed to the reaction between RuP^- and oxidised ascorbate species, present in much higher concentration compared to the RuP^- species due to the known degradation pathways of ascorbate,[51] which could not be prevented even when the highest purity reagents were used.

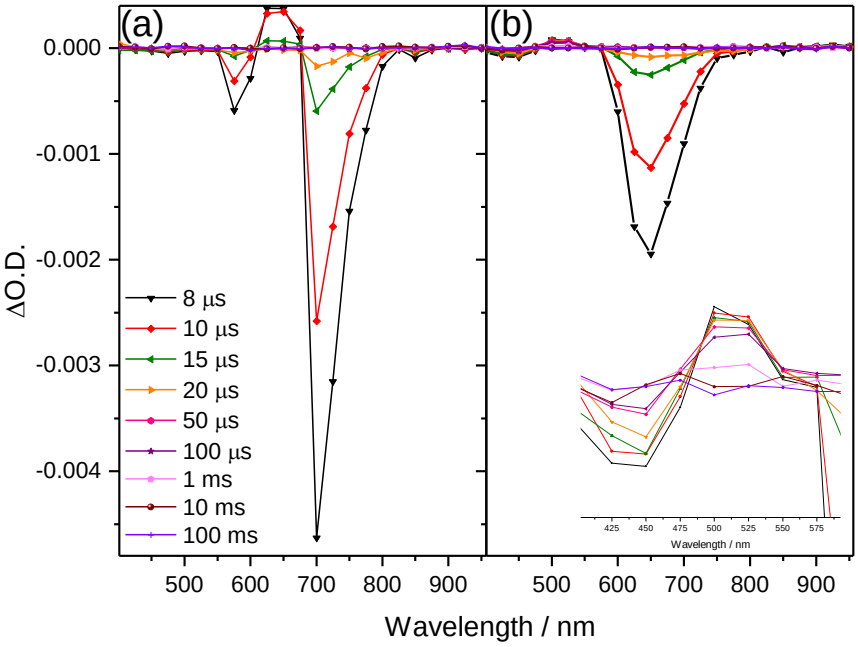

Figure 87 – Transient absorption spectra of ZrO_2 films modified with RuP in (a) water and (b) ascorbate buffer, pH = 4. Samples excited at 355 nm with a laser intensity of 150 µJ cm^{-2} under argon.

The transient absorption spectrum of a ZrO_2 film modified with both RuP and Ni(cycP) under argon is shown in Figure 88(a). The spectrum shows the same features of the ZrO_2/RuP sample in ascorbate buffer, with the bleach at 450 nm arising from the loss of the ground state, the positive feature at 510 nm indicating the formation of RuP^- and the remaining emission of the MLCT excited state at 650 nm. Again, no feature at 700 nm, indicating formation of RuP^+, was observed, confirming our expectation that RuP* and Ni(cycP) do not interact, although we note that a positive feature at that wavelength could be obscured by the strong emission peak. Interestingly, the decay of the 510 nm feature was much faster for the ZrO_2/RuP/Ni(cycP) sample than for the ZrO_2/RuP sample, indicating

that electron transfer from RuP^- to Ny(cycP) is occurring. Unfortunately, observation of the newly formed $Ni(cycP)^-$ was precluded by the low extinction coefficient of Ni(cycP) (ε_{344nm} = 24 M^{-1} cm^{-1} and ε_{533nm} = 12 M^{-1} cm^{-1} in aqueous solution). The decay of the RuP^- species (Figure 88(b)) can be fitted to a single stretched exponential function for both the sample without the catalyst and the sample with the catalyst. The stretched exponential function has the form $\Delta O.D._{510\ nm} = y_0 + A_1 e^{-(kt)^{\beta}}$, which allows the calculation of an apparent rate constant k_{app}.

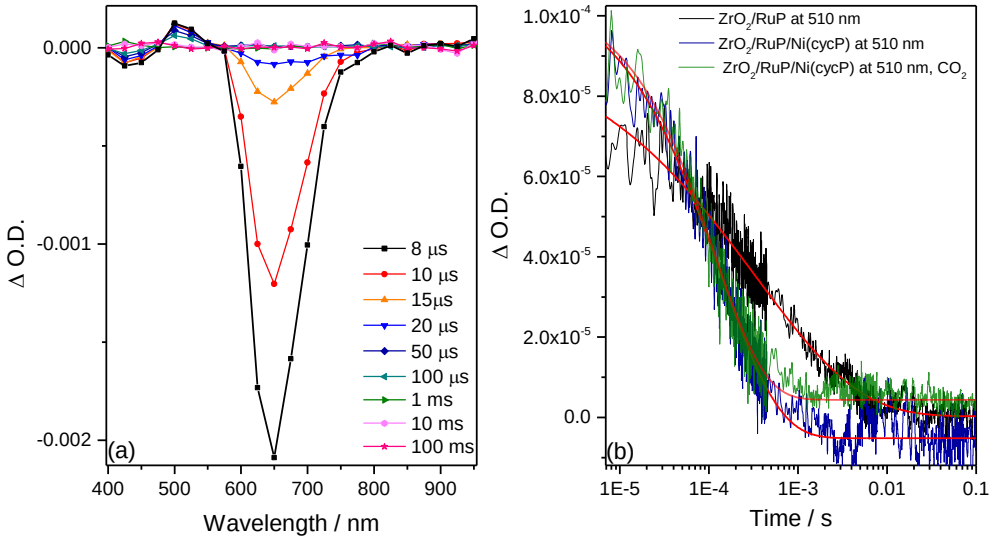

Figure 88 – (a) Transient absorption spectrum for a ZrO_2 film modified with RuP and Ni(cycP) in the presence of ascorbate buffer (0.1 M, pH = 4); the sample was excited at 355 nm with a light intensity of 150 µJ cm^{-2}. (b)Transient absorption decays at 510 nm for a ZrO_2/RuP sample in ascorbate buffer (black), a ZrO_2/RuP/Ni(cycP) sample in ascorbate buffer under argon (blue) and CO_2 (green).

During the TAS experiment, an excitation wavelength of 355 nm was used, with a low repetition rate to avoid accumulation of Ni^{I}(cycP). Under these experimental conditions it is possible to assume that [Ni^{II}(cycP)] >> [RuP^-], as (a) 355 nm is at the edge of the MLCT band of RuP, and (b) the laser intensity used for the experiments was low (150 µJ cm^{-2}), giving rise to a maximum RuP^- concentration per laser pulse (10^{13} molecules cm^{-2}) *ca.* two orders of magnitude below the concentration of Ni(cycP) on the ZrO_2 nanoparticles as calculated by ICP-OES (10^{15} molecules cm^{-2}). It follows that it is possible to approximate [Ni^{II}(cycP)]$_t$ ~ [Ni^{II}(cycP)]$_0$, and the rate equation for the loss of RuP^- will be:

$$\frac{d[RuP^-]}{dt} = -k_{et}[RuP^-][Ni(cycP)]_0 - k_{rec}[RuP^-][AA^{+\cdot}]_0 \quad (7)$$

$$\frac{d[RuP^-]}{dt} = -k_{app}[RuP^-] \quad (8)$$

$$k_{app} = k_{rec}[AA^{+\cdot}]_0 + k_{et}[Ni(cycP)]_0 \quad (9)$$

In the absence of the catalyst (ZrO_2/RuP) $k_{app} \approx k_{rec}[AA^{+\cdot}]_0$ = 1.4 x 10^3 s^{-1} (Scheme 27). In the presence of the catalyst the calculated k_{app} was much higher (k_{app} = 7.8 x 10^3 s^{-1}), which gives rise to a $k_{et}[Ni^{II}(cycP)]_0$ = 6.4 x 10^3 s^{-1}, by assuming that the two decays occur *via* simple competitive pathways, and that back-electron transfer from $Ni(cycP)^-$ to RuP does not occur as it is themodynamically unfavoured by *ca.* 0.3 V. According to the relationship in Eq. 10, which is the relative yield (ϕ) for a branch of two competing pathways in Scheme 27,[51] it is possible to estimate a yield of relative electron transfer from the dye to the catalyst in the immobilised system of 82 %.

$$\Phi_{[Ni^I(cycP)]} = \frac{k_{et}[Ni(cycP)]_0}{k_{et}[Ni(cycP)]_0 + k_{rec}[AA^{+\cdot}]_0} \quad (10)$$

The TAS kinetics for the ZrO_2/RuP/Ni(cycP) sample was recorded under CO_2 as well (Figure 88(b)), however no changes are noted when compared with the sample under argon. This is attributed to the slow nature of the CO_2 reduction reaction, which prevents the observation of charge carrier dynamics associated with this process.

The electron transfer kinetics of the immobilised system have been compared to the homogenous system by carrying out TAS measurements of the two complexes in an ascorbate solution (Figure 89), in concentrations equal to the amounts of RuP and Ni(cycP) used in the control experiment (Figure 81, experiment 5). In the absence of Ni(cycP) a k_{app} ~ 1.8 x 10^2 s^{-1} is calculated, while in the presence of the catalyst the measured k_{app} was 1.9 x 10^2 s^{-1}. This value corresponds to a $k_{et}[Ni^{II}(cycP)]^+]_0$ = 0.1 x 10^2 s^{-1}, with an electron transfer yield of 5%. The values measured here rely on a single concentration measurement, and as the inaccuracies with deriving the k_{app} from a single concentration of Ni(cycP) were deemed too high, the k_{app} was measured for a range of concentrations

of Ni(cycP); a plot of k_{app} *vs.* the concentration of Ni(cycP) should follow a linear relationship, Figure 89, the slope of which will yield the value of the molar rate constant k_{et} = 2.8 x 10^6 M^{-1} s^{-1}, in line with the previous single point measurement once the concentration of the catalyst is factored in.

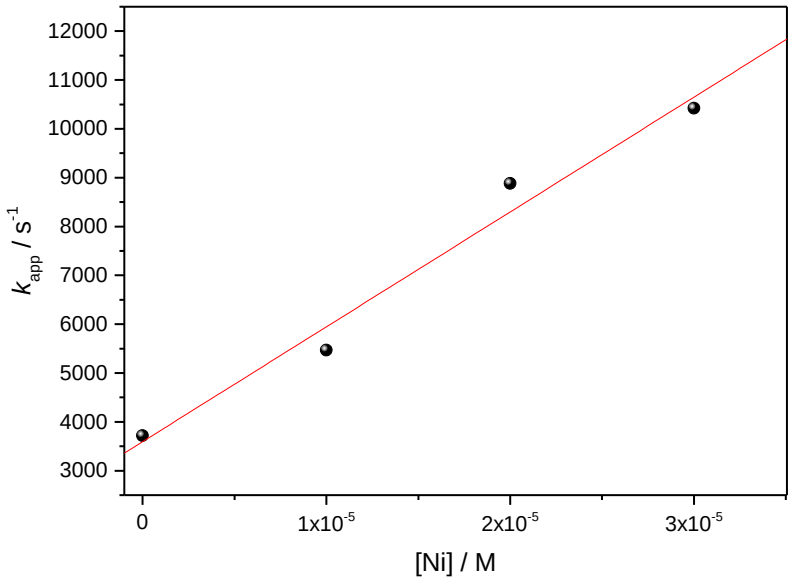

Figure 89 – Apparent rate constant relationship with the concentration of Ni(cycP), calculated by monitoring the transient absorption decay at 510 nm for a solution of RuP (9 μM), and adding increasing amounts of Ni(cycP).

The spectroscopic data presented above demonstrates the validity of the on-particle approach. The transient absorption experiments clearly show a faster electron transfer from the reduced sensitiser RuP^- to the nickel catalyst, compared to when the components are in solution (Scheme 28). Moreover, the electron transfer was found to be faster than in the previously studied supramolecular complex, with a k_{et} that was *ca.* two orders of magnitude larger.[51] This is hypothesised to be an effect of the close proximity of RuP and Ni(cycP) when bound to the ZrO_2 surface, together with the absence of covalent linkages which might hinder fast electron transfer from one metal centre to the other.

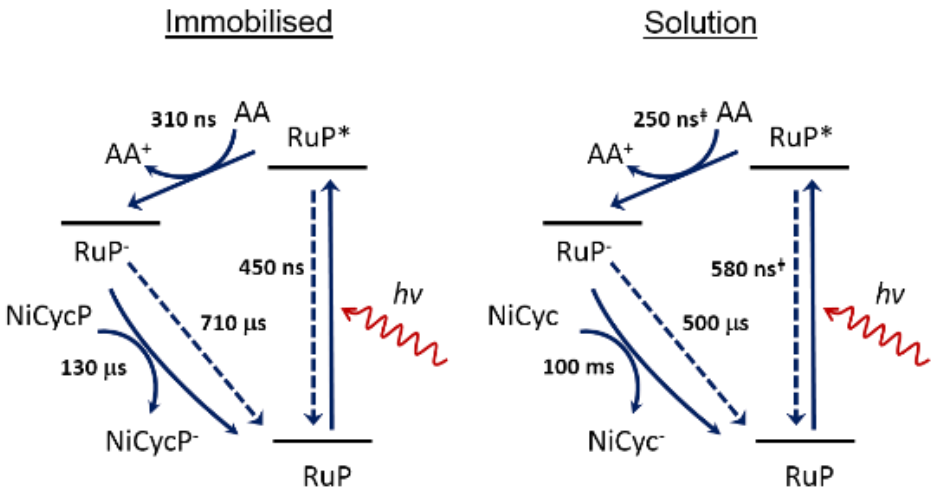

Scheme 28 - Kinetic scheme for the light driven reduction of NiCycP leading to CO_2 reduction using on particle ZrO_2/RuP/NiCycP compared to the dye and catalyst in solution. Lifetimes of exponential fits from TAS and emission studies are given in bold. ‡Values taken from ref.[2].

4.2.4 Conclusions

Immobilising a sensitiser and a molecular catalyst on an inert support with the aim of enabling fast electron transfer yielded good results for the photocatalytic reduction of CO_2 to CO. The on-particle system allowed the screening of several ratios of dye and catalyst, and the study of the electron transfer kinetics *via* spectroscopic methods. Furthermore, the photocatalytic system described is amongst the few known photocatalysts for CO_2 reduction in water. Due to time constraints, a full optimisation with the aim of increasing CO yields and suppressing H_2 production was not possible, however future studies will aim at (a) screening different hole scavengers and (b) substitute the costly RuP with a cheaper alternative.

Ascorbate has been shown to be unstable at prolonged periods of irradiation, precluding any significant studies on the stability of the system. Furthermore, the scavenging ability of ascorbate has been shown to be lower than other available systems. In particular, a study by Ishitani *et al.*[57] has recently highlighted the importance of choosing the right scavenger for each photocatalytic experiment. Testing different scavengers might prove beneficial for the selectivity of CO as well.

Ultimately, a photocatalytic device for CO_2 reduction has to operate in water, and has to be composed of cheap and abundant material. Finding an alternative dye to the expensive RuP to drive the reduction of the nickel catalyst is therefore an attractive improvement for the photocatalytic system described herein. In the next section, Ni(cycP) will be anchored on ZnSe quantum dots for the photodriven reduction of CO_2 in water, with the aim of obtaining a cheaper and more efficient system.

4.3 – Ni(cycP) anchored to QDs for the photochemical reduction of CO_2

4.3.1 Results and discussion

Attempts to use water-soluble CdS nanocrystals (capped with cysteine) (Ø ~ 4 nm) coupled to Ni(cycP) for photocatalytic CO_2 was attempted during the course of this PhD project, but no activity was achieved for CO_2 reduction; we hypothesised that the inactivity of the system was largely caused by poor electron transfer from the QDs to the catalyst, which could not be anchored on the surface of the quantum dots due to the presence of the capping ligand, hindering access to the CdS for the catalyst in solution. Furthermore, the conduction band potential of the QDs was found to be -0.7 V_{NHE}, which is not negative enough to provide the driving force necessary for electron transfer to Ni(cycP) ($Ni^{II/I}$ ~ -0.8 V_{NHE} on a surface).

Recently, a mild ligand stripping technique has been reported which yielded well dispersed quantum dots stabilised by BF_4^- anions and DMF molecules. By applying this technique, Reisner *et al.*[58] were able to significantly improve the photocatalytic production of hydrogen by CdS quantum dots decorated with a Co molecular catalyst which was functionalised with a phosphonate group. The same authors have applied the ligand stripping method to a variety of semiconductor nanocrystals for photochemical applications, and have kindly agreed to test their semiconductor samples with our nickel molecular catalysts for the visible-light photodriven CO_2 reduction. In the following section, the work carried out in collaboration with the University of Cambridge will be presented. Prof. Erwin Reisner's team has carried out the synthesis and characterisation of the stripped ZnSe quantum dots

and the photocatalytic experiments, while I have carried out the transient absorption spectroscopy experiments with Mr Jonathan Lee, of the University of Liverpool Physics department. A brief summary of the work done in Cambridge is given below, to provide a context for the kinetic studies carried out here. Dr. Moritz Kuehnel and Constantin Sahm, who carried out the work in Cambridge, kindly agreed on providing a few of their experimental results for this purpose, for which I am very grateful.

Figure 90 shows the valence and conduction band potentials for a wide array of semiconductor materials (*N.B.*, the values shown are valid for bulk materials, therefore a wider bandgap is expected for quantum dots of the materials considered), at pH 0 *vs.* NHE.

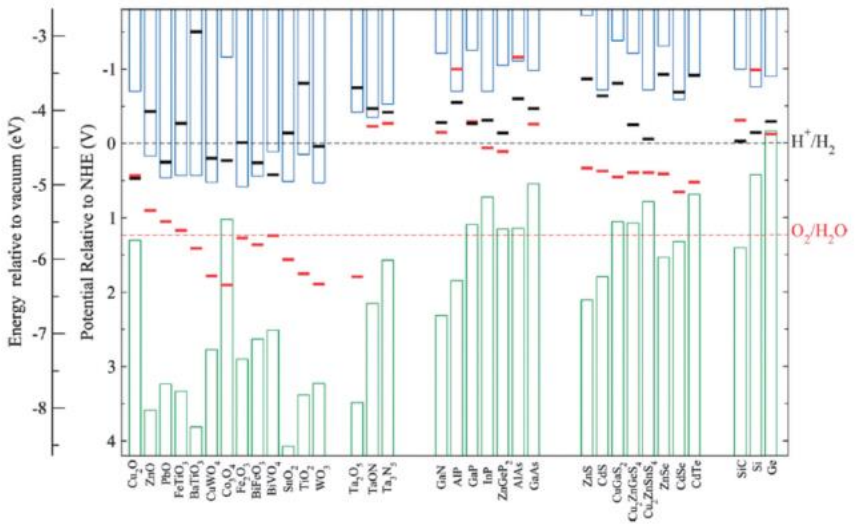

Figure 90 – Semiconductor valence band (green) and conduction band (blue) positions at pH 0, reported relatively to vacuum in eV and relative to the NHE in V. The dotted lines represent the water oxidation and reduction potentials. The black and red bars indicate the semiconductor oxidation (red) and reduction (black) potentials, which determine the stability of the material. Reproduced from [59]

Based on our electrochemical studies (Chapter 2 and 3) of Ni(cycC) and Ni(cycP), CdS, CdSe and ZnSe potentially all have sufficient driving force for electron transfer from the QDs to the molecular catalysts to occur (assuming a Nernstian shift of the conduction band edge with the pH). An initial screening of different QDs with Ni(cycC) (Figure 91) revealed ZnSe to be the best performing material, in agreement with the conduction band potential of this material being the more negative

amongst the QDs studied, therefore all the following photocatalytic and spectroscopic experiments were carried out using ZnSe QDs.

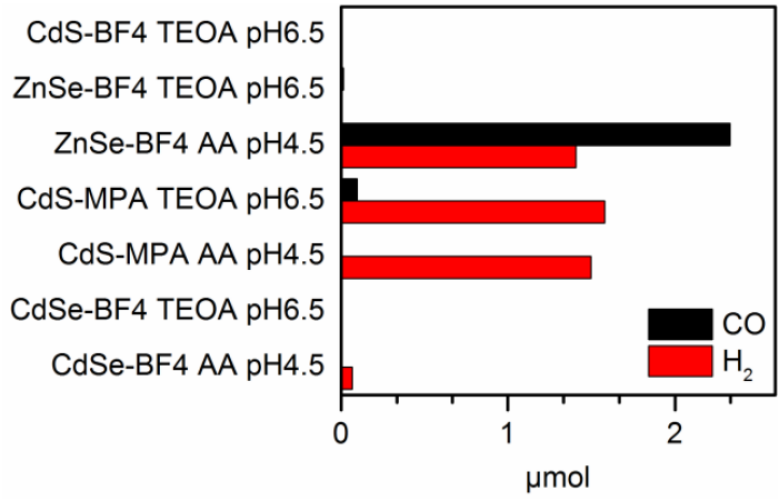

Figure 91 – Quantities of H_2 and CO generated by Ni(cycP)(200 nmoles) coupled with different QD materials and scavengers (0.1 M). Data recorded after 4 hours of irradiation under a CO_2 atmosphere (100 mW cm^{-2}, λ = 400 nm).Carried out by Dr. Moritz Kuehnel and Constantin Sahm.

4.3.2 Synthesis and photochemical studies

The quantum dots (QDs) were prepared with a heat-up method, which consists in heating a solution of $ZnSt_2$ (zinc stearate) and selenium powder in octadecene (Scheme 29). This method yields stearate-capped nanocrystals, the size of which is easily controlled by varying the reaction time and stopping the growth by rapid cooling of the reaction mixture; longer reaction times yield larger quantum dots, absorbing to higher wavelengths. The quantum dots synthesised with this procedure are insoluble in polar solvents, due to the long alkyl chain of the stearate capping ligand. The particles were stripped of the ligand using a recently reported method,[60] to obtain BF_4^- capped particles (Scheme 29), which are easily suspended in DMF to give clear yellow suspensions.

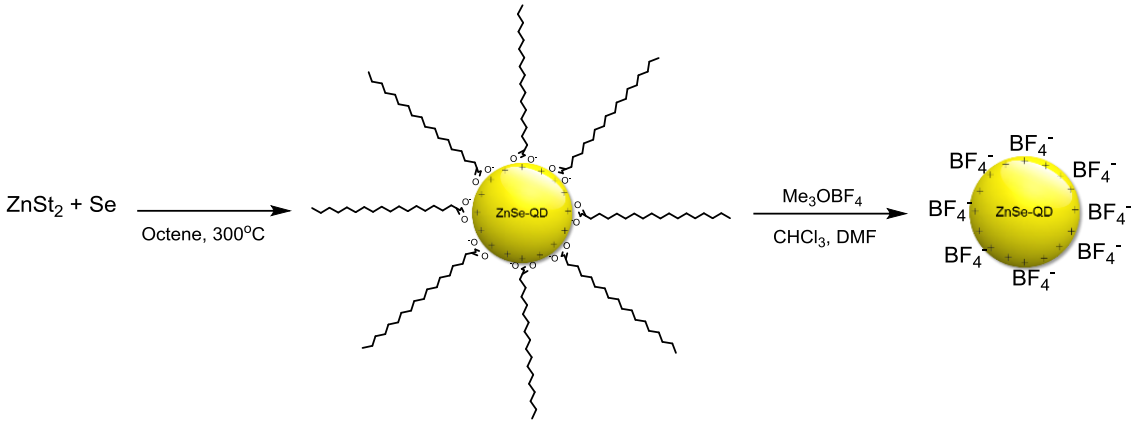

Scheme 29 – Synthethic steps to obtain "stripped" ZnSe-QD stabilised by BF_4^- anions. Carried out by Dr. Moritz Kuehnel and Constantin Sahm.

The particles have been characterised by TEM, powder X-ray diffraction, UV-vis and IR spectroscopy, which revealed well dispersed, highly crystalline particles with an average size of 4.5 ± 0.53 nm; the as-prepared suspension of the quantum dots is highly concentrated, with the concentration (measured by inductively coupled plasma optical emission spectroscopy, ICP-OES, and considering the average number of Zn^{2+} atoms per QD) varying significantly in different batches.

Ni(cyc), Ni(cycC) and Ni(cycP) prepared at the University of Liverpool were all tested for their ability to anchor to the stripped QDs, by stirring a solution of QDs and catalyst (0.5 μM and 10 μM, respectively) in water for 2 hours, then centrifuging the QDs out of the supernatant liquid and measuring the content of Zn and Ni by ICP-OES. Figure 92 shows the results obtained for the three complexes. Surprisingly, Ni(cyc)shows a degree of adsorption which is comparable to the carboxylic acid derivative, with the phosphonic acid derivative showing higher uptake: 13% of the complex present in the soaking solution binds on the QDs, corresponding to 2.52 moles of Ni(cycP) per mole of QDs.

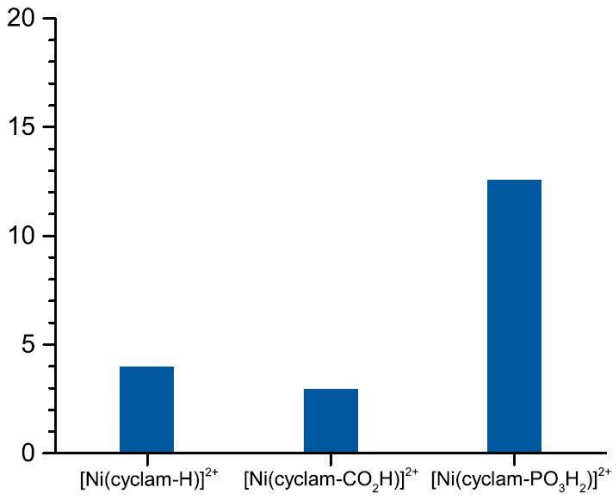

Figure 92 – Catalyst uptake by the ZnSe-QD, expressed in % relative to the initial amount of catalyst present in the soaking solution. Carried out by Dr. Moritz Kuehnel and Constantin Sahm.

A screening of the three different complexes for photocatalytic CO_2 reduction was carried out by irradiating a CO_2 purged solution of the QD, catalyst and ascorbate buffer as the hole scavenger (pH 5.5) with visible light and measuring the gas headspace with GC (Figure 93). The results indicated that Ni(cycP) gave the higher yield of CO compared to Ni(cyc)and Ni(cycC), indicating that a higher amount of anchored catalyst promotes electron transfer.

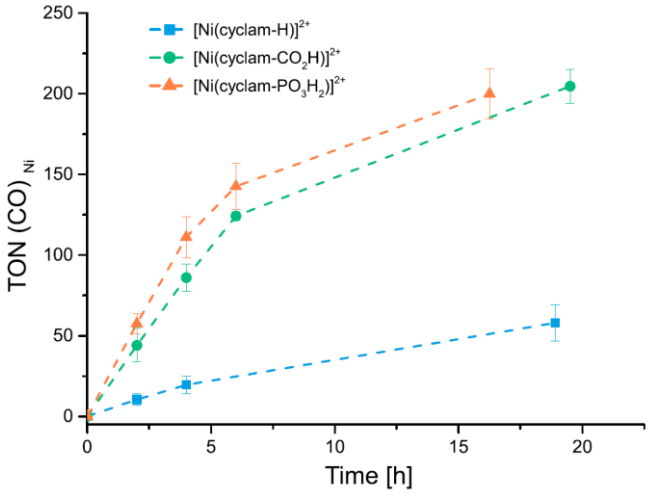

Figure 93 – TON of CO (relative to the amount of Ni catalyst present in the system) obtained by the three catalysts studied. Carried out by Dr. Moritz Kuehnel and Constantin Sahm.

Despite the similarity of affinity for ZnSe of Ni(cyc) and Ni(cycC), a large difference in TON_{CO} is observed, likely indicating that the binding of Ni(cyc) is more labile compared to Ni(cycC), due to the absence of a suitable binding group on the catalyst framework. Due to the higher TON_{CO} obtained with Ni(cycP), this complex was chosen for further optimisation. Optimisation was carried out by the Cambridge University team by screening different hole scavengers, pH values, QDs concentration and catalyst loading. The best results were obtained using ascorbate buffer at pH 5.5 (0.1 M), using a 0.5 μM suspension of QDs with a catalyst loading of 1:20 (catalyst concentration = 10 μM). The best result was chosen as a compromise between yield of CO and selectivity of CO over H_2. Indeed, even the best system shows significant hydrogen production, with a selectivity of *ca.* 30% after 4 hours of irradiation, however this was attributed to free surface sites on the stripped QDs promoting the side reaction. The addition of small amounts of 2-(dimethylamino)ethanethiol (DMAET) (1:50 ratio of QD:DMAET), a capping ligand, was found to greatly reduce the amount of hydrogen produced during photocatalysis, giving a selectivity of 45% compared to the sample without DMAET (30%). Interestingly, as well as inhibiting proton reduction, the addition of DMAET causes a dramatic increase in CO production, with a TON_{CO} of 300 after 17 hours, compared to the value of *ca.* 200 obtained with the sample without DMAET in the same conditions. It is proposed that DMAET binds to the QDs *via* the thiol group, leaving the amino group free, which is likely to be protonated at pH 5.5, giving the nanoparticles a net positive charge. This could hinder proton penetration to the surface due to electrostatic repulsion, lowering H_2 production, and increasing catalyst uptake on the QD, therefore increasing CO production.

Several control experiments were carried out to ensure that all the components of the photocatalytic system were essential for CO_2 reduction. All the control experiments showed only small amounts of CO produced. In addition, photocatalytic experiments ran in the presence of $^{13}CO_2$ showed the presence of only ^{13}CO, as measured by IR spectroscopy. Finally, the external quantum efficiency

(EQE) was measured to be 3.9% for H_2 and CO evolution combined, calculated according to the following equation:

$$EQE\ (\%) = \frac{2\ nCON_A hc}{t_{irr}\lambda IA} \quad (10)$$

Where nCO is the number of moles of CO, N_A is Avogadro's number, h is Planck's constant, c is the speed of light, λ is the wavelength of irradiation, I is the light intensity and A is the illuminated area.

4.3.3 TAS spectroscopy of ZnSe QDs

The ultrafast dynamics of charge carriers in ZnSe quantum dots have been studied in the past with TA spectroscopy.[61] The samples reported were ZnSe nanocrystals capped with thioglycolic acid (TGA) and dispersed in aqueous solution, and therefore are different from the QDs studied here, however the data already reported can be used as a guideline to identify the main spectral features. The sample received from Cambridge was a concentrated sample of the stripped QDs in DMF (0.1733 mM as determined by ICP-OES), to use as stock for the preparation of dilute samples for the spectroscopic experiments. It was found that the QDs have a strong tendency to aggregate upon addition to an aqueous solution, causing precipitation of the QDs out of solution and making the measurement of the transient spectra challenging. As the particles are well dispersed in DMF, the quantum dots in this solvent were studied first, using the same concentration of QDs typical of a photocatalytic experiment. The detailed protocol is described in section 4.4.1; briefly, 5.8 μl of the stock solution were diluted in 2 ml (the final concentration of the QDs was 0.5 μM). The steady state UV-vis and emission spectra were measured, (Figure 94). The UV-vis spectrum showed a strong feature at 415 nm, which corresponds to an electronic transition from the valence band to the conduction band, and a tail, commonly observed in semiconductor nanocrystals,[62–67] which may indicate the presence of a series of close energy states to either the valence band or the conduction band, due to defects in the material. The emission spectrum recorded after excitation at 310 nm showed an emission maximum at 460 nm and a tail of emissive states at higher wavelengths.

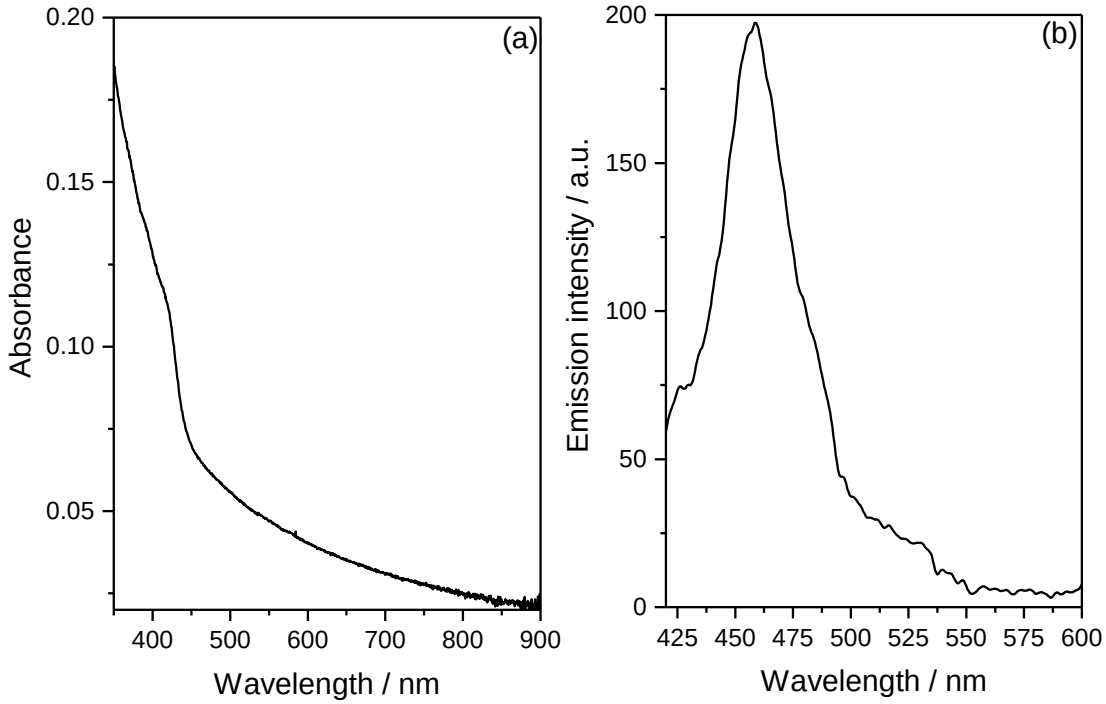

Figure 94 – (a) Ground state UV-vis spectrum of the DMF colloidal solution (0.5 μM) prior to the TAS experiment, and (b) emission spectrum of the DMF colloidal solution, recorded following excitation at 310 nm.

Based on the steady state spectra obtained, two possible models for electron-hole separation and recombination were proposed, where (i) the excited electrons decay to trap states close to the conduction band edge, and subsequently recombine, giving rise to the tail observed in the emission spectrum and (ii) trap states close to the VB edge are present in the material, which give rise to trapped holes followed by recombination[67] (Scheme 30).

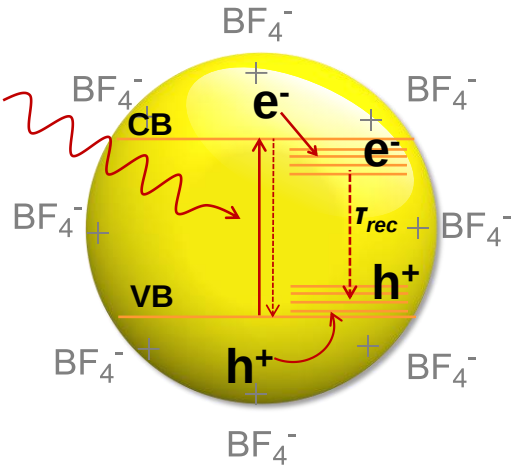

Scheme 30 – The likely charge carrier dynamics for the ZnSe-QD suspended in DMF.

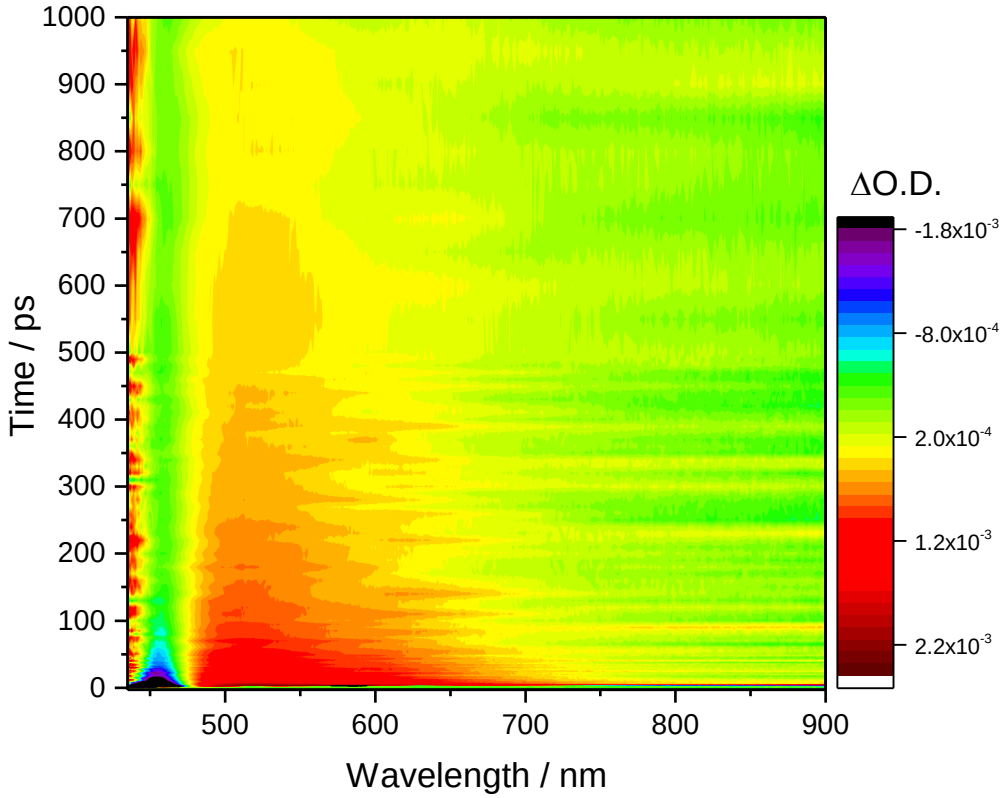

Figure 95 – Ultrafast transient absorption spectrum for a sample of QDs in DMF. The sample was excited at 400 nm.

The transient spectrum of the ZnSe-QD in DMF was recorded by exciting the sample at 400 nm and monitoring absorbance changes in the 400-900 nm range, as shown in Figure 95; the colour plot shows ΔO.D. as a function of time and wavelength, where blue tones are negative signals and red and orange are positive signals. A strong bleach, which represents the loss of the ground state absorption

(Figure 95), was observed at 455 nm, followed by a broad positive signal at *ca*. 500 nm. The decay of the two main features can be fitted to a double exponential function, Figure 96(a), with lifetimes of $\tau_{1(450\ nm)} = 3 \pm 0.2$ ps and $\tau_{2(450\ nm)} = 32 \pm 3$ ps for the negative feature and $\tau_{1(500\ nm)} = 22 \pm 2$ ps and $\tau_{2(500\ nm)} = 366 \pm 22$ ps for the positive feature. The positive signal has been previously assigned to photoholes,[61] in line with our emission studies, therefore this formed the starting hypothesis. The decay of the positive signal indicates that recombination is a fast process on the order of picoseconds.

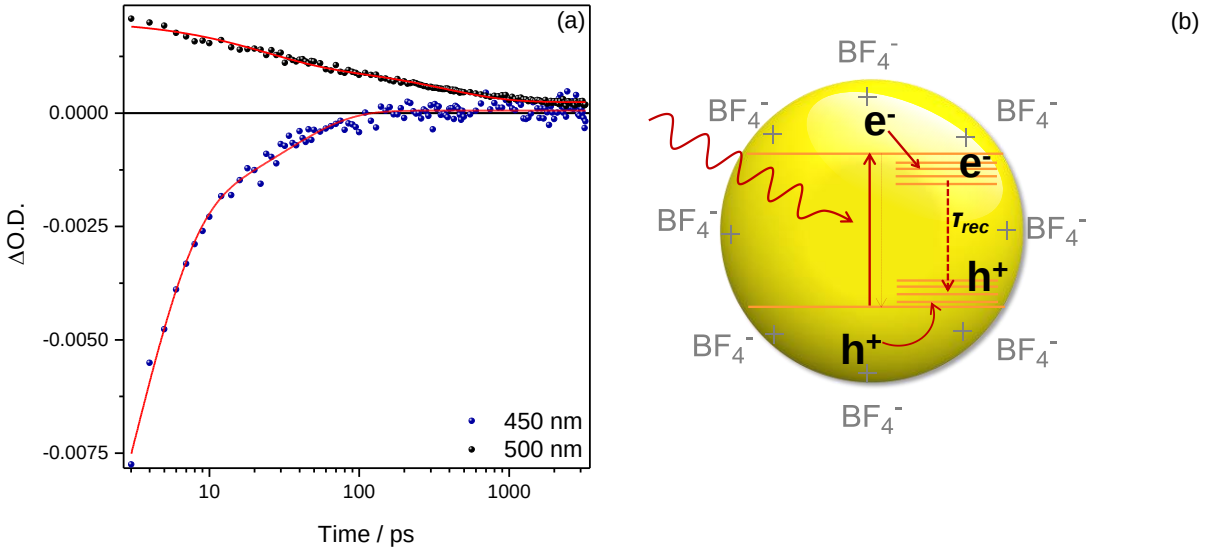

Figure 96 - (a) Transient absorption decays for the QDs in DMF measured at 450 and 500 nm and (b) scheme of the charge carrier dynamics occurring during the TAS experiment.

Spectra of the QDs in neat water were challenging to obtain, due to the rapid aggregation of the nanocrystals in this solvent, even when the sample was prepared rigorously under argon (the presence of trace oxygen was observed to significantly accelerate aggregation). Adding the capping ligand DMAET, in the concentrations used for the photocatalytic experiments, proved to stabilise the QDs enough so that spectra could be obtained. Unfortunately experiments in DMF with added DMAET were not possible. The steady state spectra are shown in Figure 97.

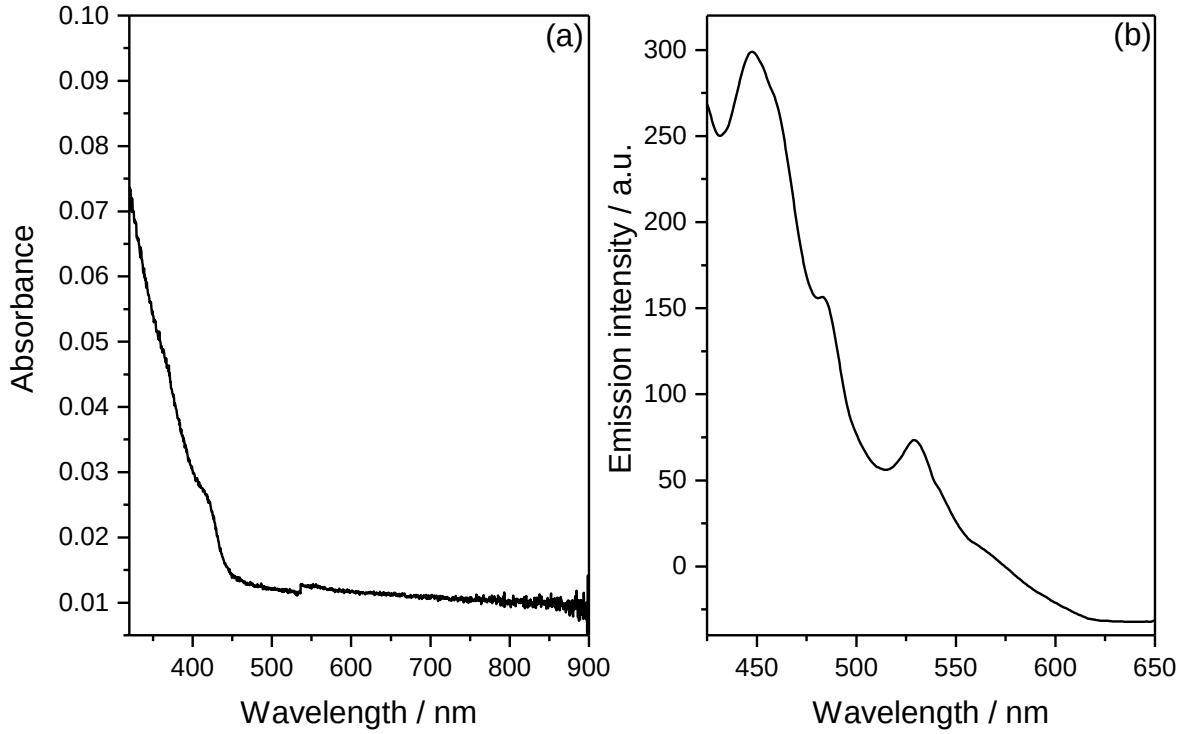

Figure 97 - (a) Ground state UV-Vis spectrum of ZnSe-QD (0.5 μM) in H_2O containing DMAET in a 50:1 ratio DMAET:QD prior to the TAS experiment, and (b) emission spectrum of the same colloidal solution, recorded following excitation at 310 nm.

The UV-Vis spectrum (Figure 97(a)) of the ZnSe in the aqueous solution was found to be similar than the one of the DMF sample, however the emission spectrum (Figure 97(b)) clearly showed the presence of more defined states within the emission tail, at *ca.* 485 and 530 nm, indicating that in water the emissive states previously observed in the DMF solution are more prevalent. This is tentatively attributed to the number of defects increasing on the QDs due to the poor stability in water.

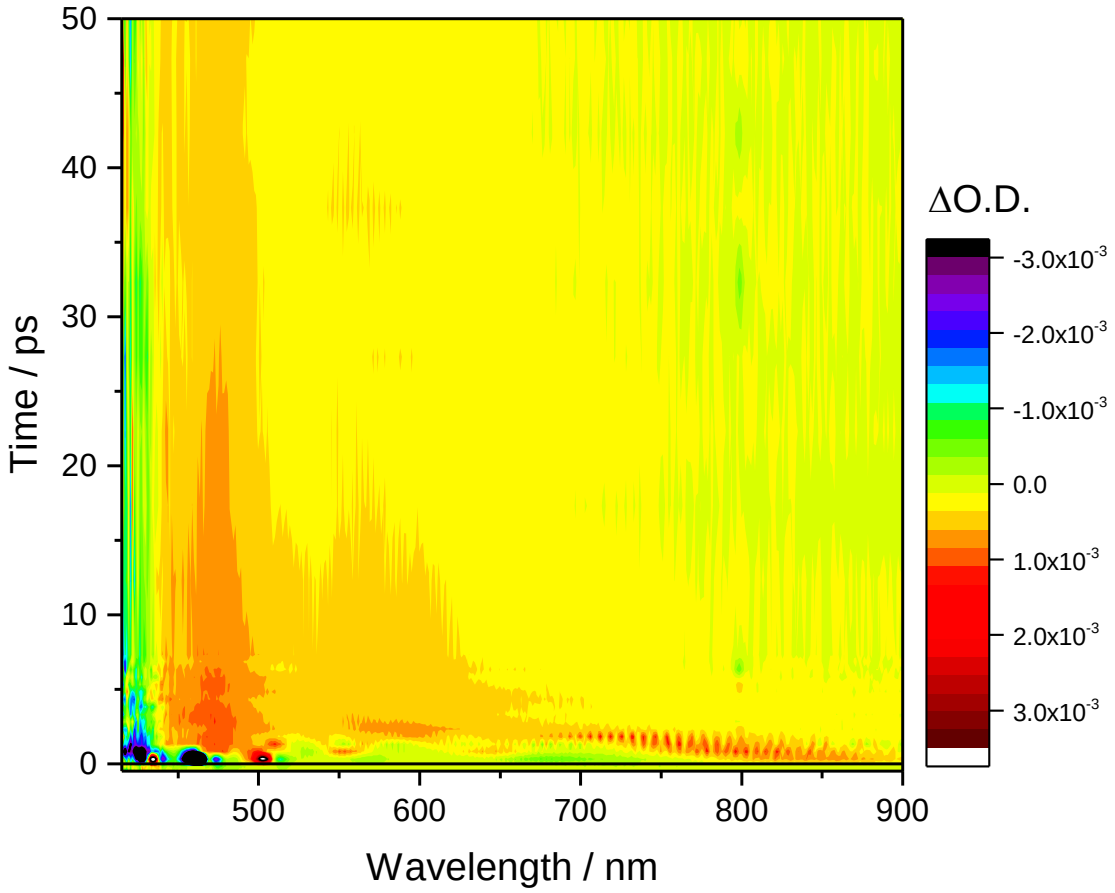

Figure 98 - Ultrafast transient absorption spectrum for a sample of QDs in H_2O containing DMAET in a ratio of 50:1 DMAET:QD. The sample was excited at 400 nm.

The transient absorption spectrum of the QDs in water in the absence of the scavenger or the catalyst showed a similar behaviour to the DMF sample, with a fast bleach at 420 nm, and a broad positive hole signal. It is notable however that in the H_2O sample the broad feature showed, in line with the steady state emission spectrum, more defined regions, at 470 and 580 nm. Interestingly, these defined regions in the TA spectrum correspond to the same wavelengths at which the ground state emission spectrum showed shoulders (Figure 97(b)), indicating that the decay of the positive signal observed is a measure of recombination of holes with excited electrons (Figure 99(b)). The kinetic traces recorded at 425 nm, 470 nm and 580 nm are shown in Figure 99(a). Again, the experimental traces fit to double exponential functions with lifetimes of $\tau_{1(425\ nm)} \sim 1 \pm 0.2$ ps and $\tau_{2(425\ nm)} = 35 \pm 10$ ps

for the negative feature, $\tau_{1(470\ nm)}$ = 25 ± 4 ps and $\tau_{2(470\ nm)}$ = 410 ± 90 ps for the 470 nm trace and $\tau_{1(580\ nm)}$ = 5.7 ± 0.7 ps and $\tau_{2(580\ nm)}$ = 290 ± 20 ps for the 580 nm trace.

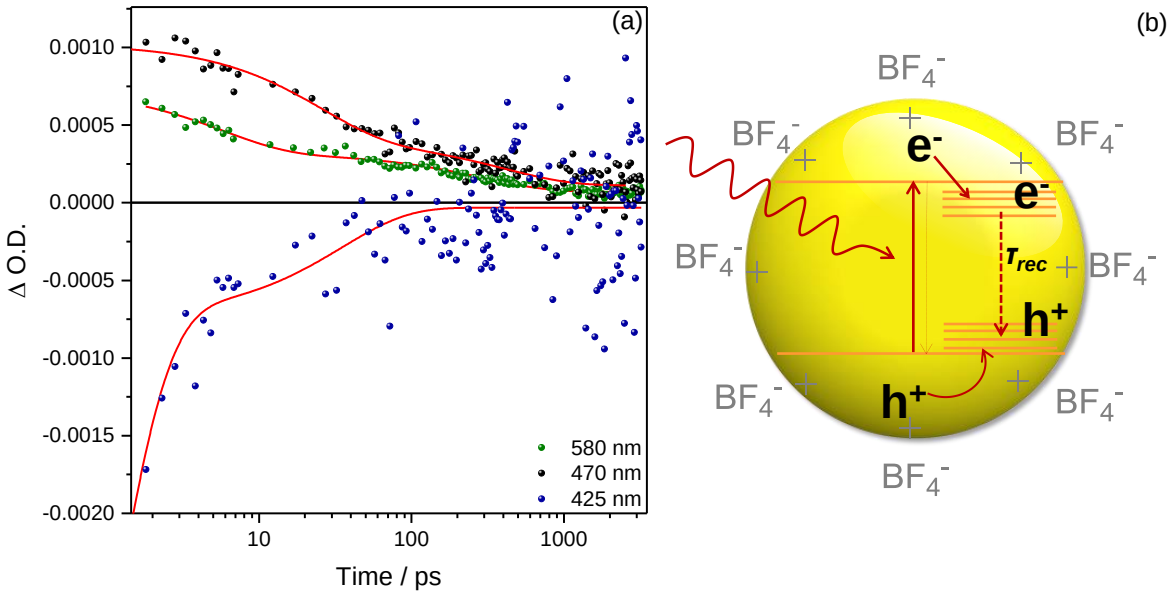

Figure 99 – (a) Transient absorption decays for the sample measured at 425, 470 and 580 nm and (b) scheme of the charge carrier dynamics occurring during the TAS experiment.

Upon addition of ascorbate the UV-Vis spectrum appeared essentially unchanged (Figure 100(a)), however the steady state emission was partially quenched, as shown in Figure 100(b), indicating that the ascorbate was rapidly scavenging the photogenerated holes. In line with the steady state emission spectrum, the TA spectrum of the solution showed the positive signals at 470 and 580 nm disappearing, and instead the spectrum showed a broad negative bleach at *ca.* 520 nm. As it appeared to be quenched in the presence of a hole scavenger, the positive signal is confirmed to be a photohole signal. A new broad bleach was observed at 520 nm; long-lived emissions are corrected for by the TAS software during data analysis, and stimulated emissions generally appear as sharp signals, therefore emission is ruled out as the cause of the broad bleach.

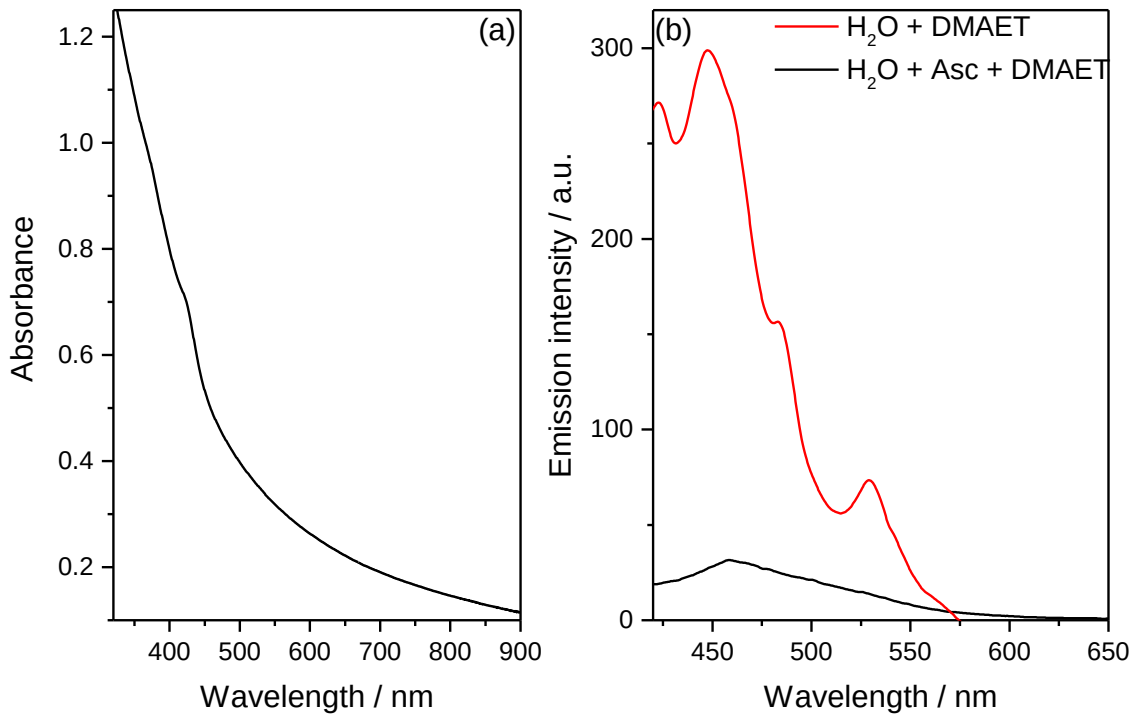

Figure 100 - (a) Ground state UV-vis spectrum of ZnSe-QD (0.5 μM) in H_2O containing DMAET in a 50: ratio DMAET:QD and 0.1 M ascorbate buffer (pH = 6.5) prior to the TAS experiment, and (b) emission spectrum of the same colloidal solution, recorded following excitation at 310 nm.

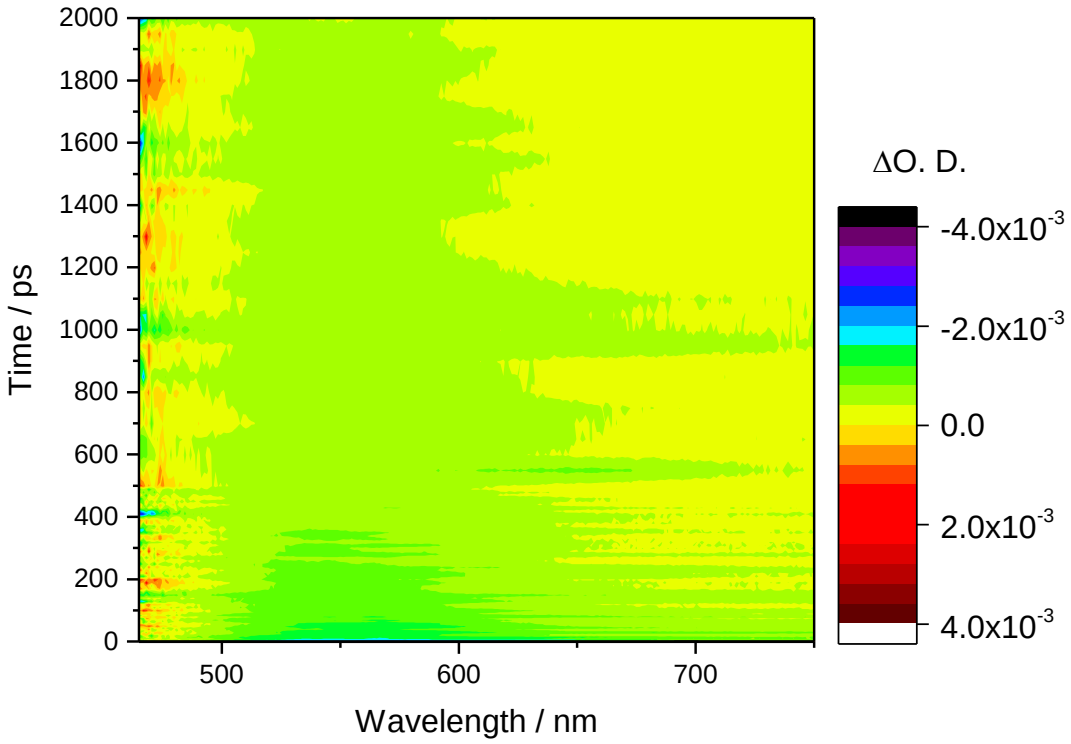

Figure 101 - Ultrafast transient absorption spectrum for a sample of QDs in 0.1 M ascorbate buffer (pH = 6.5) containing DMAET in a ratio of 50:1 DMAET:QD. The sample was excited at 400 nm.

As the holes are scavenged, the positive signal assigned to those holes is no longer seen. The negative feature is assigned to long-lived electrons which are now more likely to have decayed to trap states close to the conduction band edge following excitation (Figure 102(b)). The lifetime of the new signal is calculated by fitting the experimental trace to a triple exponential function (Figure 102(a)), with $\tau_{1(520\ nm)}$ = 3.7 ± 0.4 ps, $\tau_{2(520\ nm)}$ = 113 ps ± 16 and $\tau_{3(520\ nm)}$ = 2.3 ± 0.79 ns. It is notable that the negative signal does not recover within the timescale of the instrument. The TA spectrum at longer timescales was also measured, however the combined time resolution of the instruments available is such that the ns-µs window is not observable, and the µs TA spectrum showed no feature.

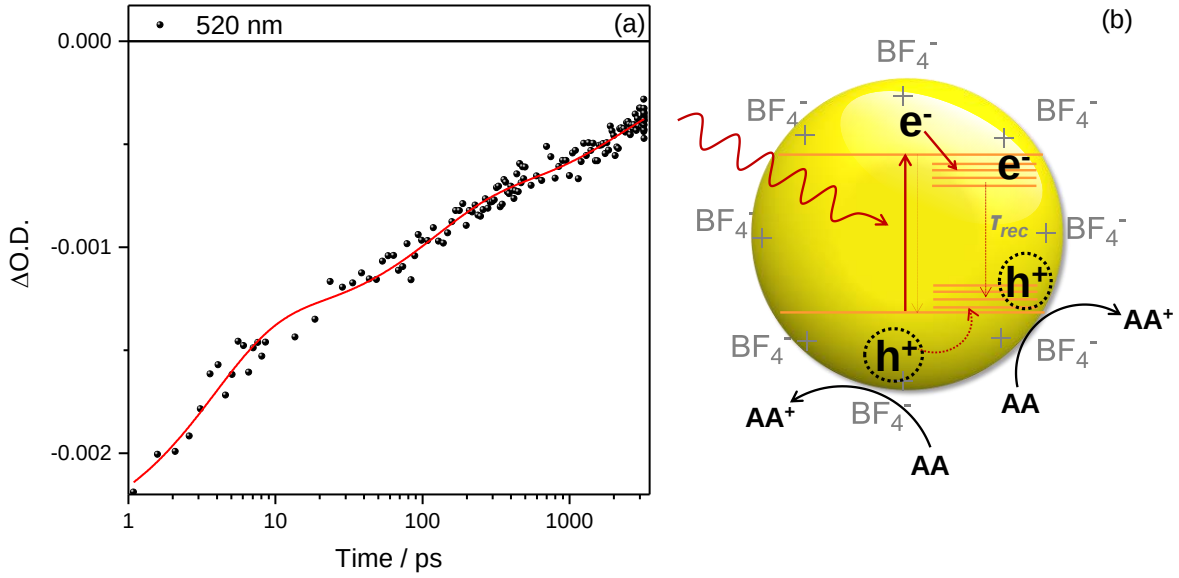

Figure 102 – (a) Transient absorption decays for the sample measured at 520 nm; (b) scheme of the charge carrier dynamics occurring during the TA experiment.

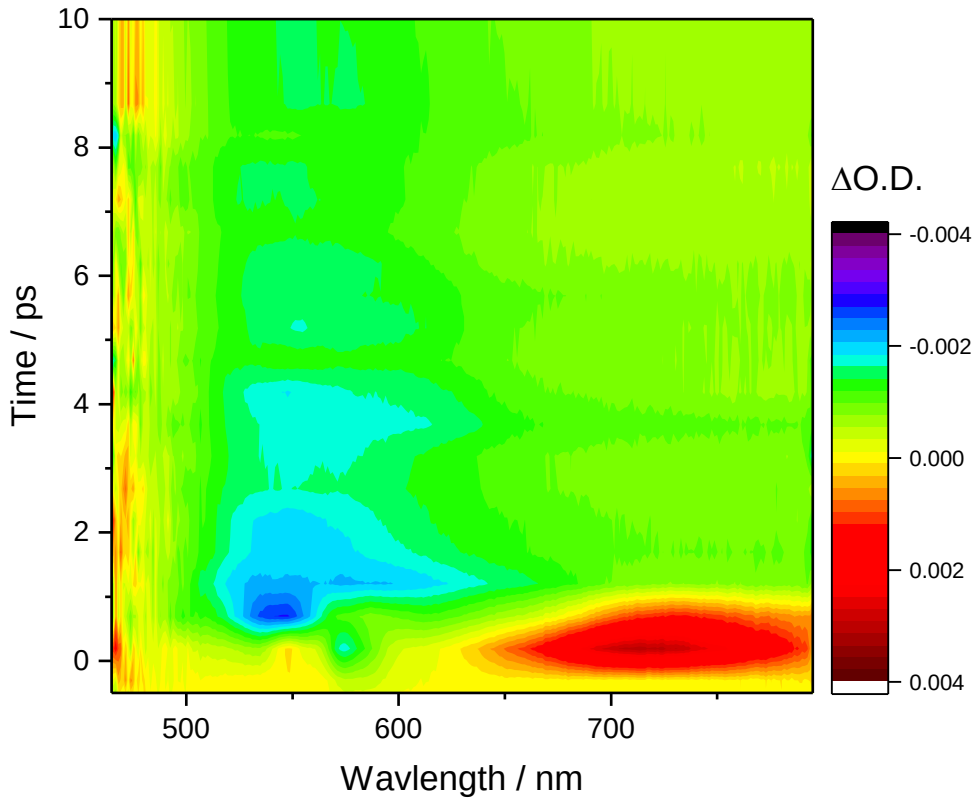

Figure 103 – Ultrafast transient absorption spectrum for a sample of QDs in 0.1 M ascorbate buffer (pH = 6.5) containing DMAET in a ratio of 50:1 DMAET:QD. The sample was excited at 400. Expanded from Figure 101.

By focusing our attention on the first few picoseconds of the TA spectrum (Figure 103), it was possible to note a strong positive feature at *ca.* 720 nm, which decayed very rapidly, at the same time as the negative signal assigned to trapped electrons appeared. The kinetics of the signal indicated that the lifetime of the electron trapping process is on the order of a picosecond, however the fit used relied on few data points, and the error on the lifetime is 50%, therefore this is only an estimate. This positive signal is assigned to the electron trapping process.

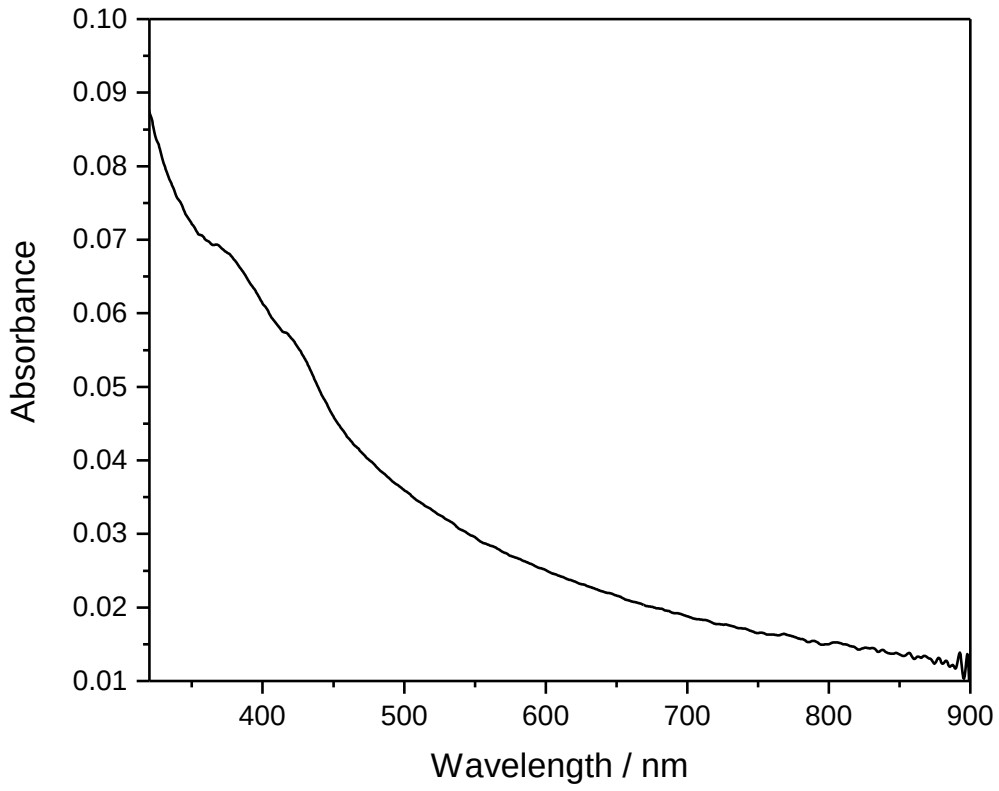

Figure 104 - Ground state UV-vis spectrum of ZnSe-QD (0.5 μM) in 0.1 M ascorbate buffer (pH = 6.5) containing DMAET in a 50:1 ratio DMAET:QD and Ni(cycP) in a ratio of 20:1 cat:QD prior to the TAS experiment.

The UV-vis spectrum of a QD sample containing Ni(cycP) in a 20:1 ratio (cat:QD) and ascorbate buffer appeared similar to the one obtained without the catalyst (Figure 104). The same behaviour was obtained in the TA spectrum as well, Figure 105, with the appearance of the same broad bleach as the main feature. Interestingly, the signal recovers faster than in the sample without Ni(cycP). The change in optical density at 520 nm with time is shown in Figure 106(a); as for the previous sample, the signal does not completely recover during the timescale of the experiment. Nevertheless, when fitted to a three exponential function, the lifetimes of the signal for the sample containing Ni(cycP) were found to be $\tau_{1(520\ nm)}$ = 1.1 ± 0.3 ps, $\tau_{2(520\ nm)}$ = 44.5 ps ± 6 and $\tau_{3(520\ nm)}$ = 873 ± 156 ps, much lower than what was found in the sample without the catalyst. This faster recovery is assigned to electron transfer of the trapped electrons from the ZnSe QD to Ni(cycP), in line with the observed photocatalytic results.

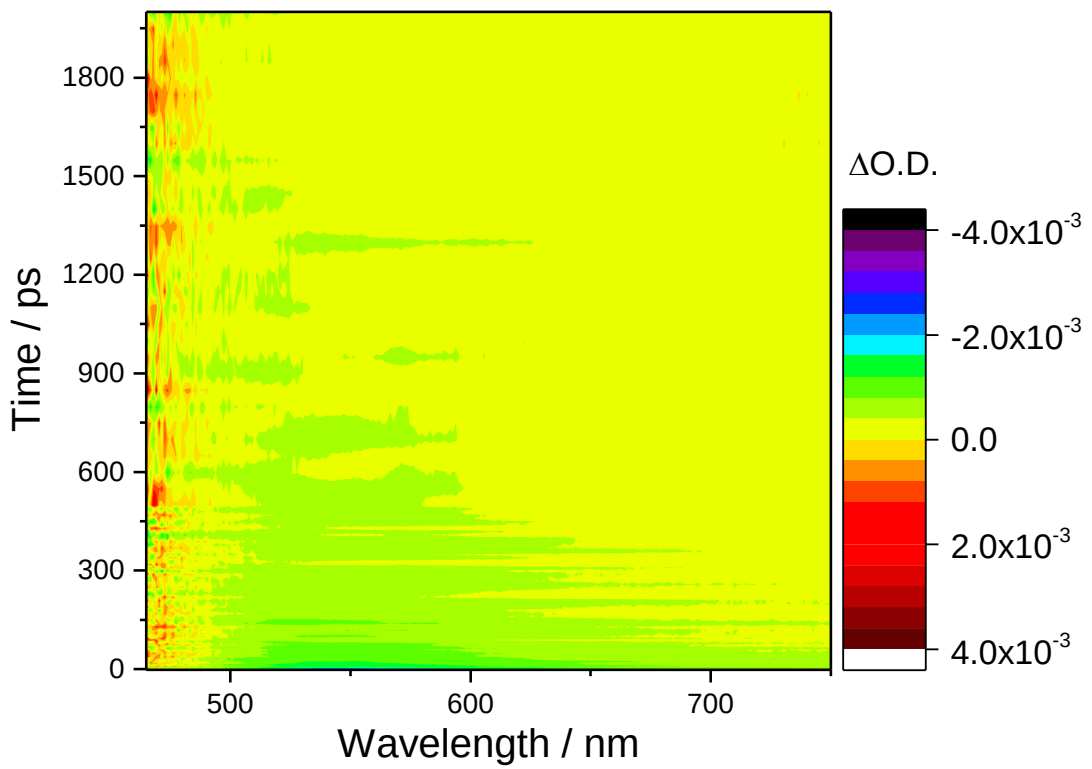

Figure 105 - Ultrafast transient absorption spectrum for a sample of QDs in 0.1 M ascorbate buffer (pH = 6.5) containing DMAET in a ratio of 50:1 DMAET:QD and Ni(cycP) in a ratio of 20:1 cat:QD. The sample was excited at 400 nm.

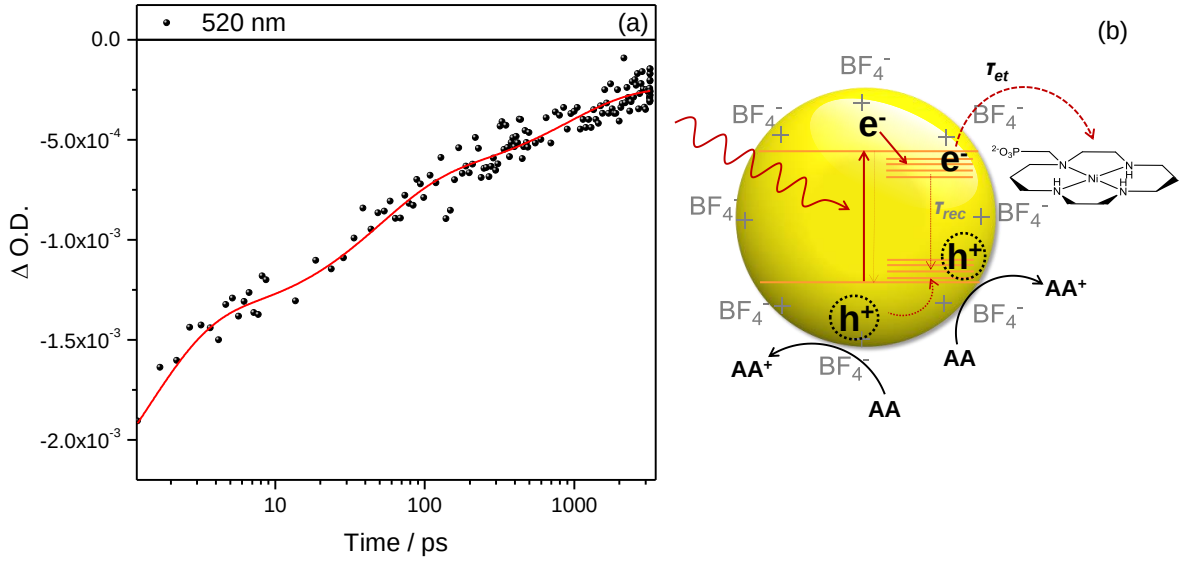

Figure 106 – (a) Transient absorption decays for the sample measured at 520 nm; (b) scheme of the charge carrier dynamics occurring during the TAS experiment.

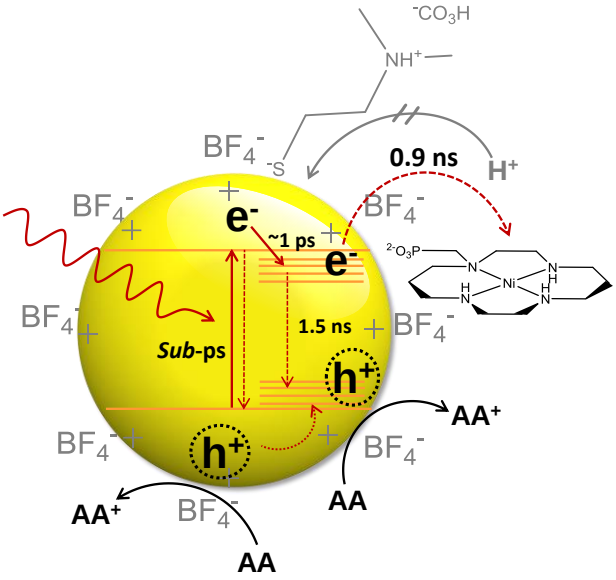

Scheme 31 – Kinetics of the ZnSe-QD/Ni(cycP) assembly when the system is irradiated with visible light, as measured by transient absorption spectroscopy.

Scheme 31 shows charge carrier dynamics that were obtained *via* ultrafast TA spectroscopy. The stripped nanoparticles are significantly more active for CO_2 reduction than the fully capped ones, however they are not very selective on account of protons being reduced at the surface of the QDs. Furthermore, while the QDs are well dispersed in DMF, they tend to form opalescent solutions in water, typical of aggregation. The addition of small amounts of DMAET as the capping ligand (ratio of 50:1 with the QDs) suppresses hydrogen production, possibly by blocking the active sites on the surface, and helps to stabilise the QDs enough to allow the recording of TA spectra. This technique indicates that charge separation is very fast (< 1 ps), with a series of states close to the valence band giving rise to broad signals, and that recombination is the main pathway in the absence of scavengers or catalysts. When ascorbate is added, excitation from sub-bandgap states is prevented due to the holes being scavenged, and electron excitation from the valence band is seen instead, confirmed by the disappearance of the positive signal at 470 nm, which was assigned to the photoholes. Instead a very fast process is observed at 720 nm, which is assigned to decay of the photogenerated electrons to trap states below the conduction band. A broad bleach, recovering in *ca.* 1.5 ns, appears

immediately after the trapping signal disappears, due to the generation of long-lived electrons in the trap states. In the absence of the catalyst, the long-lived bleach is due to the de-trapping of the residual electrons and recombination *via* oxidised scavenger. In the presence of the catalyst, the recovery of the trapped electrons is twice as fast (900 ps), indicating that electron transfer from the QDs to the catalyst is faster than recombination, and partially suppresses it.

4.3.4 Conclusions

Anchoring Ni(cycP) to ligand-free ZnSe quantum dots achieved visible-light CO_2 reduction to CO as the main product, with small amounts of H_2 as the side product. The new system is composed only of cheap and abundant materials, and furthermore is active in water. The current benchmark for light-driven CO_2 reduction is a carbon nitride photosensitiser decorated with Ag nanoparticles with an anchored binuclear ruthenium complex,[68] which reduces CO_2 to formic acid. The highest efficiency of the system was reached in DMA with TEA as the sacrificial electron donor, with a calculated external quantum efficiency (EQE) of 5.2%, however it was demonstrated that CO_2 reduction was maintained in water as well, with lower yields of HCOOH. The external quantum efficiency of the ZnSe-QD/Ni(cycP) photocatalyst was measured to be 3.9% for H_2 and CO production combined, lower than that achieved by Ishitani and co-workers. However we note that the EQE calculated here is achieved with abundant materials.

We have examined the kinetics of the charge carries in detail by using a combination of steady state emission spectroscopy and ultrafast TAS spectroscopy. We have built a complete kinetic model for the ZnSe-QD/Ni(cycP) photocatalyst. The transient absorption spectroscopy experiments elucidated the behaviour of the charge carriers in the ZnSe-QD/Ni(cycP) photocatalyst, showing that the electron transfer from the QDs to the molecular catalyst is faster than recombination, and therefore favoured during photocatalytic experiments.

4. 4 Materials and methods

4.4.1 Materials

The starting materials and solvents for the synthesis were purchased by Sigma Aldrich, Fisher Scientific or VWR, and used without further purification unless otherwise specified. 4,4'-dibromo-2.2'-bipyiridine was purchased from TCI chemicals. Milli-Q water (18.2 MΩ) was used throughout. All electrolyte salts and solvents were purchased from Sigma Aldrich or VWR and used without further purification. Ar, N_2 and CO_2 were purchased from BOC at CP or higher grade.

Diethyl 2,2'-bipyridine-4,4'-diphosphonate (1)

In strictly anhydrous conditions 4,4'-dibromo-2.2'-bipyiridine (140 mg, 1 eq.), diethyl phosphite (0.12 ml, 2.1 eq.) and triethylamine (0.18 ml, 3 eq.) are dissolved in dry toluene (10 ml), and tetrakis(triphenylphosphine)Pd(0) (47 mg, 0.1 eq.) is added last. The mixture is refluxed for 4 hours, then it is filtered while hot. The solvent is removed, and hexane is added. The mixture is refluxed for two hours, to yield a clear solution and an orange oil in the bottom. The solution is decanted, and the solvent rotary evaporated. The residue is purified *via* flash column chromatography ($CHCl_3$:acetone 9:1) to yield the pure Diethyl 2,2'-bipyridine-4,4'-diphosphonate as a white-pink solid. Obtained: 120 mg, yield 64%. **^{1}H NMR** (400 MHz, CHLOROFORM-*d*) δ ppm 8.79 (t, *J* = 5.1 Hz, 2H), 8.72 (d, *J* = 14.2 Hz, 2H), 7.67 (ddd, *J* = 13.0, 4.8, 1.2 Hz, 2H), 4.14 (qdd, *J* = 8.2, 7.3, 3.0 Hz, 8H), 1.31 (t, *J* = 7.1 Hz, 12H). **^{31}P NMR** (162 MHz, CHLOROFORM-*d*) δ ppm 14.66 (s).

$Ru(bpy)_2Cl_2$ (2)

$RuCl_3 \cdot H_2O$ (100 mg, 1 eq.) and LiCl (107 mg, 5 eq.) are dissolved in 7 ml of DMF under constant stirring. 2,2'-bipyridine (190, 2.5 eq.) is added, and the mixture is refluxed overnight. The mixture is cooled down, acetone (20 ml) is added and the solution is kept at 0°C for 8 hours. The purple precipitate is filtered and washed with acetone (3x5 ml), cold diethyl ether (3x5 ml) and finally with cold water (3x5 ml) to yield a dark purple crystalline powder. Obtained: 200 mg, yield 80%. **^{1}H NMR**

(400 MHz, DMSO) δ ppm 9.95 (d, *J* = 5.4 Hz, 2H), 8.63 (d, *J* = 8.0 Hz, 2H), 8.47 (d, *J* = 7.9 Hz, 2H), 8.06 (t, *J* = 7.3 Hz, 2H), 7.76 (t, *J* = 6.3 Hz, 2H), 7.67 (t, *J* = 7.7 Hz, 2H), 7.50 (d, *J* = 5.4 Hz, 2H), 7.10 (t, *J* = 6.2 Hz, 1H).

$[Ru(bpy)_2(bpy\text{-}PO_3H_2)]Br_2$ (RuP, 4)

Diethyl 2,2'-bipyridine-4,4'-diphosphonate (35 mg, 1 eq.) and $Ru(bpy)_2Cl_2$ (50 mg, 1.25 eq.) are dissolved in a 1:1 mixture of ethanol and water, and the solution is refluxed in the dark for 3 hours. The solvent is removed to yield a reddish-brown residue. This is dissolved in the minimum amount of a 9:1 acetone:water mix, and purified *via* flash column chromatography. The ruthenium starting material is eluted with a 9:1 acetone:water mobile phase. The $[Ru(bpy)_2(bpy\text{-}P(O)(OEt)_2]$ product is eluted as the NO_3 salt by eluting the column with acetone:water:KNO_{3sat} 9:1:0.1 (10 drops of KNO_3 saturated solution in 100 ml of mobile phase). The solution is concentrated until only water is left, and KPF_6 (150 mg, 10 eq.) is added. The $[Ru(bpy)_2(bpy\text{-}P(O)(OEt)_2](PF_6)_2$ thus formed is extracted from the aqueous phase with dichloromethane (3x20 ml) the organic fractions are combined, dried over $MgSO_4$, then filtered. The solvent is rotary evaporated to yield an orange-red solid which was found to be pure by ^{31}P-NMR (δ ppm 11.14(s)). The solid is dissolved in HBr (3 ml) and is heated at 110°C in the dark overnight. The solvent is removed under vacuum using a liquid nitrogen trap. The residue is dissolved in the smallest amount of methanol and stirred until complete dissolution, and the pure product is precipitatd out by adding diethyl ether. The deep red powder was filtered, washed with diethyl ether and dried under vacuum. Obtained: 30 mg, yield 41%. **^{1}H NMR** (400 MHz, DEUTERIUM OXIDE) δ ppm 8.77 (d, *J* = 12.6 Hz, 1H), 8.54 (d, *J* = 8.2 Hz, 2H), 8.06 (t, *J* = 7.9 Hz, 2H), 7.93 (dd, *J* = 5.6, 3.3 Hz, 1H), 7.80 (dd, *J* = 9.5, 5.5 Hz, 2H), 7.57 (dd, *J* = 11.5, 5.7 Hz, 1H), 7.43 – 7.32 (m, 2H). **^{31}P NMR** (162 MHz, DEUTERIUM OXIDE) δ ppm 6.88 (s).

General procedure for the preparation of the ZrO_2 nanoparticles

ZrO_2 nanoparticles (Sigma Aldrich) were calcined at 350°C for 30 minutes prior to soaking experiments. A solution of Ni(cycP) 0.1 mM in ethanol was used throughout, and the concentration of RuP was adjusted to obtain the desired ratio and catalyst and dye. The particles were suspended in the solution in a ratio of 10 mg per ml of solution, and were stirred for 48 hours at room temperature. After this time, the particles were centrifuged (3x30 mins at 8000 RPM). The soaking solution was decanted, and the particles were washed with ethanol once, then centrifuged again and dried under vacuum. They were ground with a mortar and pestle and stored in the dark.

General procedure for the photochemical experiments

2 mg of the nanoparticles were suspended in 2 ml of freshly prepared ascorbate buffer 0.1M (pH 4 or 5) in a 5 ml glass vial equipped with a magnetic stirring bar and a septum screw cap. The vial was sealed and purged with either argon or CO_2 for 30 minutes. The sample was illuminated with either a 150 W Xe arc lamp (Applied Photophysics) or a 300 W Xe lamp (LOT Quantum Design), under constant stirring. The IR radiation was filtered with a KG1 filter (Thorlabs), and light with $\lambda < 375$-420 nm was blocked using long pass filters (Thorlabs or Edmund Optics). The light intensity incident to the sample was measured with an optical power meter and a thermal sensor (Thorlabs) and set to either 40 or 50 mW cm^{-2} by changing the distance of the sample from the light source. Care was taken to ensure that the entire sample was illuminated during experiments. The nature of the reaction products was verified by gas chromatography using an Agilent 6890N with helium N6 (BOC) as the carrier gas (5 mol min^{-1}), equipped with a 5 Å molecular sieve column (ValcoPLOT, 30 m length, 0.53 mm ID) and a pulsed discharge detector (D-3-I-HP, Valco Vici). The peak areas for H_2 and CO were quantified by calibration with a custom-ordered calibrant gas containing 500 ppm of H_2 and 200 ppm of methane and CO. Calibrations were carried out daily.

Preparation of films for electrochemical and TAS experiments

ZrO_2 films were prepared by depositing ZrO_2 colloidal paste (average particle diameter = 20 nm) on fluorine-doped tin oxide (FTO) slides. The slides were sonicated in water for 20 minutes, then in ethanol for 20 minutes, and finally calcined in the furnace at 400°C for 30 minutes before the deposition. The paste was deposited on the films and spread with a glass rod. The films were allowed to dry before the slides were heated at 450°C for 30 minutes. The films were dip coated in solutions of either RuP 0.5 mM in ethanol or RuP 0.5 mM/Ni(cycP) 0.1 mM in ethanol for 48 hours, then they were copiously rinsed with ethanol and dried with a stream of nitrogen. Prior to the TAS experiments, the films were placed in a quartz cell which was filled with either water or ascorbate buffer 0.1 M (pH = 4) and sealed. The solution was degassed for 30 minutes with argon.

General procedure for the ZnSe-BF_4 QD-cat sample preparation

The ZnSe-BF_4 was received as a concentrated (0.1733 mM by ICP-OES) stock solution in anhydrous DMF under argon, and was afterwards stored in the fridge in the dark. Extreme care was taken to ensure that the stock solution was kept under argon at all times during the sample preparation. A solution of either water, water + 25 μM DMAET (2-(dimethylamino)ethanethiol hydrochloride, 2.5 mM stock solution), ascorbate buffer (0.1 M, pH 6.5) + 25 μM DMAET or ascorbate buffer (0.1 M, pH 6.5) + 25 μM DMAET + 10 μM Ni(cycP) was purged with argon for 30 minutes, and 5.8 μl of the quantum dots were added to give a total volume of 2 ml. The solution was argon purged for a further 15 minutes. 300 μl were transferred into a 1 mm path length quartz cuvette for the microsecond TAS experiments or 500 μl were transferred into a 2 mm path length quartz cell for the femtosecond TAS experiments.

4.4.2 Spectroscopic characterisation

ESI-MS and elemental analysis were carried out by the University of Liverpool analytical services. ICP-OES analysis was carried out either by the University of Liverpool analytical services or the

Centre for Chemical Instrumentation and Analytical Services (University of Sheffield). FTIR was carried out on a Bruker Vertex instrument. The FTIR spectra of the gaseous reaction products of the photochemical experiments were carried out using a custom-made cell with a path length of 10 cm. The headspace of the reaction vessel was injected using a gas-tight syringe in the cell *via* a septum. UV-Vis spectra were recorded on a Shimadzu UV-2600 spectrophotometer. Steady-state emission measurements were carried out using a Perkin-Elmer LS55 fluorimeter, while for the time resolved emission measurements samples were excited by a UV laser (355 nm, 6 ns, <40 μJ cm^{-2}, 0.5 H_z) and the RuP* emission at 650 nm was passed through a monochromator (OBB) and a long pass 400 nm filter (OD 4, Edmund optics) before detection by a fast Si photodiode (HCA-S-200M) coupled to an amplifier (HVA-200M-40-B). The instrument response function of the system was measured from the scattered 355 nm light off a $BaSO_4$ sample, with the 400 nm long pass filter removed and found to be on the order of 10 ns at the gain levels and oscilloscope settings used. Kinetic traces are recorded by averaging 128 laser shots. ^{1}H, ^{13}C and ^{31}P NMR spectra were recorded on a Bruker 400 MHz spectrometer. Chemical shifts (δ) are reported in ppm relative to residual solvent signals for ^{1}H and ^{13}C NMR (^{1}H NMR: 7.26 ppm for $CDCl_3$, 4.79 ppm for D_2O, 2.50 for DMSO. ^{13}C NMR: 77.1 ppm for $CDCl_3$, 39.5 for DMSO). Coupling constants (J) are reported in Hz. Multiplicities are reported as follows: s, singlet, d, doublet, dd, doublet of doublets, ddd doublet of doublet of doublets, t triplet, dt, doublets of triplets, q, quartet, qdd, quartet of doublet of doublets m, multiplet, c, complex, and br, broad.

XPS measurements were performed in a standard ultrahigh vacuum (UHV) chamber operating at a base pressure of less than 2×10^{-10} mbar with hydrogen as the main residual gas, using a PSP Vacuum Technology non-monochromatic Al K_α X-ray source ($h\nu$ = 1486.6 eV) typically operating at 144 W, together with a PSP Vacuum Technology electron-energy analyzer operating with a typical constant pass energy of 20 eV. Calibration of the spectrometer was performed using a polycrystalline silver foil, cleaned in vacuo. The Ag $3d_{5/2}$ photoelectron line had a binding energy (BE) of 368.3 eV and a

full-width at half-maximum (FWHM) of 1.2 eV. Charge compensation was achieved by setting the binding energy of the main adventitious C 1s peak to 285.0 eV.

Transient absorption spectroscopy

The microsecond TAS experiments were carried out using the third harmonic of a Nd:YAG laser (Continuum, Surelite I-10, 355 nm, 6 ns pulse width) operating at 0.33 Hz as the UV excitation source. The repetition rate was chosen to ensure that all charge carriers had fully decayed prior to the next excitation event. A liquid light guide transmitted the laser pulse to the sample. A laser intensity of *ca.* 150 μJ cm^{-2} at 355 nm was incident on the sample, unless otherwise specified. A 75 W Xe lamp (OBB Corp.) coupled to monochromator (OBB Corp., set to 4 nm resolution) was used as the probe light and the change in optical density of the sample was calculated by measuring the transmitted light using a Si Photodiode (Hamamatsu) and a homemade amplification system coupled to both an oscilloscope (Textronix TDS 220) and data acquisition card (National Instruments NI-6221). The oscilloscope data were used to study the microseconds time scales while the DAQ card acquired the milliseconds to seconds data. The data shown are the result of averaging 300 laser shots per trace. Full spectra were obtained by measuring a kinetic trace every 25 nm.

Femtosecond TA spectroscopy was carried out using a PHAROS laser (Light Conversion, Ltd) operating at 10 kHz coupled to an ORPHEUS optical parametric amplifier (Light Conversion, Ltd) in tandem with a LYRA harmonic generator (Light Conversion, Ltd) to produce the desired wavelength for sample excitation. The pump beam intensity was adjusted with a neutral density filter so as to achieve approximately equal photon fluxes at different wavelengths. Typical pulse energies were on the order of 10 nJ. The pump wavelength was tuned to 400 nm. A portion of the PHAROS output was also split off to pump a sapphire crystal to generate a white light continuum for the probe beam, which provided spectral observation in the region 450-900 nm. The probe beam was focused to a spot size of ~100 μm diameter on the sample and was overlapped completely by the pump beam. Spectra were acquired with a HELIOS transient absorption spectrometer (Ultrafast Systems, LLC).

The time resolution of the setup is ~ 400 fs. Measurements were performed by randomly stepping the optical delay line and averaging for 1 s at each delay time. Between three to five consecutive scans were collected and aggregated to produce each spectrum. Sample solutions were measured in a 1 or 2 mm path length quartz cuvette, under an inert atmosphere.

4.5 References

1. M. Hansen, F. Li, L. Sun, and B. König, *Chem. Sci.*, 2014, **5**, 2683.

2. M. A. Gross, A. Reynal, J. R. Durrant, and E. Reisner, *J. Am. Chem. Soc.*, 2014, **136**, 356–366.

3. M. A. Gross, A. Reynal, J. R. Durrant, and E. Reisner, *J. Am. Chem. Soc.*, 2014, **136**, 356–366.

4. J. Willkomm, K. L. Orchard, A. Reynal, E. Pastor, J. R. Durrant, and E. Reisner, *Chem. Soc. Rev.*, 2016, **45**, 9–23.

5. K. Sayama and H. Arakawa, *J. Phys. Chem.*, 1993, **97**, 531–533.

6. B. I. Lemon, F. Liu, and J. T. Hupp, *Coord. Chem. Rev.*, 2004, **248**, 1225–1230.

7. L. Zhang and J. M. Cole, *ACS Appl. Mater. Interfaces*, 2015, **7**, 3427–3455.

8. E. Bae and W. Choi, *J. Phys. Chem. B*, 2006, **110**, 14792–9.

9. I. Gillaizeau-Gauthier, F. Odobel, M. Alebbi, R. Argazzi, E. Costa, C. A. Bignozzi, P. Qu, and G. J. Meyer, *Inorg. Chem.*, 2001, **40**, 6073–6079.

10. E. Bae and W. Choi, *J. Phys. Chem. B*, 2006, **110**, 14792–14799.

11. T. Hirao, T. Masunaga, Y. Ohshiro, and T. Agawa, *Tetrahedron Lett.*, 1980, **21**, 3595–3598.

12. P. Péchy, F. P. Rotzinger, M. K. Nazeeruddin, O. Kohle, S. M. Zakeeruddin, R. Humphry-Baker, and M. Grätzel, *J. Chem. Soc. Chem. Commun.*, 1995, **0**, 65.

13. K. Hanson, M. K. Brennaman, H. Luo, C. R. K. Glasson, J. J. Concepcion, W. Song, and T. J. Meyer, *ACS Appl. Mater. Interfaces*, 2012, **4**, 1462–1469.

14. J. T. Hyde, K. Hanson, A. K. Vannucci, A. M. Lapides, L. Alibabaei, M. R. Norris, T. J. Meyer, and D. P. Harrison, *ACS Appl. Mater. Interfaces*, 2015, **7**, 9554–9562.

15. C. Stern, A. B. Lemeune, Y. Gorbunova, A. Tsivadze, and R. Guilard, *Turkish J. Chem.*, 2014, 38, 980–993.

16. Z. Chen, J. J. Concepcion, J. F. Hull, P. G. Hoertz, and T. J. Meyer, *Dalton Trans.*, 2010, **39**, 6950–6952.

17. J. A. Anderson and J. L. G. Fierro, *J. Solid State Chem.*, 1994, **108**, 305–313.

18. D. Barreca, G. A. Battiston, R. Gerbasi, E. Tondello, and P. Zanella, *Surf. Sci. Spectra*, 2000, **7**, 303.

19. D. Majumdar and D. Chatterjee, *Thin Solid Films*, 1991, **206**, 349–354.

20. D. D. Sarma and C. N. R. Rao, *J. Electron Spectros. Relat. Phenomena*, 1980, **20**, 25–45.

21. S. A. Steiner, T. F. Baumann, B. C. Bayer, R. Blume, M. A. Worsley, W. J. MoberlyChan, E. L. Shaw, R. Schlögl, A. J. Hart, S. Hofmann, and B. L. Wardle, *J. Am. Chem. Soc.*, 2009, **131**, 12144–12154.

22. D. J. Morgan, *Surf. Interface Anal.*, 2015, **47**, 1072–1079.

23. B. Varughese, S. Chellamma, and M. Lieberman, *Langmuir*, 2002, **18**, 7964–7970.

24. Y. Zhang, C. Bao, G. Wang, Y. Song, L. Jiang, Y. Song, K. Wang, and D. Zhu, *Surf. Interface Anal.*, 2006, **38**, 1372–1376.

25. J. Matienzo, L. I. Yin, S. O. Grim, and W. E. Swartz, *Inorg. Chem.*, 1973, **12**, 2762–2769.

26. J. F. M. and G. E. M. Briggs, D. C. D. Wanger, W. M. Riggs, L. E. Davis, *Surf. Interface Anal.*,

1981, **3**, v–v.

27. M. C. Biesinger, L. W. M. Lau, A. R. Gerson, and R. S. C. Smart, *Appl. Surf. Sci.*, 2010, **257**, 887–898.

28. M. C. Biesinger, B. P. Payne, A. P. Grosvenor, L. W. M. Lau, A. R. Gerson, and R. S. C. Smart, *Appl. Surf. Sci.*, 2011, **257**, 2717–2730.

29. A. P. Grosvenor, M. C. Biesinger, R. S. C. Smart, and N. S. McIntyre, *Surf. Sci.*, 2006, **600**, 1771–1779.

30. L. M. Moroney, R. S. C. Smart, and M. W. Roberts, *J. Chem. Soc. Faraday Trans. 1 Phys. Chem. Condens. Phases*, 1983, **79**, 1769.

31. M. Wyn Roberts, R. St, and C. Smart, *J . Chem. Soc. Faraday Trans. I*, 1984, **80**, 2957–2968.

32. M. C. Biesinger, B. P. Payne, L. W. M. Lau, A. Gerson, and R. S. C. Smart, *Surf. Interface Anal.*, 2009, **41**, 324–332.

33. A. F. Carley, S. D. Jackson, J. N. O'Shea, and M. W. Roberts, *Surf. Sci.*, 1999, **440**, L868–L874.

34. B. P. Payne, A. P. Grosvenor, M. C. Biesinger, B. A. Kobe, and N. S. McIntyre, *Surf. Interface Anal.*, 2007, **39**, 582–592.

35. Y. Ueda, H. Takeda, T. Yui, K. Koike, Y. Goto, S. Inagaki, and O. Ishitani, *ChemSusChem*, 2015, **8**, 439–42.

36. A. Králík, M. Hansen, and B. König, *RSC Adv.*, 2016, **6**, 5739–5744.

37. J. L. Grant, K. Goswami, L. O. Spreer, J. W. Otvos, and M. Calvin, *J. Chem. Soc., Dalt. Trans.*, 1987, 2105–2109.

38. G. McDermott, S. M. Prince, A. A. Freer, A. M. Hawthornthwaite-Lawless, M. Z. Papiz, R. J. Cogdell, and N. W. Isaacs, *Nature*, 1995, 374, 517–521.

39. S. Bahatyrova, R. N. Frese, C. A. Siebert, J. D. Olsen, K. O. Van Der Werf, R. Van Grondelle, R. A. Niederman, P. A. Bullough, C. Otto, and C. N. Hunter, *Nature*, 2004, **430**, 1058–1062.

40. H. Inoue, T. Shimada, Y. Kou, Y. Nabetani, D. Masui, S. Takagi, and H. Tachibana, *ChemSusChem*, 2011, 4, 173–179.

41. B. M. Kwon, C. S. Foote, and S. I. Khan, *J. Am. Chem. Soc.*, 1989, **111**, 1854–1860.

42. A. E. Kellie and S. S. Zilva, *Biochem. J.*, 1938, **32**, 1561–5.

43. C. L. Arcus and S. S. Zilva, *Biochem. J.*, 1940, **34**, 61–6.

44. S. Jingyan, L. Yuwen, W. Zhiyong, and W. Cunxin, *J. Pharm. Biomed. Anal.*, 2013, **77**, 116–119.

45. G. Vernin, S. Chakib, S. M. Rogacheva, T. D. Obretenov, and C. Párkányi, *Carbohydr. Res.*, 1997, **305**, 1–15.

46. B. H. Bielski, A. O. Allen, and H. A. Schwarz, *J Am Chem. Soc.*, 1981, **3**, 3516–3518.

47. J. Yuan and F. Chen, *J. Agric. Food Chem.*, 1998, **46**, 5078–5082.

48. H. Borsook, H. W. Davenport, C. E. P. Jeffreys, and R. C. Warner, *J. Biol. Chem.*, 1937, **117**, 237–279.

49. E. Kimura, E. Kimura, X. Bu, X. Bu, M. Shionoya, M. Shionoya, S. Wada, S. Wada, S. Maruyama, and S. Maruyama, *Inorg. Chem.*, 1992, **31**, 4542–4546.

50. E. Kimura, S. Wada, M. Shionoya, and Y. Okazaki, *Inorg. Chem.*, 1994, **33**, 770–778.

51. C. Herrero, A. Quaranta, S. El Ghachtouli, B. Vauzeilles, W. Leibl, and A. Aukauloo, *Phys. Chem. Chem. Phys.*, 2014, **16**, 12067.

52. S. Lehrer, *Biochemistry*, 1971, **10**, 3254–3263.

53. S. Y. Ryu, M. Yoon, S. C. Jeoung, and N. Song, *Photochem. Photobiol. Sci.*, 2005, **4**, 54–60.

54. H. Park, E. Bae, J. J. Lee, J. Park, and W. Choi, *J. Phys. Chem. B*, 2006, **110**, 8740–8749.

55. T. Hannappel, B. Burfeindt, W. Storck, and F. Willig, *J. Phys. Chem. B*, 1997, **101**, 6799–6802.

56. J. Hankache and O. S. Wenger, *Chem. Commun.*, 2011, **47**, 10145–7.

57. Y. Tamaki, K. Koike, and O. Ishitani, *Chem. Sci.*, 2015, **6**, 7213–7221.

58. C. M. Chang, K. L. Orchard, B. C. M. Martindale, and E. Reisner, *J. Mater. Chem. A*, 2016, **4**, 2856–2862.

59. W. A. Smith, I. D. Sharp, N. C. Strandwitz, and J. Bisquert, *Energy Environ. Sci.*, 2015, **8**, 2851–2862.

60. E. L. Rosen, R. Buonsanti, A. Llordes, A. M. Sawvel, D. J. Milliron, and B. A. Helms, *Angew. Chemie Int. Ed.*, 2012, **51**, 684–689.

61. V. V Matylitsky, A. Shavel, N. Gaponik, and A. Eychmu, *J. Phys. Chem. C*, 2008, **112**, 2703–2710.

62. J. Dana, T. Debnath, and H. N. Ghosh, *J. Phys. Chem. Lett.*, 2016, **7**, 3206–3214.

63. M. Jagadeeswararao, A. Swarnkar, G. B. Markad, and A. Nag, *J. Phys. Chem. C*, 2016, **120**, 19461–19469.

64. J. R. Caram, S. N. Bertram, H. Utzat, W. R. Hess, J. A. Carr, T. S. Bischof, A. P. Beyler, M. W. B. Wilson, and M. G. Bawendi, *Nano Lett.*, 2016, **16**, 6070–6077.

65. W.-S. Chae, T. D. T. Ung, and Q. L. Nguyen, *Adv. Nat. Sci. Nanosci. Nanotechnol.*, 2013, **4**, 45009.

66. M. G. Kotresh, K. S. Adarsh, M. A. Shivkumar, and S. R. Inamdar, *J. Fluoresc.*, 2016, **26**, 1249–1259.

67. D. H. Jara, K. G. Stamplecoskie, and P. V Kamat, *J. Phys. Chem. Lett.*, 2016, **7**, 1452–1459.

68. R. Kuriki, H. Matsunaga, T. Nakashima, K. Wada, A. Yamakata, O. Ishitani, and K. Maeda, *J. Am. Chem. Soc.*, 2016, **138**, 5159–5170.

“Do what I do. Hold tight and pretend it’s a plan!”

- *The Doctor*

5

In-situ SFG spectroelectrochemistry studies of CO_2 reduction intermediates

5.1. Scope of the chapter

The reduction of CO_2 to CO is a multielectron, multiproton reaction, and as such it generally involves several steps and therefore several intermediates. In the first chapter, the most investigated classes of CO_2 reduction electrocatalysts have been described. In most cases, the mechanism for electrocatalysis is still under investigation, with several pathways being debated in the literature.[1,2] Having a deep knowledge of the mechanism of catalytic reactions can lead to rational design of more efficient catalysts. Detection of reaction intermediates is however a complex endeavour, due to the transient nature of the species; spectroelectrochemical (SEC) techniques can offer important insights into the mechanism, however they often lack the time resolution or surface specificity to directly observe species as they are formed at the electrode surface. Amongst SEC techniques, SFG (Sum Frequency Generation) spectroscopy stands out due to its intrinsic surface selectivity, which allows the study of species at the electrode surface, rather than in the bulk. This technique has been used previously to investigate catalysts immobilised on a surface, however molecular CO_2 reduction complexes under potentiostatic control have not been studied.

Here we aim to develop the application of SFG spectroscopy to study molecular catalysts near or on electrode surfaces under potentiostatic control, making use of the high sensitivity, surface selectivity and (possible) time-resolution of the technique to identify electrode-catalyst interactions and short-lived intermediates. The work outlined in this chapter has been carried out in collaboration with Dr Paul Donaldson and the Central Laser Facility (CLF) (Harwell Campus, Oxfordshire). The instrument set up has been carried out by Dr Paul Donaldson, while the electrochemical cell design, electrochemical measurement and data analysis have been carried out by myself. The ULTRA laser system available at the Harwell campus is ideal for SFG spectroelectrochemical (SFG-SEC) measurements (Scheme 32); the laser has a high repetition rate (10 kHz), in contrast to commercial SFG spectrometers (50 Hz). This allows the

collection of spectra with good signal-to-noise much more quickly than with conventional laser systems, making it possible to record spectra while the electrochemical potential sweep measurement is running. Furthermore the availability of synchronised ps and fs laser pulses is a great benefit. By deriving a mid IR (Infrared) fs pulse (50 fs) it is possible to simultaneously probe a broad region of the IR spectrum (ca. 400 cm^{-1}), while a ps (*ca.* 1.5 ps) narrow-spectral band visible pulse enables the experiment to operate with a suitable resolution (<15 cm^{-1}) in the work described herein.

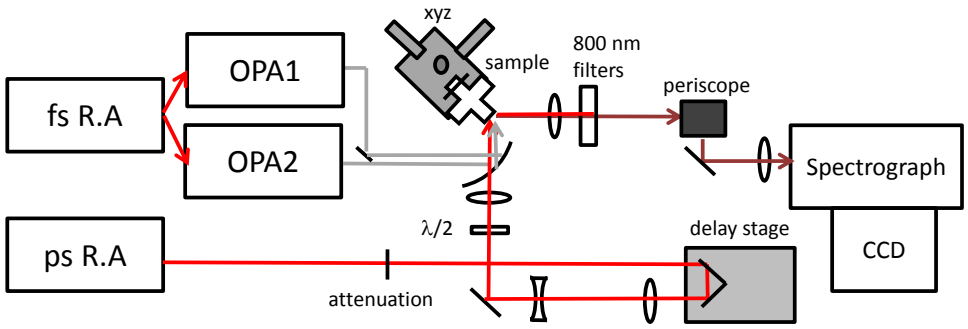

Scheme 32 – Experimental apparatus for the SFG-SEC experiments carried out is this chapter. Full experimental details can be found in the experimental section of this chapter.

$[Mn(bpy)(CO)_3Br]$ is an ideal complex for a first study using the newly developed *in situ* SFG-SEC experiment at the CLF. Despite the high level of interest in this class of catalysts it is apparent that significant mechanistic questions still remain. Furthermore, metal carbonyl υ(CO) modes, which have strong IR extinction coefficients and frequencies that are strongly dependent on the electron density at the metal centre, are ideal reporter groups to study using SFG spectroscopy. Therefore, in the first section of the chapter we report on an initial examination of $[Mn(bpy)(CO)_3Br]$ in MeCN (acetonitrile) on a polycrystalline gold electrode. Gold is chosen as the working electrode due to its high reflectivity in the visible, simplifying a reflection mode IR-Vis SFG experiment. We envisaged that SFG spectroscopy could give

valuable new information of the known electrochemically generated species with the electrode surface and potentially allow us to identify new intermediate species in the catalytic cycle.

In Chapter 2 we have shown the properties of a new nickel complex, Ni(cycC), towards the electrochemical reduction of CO_2 to CO in water. Our results indicated that the complex has a similar behaviour to the parent complex Ni(cyc) when catalysis is carried out at pH 5. Furthermore, Ni(cycC) showed a dramatic increase in catalytic activity at pH 2, and through the use of electrochemical and spectroscopic techniques we were able to correlate the increase in catalytic activity to the protonation of the carboxylic acid. It is believed that the presence of the proton opens a second catalytic pathway, whereby CO_2 binding to the nickel centre is stabilised through interaction with the carboxylic acid proton, aiding the CO_2 reduction reaction, however no spectroscopic evidence of this mechanism was obtained. It has been shown in many studies,[3] and confirmed in the previous chapters of this thesis, that the active species for CO_2 reduction by nickel macrocycles is a reduced species which is adsorbed on the mercury surface, with little contribution to the catalysis from the catalyst in the bulk. It was envisaged that once optimised the SFG-SEC experiment may be applicable to NiCyc on a Hg/Au electrode. The last section of the results and discussion section will show the efforts towards the study of the mechanism of CO_2 reduction by Ni(cycC).

5.2 results and discussion

5.2.1 Cell design

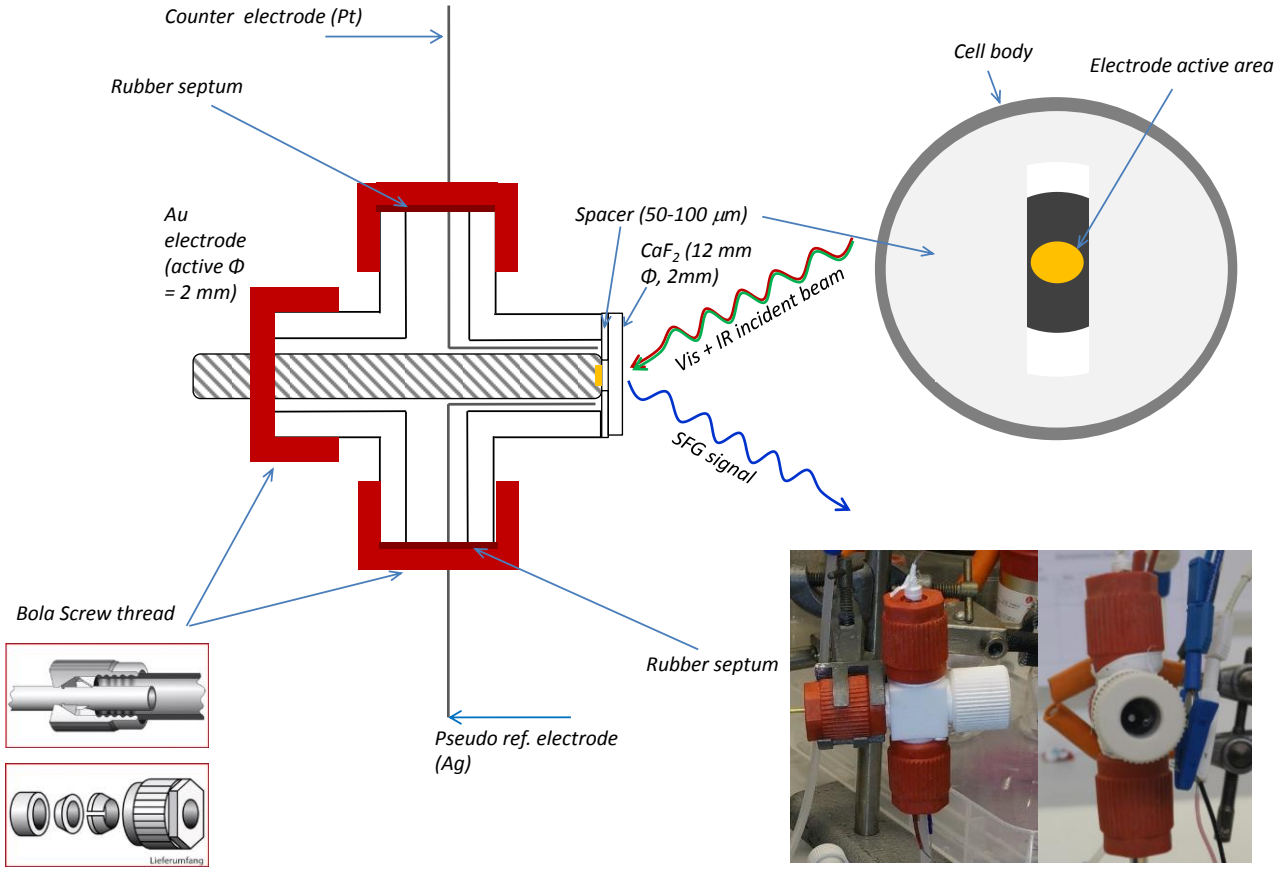

Scheme 33 – Side and top view of the spectroelectrochemical cell designed for the SFG experiments.Side and front pictures of the assembled SEC cell are shown in the bottom left corner.

A custom made electrochemical cell was built to meet the requirements of the SFG experiment based upon a rigid Teflon cross piece *ca.* 60 mm by 60 mm, Scheme 4. The cross piece is designed to have Bola gas tight screw fittings and the design is chosen as it provides the opportunity to adjust the height of the working electrode if required (Scheme 33). The cell window was CaF_2 (2 mm thickness), secured to the cross piece *via* a screw cap, made gas tight by the use of an o-ring. Although SFG spectroscopy is intrinsically a surface sensitive technique the presence of the electrolyte solution in the path of the IR beam prior to the surface will lead to an attenuation of the IR beam. This is due to the potential absorption losses from

the solvent, supporting electrolyte and catalyst which will cause a large decrease of the SFG intensity. To avoid this issue, a thin layer of the electrolyte solution was one of the main requirements for the electrochemical cell. The minimum path length was set by placing a 50 μm Teflon spacer between the window and the electrode. The counter electrode (platinum wire) and reference electrode (silver wire *pseudo* reference electrode) were inserted from the side arms of the cross cell, which were made gas-tight with a Bola fitting and a rubber septum, and were bent 90° to place the tip of the wires as close to the working electrode as possible. The sample was prepared by purging the cell with either argon or CO_2 and transferring the pre-purged electrolyte and catalyst solutions *via* cannula transfer. Initial tests for the suitability of the cell for electrochemical measurements were carried out by using a ferrocene solution in MeCN with the electrode pulled back from the spacer (Figure 107).

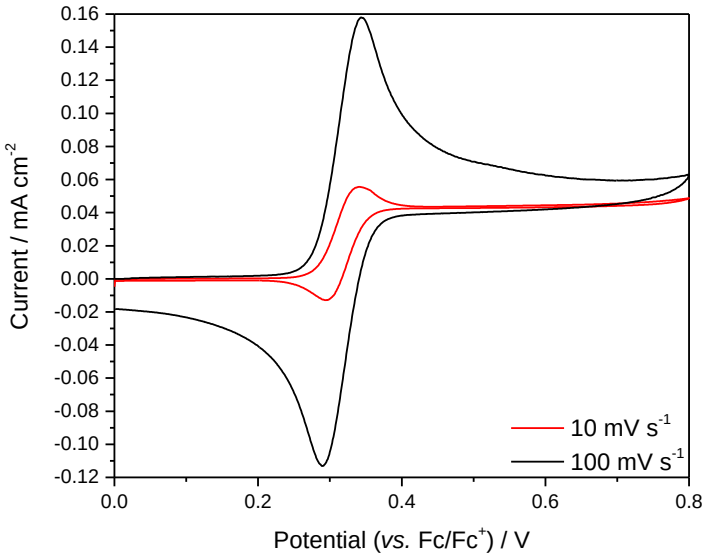

Figure 107 – Cyclic voltammetry (CV) of a 1 mM solution of ferrocene in MeCN, with 0.1 M $TBAPF_6$ as the supporting electrolyte and gold working electrode using the SFG-SEC cell.

5.2.2 *In-situ* SFG-SEC of [Mn(bpy)(CO)$_3$Br]

The cyclic voltammetry (CV) of [Mn(bpy)(CO)$_3$Br] under argon using a gold disc working electrode recorded in the SFG-SEC cell is shown in Figure 108(b). The electrochemical

response obtained was similar to the CVs carried out on the more commonly used glassy carbon electrode,[4] Figure 108(b), With two reductions, at -1.0 V_{Ag+} and -1.2 V_{Ag+}, and two oxidations, at -0.9 V_{Ag+} and 0 V_{Ag+}. The presence of small amounts of oxygen within the cell was also noticed, with the first scan showing a reduction peak at *ca.* -0.5 V_{Ag+}, which decreased significantly in later scans, suggesting that during transfer of the electrolyte some air may be entering the cell (*Note: experiments are carried out at the UK-CLF using only a basic gas line).* It was found however, that carrying out a single CV cycle prior to the spectroelectrochemical experiment was sufficient to consume the majority of the oxygen present in the diffusion layer and the rate of diffusion was such in the thin path length cell that the remaining oxygen in the bulk did not diffuse to the electrode surface on the time scale (<5 mins) of a typical SFG experiment.

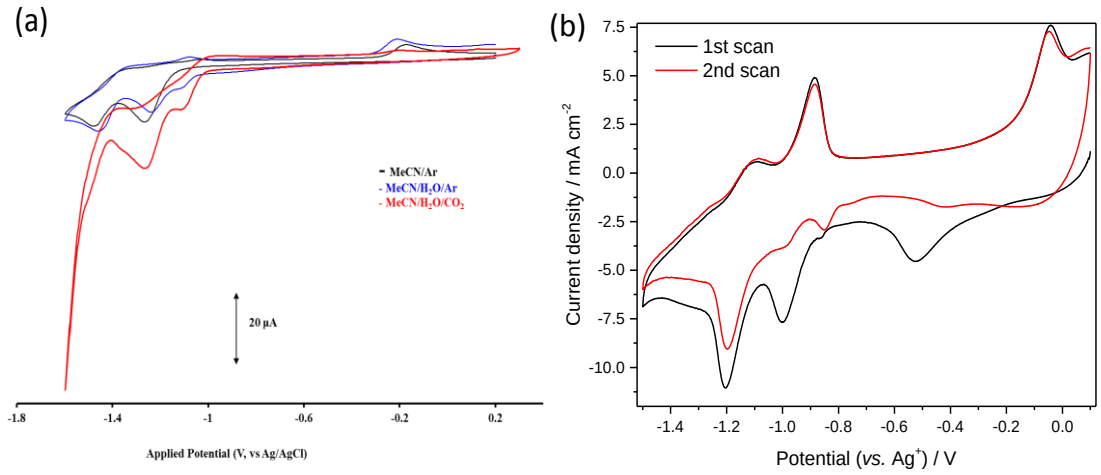

Figure 108 – CVs of a 1 mM solution of [Mn(bpy)(CO)$_3$Br] in MeCN (0.1 M TBAPF$_6$) purged with argon or CO$_2$, 50 mVs^{-1}, (a) GCE in a conventional electrochemical cell and (b) gold working electrode in the SFG-SEC cell.

The cell was aligned in the laser enclosure and connected to a portable potentiostat (see section 5.3 for full details), which was small enough that it could also be housed in the enclosure, and connected to a laptop. The laser beams were aligned on the surface of the electrode, and the IR beam was tuned to the desired range of interest; for the experiments on [Mn(bpy)(CO)$_3$Br]

three spectral windows were recorded (the IR beam wavelength was centred at 2200, 1900 and 1700 cm^{-1}). Experiments were carried out with *ppp* (SFG, Vis, IR) polarisation unless otherwise stated, only a limited number of studies also used *psp*. In a typical experiment, a CV at slow scan rate (50 – 5 mV s^{-1}, with a potential window of 1.6-1.7 V) was run whilst the SFG data was acquired. SFG spectra were typically averaged for either 2 or 5 seconds dependent on the CV scan rate, so that one SFG trace would correspond to a potential window of 100 mV during a 50 mV s^{-1} CV or 25 mV for CVs that were run at 5 mVs^{-1}, in order to obtain higher S:N whilst maintaining a good potential resolution. Data is shown from a single CV experiment, and unless stated otherwise is not co-added from multiple individual experiments.

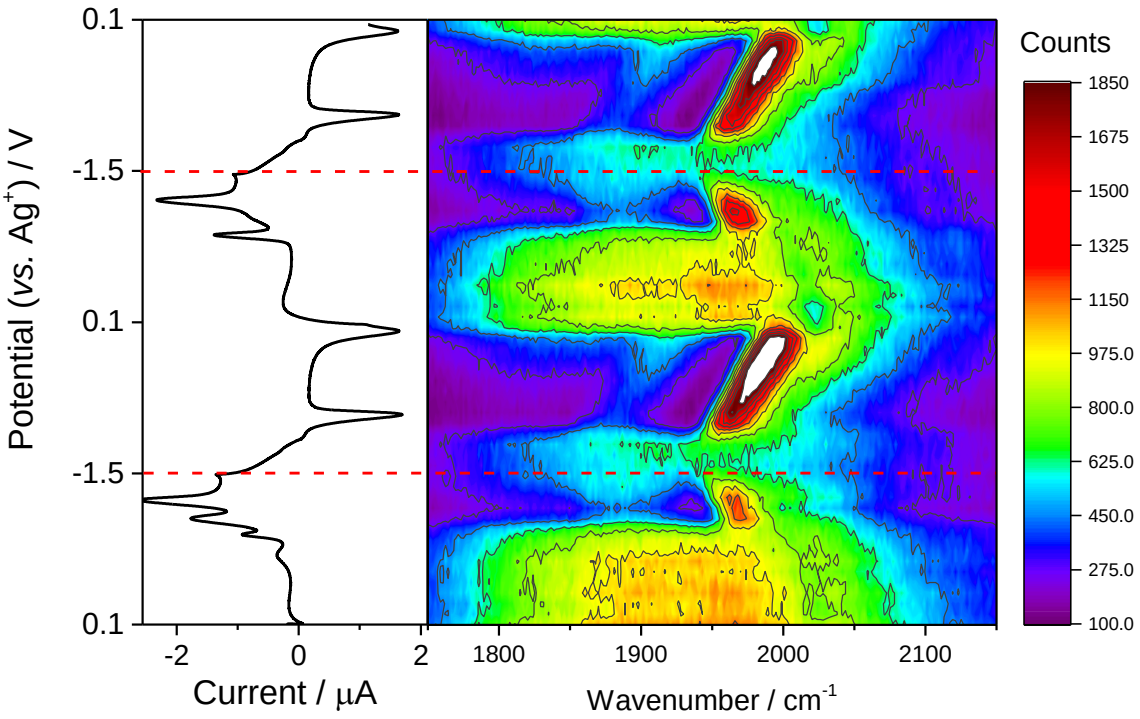

Figure 109 – SFG spectroelectrochemistry of a [Mn(bpy)(CO)$_3$Br] 1 mM solution in MeCN (0.1 M TBAPF$_6$), obtained by recording an SFG spectrum every 2 s while running a CV at 50 mVs^{-1}(2 scans) on a gold working electrode. The dotted lines indicate the potential at which the CV scan direction was reversed, and are added to aid visualisation.

Figure 109 shows the data obtained from a SFG-SEC experiment of the metal-carbonyl region (1750-2150 cm^{-1}) of [Mn(bpy)(CO)$_3$Br] under potentiostatic control. On the left, CV (2 scans

at a scan rate of 50 mVs^{-1}) is presented with potential on the vertical axis. On the right is data acquired by the SFG spectrometer presented as IR wavenumber (x-axis) *vs.* potential (y-axis) with the SF intensity in the z direction (given by the colour coded contour scale). From Figure 109 it is clear that a dependence between the redox events present in the CV and the recorded SFG spectra is occurring. As the SFG technique is sensitive only to species at surfaces or interfaces the SF signals may arise from either species at the electrolyte/front window or the electrode surface. The potential dependence of the SFG spectrum leads us to assign the data to the different intermediates of $[Mn(bpy)(CO)_3Br]$ present at the electrode, or within the double-layer.

At the beginning of the SFG-SEC experiment (0.1 V to -0.5 V), the non-resonant background (1750-2150 cm^{-1}) was the main feature of the spectrum, appearing as a broad band, with the same width and intensity profile as the IR incident pulse, Figure 109. Careful inspection of the SFG spectrum at -0.1 V does also indicate the presence of three peaks overlapping with the broad non-resonant background: two positive peaks at 1955 cm^{-1} and 2036 cm^{-1}, and a negative peak at 2020 cm^{-1}. The spectrally narrow bands of these peaks indicate that they correspond to a resonant SF response, Figure 110. The frequency of the inverted peak corresponds to the 1a' υ(CO) carbonyl mode of the starting $[Mn(bpy)(CO)_3Br]$ complex, and is therefore assigned to this species (see Table 20 for literature values of the species considered[5]).

Table 20 – Characteristic IR frequency for the electrochemical products of $[Mn(bpy)(CO)_3Br]$, from ref. [5]

Species	ν(CO) (cm^{-1})
$[Mn(bpy)(CO)_3Br]$	2025(s), 1936(m), 1913(m)
$[Mn(bpy)(CO)_3(MeCN)]^+$	2049(s), 1965 (m), 1953(m)
$[Mn(bpy)(CO)_3]_2$	1975(m), 1963(w), 1936(s), 1886(m), 1866(m)
$[Mn(bpy)(CO)_3]^-$	1916(s), 1814(s, br.)

The slight shift in the wavenumbers *versus* the literature report is likely due to the [Mn(bpy)$(CO)_3$Br] being at the electrode surface. The appearance of a negative signal in SFG spectra is not uncommon, and it can either be related to (a) the presence of the same species in the bulk solution in large concentrations, absorbing the IR radiation and therefore resulting in a decrease in intensity of the non-resonant response at the specific wavelength, or (b) to the interference between resonant vibrations and the non-resonant background giving rise to an out-of-phase response[6]. For the first option to be true the inverted peak should be present in all the recorded spectra regardless of the applied potential – essentially the bulk concentration of the IR absorber is unlikely to be greatly lowered during the CV experiment, and this does not appear the case. The two positive SF signals at 1955 cm^{-1} and 2036 cm^{-1} can be assigned to the 2a' and 1a' υ(CO) modes of the solvo-complex, [Mn(bpy)$(CO)_3$(MeCN)]$^+$. Both [Mn(bpy)$(CO)_3$Br] and [Mn(Bpy)$(CO)_3$(MeCN)]$^+$ have 3 strong IR active υ(CO) modes (1a', a'' and 2a'), Table 20,[5] however here not all of these are observed throughout the SFG experiment. In Figure 110 it is possible that all 3 metal carbonyl stretches are present for each complex, but not visible due to the presence of the large non-resonant signal and relatively low S:N. Alternatively it may be envisaged that the orientation of the complexes at the electrode may be leading to some vibrational modes becoming SF inactive. In the following paragraphs this possibility will be explored further.

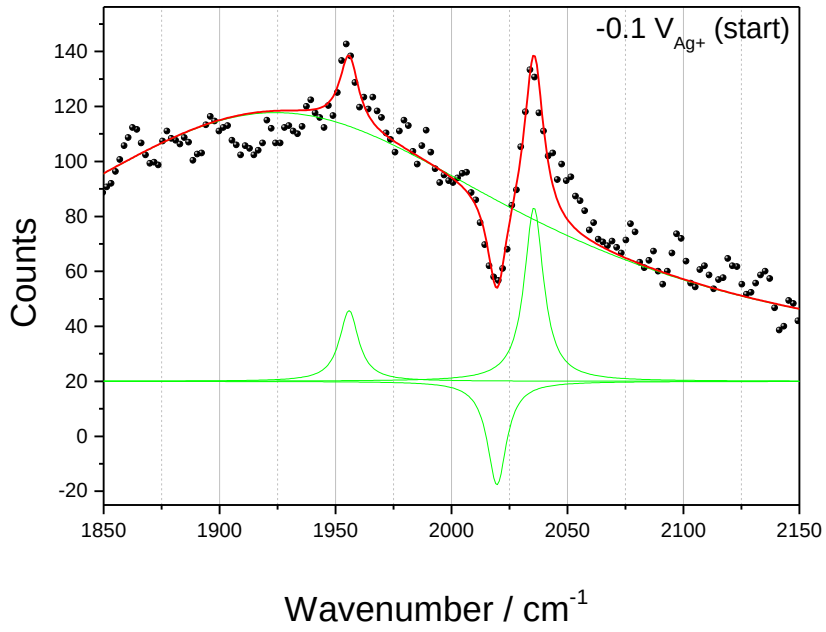

Figure 110 – SFG spectrum, recorded by averaging every 2 seconds, at -0.1 V_{Ag+}, for a 1 mM solution of [Mn(bpy)(CO)$_3$Br] in MeCN (0.1 M TBAPF$_6$) purged with argon, 50 mVs^{-1}, gold working electrode..

As the potential was scanned cathodically, the non-resonant background was partially suppressed and a strong feature at *ca.* 1960 cm^{-1} was observed at potentials where [Mn(bpy)(CO)$_3$Br] undergoes the first reduction (*ca.* -0.95 V_{Ag+}). The resonant mode is shifted to lower wavenumbers as the potential is swept cathodically (see below*)* and disappears at potentials corresponding to the second reduction (*ca.* -1.3 V_{Ag+}). Following 1 e$^-$ reduction [Mn(bpy)(CO)$_3$Br] dimerises [4,7,8] to form [Mn(CO)$_3$(bpy)]$_2$ and the intense peak appearing at 1960 cm^{-1} is assigned to one of the ν(CO) of the dimer [Mn(bpy)(CO)$_3$]$_2$.[7,8] The strong SF response is also in-line with the known UV/Vis spectrum of [Mn(bpy)(CO)$_3$]$_2$, a species that has λ_{max} = 394, 461, 633 and 806,[4] with the wavelength of the visible laser beam (800 nm) leading to a further resonant enhancement of the SF output, essentially a double-resonant SF transition.[9] In solution the [Mn(bpy)(CO)$_3$]$_2$ complex has been shown to have four characteristic CO vibration modes in previous bulk IR-SEC experiments[7,8], at 1980, 1936, 1886 and 1867 cm^{-1}. The large shift between the IR mode in solution (1980 cm^{-1}) and whilst on the

gold electrode (1960 cm^{-1} at -0.95 V_{Ag+}) will be discussed further below. In Figure 109 a broad spectral feature from ~1850 – 1930 cm^{-1} can also be observed at *ca.* -0.95 V_{Ag+} however the presence of the non-resonant background makes assignment complicated. Experiments carried out at 5 mV s^{-1} (Figure 111) provide further evidence for spectral features at *ca.* 1830 and 1880 cm^{-1} (Figure 112) however again the presence of the non-resonant background makes accurate band positions difficult to obtain.

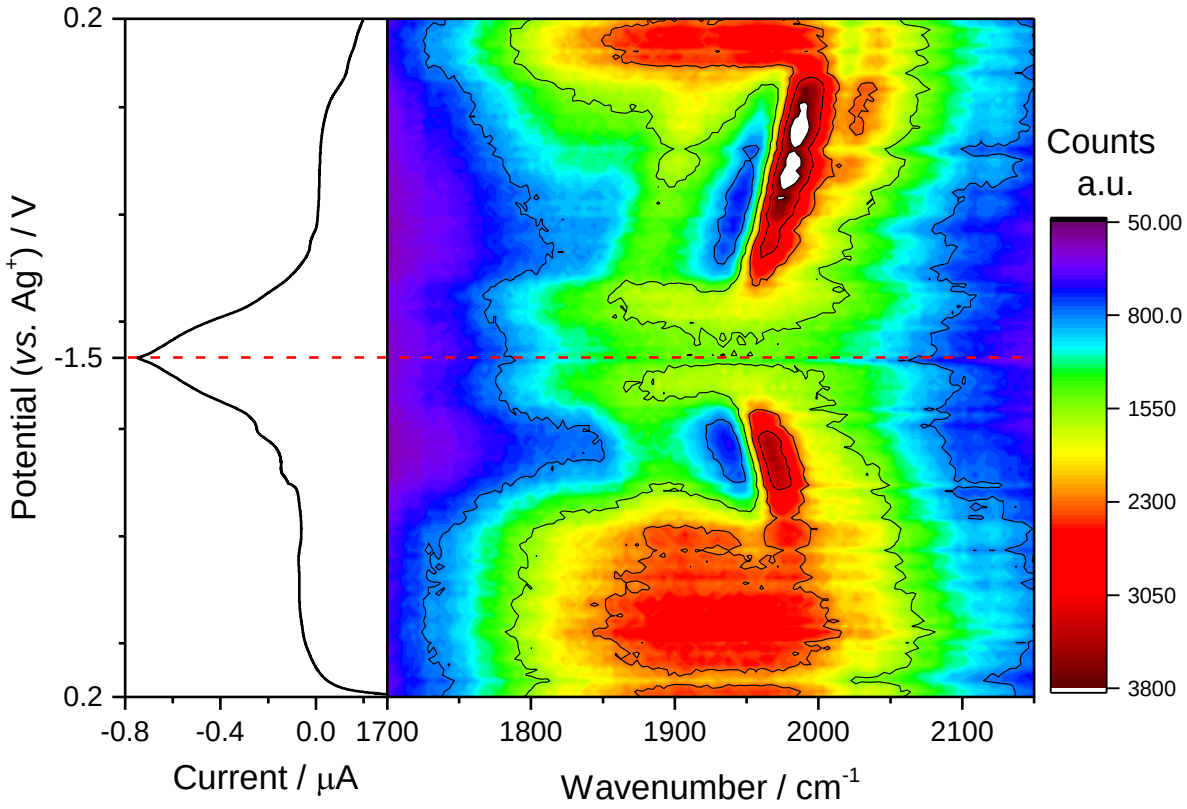

Figure 111 - SFG spectroelectrochemistry of a [Mn(bpy)(CO)$_3$Br] 1 mM solution in MeCN (0.1 M TBAPF$_6$), obtained by recording an SFG spectrum every 5 s while running a CV at 5 mVs^{-1}(1 scan) on a gold working electrode. The dotted line indicates the potential at which the CV scan direction was reversed, and is added to aid visualisation.

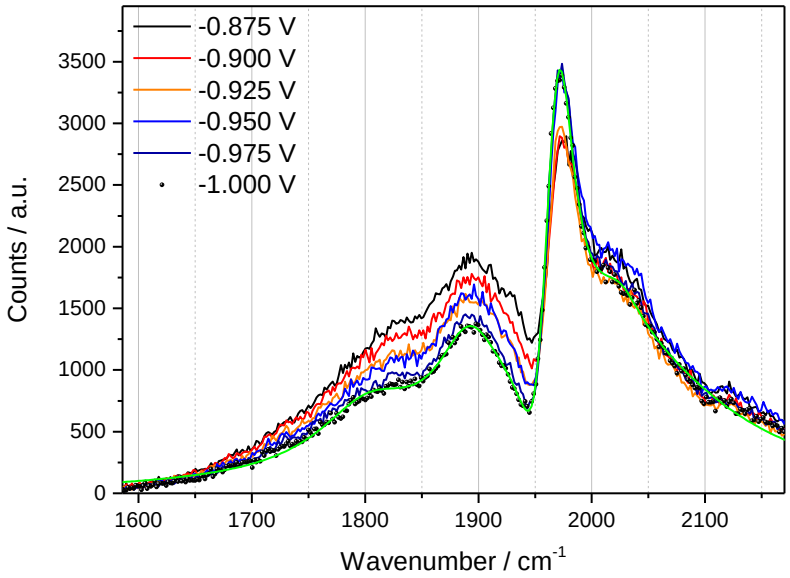

Figure 112 - SFG spectra, recorded by averaging every 5 seconds, at the potentials indicated, for a 1 mM solution of [Mn(bpy)(CO)$_3$Br] in MeCN (0.1 M TBAPF$_6$) purged with argon, 5 mVs^{-1}, gold working electrode.

The non-resonant background arises primarily from the $X_{NR}^{(2)}$ contribution of the Au-electrolyte interface.[10] It has been shown previously that the non-resonant component of the SFG intensity could be suppressed by applying a time delay between the broad band IR pulse and the narrow band visible pulse[11]. This is possible due to the different time dependencies of the induced resonant and non-resonant polarisations at metal interfaces (Figure 113) and the pulse widths of the IR and Vis lasers. To obtain a spectrally narrow visible pulse the principle of indetermination dictates that the beam must be temporally broad (here on the order of 1.5 ps FWHM (Full width at half maximum), giving a ~15 cm^{-1} FWHM). For the IR beam, which is desired to have a spectrally broad output, is achieved by the use of a ~50 fs FWHM IR pulse, this is visualised in Figure 113 by the narrow IR pulse shown in purple and the broad visible pulse shown in green. When the fs-IR beam is tuned to a resonant transition first-order polarisation induced by the IR beam, it decays with a characteristic lifetime dependent on the nature of the vibration and the solvent environment and for metal carbonyl modes in MeCN lifetimes of up to 50-500 ps have been reported,[12] shown in gold/orange on Figure 113. The

lifetime of any non-resonant state induced by the IR beam is anticipated to be significantly shorter (< 1 ps). When both beams overlap temporally and spatially (Figure 113(B)), both the resonant and the non-resonant states can interact with the visible pulse leading to a non-resonant and resonant contribution to the SF spectrum; introducing a time delay allows the non-resonant contribution to decay significantly before the peak of the visible pulse is incident. In contrast, the longer lifetime of the resonant IR transition means that a significant population still exists (Figure 113(C)).

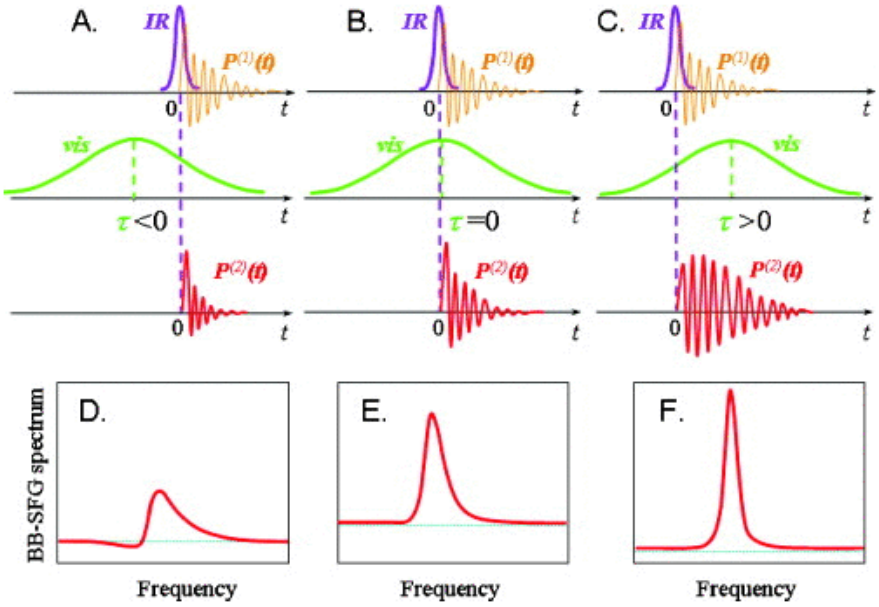

Figure 113 – Scheme illustrating the pulse shapes characteristic of an SFG experiment with time; (A) the IR pulse is sent after the visible pulse, (B) the IR pulse is sent at the same time as the visible pulse and (C) the IR pulse is sent before the visible pulse.

Here we have also carried out SFG-SEC experiments of [Mn(bpy)$(CO)_3$Br] in MeCN under argon using a -1.5 ps delay between the visible and IR pulses (Figure 114, the negative sign on the time delay indicates arrival of the IR pulse ahead of the visible). The size of the delay was chosen by stepping the delay time 0.1 ps at a time, while keeping the cell at open circuit potential, to achieve the greatest level of non-resonant background suppression whilst maintaining some resonant signal from [Mn(bpy)$(CO)_3$Br]. As seen in Figure 114 the

application of the time delay did not completely suppress the non-resonant background and it did also lead to a significant loss in resonant signal. Nevertheless, it was still possible to identify many of the key spectral features, Figure 114. Most notably at *ca.* -1 V_{Ag+} a clearer spectrum of $[Mn(bpy)(CO)_3]_2$ is recorded (Figure 115) which can be fitted using multiple Lorentzian peak functions with bands at 1961, 1891 and 1859 cm^{-1} overlaid with a broad residual non-resonant signal, in good agreement with previous observations for the same complex in solution (Table 20). In solution $[Mn(bpy)(CO)_3]_2$ also has a υ(CO) mode at 1936 cm^{-1} which appears to be absent in the SF spectrum, this may be due to the orientation of the $[Mn(bpy)(CO)_3]_2$ on the surface of the electrode and remains under investigation.

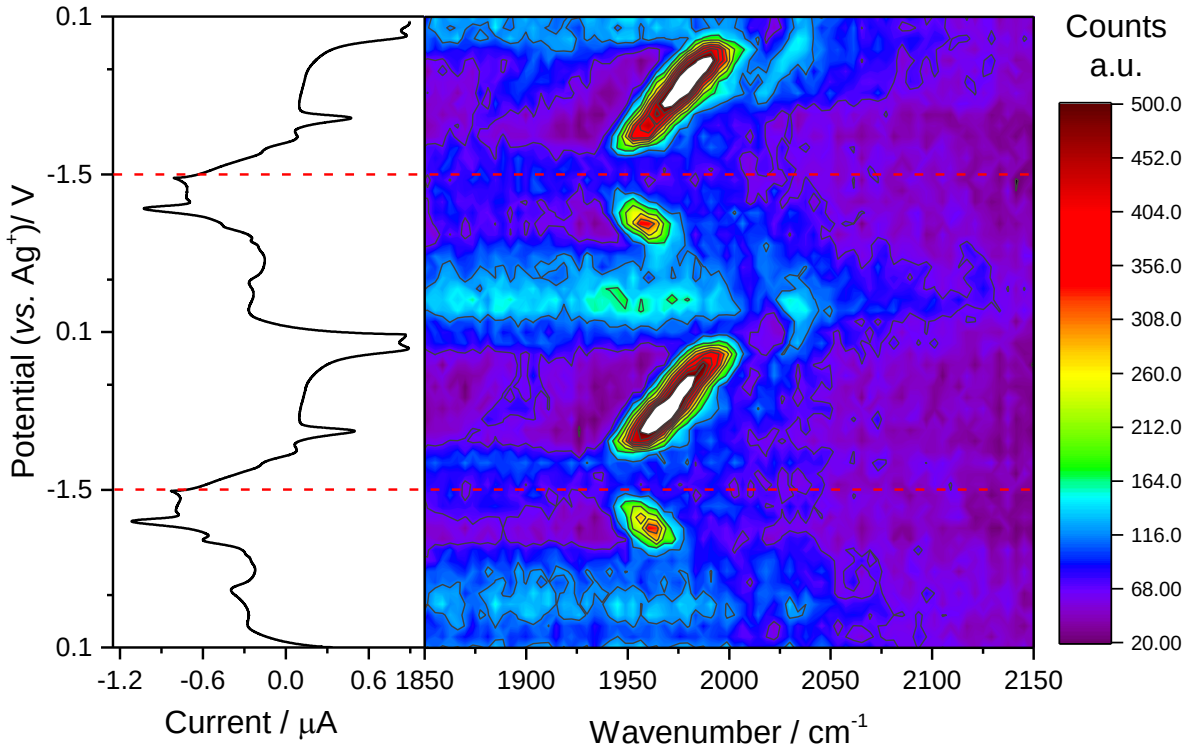

Figure 114 - SFG spectroelectrochemistry of a $[Mn(bpy)(CO)_3Br]$ 1 mM solution in MeCN (0.1 M $TBAPF_6$), obtained by recording an SFG spectrum every 2 s while running a CV at 50 mVs^{-1}(2 scans) on a gold working electrode, time delay = -1.5 ps. The dotted lines indicate the potential at which the CV scan direction was reversed, and are added to aid visualisation.

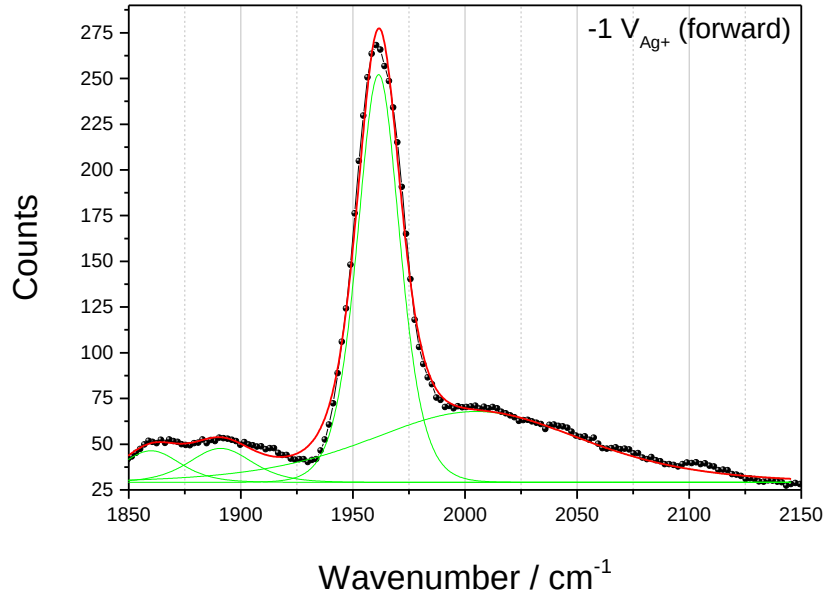

Figure 115 –SFG spectrum, recorded by averaging every 2 seconds, at -1 V_{Ag+}, for a 1 mM solution of [Mn(bpy)(CO)$_3$Br] in MeCN (0.1 M TBAPF$_6$) purged with argon, 50 mVs^{-1}, gold working electrode, time delay = -1.5 ps.

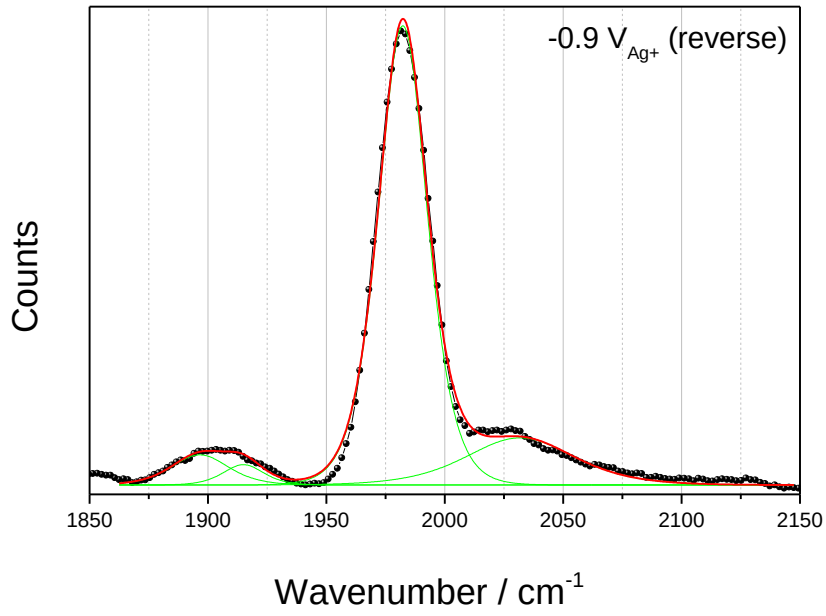

Figure 116 – SFG spectrum, recorded by averaging every 2 seconds, at -0.9 V_{Ag+}, for a 1 mM solution of [Mn(bpy)(CO)$_3$Br] in MeCN (0.1 M TBAPF$_6$) purged with argon, 50 mVs^{-1}, gold working electrode, time delay = -1.5 ps.

In Figure 109 and Figure 111 (no non-resonant suppression, 50 mV and 5 mV s^{-1}) and Figure 114 (-1.5 ps delay suppression, 50 mV s^{-1}) the second reduction in the CV (*ca.* -1.25 V_{Ag+}) leads to the loss of the spectral features assigned to the [Mn(bpy)(CO)$_3$]$_2$ species. Bulk IR-SEC

experiments have assigned this reduction to the formation of the doubly reduced $[Mn(bpy)(CO)_3]^-$ following the dissociation of $[Mn(bpy)(CO)_3]_2$, and this species is characterised by two ν(CO) stretches, at 1916 and 1814 cm^{-1} (Table 20).[7] In the SFG-SEC experiment neither resonant peak was observed at the potentials where the doubly reduced species was expected (-1.25 V_{Ag+} - -1.5 V_{Ag}) to occur. In contrast, the disappearance of $[Mn(bpy)(CO)_3]_2$ in the spectrum was followed by a relatively flat spectrum, indicating the absence of manganese carbonyl species at the surface at these potentials. During the reverse sweep (-1.5 to 0.1 V_{Ag+}) $[Mn(bpy)(CO)_3]_2$ is seen to reform (υ(CO) at 1955 cm^{-1}), at the potential corresponding to the first reoxidation (-0.9 V_{Ag+}, Figure 116), indicating that the electrochemical processes occurring in this study are similar to those previously reported. The lack of observation of $[Mn(bpy)(CO)_3]^-$ by our surface selective SFG-SEC experiment may indicate that once formed this catalytically active species is rapidly transferred into the bulk solution (indeed a large reorganisation in the solvent structure at the electrode at this potential is demonstrated later), or that any $[Mn(bpy)(CO)_3]^-$ is orientated in such a manner on the electrode surface to make all three carbonyl modes SF inactive.

During the anodic sweep $[Mn(bpy)(CO)_3]_2$ was electrochemically stable over a large potential window with reoxidation occurring at *ca.* 0 V_{Ag+} (Figure 109, Figure 111 and Figure 114). Interestingly the frequency of the SF modes of $[Mn(bpy)(CO)_3]_2$ were also found to be strongly dependent upon the applied potential during the anodic sweep. The shift in frequency of a vibrational mode in the presence of an external electric field is known as a Stark shift[13,14] and the magnitude of a Stark shift can be used to provide insights into the level of interaction and degree of charge screening between the vibrational modes and the electrode material.[15,16] For example SFG studies of ionic liquids for CO_2 reduction have shown that by analysing the Stark shift of a species it is possible to obtain information about the effect of the electric field on the species under analysis and the double layer properties. Baldelli[15] was able to determine the

extent of the interaction of CO adsorbed on a platinum electrode in a solution of EMIM-BF_4 (1-Ethyl-3-Methylimidazolium Tetrafluoroborate) by measuring the Stark shift of the υ(CO) mode and determined the size of the Helmoltz layer to be ~ one ion thick. Similarly, Dlott *et al.*[17] studied the same effect on a silver electrode. While the Stark shift found by Baldelli for CO adsorbed on Pt was 33-35 $cm^{-1}\,V^{-1}$, Dlott *et al.* measured a maximum Stark shift of *ca.* 50 $cm^{-1}\,V^{-1}$ for CO on Ag during CO_2 reduction (although we note that while the ionic liquid studied was the same, the electrolyte solution was slightly different). Notably this larger Stark shift only occurred at potentials cathodic of the onset of CO_2 reduction, indicating that a large rearrangement of the double layer may be occurring at the onset potential as the field experienced by CO on the Au significantly increased. Figure 117 shows the Stark shift for the dominant carbonyl stretch of $[Mn(bpy)(CO)_3]_2$ (*ca.* 1960 cm^{-1} at -1V). The shift shows a linear relationship with the potential, the slope of which is 35 ± 3 $cm^{-1}\,V^{-1}$ and 41 ± 5 $cm^{-1}\,V^{-1}$ for the cathodic and anodic sweeps respectively. The value for the Stark shift, similar to that observed by Baldelli,[15] indicates that $[Mn(bpy)(CO)_3]_2$ is interacting strongly with the electrode surface. The large Stark shift is in-line with the overall shift in frequency *versus* solution.

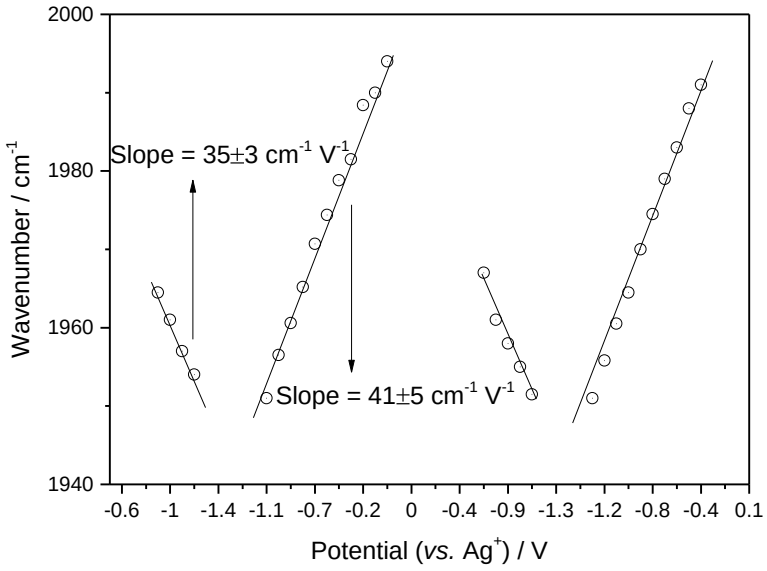

Figure 117 – Stark shift for the dominant SF ν(CO) mode of $[Mn(bpy)(CO)_3]_2$, calculated by plotting the peak value versus the potential, and applying a linear fit to calculate the slope. For a SFG-SEC experiment of 1mM, CVs run at 50 mV s^{-1} in MeCN, Ar purged.

Electric field gradient contributing to the shift of the peak cannot be entirely discounted, and calculations would be needed to account for it,[18] however it is unlikely, as effects due to the field gradient are usually noted for species with a very large internal dipole, such as proteins.

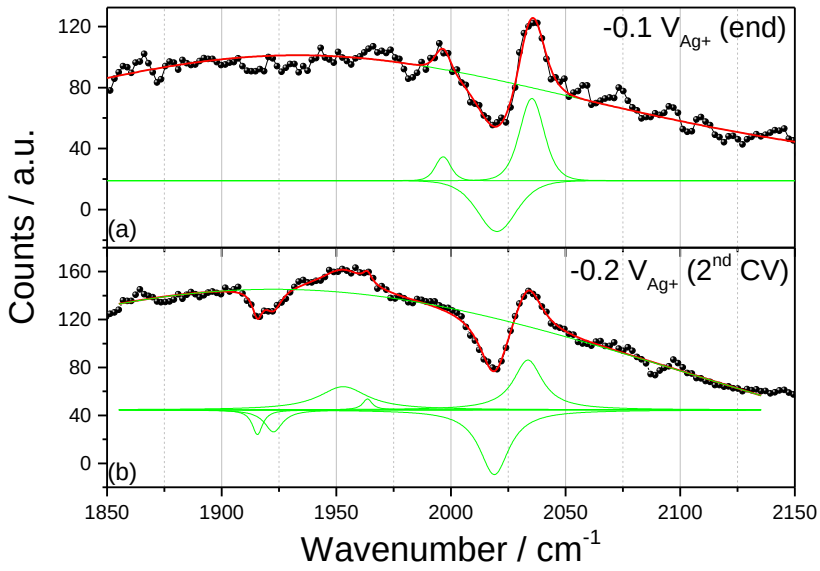

Figure 118 – SFG spectra, recorded by averaging every 2 seconds, at (a) -0.1 V_{Ag+} and (b) at -0.2 V_{Ag+}, for a 1 mM solution of [Mn(bpy)(CO)$_3$Br] in MeCN (0.1 M TBAPF$_6$) purged with argon, 50 mVs^{-1}, gold working electrode, time delay = -1.5 ps.

At the potential where [Mn(bpy)(CO)$_3$]$_2$ oxidation occurs (*ca.* -0.1 V_{Ag+}, Figure 109, Figure 111, Figure 114 and Figure 118(a)), we observe a loss of the dominant [Mn(bpy)(CO)$_3$]$_2$ peak at 1996 cm^{-1} (-0.1 V_{Ag+}) and the growth of resonant features that can be assigned to [Mn(bpy)(CO)$_3$Br] and [Mn(bpy)(CO)$_3$(MeCN)]$^+$ (2020 cm^{-1} (inverted) and 2035 cm^{-1} respectively, Figure 118(a)), demonstrating that the SFG-SEC experiment is able to monitor the reduction of [Mn(bpy)(CO)$_3$]$_2$ and subsequent fragmentation.

As noted above both [Mn(bpy)(CO)$_3$Br] and [Mn(bpy)(CO)$_3$(MeCN)]$^+$ would be expected to have 3 IR active υ(CO) modes. Interestingly when the SFG-SEC experiment was continued for a 2nd CV cycle (0.1 to -1.5 V_{Ag+}) a clear change in the spectra of [Mn(bpy)(CO)$_3$Br] and

$[Mn(bpy)(CO)_3(MeCN)]^+$ could be observed. Between -0.2 V_{Ag+} and -0.7 V_{Ag+} new SF signals are noted (Figure 118(b)), which correspond to the carbonyl stretches of $[Mn(bpy)(CO)_3Br]$ (negative peaks at 1915 and 1922 cm^{-1}) and $[Mn(bpy)(CO)_3]MeCN^+$ (positive peaks at 1952 and 1966 cm^{-1}). The presence of the new SF features could be due to an increase in the surface concentration of both $[Mn(bpy)(CO)_3Br]$ and $[Mn(bpy)(CO)_3(MeCN)]^+$ without a change in geometry, however we do not observe an increase in the intensity of the bands at 2020 cm^{-1} (inverted) and 2035 cm^{-1} (Figure 118(a) *vs*. (b)), which would suggest that this hypothesis can be discounted. Alternatively, the appearance of the new bands could be due to a potential induced geometric reorientation of the complexes on the surface of the electrode leading to υ(CO) modes which had previously been SF inactive (or only partially active) becoming SF active. Close inspection indicates that a similar potential dependent re-orientation may also be occurring in the 1st CV cycle however typically lower S:N was achieved in scan 1, the reasons for which are not currently understood.

In principle, from SFG experiments recorded using different polarisation combinations of the IR, vis, SFG to study a molecule on a well-defined single crystal surface it is possible to predict the SF intensity for different vibrational transitions as the orientation of the molecule on a surface is changed.[19] However here we have used a polycrystalline gold electrode which complicates such an analysis, and DFT calculations to explore this system are still on-going. A simpler approach based upon the expected number of IR modes from the IR surface selection rule on metals[20] has been used to rationalise the data instead. The surface selection rule allows the prediction of the IR active modes for a species adsorbed at a metal surface, and it states that only molecules with a component of the dipole moment perpendicular to the surface will have an IR active mode, due to the dipole of the adsorbate inducing opposite image charges in the metal. Therefore, only modes with a dipole mode non parallel to the surface will be seen in the spectrum; to be SFG active we initially require an IR absorption to occur.

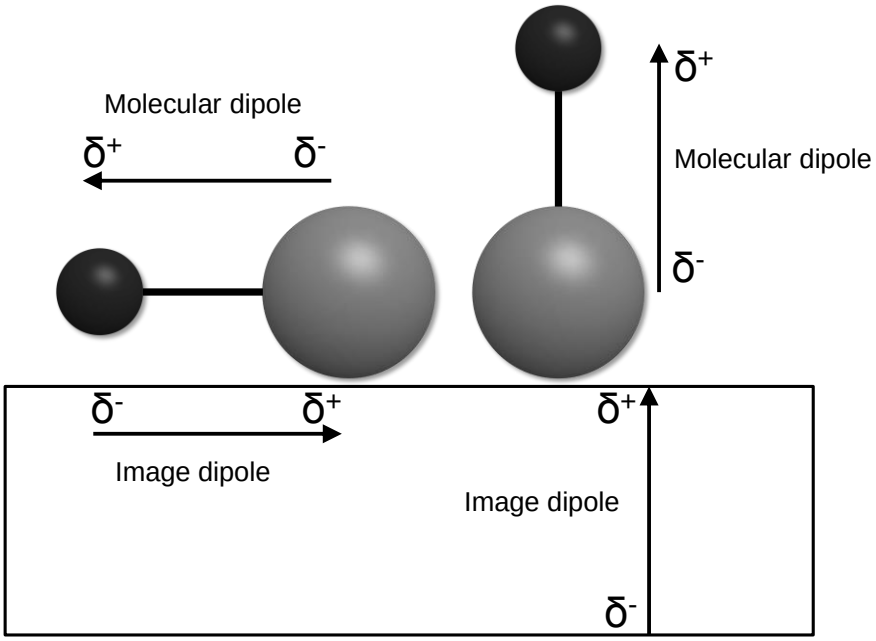

Figure 119 – Schematic representation of the surface selection rule.

Several orientiations of [Mn(bpy)(CO)$_3$Br] on a surface could be considered, Figure 120. The orientations proposed do not represent a complete analysis of all possible surface orientations and theory would be of great benefit to support the identification of the most likely alignments, however energy minimisations of adsorbates on an electrode in the presence of solvent, electrolyte salt and at a range of potentials is a non-trivial task. We have calculated and optimised the [Mn(bpy)(CO)$_3$Br] structures in the gas phase using the Gaussian software, and the vibrational spectra have been calculated. The basis sets used for Mn were B3LYP and Lan2DZ, while the 6-31G* basis set was used for all other elements.[21–24] In line with the literature we find 3 CO stretchings, 1a', a'' and 2a'. The frequency of the IR modes is overestimated, as is common for this type of calculation,[21] however the trends are in line with experimental values. Visualisation of the vibrational displacements (blue arrows) and the net dipole derivative (gold arrow) allow us to examine potential surface orientations to see the

number of IR modes that have a non-zero dipole moment in the axis perpendicular to the surface. With this simple method, it was possible to identify orientations with 1, 2 or 3, IR active modes, suggesting that 1 and 3 may account for the SF response (other orientations may be possible); note that placing the Br (or solvent) as the group in contact with the surface will give only 2 active modes (a' and 2a').

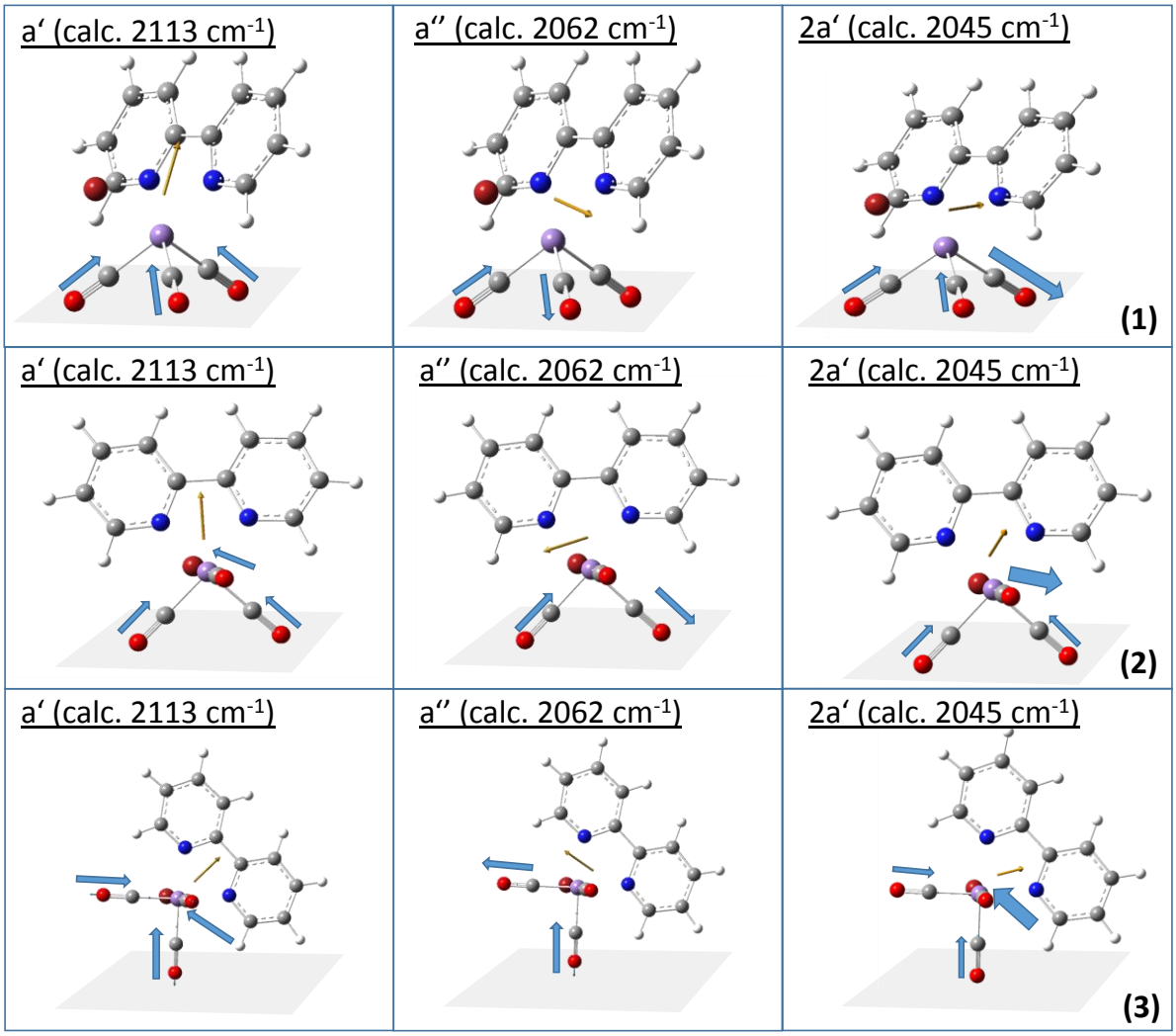

Figure 120 – Calculated dipole moments for the 1a', a'' and 2a' CO stretchings of [Mn(bpy)(CO)$_3$Br] for three different possible orientations, using the Gaussian software.

Although the non-resonant background can obstruct the identification of resonant modes it is also in its own right a useful probe of electrochemical surfaces, having been shown to be highly

dependent on the applied potential, generally showing a parabolic trend in the magnitude of the SF_{NR} and the potential.[17] As the non-resonant background is associated with the metal electrode, it is heavily dependent on the electronic transitions of the material, and therefore on the applied potential, hence acting as a probe for interactions at the electrode surface. A region of the IR spectrum (2100-2500 cm^{-1}, Figure 121) which was expected to be free of bands characteristic of $[Mn(bpy)(CO)_3Br]$, or any other electrochemical product was chosen to investigate the behaviour of the non-resonant background in the presence of the complex.

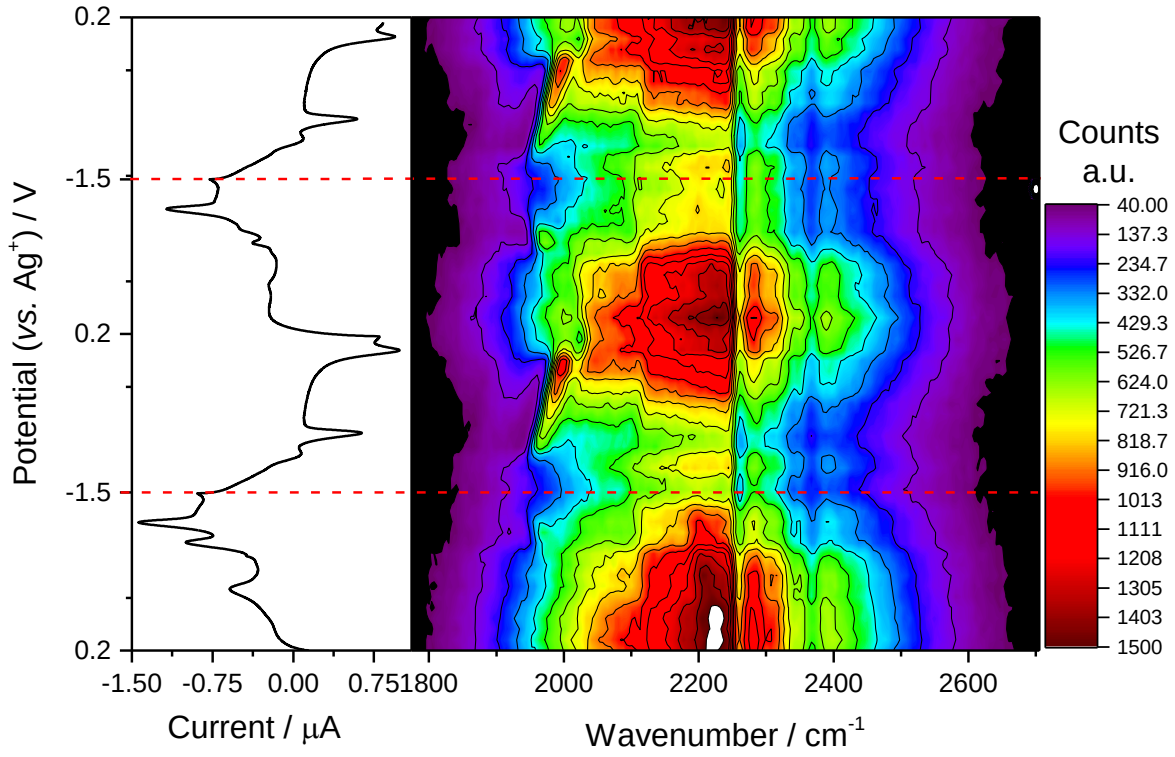

Figure 121 - SFG spectroelectrochemistry of a $[Mn(bpy)(CO)_3Br]$ 1 mM solution in MeCN (0.1 M $TBAPF_6$), obtained by recording a SFG spectrum every 2 s while running a CV at 50 mVs^{-1}(2 scans) on a gold working electrode. The dotted lines indicate the potential at which the CV scan direction was reversed, and are added to aid visualisation.

In Figure 121 the strong resonant $[Mn(bpy)(CO)_3]_2$ band is still visible at *ca.* 1990 cm^{-1}, showing the same behaviour as seen previously (Figure 109, Figure 111). In Figure 121 the SF intensity from a wavenumber close to the peak values of the non-resonant background (2220 cm^{-1}) was plotted as a function of time (Figure 122), together with the classic potential *vs.* time

profile typical of a cyclic voltammogram. MeCN has modes at 2260 and 2370cm^{-1} and these are not expected to interfere with the SF response at 2220 cm^{-1}. The intensity of the non-resonant background decreases as the potential is scanned more negative, while it increases when the direction of the scan is reversed, in line with past reports, Figure 122.[17] The spectrum shows however some regions where the parabolic behaviour is not maintained. Similar behaviour has been seen elsewhere[17] and assigned to potentials where the double layer undergoes a major structural reorganisation following a dramatic redox event and here we assign the non-parabolic behaviour to a similar effect.

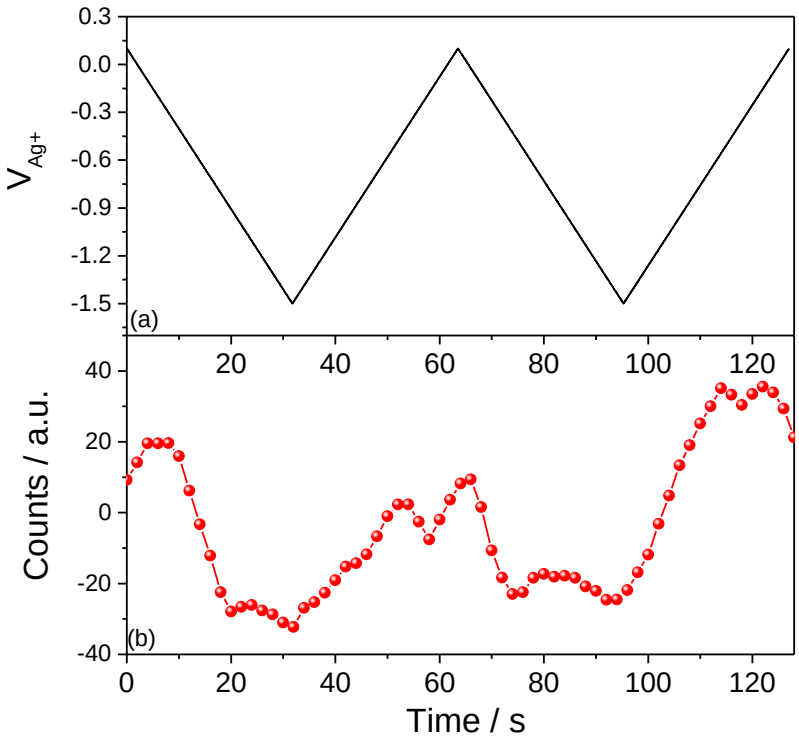

Figure 122 – (a) Potential scan applied during the SFG-SEC experiment (2 CVs); (b) peak intensity of the non-resonant background with time for a [Mn(bpy)(CO)$_3$Br] 1 mM solution in MeCN (0.1 M TBAPF$_6$), recorded at 50 mV s^{-1}, gold working electrode.

The first anomaly in the parabolic behaviour is observed at 20-30 s after the start of the CV, with a slight rise of the non-resonant background. This is the region close to where the potential sweep is switched (vertex 1); at these potentials (-0.8 - -1.5 - -1.2 V$_{Ag+}$) the [Mn(bpy)(CO)$_3$]$_2$

is reduced and we would expect the doubly reduced $[Mn(bpy)(CO)_3]^-$ to be present, prior to its oxidation to reform the $[Mn(bpy)(CO)_3]_2$, although no evidence of the carbonyl vibrational modes (1909 and 1810 cm^{-1}) of $[Mn(bpy)(CO)_3]^-$ was observed in the SFG-SEC spectra (see above, Figure 109, Figure 111 and Figure 114). It is therefore apparent that following $[Mn(bpy)(CO)_3]_2$ reduction and prior to $[Mn(bpy)(CO)_3]_2$ re-formation, a large reorganisation of the double layer occurs. This is in-line with the Stark shift plots which show $[Mn(bpy)(CO)_3]_2$ to be strongly associated to the Au electrode surface so its removal would trigger a reorganisation. In order to probe the processes occurring within the double layer at potentials where we expect $[Mn(bpy)(CO)_3]^-$ to be present, experiments using a -1.8 ps time delay to suppress the NR background have been carried out (Figure 123) in this spectral region that reveals a new feature at 2245 cm^{-1} appearing after $[Mn(bpy)(CO)_3]_2$ reduction, corresponding to one of the vibrational modes characteristic of MeCN. We hypothesise that the doubly reduced complex is rapidly removed from the surface of the negatively charged electrode due to electrostatic repulsion with MeCN, instead being found at the surface and in ordered structures within the double layer.

The second anomaly in the parabolic behaviour of the non-resonant background is found at the potential where the first CV ends and the second one begins (*ca.* 0.1 V_{Ag+}), which corresponds to the $[Mn(bpy)(CO)_3]_2$ reoxidation and disappearance to form the starting $[Mn(bpy)(CO)_3Br]$ and $[Mn(bpy)(CO)_3(MeCN)]^+$ complexes, Figure 121. It appears therefore that the disappearance of $[Mn(bpy)(CO)_3]_2$ is the main cause of the unusual behaviour of the non-resonant background, likely due to the strong affinity shown by the complex with the Au surface (and reflected in the Stark Shift observed).

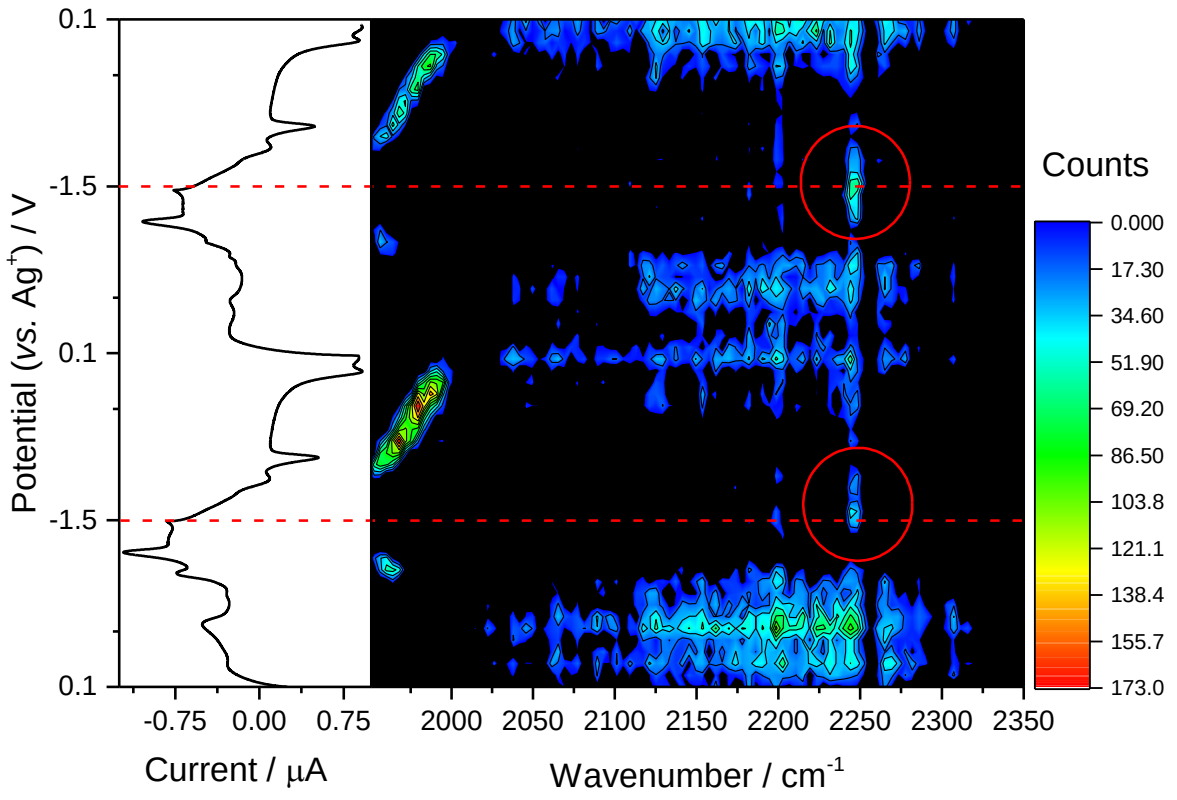

Figure 123 - SFG spectroelectrochemistry of a [Mn(bpy)(CO)$_3$Br] 1 mM solution in MeCN (0.1 M TBAPF$_6$), obtained by recording a SFG spectrum every 2 s while running a CV at 50 mVs^{-1}(2 scans) on a gold working electrode, time delay = -1.8 ps. The dotted lines indicate the potential at which the CV scan direction was reversed, and are added to aid visualisation.

To explore the mechanism of CO_2 reduction the SFG-SEC experiment was carried out on CO_2 purged solutions; the mechanism of CO_2 reduction by [Mn(bpy)(CO)$_3$Br] is well known to require a source of protons, without which catalysis does not take place at a meaningful rate. Two catalytic pathways have been proposed and calculations have indicated[2] they may switch depending upon the proton concentration. Initially we have studied a CO_2 purged solution of [Mn(bpy)(CO)$_3$Br] in MeCN without the deliberate addition of protons (the sample is not anhydrous, making it likely the water content is on the order of 100 ppm or more (from the supplier's website) in order to understand whether CO_2 binding occurs in the absence of water and in the hope that the decreased proton concentration will lead to the build-up of an intermediate species. The SFG spectra obtained are shown in Figure 124; as expected the CV

does not show any remarkable increase in the current density compared to an experiment under argon, indicating that catalytic CO_2 reduction is not occurring at significant levels.

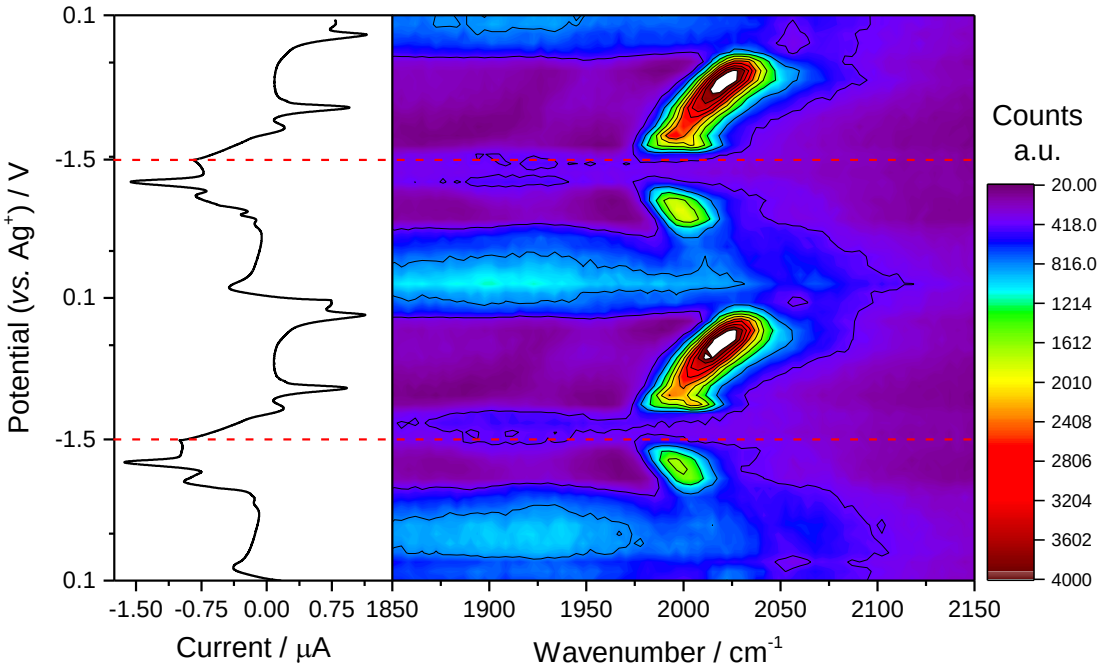

Figure 124 - SFG spectroelectrochemistry of a [Mn(bpy)(CO)$_3$Br] 1 mM solution in MeCN (0.1 M TBAPF$_6$) under CO_2, obtained by recording a SFG spectrum every 2 s while running a CV at 50 mVs^{-1}(2 scans) on a gold working electrode, -1.5 ps time delay. The dotted lines indicate the potential at which the CV scan direction was reversed, and are added to aid visualisation.

The spectrum shows few differences with the argon examples (Figure 109, Figure 111 and Figure 114), with modes corresponding to [Mn(bpy)(CO)$_3$Br], [Mn(bpy)(CO)$_3$(MeCN)]$^+$ and [Mn(bpy)(CO)$_3$]$_2$ all being present. As with previous experiments multiple spectra are dominated by the [Mn(bpy)(CO)$_3$]$_2$ peak, appearing at the expected potentials, and showing the same Stark shift as for the argon data. Interestingly, a new feature also appears at *ca*. 1970 cm^{-1} (-0.7 V_{Ag+}) appearing as a shoulder on the dominant spectral feature of [Mn(bpy)(CO)$_3$]$_2$ at 1950 cm^{-1}, being more prominent when the potential is scanned anodically, at similar

potentials to where we observe the reformation of $[Mn(bpy)(CO)_3]_2$ from the active catalyst species $[Mn(bpy)(CO)_3]^-$ (-0.7 - -0.6 V_{Ag+}) (Figure 125).

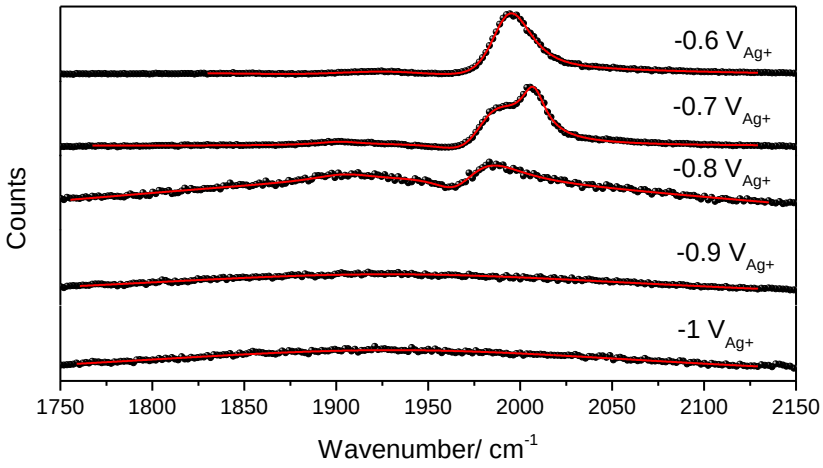

Figure 125 – SFG spectra, recorded at the potentials indicated by averaging every 2 seconds, for a 1 mM solution of $[Mn(bpy)(CO)_3Br]$ in MeCN (0.1 M $TBAPF_6$) purged with CO_2, 50 mVs^{-1}, gold working electrode, -1.5 ps time delay.

The experiment was repeated by carrying out a slow scan rate CV (5 mVs^{-1}) and averaging spectra for 5 seconds to gain a high potential resolution without a loss in S:N; each SFG trace will therefore correspond to a 25 mV region of the CV. Again, a new peak at 1970 cm^{-1} appeared in the spectra during the reoxidation scan under CO_2 ; the new feature seems to be present only for 75-100 mV (between -1.025 and -0.95 V_{Ag+}) in contrast with the peak previously assigned to the $[Mn(bpy)(CO)_3]_2$, which is longer lived. An equivalent experiment under argon clearly shows that this peak is not present without CO_2 (Figure 126). Furthermore we note that the new feature does not show a Stark shift, in contrast to the dominant mode of $[Mn(bpy)(CO)_3]_2$, indicating that the new feature is not characteristic of the same species.

Intriguingly the stability of the new SF signal is shown to not directly relate to the applied potential. In the 50 mV s^{-1} experiment it is noted in two consecutive SFG traces, corresponding to *ca.* 4 seconds of experiment (200 mV) (Figure 125), while in the slow scan rate experiment

(5 mV s^{-1}) the new peak appeared in 4 spectra, corresponding to 20 seconds and 100 mV (Figure 126).

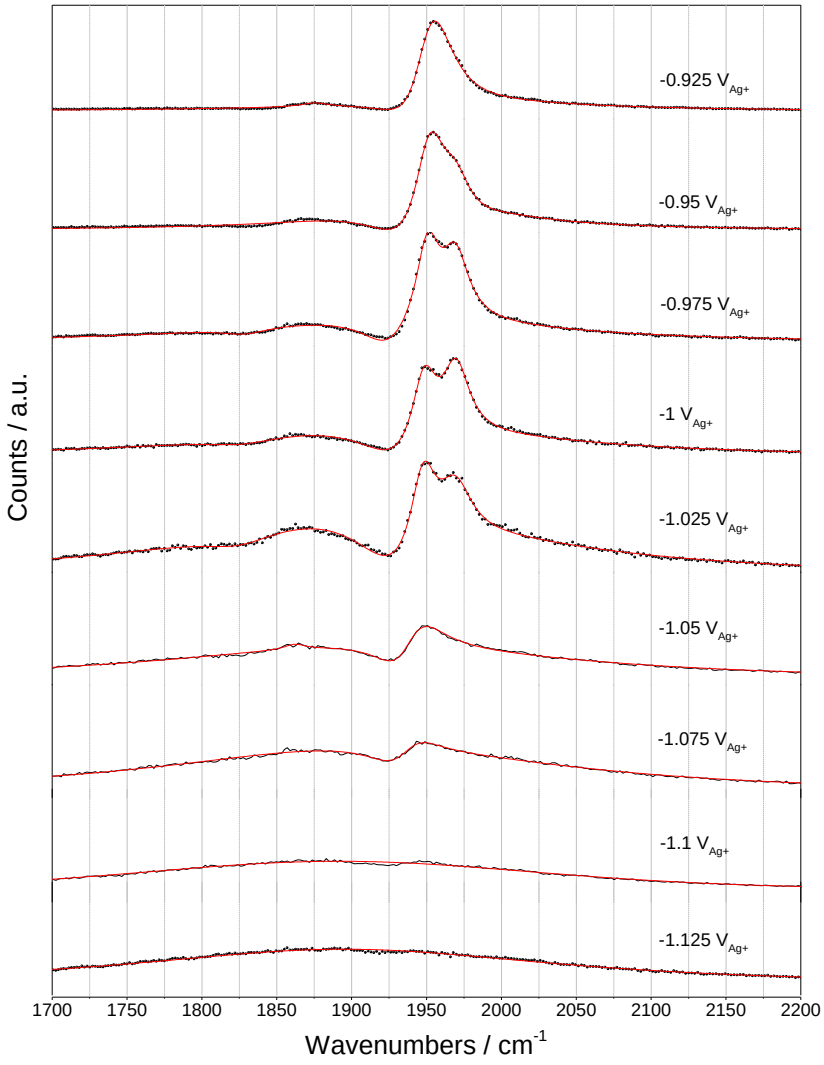

Figure 126 - SFG spectra, recorded at the potentials indicated by averaging every 5 seconds, for a 1 mM solution of [Mn(bpy)(CO)$_3$Br] in MeCN (0.1 M TBAPF$_6$) purged with CO$_2$, 50 mVs^{-1}, gold working electrode.

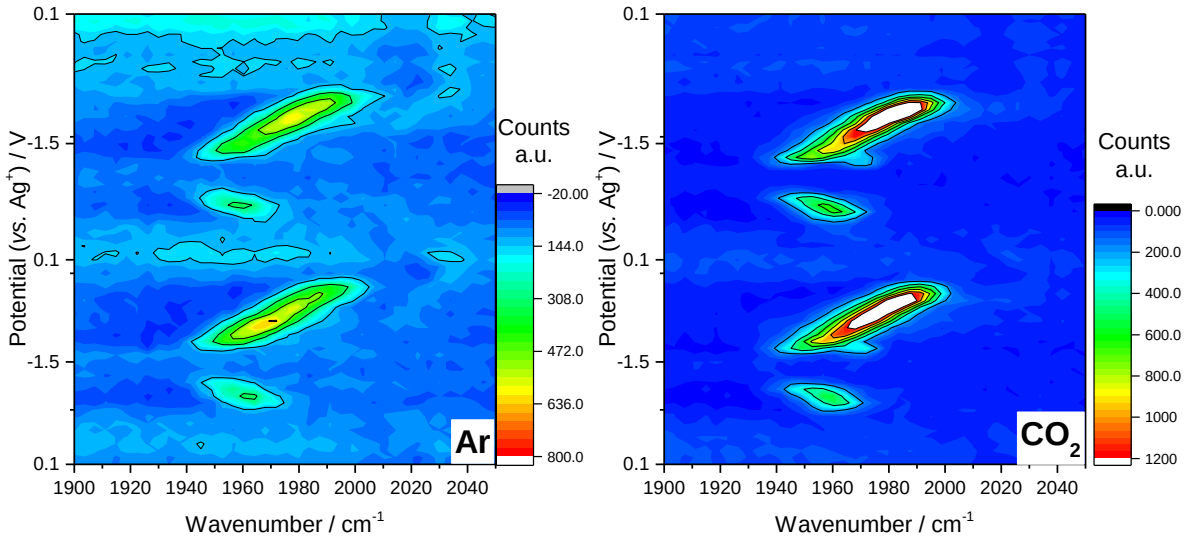

Figure 127 - SFG spectroelectrochemistry of a [Mn(bpy)(CO)$_3$Br] 1 mM solution in MeCN (0.1 M TBAPF$_6$) under argon (left) and CO$_2$,(right) obtained by recording a SFG spectrum every 2 s while running a CV at 50 mVs^{-1}(2 scans) on a gold working electrode. Time delay = -1.5 ps (argon plot) and -1.8 ps (CO$_2$ plot).

We hypothesise that the peak at 1970 cm^{-1} could be due either to a different orientation and distinct population of the [Mn(bpy)(CO)$_3$]$_2$ on the surface of the electrode, or be from a new species forming after the catalytic cycle has been interrupted. The latter hypothesis would be supported by the peak only being present in the reverse sweep of the CV, indicating that the species can form only after the catalytically active [Mn(bpy)(CO)$_3$]$^-$ complex has been formed and in the presence of CO$_2$.

The SFG-SEC analysis of the 1400-1900 cm^{-1} region under CO$_2$ is shown in Figure 128. A feature is also noted at 1458 cm^{-1}, which is present at the potentials where the [Mn(bpy)(CO)$_3$]$_2$ is the dominant species at the electrode surface. Interestingly, the peak at 1458 cm^{-1} shows a similar stark shift (29±2 V cm^{-1}) as the [Mn(bpy)(CO)$_3$]$_2$ peak at *ca.*1950 – 1990 cm^{-1} indicating that the two vibrational modes have a similar level of interaction with the Au surface, potentially due to them being from the same or similar molecule. The SF mode at 1458 cm^{-1} is therefore assigned to a bipyridine mode of the [Mn(bpy)(CO)$_3$]$_2$ species.

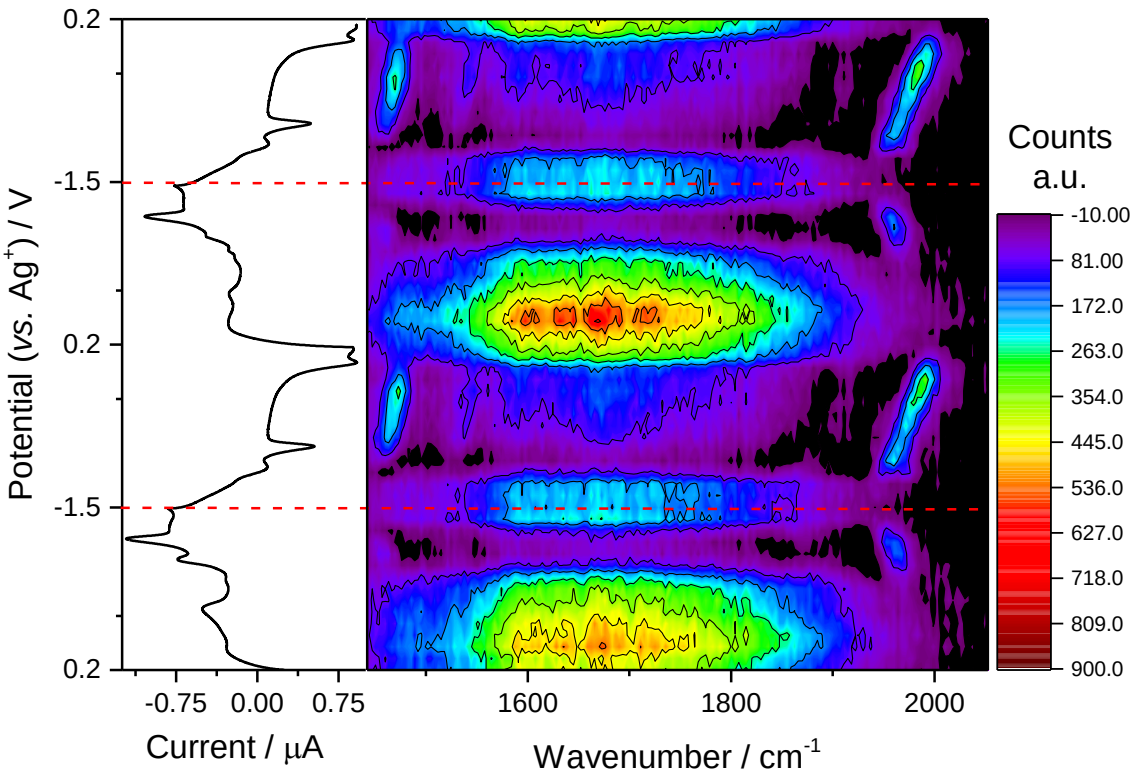

Figure 128 - SFG spectroelectrochemistry of a [Mn(bpy)(CO)$_3$Br] 1 mM solution in MeCN (0.1 M TBAPF$_6$) under CO$_2$, obtained by recording a SFG spectrum every 2 s while running a CV at 50 mVs^{-1}(2 scans) on a gold working electrode. The dotted lines indicate the potential at which the CV scan direction was reversed, and are added to aid visualisation.

Interestingly, a transient feature at 1646 cm^{-1} is also observed in the spectrum when the 1970 cm^{-1} band is observed, as the potential is swept positive from the region where catalysis is expected to occur (-1.5 V_{Ag+}) to that where re-oxidation of the catalyst to [Mn(bpy)(CO)$_3$]$_2$ takes place (-1.1 V_{Ag+}, reverse scan), Figure 129. The new spectral feature is present in both CV cycles. The frequency of the new SF mode is consistent with a metal carboxylate, potentially of the proposed catalytic intermediate [Mn(bpy)(CO)$_3$(COOH)] that has not been previously observed, with the possibility that the 1970 cm^{-1} band is due to a metal carbonyl stretching mode of this complex, however the feature appeared in a single experiment, and further tests, including repeat experiments, are required to allow assignment.

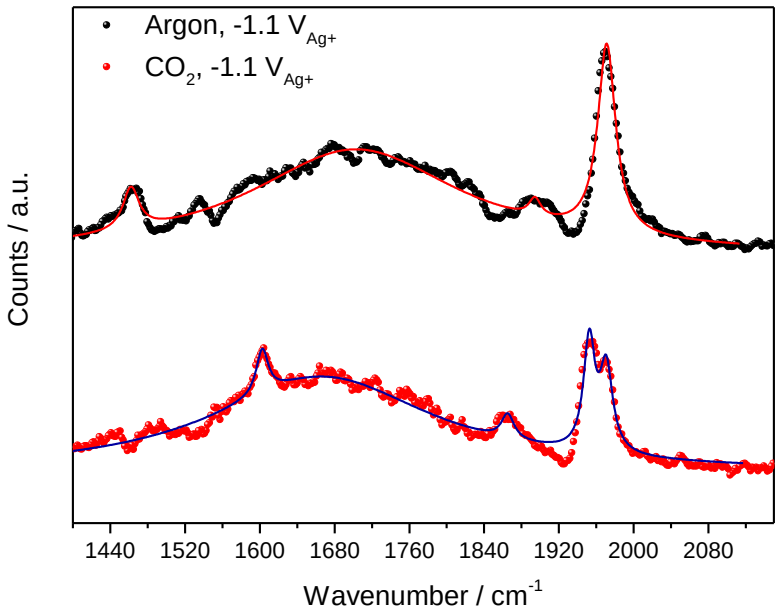

Figure 129 – SFG spectra , recorded at -1.1 V_{Ag+} by averaging every 2 seconds, for a 1 mM solution of $[Mn(bpy)(CO)_3Br]$ in MeCN (0.1 M $TBAPF_6$) purged with argon or CO_2, 50 mVs^{-1}, gold working electrode.

In line with past reports, addition of 2% water to the MeCN solution led to CVs showing a large increase in current density, onsetting at *ca.* -1.2 V_{Ag+}, indicating CO_2 reduction is taking place, (Figure 130).

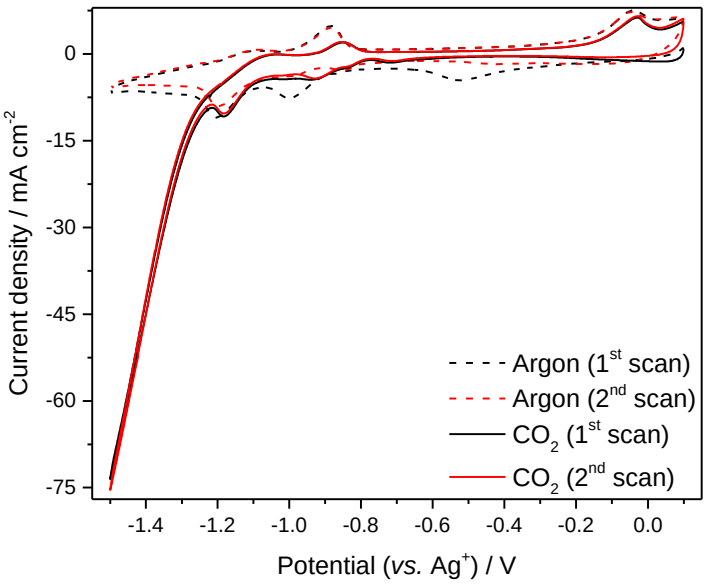

Figure 130 - CVs of a 1 mM solution of $[Mn(bpy)(CO)_3Br]$ in MeCN (0.1 M $TBAPF_6$) purged with argon (dashed lines) and CO_2+1% H_2O(solid lines), 50 mVs^{-1}, gold working electrode in the SFG-SEC cell.

During this experiment, alignment of the SFG-SEC cell with the laser beams was partially lost, resulting in a much lower signal, with poorly resolved spectra. An attempt was also made to carry out experiments with $^{13}CO_2$ to clarify the assignments made, by purging a solution of [Mn(bpy)$(CO)_3$Br] in dry MeCN with argon for 30 minutes and subsequently with $^{13}CO_2$ for 5 minutes, however the alignment of the sample was also poor, and the low signal-to-noise ratio obtained yielded inconclusive spectra. Due to limited time at the experimental facility no further experiments were possible.

As the SFG-SEC experiment has now been developed and tested, in the next section the SFG-SEC technique will be applied to the study of the more challenging reaction mechanism of Ni(cycC) on mercury amalgam electrodes in water at low pH values (see Chapter 2).

5.2.3 *In-situ* SFG-SEC of Ni(cycC)

Ni(cycC) was initially studied using the SFG-SEC technique as the presence of the carboxylic acid represents a potential SF spectroscopic handle, which would make the detection of any species of interest less complicated than for Ni(cyc), which is not characterised by any easily accessible strong IR modes beyond the υ(C-H), the analysis of which can be complicated by even trace organic contaminants. The υ(N-H) modes are planned to be studied in the future as they are challenging to observe in water. The strong IR absorption of water overlaps with this spectral feature and exchange between N-H/N-D groups complicates the use of deuterated solvents (previous studies indicate that scrambling of labelled N-H modes in Ni(cyc) occurs within a few hours[25]).

As Ni(cyc) and its derivatives have been shown to be extremely active when adsorbed on the surface of mercury electrodes,[3] the SFG-SEC experiments were carried out by using a mercury amalgam electrode; this was prepared by dipping a gold disc electrode in mercury for 30-60

seconds and leaving it to dry overnight. During the set-up of the cell in the laser enclosure, it became apparent that the as-prepared amalgam was highly scattering, preventing detection of the SF signal in a reflection mode. The issue was solved by taking extreme care to polish the gold surface prior to amalgamation, and by applying an extremely light polish with 0.05 nm Al_2O_3 slurry to the dried amalgam. Using this preparation method light scatter was reduced, and the use of a collimating lens placed between the sample and the detector allowed significant amounts of the signal to be detected.

Ni(cycC) was studied by preparing 1 mM solutions in D_2O, to prevent the adsorption of water from interfering with the expected stretching modes (1706 cm^{-1} for the protonated complex and 1627 cm^{-1} for the deuterated complex, see Chapter 2) of the carboxylic acid, using KCl as the supporting electrolyte (0.1 M) and a 1 M solution of DCl to adjust the pH of the solutions to 2.

Preliminary experiments highlighted one other limitation; the mercury amalgam was found to be highly unstable to the visible beam at high energy (12 μJ, full experimental details for the SFG-SEC experiments are found at the end of the chapter); blemishes were clearly visible on the surface of the electrode, even after short exposures to the laser beams. This was likely caused by local overheating, which removed the mercury from the amalgam; lowering the visible pulse intensity to 3 μJ appeared to make the electrode stable over more prolonged periods of time, e.g. one day of experiments. Lowering the intensity of the incident light however resulted in significant losses of the SF signal.

The SFG-SEC experiment was initially carried out as previously described for the [Mn(bpy)$(CO)_3$Br], by recording SFG spectra while carrying out a cyclic voltammogram. Due to the high current densities generated by the complex at pH = 2, even in the absence of CO_2, the potential window of study was limited to -0.3 to -1.5 V_{Ag+} and the scan rate kept at 10 mVs^{-1}. It is desirable to avoid the formation of large bubbles of gas, which could compromise both

the electrochemical and spectroscopic measurements. SFG signals were averaged for 2 seconds per spectrum.

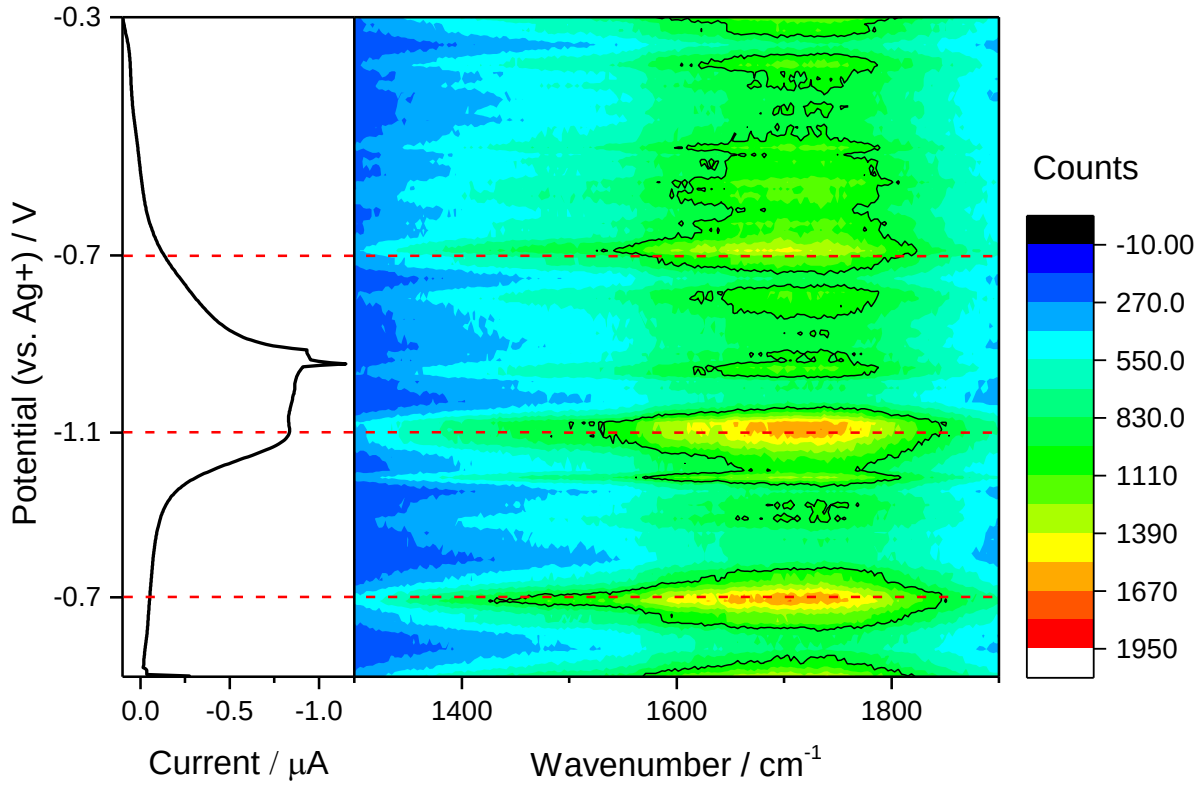

Figure 131 - SFG spectroelectrochemistry of a Ni(cycC) 1 mM solution in D_2O (0.1 M KCl) under argon (pH = 2), obtained by recording a SFG spectrum every 2 s while running a CV at 10 mVs^{-1}(1 scan) on an Au/Hg amalgam working electrode. The dotted lines indicate the main SFG events, and are added to aid visualisation.

The cyclic voltammogram of Ni(cycC) at pH 2 under argon (Figure 131) showed the expected behaviour, with an irreversible wave at -1.2 V_{Ag+} which can be assigned to the $Ni^{II/I}$ couple, overlapped with the catalytic wave due to proton reduction. Between 1300 and 1850 cm^{-1} the SFG spectra are heavily dominated by the non-resonant background, with no significant signal appearing throughout the scanned potential. By plotting the peak of the non-resonant background as a function of time (and therefore potential), as shown in Figure 132, it is clear that it does not follow a parabolic behaviour, as previously observed for $[Mn(bpy)(CO)_3Br]$, with regions of high NR intensity that are seemingly independent of the observed potential.

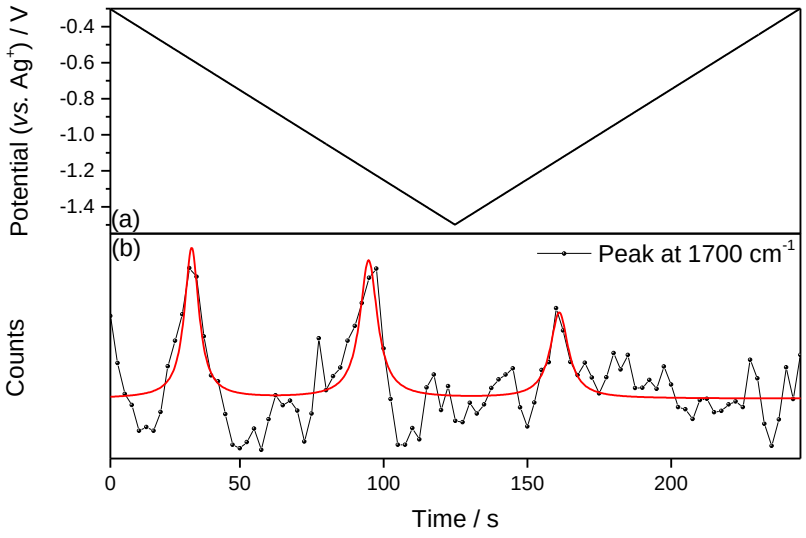

Figure 132 - (a) Potential scan applied during the SFG-SEC experiment (1 CV, 0.1 V s^{-1}); (b) peak intensity of the non-resonant background with time. The red line shows a lorentzian fitting of the experimental trace.

As shown in 2.2.4, Ni(cycC) reductively adsorbs on the surface of the mercury electrode at potentials more positive than the thermodynamic potential for the $Ni^{II/I}$ couple under diffusion control. The surface coverage is dependent on the applied potential, however the dependence is non-linear, instead it shows two potential values at which the surface coverage increases step-wise (Figure 133). This step-wise increase in the surface coverage has been attributed previously to a structural rearrangement of Ni(cyc) on the surface to allow the formation of a monolayer, accompanied by changes in the capacitive properties of the double layer as a consequence of the electrode being saturated with the nickel complex. Comparing the behaviour of the non-resonant background with the behaviour of the surface coverage we find that there is a very close correlation between the potential values at which a peak in the intensity of the non-resonant background is observed (as the two experiments are carried out with *pseudo*-reference electrodes, here, the potentials were compared and by using the potential of the $Ni^{II/I}$ couple as an internal standard.), and the potentials at which the surface coverage

increases step-wise, Figure 131, confirming the dramatic change in the properties of the double layer due to adsorption of Ni(cycC) taking place.

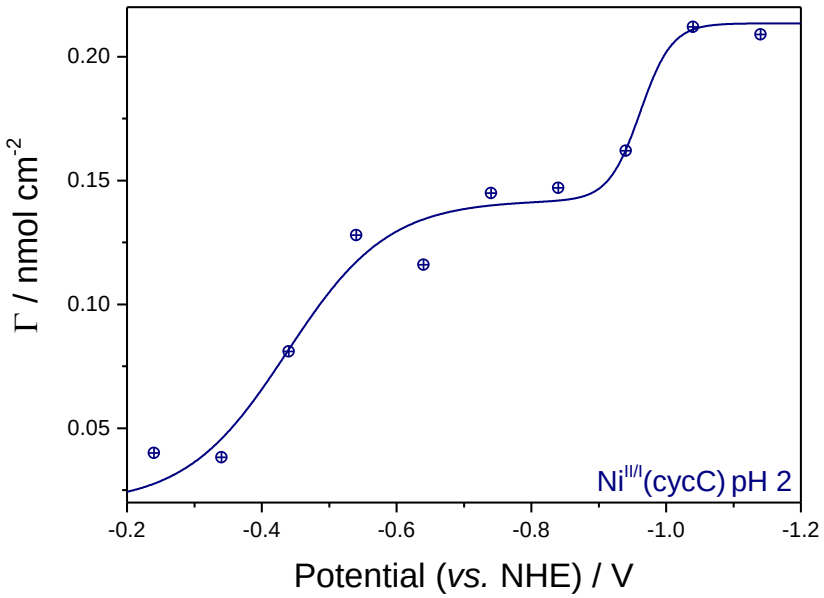

Figure 133 - Dependence of the surface coverage of Ni(cycC) with the potential for 0.1 mM solutions of catalyst, 0.1 M $NaClO_4$, pH 2. The potential was referenced using the $Ni^{II/I}$ couple as an internal standard, then converted to NHE

Several attempts were made to improve the S:N to obtain clearer resonant signals during the CV SFG-SEC experiment, however none were successful. Therefore a different experiment was carried out, where the potential was kept at a value where no processes are expected to occur (-0.25 V_{Ag+}), while collecting SFG spectra for one minute, and then stepping the potential to -1.1 V_{Ag+}, where a monolayer of the complex is expected to form (based on the double potential-step results obtained previously and the response of the non-resonant behaviour) and collecting SFG spectra for the same amount of time. The spectra were manually subtracted, and the difference SF spectra is shown in Figure 134. Two peaks which appear to be resonant features, at 1710 and 1755 cm^{-1} are present. While the first corresponds to the same frequency previously found for the ν_s(CO) of the protonated carboxylic acid of Ni(cycC), the latter is

currently unknown. Furthermore we note that the signal-to-noise ratio for the two features is *ca.* 2:1, which makes the assignment tentative.

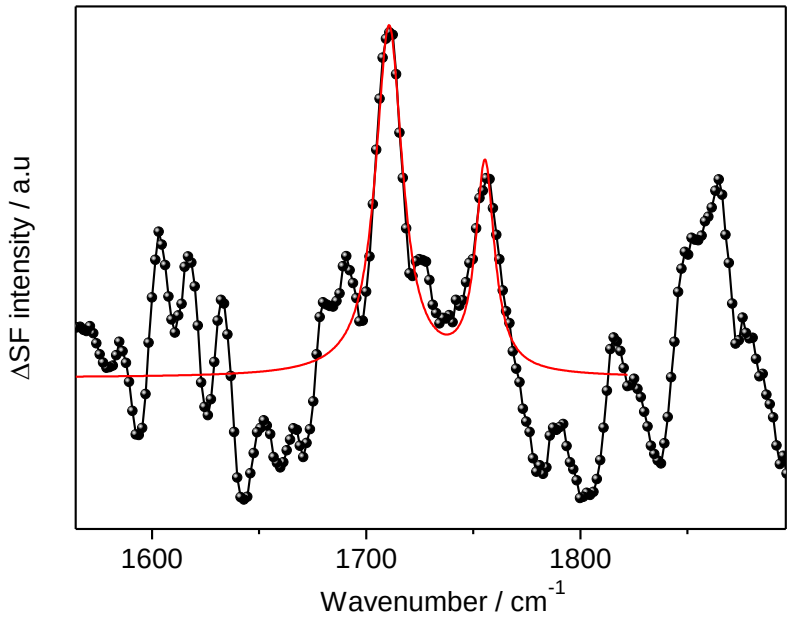

Figure 134 – SFG spectrum obtained by subtracting a spectrum recorded at -0.25 V_{Ag+} (60 s average) from one spectrum recorded at -1.1 V_{Ag+}, (60 s average), for a 1 mM solution of Ni(cycC) in D_2O with 0.1 M KCl as the supporting electrolyte (pH = 2) under argon, Au-Hg amalgam.

Further investigations on the adsorption structure of the complex, which has never been experimentally observed on Hg or amalgam surfaces, and of the mechanism for CO_2 reduction by Ni(cycC), were prevented by the difficulty in obtaining a stable signal; the preparation of the mercury amalgam proved highly irreproducible as polishing the surface of the amalgam always involved the risk of exposing the bare gold underneath. Furthermore, albeit polishing did improve the properties of the electrode for the SEC experiment, the metal surface was still unstable to prolonged irradiation; this led to poorly resolved data, characterised by a large non-resonant background. The use of time delays as a tool to suppress the non-resonant background resulted in signals which were too low. Future improvements for these experiments will include studies on the reproducibility of the mercury amalgam surface, to improve the reflective

properties, and modification of the laser set-up to improve the non-resonant background suppression and the signal-to-noise ratio will be of fundamental importance to the success of the experiments. Regarding this topic, the use of a Fabry-Perot etalon[26] device has been found extremely effective in suppressing the non-resonant background, through the shaping and broadening of a fs visible laser pulse to give a time-asymmetric spectrally narrow visible pulse which enables significantly greater levels of discrimination between the non-resonant and resonant signal. Initial experiments with such a device indicate a greater than 4 fold improvement in the achievable S:N.

5.2.4 Conclusions

In conclusion, we have shown that the SFG spectroscopic technique can be coupled with cyclic voltammetry to carry out *in situ* measurements. With this method, it was possible to detect the different transient species formed at the electrode during cyclic voltammetry of [Mn(bpy)$(CO)_3$Br], and to propose the surface orientation of the species on the Au. Furthermore, by carrying out the SFG-SEC experiment on CO_2 purged solutions for the complex it was possible to observe transient species, tentatively proposed to be the carboxylate complex [Mn(bpy)$(CO)_3$(COOH)], which has been proposed to be the first intermediate in the CO_2 reduction mechanism by the Mn complexes.[2,4,8,27]

Although it was not possible to study the mechanism of CO_2 reduction by Ni(cyc) and Ni(cycC) using the SFG-SEC experiment, which was the main objective of this chapter, the results obtained during the analysis of [Mn(bpy)$(CO)_3$Br] proved SFG-SEC to be a powerful tool. It was possible to record the transformations *in situ* at the electrode/electrolyte interface in real time (from a single CV experiment) while the potential was scanned. This is in contrast to more traditional IR-SEC techniques, which often rely on the complete transformation of the bulk species in order to detect intermediates, which will not necessarily correspond to the transient species present in the double layer.

5.3 Materials and methods

5.3.1 Materials

2,2'-bipyridine and $Mn(CO)_5Br$ were purchased from Sigma and used as received. [Mn(bpy)(CO_3Br] was synthesised according to literature procedures.[4] Milli-Q water (18.2 MΩ) was used throughout. All electrolyte salts and solvents were purchased from Sigma Aldrich or VWR and used without further purification. Ar, N_2 and CO_2 were purchased from BOC at CP grade or higher. The pH of aqueous solutions was adjusted by adding 1 M $HClO_4$ or NaOH to the pre-purged solution until the desired value was reached, measuring with a Hannah pH probe, which was calibrated daily.

5.3.2 Spectroelectrochemical cell and sample preparation

The custom-built SEC cell was a Teflon cross piece (57 x 57 mm) equipped with gas tight Bola screw fittings on three sides and a septum gas tight screw fitting. In place of the septum, a CaF_2 window (Crystran, Ø = 14 mm, thickness = 2 mm) was placed, and a seal was ensured with a Viton o-ring (Ø = 16 mm) placed between the window and the cap and a pre-cut Teflon spacer (thickness = 0.05 mm) placed between the window and the main body of the cell. The side screw caps were equipped with rubber septa through which a platinum wire (the counter electrode) and a silver wire (the *pseudo*-reference electrode) bent at 90° were inserted. The silver wire was cleaned by polishing with sandpaper and rinsing with 0.1 M HNO_3, water and acetone, while the platinum wire was cleaned by annealing with a blow torch. Care was taken to ensure that the two wires were touching the Teflon spacer, as to minimise the distance with the working electrode.

The working electrode was either a gold polycrystalline disc (Ø = 16 mm) or a Au-Hg amalgam. The gold disc was hand polished to mirror finish using decreasing sizes of diamond (15, 6 and 1 μm) and alumina (0.5 μm) slurry before every experiment. The amalgam was

prepared by dipping the freshly polished gold disc electrode in mercury for 1 minute, followed by drying overnight. Before the experiment, a light polish with alumina slurry (0.5 μm) was applied to the electrode, taking care not to expose the gold surface under the amalgam. The electrode was inserted into the last remaining port of the SEC cell, opposite the CaF_2 window, and secured with the gas-tight fitting, taking care that the Peek body of the electrode was touching the Teflon spacer to ensure the correct pathlength. The cell was assembled and purged with argon or CO_2 for 30 minutes, and the pre-purged solutions of the analytes were transferred *via* cannula transfer. The electrochemistry was carried out by using a Palmsens[3] potentiostat (Alvatek).

5.3.3 Laser apparatus

A single OPA-DFG unit driven by the 50 fs ULTRA system at the Central Laser Facility generates IR light across a 500 cm^{-1} useable bandwidth at 10 kHz. Both the 800 nm 10 kHz Ti:Sapphire ps and fs amplifier arms of ULTRA were operated together for the experiments. The ps 800 nm beam was optimised for bandwidth by shaping the seed pulses (Fastlite) to give a ~1 nm FWHH amplified output corresponding to a 15 cm^{-1} bandwidth and ~1.5 ps duration. A 50 fs Ti:Sapphire amplifier output (~6W) was split to pump two separate OPAs, both generating IR light in the range of 3-10 μm using difference frequency mixing of the signal and idler in $AgGaS_2$ (Light Conversion, Topas). For the IR-Vis SFG experiments, the OPA pulse energy was between 1 - 1.5 μJ at 5 μm. The energy at the sample was around half this.

A schematic of the IR-Vis SFG experiment is shown in Scheme 32. The ps 800 nm light was attenuated to give pulse energies at the sample adjustable between 0-12 μJ. The beam was passed over a computer controlled delay line, reduced in size from the original ~ 7 to 2.5 mm FWHH using a Galilean telescope and then focused behind the sample position (f=+150 mm UVFS PCX). The spot size was set at ~300 μm FWHH at the sample using a beam profiling

camera by adjustment of the final focussing lens. The IR beam was collimated after the OPA by a ~1 m focal length concave mirror, giving ~ 7 mm FWHH, which was focussed onto the sample using a 7.5 cm focal length 90 degree off axis parabolic mirror. The parabolic mirror had a hole drilled through the centre to pass the 800 nm beam. This arrangement gave a FWHH of ~75-100 μm IR spot.

The light was focussed (f=+25 mm) onto the entrance slit of an imaging spectrograph (Holospec) and dispersed onto a high sensitivity CCD array (Andor Idus). A periscope was used to turn the IR-Vis SFG signals so that unwanted interface signals spread along the vertical, undispersed CCD axis.

The IR and 800 nm beams were overlapped at the sample position using a pinhole and their delays coarsely set by observing an IR pump-probe signal on an oscilloscope-monitored single element MCT detector in transmission from 800 nm pumped Germanium. The correct timing was then found by observing by-eye the up converted light from a 2 mm thick sample of ZnS. The IR-Vis SFG reflection off the ZnS was used for alignment to the spectrograph. The data collection was carried out with a homemade program built with Labview software.

5.4 References

1. J. D. Froehlich and C. P. Kubiak, *J. Am. Chem. Soc.*, 2015, **137**, 3565–3573.

2. C. Riplinger, M. D. Sampson, A. M. Ritzmann, C. P. Kubiak, and E. A. Carter, *J. Am. Chem. Soc.*, 2014, **136**, 16285–16298.

3. G. B. Balazs and F. C. Anson, *J. Electroanal. Chem.*, 1992, 322, 325–345.

4. M. Bourrez, F. Molton, S. Chardon-Noblat, and A. Deronzier, *Angew. Chemie Int. Ed.*, 2011, **50**, 9903–9906.

5. F. Hartl, B. D. Rossenaar, G. J. Stor, and D. J. Stufkens, *Recl. Trav. Chim. des Pays-Bas*, 1995, **114**, 565–570.

6. S. Ye and M. Osawa, *Chem. Lett.*, 2009, **38**, 386–391.

7. F. Hartl, B. D. Rossenaar, G. J. Stor, and D. J. Stufkens, *Recl. Trav. Chim. des Pays-Bas*, 2010, **114**, 565–570.

8. J. M. Smieja, M. D. Sampson, K. A. Grice, E. E. Benson, J. D. Froehlich, and C. P. Kubiak, *Inorg. Chem.*, 2013, **52**, 2484–2491.

9. M. B. Raschke, M. Hayashi, S. H. Lin, and Y. R. Shen, *Chem. Phys. Lett.*, 2002, **359**, 367–372.

10. A. L. Harris, C. E. D. Chidsey, N. J. Levinos, and D. N. Loiacono, *Chem. Phys. Lett.*, 1987, **141**, 350–356.

11. I. V. Stiopkin, H. D. Jayathilake, C. Weeraman, and A. V. Benderskii, *J. Chem. Phys.*, 2010, **132**, 234503.

12. E. J. Heilweil, R. R. Cavanagh, and J. C. Stephenson, *Chem. Phys. Lett.*, 1987, **134**, 181–

188.

13. J. Stark, *Nature*, 1913, **92**, 401–401.

14. A. Tadjeddine and P. Guyot-Sionnest, *Electrochim. Acta*, 1991, **36**, 1839–1847.

15. S. Baldelli, *J. Phys. Chem. B*, 2005, **109**, 13049–13051.

16. G. Q. Lu, A. Lagutchev, D. D. Dlott, and A. Wieckowski, *Surf. Sci.*, 2005, **585**, 3–16.

17. N. García Rey and D. D. Dlott, *J. Phys. Chem. C*, 2015, **119**, 20892–20899.

18. Q. Wan and G. Galli, *Phys. Rev. Lett.*, 2015, **115**, 246404.

19. M. L. Clark, B. Rudshteyn, A. Ge, S. A. Chabolla, C. W. Machan, B. T. Psciuk, J. Song, G. Canzi, T. Lian, V. S. Batista, and C. P. Kubiak, *J. Phys. Chem. C*, 2016, **120**, 1657–1665.

20. R. G. Greenler, D. R. Snider, D. Witt, and R. S. Sorbello, *Surf. Sci.*, 1982, **118**, 415–428.

21. A. J. Cowan, P. Portius, H. K. Kawanami, O. S. Jina, D. C. Grills, X.-Z. Sun, J. McMaster, and M. W. George, *Proc. Natl. Acad. Sci. U. S. A.*, 2007, **104**, 6933–8.

22. A. D. Becke, *J. Chem. Phys.*, 1993, **98**, 5648.

23. S. H. Vosko, L. Wilk, and M. Nusair, *Can. J. Phys.*, 1980, **58**, 1200–1211.

24. C. Lee, W. Yang, and R. G. Parr, *Phys. Rev. B*, 1988, **37**, 785–789.

25. Jesse Dan Froehlich, 2015.

26. B. Braunschweig, P. Mukherjee, R. B. Kutz, A. Wieckowski, and D. D. Dlott, *J. Chem. Phys.*, 2010, **133**, 234702.

27. D. C. Grills, J. Farrington, B. H. Layne, S. V. Lymar, B. a Mello, J. M. Preses, and J. F. Wishart, *J. Am. Chem. Soc.*, 2014, 140328210527004.

Conclusions and future work

In this thesis, the electrochemical and photochemical CO_2 reduction to CO by new derivatives of Ni(cyc) has been carried out.

In chapters 2 and 3, the synthesis of two new nickel complexes of substituted tetraazamacrocycles, Ni(cycC) and Ni(cycP) have been shown, together with their electrochemical properties for the catalytic CO_2 reduction and their ability to bind to semiconductor oxides and enable efficient electron transfer from the excited semiconductor.

In the example of Ni(cycC), it was demonstrated that modification of the ligand framework without decreasing the CO_2 reduction activity was possible, by carrying out the electrocatalysis at pH 5. Furthermore, the presence of an ancillary functional group close to the metal centre was shown to dramatically improve catalysis at low pH values. The activity of Ni(cycC) has been benchmarked against the most well-known CO_2 reduction molecular catalysts, using various techniques known in the literature, and what became apparent was that despite the higher TOF shown by the catalysts, compared to many other known complexes, Ni(cycC) appears to be more susceptible to inhibition than the parent Ni(cyc).

In contrast, modification of the cyc framework with a methylene-phosphonic acid on one of the amine position to yield Ni(cycP) was shown to affect CO_2 reduction catalysis in a negative way, with decreased current densities and poor selectivity for CO over H_2. This behaviour is in

line with past reports of modified cyc complexes of nickel, however the reasons for the decrease in activity are still unclear.

Future research in the field of Ni(cyc) and derivatives will have to address the two main drawbacks for this class of catalysts, product inhibition and decrease in activity upon modification. The first issue could be solved by adding efficient CO scavengers to the reaction mixtures. This method has been shown as a prove of principle by adding a nickel macrocycle with a strong affinity to CO to a mixture of Ni(cyc) in MeCN:H_2O, however less costly materials which are easier to purify would be of great interest to the current research on CO_2 reduction. The second issue will be solved only once a deep knowledge of the CO_2 reduction mechanism will be found. While hypothesised, the CO_2 reduction mechanism by Ni(cyc), and in particular the structure of the adsorbed species on the mercury surface and the CO_2 and CO adducts, are still unknown. Disclosing the nature of these species, perhaps by using spectroelectrochemical techniques such as SFG, could allow the rational design of new macrocyclic complexes, such as macrocycles bearing ancillary groups participating in the catalytic steps, as has been shown in the recent literature, and with Ni(cycC), for proton sources in the second coordination sphere of a catalyst.

Covalently binding Ni(cycC) to TiO_2 and $Ti_{0.8}Zr_{0.2}O_2$ proved the advantages of an heterogeneous photocatalyst over the coupling of a photosensitiser and a catalyst in solution: the complex immobilised on the semiconductors showed faster electron transfer than Ni(cyc) in solution in the presence of the semiconductor film. While a carboxylic acid proved a labile group for CO_2 reduction photocatalysis, the phosphonate group on Ni(cycP) was shown to be much more stable. The higher stability came at the cost of a slower electron transfer, and future work could explore different anchoring groups which show both fast electron transfer and high stability in aqueous environments.

In chapter 4 the photocatalytic activity of Ni(cycP) for CO_2 reduction was shown in two different systems. Initially, the catalyst was co-anchored to an inert support with a ruthenium dye, RuP, and it was shown that the heterogeneous system was more active than the two components in solution by carrying out photocatalytic experiments and spectroscopic studies. While we demonstrated successful CO_2 reduction to CO in water, the selectivity was found to be poor (4:1 H_2:CO), and future work will look at the reasons for the low selectivity; furthermore, the use of different hole scavengers and cheaper dyes will be explored in order to further improve the photocatalyst. Subsequently, ZnSe quantum dots have been showed to be efficient photosensitisers for the CO_2 reduction to CO when Ni(cycP) was immobilised on the surface, and the kinetics of the charge carriers have been studied in detail with ultrafast transient absorption spectroscopy. We found that the lifetime of the photogenerated holes and electrons is determined by the presence of trap states close to the VB and the CB, respectively, which are due to defects on the surface. The presence of the long-lived photoelectrons in the presence of a hole scavenger allows efficient electron transfer to the immobilised Ni(cycP). In the future, it would be interesting to explore the presence of trap states further, for example by purposefully introducing defects in the material.

Finally, in the last chapter we have set-up an *in situ* SFG-SEC experiment in collaboration with the UK-CLF facility, and we have used it to demonstrate that it is possible to observe reaction intermediates, as they are formed at the electrode during a CV, by analysing the SFG-SEC spectra of [Mn(bpy)(CO)Br], a well-known CO_2 reduction catalyst. We were able to identify the major intermediate species that form as the potential is scanned under argon, demonstrating the usefulness of the technique. Furthermore, we were able to obtain preliminary data on the SFG-SEC of Ni(cycC), and its adsorption on the surface of a Hg electrode. Despite the advantages of the technique, it still suffers from poor S:N ratios, the presence of the non-resonant background complicating the spectral assignments and poor time resolution. The S:N

ratio and the non-resonant background suppression can be achieved by implementing pulse shaping of the IR beam incident to the sample, and some progress has been made during the last set of experiments (not included in this thesis due to time constraints), while time resolution will be solved by careful design of the SEC cell, as for example the use of microelectrodes to reduce the cell time constant.

salimmo sù, el primo e io secondo,

tanto ch'i' vidi de le cose belle

che porta 'l ciel, per un pertugio tondo.

E quindi uscimmo a riveder le stelle.

- *Dante Alighieri*